

Synthesis, engineering and development of nano/micro antibacterial composites for drug delivery.

A thesis by

Suleman Ramzan

2019

Awarded by De Montfort University



Abstract

Antibiotic resistance is one of the greatest health concerns worldwide. Data shows within the last 50 years, the number of species and strains of pathogenic and commensal bacteria resistant to antibiotics, has increased virtually monotonically worldwide.

Research presented here shows successful synthesis of polymeric drug composites for antibacterial drug delivery, using the electro hydrodynamic atomization technique (EHDA). A biodegradable polymer poly (lactic-co-glycolic acid) (PLGA) proved to be suitable for sustained drug delivery. Materials added to the polymeric composites included the active agent amoxicillin (AMX) and metallic nanoparticles varying in size and morphology. Upon successful synthesis, the drug release, antibacterial efficacy and cell culture data, collated, confirmed the EHDA process is a good alternative method for synthesising antibacterial composite formulations. It is an easy one step process, regardless of the number of excipients added, and also allows for encapsulation of poorly soluble drugs.

The first step was to synthesise metallic nanoparticles; varying in shape and size, this would help determine if differences in shape and size of nanoparticles will have an effect on drug content and release data, as well as antibacterial efficacy. Therefore, three types of metals were chosen for their varying antibacterial activity; silver, gold and copper. Silver was synthesised varying in shape and size, including spherical, wire and polygonal or edged. Upon successful synthesis, the next step was to formulate suspensions, made up of PLGA and AMX, along with the varying metallic nanoparticles to electrospray. Two different solvents were used acetone and dichloromethane (DCM), the varying differences in characteristic qualities like electrical conductivity and viscosity, allowed for determination of a stable spray. Results showed the best solvent to use between the two was acetone due to a much higher electrical conductivity and lower viscosity.

Thereafter, the composite samples collected were analysed. Drug loading for the formulation containing PLGA and AMX (F2) only was 1.18%, but with the addition of different metallic nanoparticles it increased up to 2.57%. Drug release for F2 was at 18.6% and increased up to 56.1% depending on metallic nanoparticle added.

Metallic nanoparticles exhibit antibacterial efficacy, with AgNPs showing the greatest antibacterial activity, confirmed through disk diffusion zone sizes. Antibacterial activity enhancement was proved by formulations containing silver nanoparticles, showing increased

activity against *S. aureus* through increased disk diffusion zones compared to using AMX and silver nanoparticles on their own. AgNPs against *S. aureus* gave an average inhibition zone of 18.8 mm when compared to CuNP which only gave an average inhibition zone size of 16.07mm. Full formulation containing PLGA AMX and edge shaped silver nanoparticles (F5) proved to have the highest antibacterial efficacy when compared to the other formulations. This was explained through an increase in surface area to volume ratio of the silver nanoparticles, when compared to the spherical and wire shaped nanoparticles. Cell culture data namely the MTT assay also showed (F5) had a cell viability of 71%, this displays promising signs for this formulation for future use as an antibacterial agent.

Declaration

I declare that all the work presented in this thesis is entirely my own and has not been submitted in whole or in part of any previous professional qualification; except where stated by reference or acknowledgment.

Signature:

Date:

Acknowledgments



In the Name of Allāh, the Most Gracious, the Most Merciful

All praise and thanks to Allah who enabled me to complete this work, and guided me along this path in life. I would like to dedicate this thesis to my parents, without their support and encouragement, I wouldn't have come this far. To my mother for always pushing me to be a better person, and trying to cure me of my laziness. And especially, to my father who worked tirelessly and sacrificed a lot to help me achieve my dream. It is my father's dream that kept me motivated, his sacrifices pushed me to work harder, and in reaching this point I hope to have made him proud. I would like to thank my wife for her support, her commitment to helping me get over the line, and above all having her by my side in this final period when I needed her support the most. I would like to thank my Professor for believing in me from the very beginning, for giving me the opportunity to become a PhD student under his supervision, and for keeping faith in me after all those times I let him down. I would like to thank my close friend Ali, whose friendship I have cherished and will cherish, for all the jokes and good moments we shared together, I will never forget. To my friend Usman, I hope mentioning you here is enough to make up for not seeing you for a few months whilst I was hidden away finishing this; you are always in my prayers, and I pray Allah grants you good health. I would like to thank all my fellow lab friends who made each day enjoyable, interesting and never dull.

وَأَخْفِضْ لَهُمَا جَنَاحَ الذُّلِّ مِنَ الرَّحْمَةِ وَقُلْ رَبِّ ارْحَمْهُمَا كَمَا رَبَّيَانِي صَغِيرًا ﴿٢٤﴾

And lower to them the wing of humility out of mercy and say, "My Lord, have mercy upon them as they brought me up when I was small." (Al-Isra - 24)

“We wake up from sleep by the will of Allah, He alone, restores our souls to us, and it is He to whom all thanks are due”

Conferences

- 7th Annual Congress on Material Research and Technology. Berlin, Germany. 20-21st February 2016 - POSTER PRESENTATION.
- EPSRC EHDA Network. International PharmTech Conference. Leicester, UK. 4th November 2016 – POSTER PRESENTATION.
- 5th Quality by Design Symposium. Leicester, UK. 29th March 2017 – POSTER PRESENTATION.
- University College London 2nd International Pharmaceutical Conference. London, UK. July 2017 – POSTER PRESENTATION.
- UKPharmsci Science of Medicines APS conference. University of Hertfordshire, UK. 5-7th September 2017 – POSTER PRESENTATION.
- Pharmaceutical Science and Innovations in Pharma and Industry. London, UK. 26-27th February 2018 – ORAL PRESENTATION.
- 6th Quality by Design Symposium. Leicester, UK. 14th March 2018 – POSTER PRESENTATION.
- 7th Quality by Design Symposium. Leicester, UK. 26th March 2019 – POSTER PRESENTATION.
- Pharmaceutica Meet 2019 conference. Istanbul, Turkey. 27-28th May 2019 - POSTER PRESENTATION.
- 55th Congress of the European Societies of Toxicology (EUROTOX). Helsinki, Finland. 8-11th September - POSTER PRESENTATION.

Chapter 1 - Literature Review	1
1.1 Microorganisms	1
1.1.1 Bacteria	1
1.1.1.1 Bacterial controlled synthesis of metal oxide nanoparticles	2
1.1.1.2 Bacterial induced synthesis of metal oxide nanoparticles	3
1.1.1.3 Gram-positive bacteria	3
1.1.1.3.1 <i>Staphylococcus aureus</i> (<i>S. aureus</i>)	4
1.1.1.3.1.1 Membrane-damaging toxins.....	6
1.1.1.3.1.2 Enzymes.....	6
1.1.1.3.2.1 Methicillin-resistant <i>S. aureus</i> (MRSA) outbreak	7
1.1.1.3.2.2 Toxic shock syndrome (TSS)	7
1.1.1.4 Gram-negative bacteria	8
1.1.1.4.1 <i>Escherichia Coli</i> (<i>E. coli</i>).....	9
1.1.1.4.1.1 Urinary tract infections (UTI).....	10
1.1.1.4.1.2 <i>E. coli</i> O157:H7	11
1.1.2 Fungi.....	12
1.1.3 Viruses.....	14
1.1.3.1 Influenza virus.....	14
1.1.3.2 Human Immunodeficiency Virus (HIV).....	15
1.1.3.3 Dengue virus	16
1.2 Antibacterial Agents.....	16
1.2.1 Antibiotic Resistance.....	18
1.3 Nanotechnology	20
1.3.1 Nanoparticles.....	20
1.3.2 Metal nanoparticles as antibacterial agents.....	21
1.3.3 Silver nanoparticles	21
1.3.4 Gold nanoparticles.....	22
1.3.5 Copper nanoparticles.....	22
1.4 Electrohydrodynamic atomisation (EHDA).....	23
1.4.1 EHDA process.....	23
1.4.2 Electrospraying.....	24
1.4.2.1 Processing parameters of electrospraying.....	25
1.4.2.1.1 Electrical conductivity	25
1.4.2.1.2 Flow rate.....	25
1.4.2.1.3 Applied voltage	26
1.4.2.1.4 Capillary tip to collector distance	26

1.4.2.1.5 Temperature.....	26
1.4.2.1.6 Humidity.....	26
1.4.2.2 Applications of electrospraying	27
1.4.2.2.1 Antibacterial drugs	27
1.4.2.2.2 Anti-inflammatory drugs	27
1.4.2.2.3 Food coatings.....	28
1.4.3 Electrospinning.....	28
1.4.3.1 Processing parameters for electrospinning	30
1.4.3.1.1 Solution concentration	30
1.4.3.1.2 Molecular weight	31
1.4.3.1.3 Viscosity	31
1.4.3.1.4 Surface tension.....	31
1.4.3.1.5 Electrical conductivity	31
1.4.3.1.6 Applied voltage	32
1.4.3.1.7 Flow rate.....	32
1.4.3.1.8 Capillary tip to collector distance	32
1.4.3.1.9 Temperature.....	33
1.4.3.1.10 Humidity.....	33
1.4.3.2 Applications of electrospinning	33
1.4.3.2.1 Tissue engineering applications.....	33
1.4.3.2.2 Wound dressings	34
1.4.3.2.3 Drug delivery	34
1.4.3.2.4 Filtration	35
1.4.3.2.5 Cosmetics	36
1.4.4 Polymer choice.....	36
1.4.5 Solvent choice	38
1.4.6 Physical characterisation	38
1.4.7 Chemical characterisation.....	38
1.4.8 Coaxial EHDA	39
1.4.8.1 Coaxial electrospraying.....	39
1.4.8.2 Coaxial electrospinning.....	39
1.4.9 History.....	40
Chapter 2 – Materials and methods.....	42
2.1 Materials.....	42
2.1.1 Polymer	42
2.1.1.1 Poly(lactic-co-glycolic acid) (PLGA)	42
2.1.2 Drug.....	43

2.1.2.1 Amoxicillin (AMX)	43
2.1.3 Solvent.....	44
2.1.3.1 Dichloromethane (DCM)	44
2.1.3.2 Acetone.....	45
2.1.4 Precursor materials	46
2.1.4.1 Silver nitrate (AgNO ₃).....	46
2.1.4.2 Gold (III) chloride trihydrate (HAuCl ₄ x 3H ₂ O)	47
2.1.4.3 Copper (II) sulphate (CuSO ₄)	48
2.1.5 Capping agents	49
2.1.5.1 Trisodium citrate (Na ₃ C ₆ H ₅ O ₇).....	49
2.1.5.2 Polyvinylpyrrolidone (PVP).....	50
2.1.5.3 Sodium bromide (NaBr).....	51
2.1.6 Reducing agent.....	52
2.1.6.1 Ascorbic acid	52
2.1.7 Vehicles	53
2.1.7.1 Ethylene glycol (EG).....	53
2.1.7.2 Deionised water (D.I water)	54
2.2 Methods.....	55
2.2.1 Determination of Material Properties	55
2.2.1.1 Viscosity.....	55
2.2.1.2 Surface tension.....	56
2.2.1.3 Electrical conductivity	57
2.2.2 Electrohydrodynamic atomisation (EHDA).....	58
2.2.3 Scanning electron microscope (SEM).....	59
2.2.4 Differential scanning calorimetry (DSC).....	60
2.2.5 Thermogravimetric analysis (TGA)	61
2.2.6 Attenuated total reflection Fourier transform infrared spectroscopy (ATR-FTIR)	62
2.2.7 X-ray diffraction (XRD)	63
2.2.8 Raman spectroscopy	64
2.2.9 Zeta potential	65
2.2.10 In-vitro drug release	66
2.2.11 Ultraviolet–visible spectroscopy (UV-vis).....	67
2.2.12 Disk diffusion testing.....	68
2.2.13 Ex-vivo cell culture	69
2.2.14 Optical density	70
Chapter 3 – Synthesis of metallic nanoparticles.....	71
3.1 Introduction.....	71

3.2 Aims & Objectives.....	73
3.3 Materials and methods.....	74
3.3.1 Materials.....	74
3.3.1.1 Silver nanoparticles (AgNP).....	74
3.3.1.2 Silver nanowires (AgNW).....	74
3.3.1.3 Polygonal silver nanoparticles (AgP).....	75
3.3.1.4 Gold nanoparticles (AuNP).....	75
3.3.1.5 Copper nanoparticles (CuNP).....	76
3.3.2 Methods.....	77
3.3.2.1 Morphological observation through scanning electron microscopy (SEM).....	77
3.3.2.2 Elemental analysis through energy dispersive spectroscopy (EDS).....	77
3.3.2.3 Particle size analysis through size distribution.....	77
3.3.2.4 Attenuated total reflectance Fourier transform infrared spectroscopy (ATR-FTIR)....	77
3.3.2.5 Raman spectroscopy.....	78
3.3.2.6 Ultraviolet-visible spectroscopy (UV-Vis).....	78
3.3.2.7 X-Ray diffraction (XRD).....	78
3.3.2.8 Zeta potential.....	79
3.4 Results and Discussion.....	80
3.4.1 Synthesised metallic nanoparticle images.....	80
3.4.2 SEM/EDS.....	81
3.4.3 ATR-FTIR.....	88
3.4.4 Raman spectroscopy.....	90
3.4.5 UV-vis spectroscopy.....	91
3.4.6 XRD.....	93
3.4.7 Zeta Potential Values.....	95
3.5 Conclusion.....	98
Chapter 4 – Synthesis of polymeric composites.....	99
4.1 Introduction.....	99
4.2 Aims & Objectives.....	100
4.3 Materials and Methods.....	101
4.3.1 Materials.....	101
4.3.2 Methods.....	101
4.3.2.1 Formulation preparation.....	101
4.3.2.2 Formulation characterisation.....	102
4.3.2.3 EHDA set-up.....	102
4.3.2.4 Scanning electron microscopy (SEM)/ Energy dispersive spectroscopy (EDS).....	103
4.3.2.5 Attenuated total reflectance Fourier transform infrared spectroscopy (ATR-FTIR)..	103

4.3.2.6 Differential scanning calorimetry (DSC).....	103
4.3.2.7 Thermogravimetric analysis (TGA)	103
4.3.2.8 X-ray diffraction (XRD)	104
4.3.2.9 Zeta potential	104
4.4 Results and Discussion	105
4.4.1 Formulation characterisation	105
4.4.1.1 Viscosity	105
4.4.1.2 Surface Tension.....	106
4.4.1.3 Electrical Conductivity	106
4.4.2 Images of solution and suspension preparations	108
4.4.3 Jetting modes	109
4.4.4 Jetting maps	110
4.4.5 SEM.....	114
4.4.6 ATR-FTIR.....	127
4.4.7 DSC.....	131
4.4.8 TGA.....	133
4.4.9 X-ray diffraction (XRD)	136
4.4.10 Zeta potential values	139
4.5 Conclusion	143
Chapter 5 - Drug release kinetics, microbiological testing and cell culture studies.....	145
5.1 Introduction.....	145
5.1.1 Antibacterial agents	145
5.1.2 Antibiotic resistance.....	145
5.2 Aims & Objectives.....	146
5.3 Materials and methods.....	147
5.3.1 Materials	147
5.3.2 Methods.....	147
5.3.2.1 UV-vis and calibration curve.....	147
5.3.2.2 Drug content and encapsulation efficiency.....	147
5.3.2.3 In-vitro drug release	148
5.3.2.4 Bacterial testing.....	148
5.3.2.5 Disc diffusion	149
5.3.2.6 Scanning electron microscope (SEM)/ Energy dispersive spectroscopy (EDS)	149
5.3.2.7 Growth kinetic curves (Optical Density (OD600))	149
5.3.2.8 Ex-vivo cell culture studies (MTT assay).....	150
5.4 Results and Discussion	151
5.4.1 UV-vis and calibration curve.....	151

5.4.2 Drug content/encapsulation efficiency and drug release curve.....	152
5.4.3 Microbiological testing.....	159
5.4.3.1 Disc diffusion results.....	159
5.4.3.1.1 Metallic nanoparticles	159
5.4.3.1.2 Full formulation Results.....	166
5.4.3.2.1 SEM analysis of bacterial death	173
5.4.4 Optical Density (OD 600 _{nm}).....	175
5.4.4.1 Metal nanoparticle results	175
5.4.4.2 Full formulation results	181
5.4.5 Cell culture studies.....	186
5.5 Conclusion	194
5.6 Future work.....	196
Chapter 6 - References.....	197

List of figures

Figure 1. 1: TiO ₂ nanoparticles synthesised by <i>Lactobacillus</i> cells (Jha et al, 2009).....	3
Figure 1. 2: SEM images of <i>S. aureus</i> grown on agar at low and high magnifications (Zubair et al, 2015).....	4
Figure 1. 3: Membrane damaging toxin mechanisms (Otto, 2014).	6
Figure 1. 4: SEM image of <i>E. coli</i> grown on agar (Keerthana, 2016).....	9
Figure 1. 5: Schematic representation of EHDA set-up.....	24
Figure 1. 6: Schematic representation of coaxial EHDA set-up (Alharbi et al, 2016).	39
Figure 2. 1: Structure of PLGA 50:50 ester.....	42
Figure 2. 2: Structure of AMX.....	43
Figure 2. 3: β -lactam ring of AMX.....	43
Figure 2. 4: Structure of DCM.....	44
Figure 2. 5: Structure of acetone.....	45
Figure 2. 6: Structure of AgNO ₃	46
Figure 2. 7: Structure of H ₂ AuCl ₄ x 3H ₂ O.....	47
Figure 2. 8: Structure of CuSO ₄	48
Figure 2. 9: Structure of Na ₃ C ₆ H ₅ O ₇	49
Figure 2. 10: Structure of PVP.....	50
Figure 2. 11: Structure of ascorbic acid.	52
Figure 2. 12: Structure of EG.....	53
Figure 2. 13: Digital image of an A&D SV-10 sine wave vibro viscometer.	55
Figure 2. 14: Digital image of a White Electrical Instrument Co. OS torsion balance.	56
Figure 2. 15: Digital image of a Mettler Toledo FiveGo electrical conductivity meter.	57
Figure 2. 16: Digital image of the EHDA set up.....	58
Figure 2. 17: Digital image of Carl Zeiss Evo 15 SEM.	59
Figure 2. 18: Digital image of a Jade differential scanning calorimeter.	60
Figure 2. 19: Digital image of a PerkinElmer Pyris 1 TG analyser.	61
Figure 2. 20: Digital image of Bruker FTIR Platinum-ATR spectrophotometer.	62
Figure 2. 21: Digital image of a Bruker 2nd Generation D2 Phaser.	63
Figure 2. 22: Digital image of a Foster+Freeman Foram-2 Raman spectrometer.....	64
Figure 2. 23: Digital image of a Brookhaven NanoBrook Omni zeta potential analyser.....	65
Figure 2. 24: Digital photo of a Stuart SBS40 Shaking water bath.	66
Figure 2. 25: Digital image of a UV-Vis spectrophotometer.....	67
Figure 2. 26: Digital image of a SpectraMax Plus 384 Microplate Reader.	70

Figure 3. 1: digital images of end-point synthesis of metallic nanoparticles and their respected centrifuged nanoprecipitates. (Ai) synthesised AgNPs (Aii) collected precipitate of centrifuged AgNPs (Bi) synthesised AgNWs (Bii) collected precipitate of centrifuged AgNWs (Ci) synthesised AgPs (Cii) collected precipitate of centrifuged AgPs (Di) synthesised AuNPs (Dii) collected precipitate of centrifuged AuNPs (Ei) synthesised CuNPs (Eii) collected precipitate of centrifuged CuNPs.	80
Figure 3. 2: SEM ((i)images at low magnifiaction); ((ii) images at higher or equal magnifications); (iii) EDS analysis; (iv) particles size distribution histogram using (ii) SEM images. (A) AgNP; (B) AgNW; (C) AgP; (D) AuNP; (E) CuNP; (F) hexagonal silver nanoparticle not used.	87
Figure 3. 3: Pathway describing the growth multiple twinned seed particles prior to nanowire formation.....	87
Figure 3. 4: ATR-FTIR spectra of synthesised metallic nanoparticles; AgNP, AgNW, AuNP, AgP and CuNP.....	89
Figure 3. 5: Raman spectra of synthesised metallic nanoparticles; AgNP, AgNW, AuNP, AgP and CuNP.....	90
Figure 3. 6: UV-vis spectra of synthesised metallic nanoparticles; AgNP, AgNW, AuNP and AgP ...	92
Figure 3. 7: XRD diffractograms of synthesised metallic nanoparticles; AgNP, AgNW, AuNP, AgP and CuNP.....	94
Figure 4. 1: Digital images of solution and suspension preparations in acetone; A) F1, B) F2, C) F3, D) F4, E) F5, F) F6, G) F7.....	108
Figure 4. 2: Digital images of jetting modes through electrospraying. (A) initial droplet with no voltage applied, (B) dripping mode, (C) stable jetting mode, (D) unstable jetting mode.	109
Figure 4. 3: Jetting maps of electrospraying process to show the relationship between flow rate and applied voltage, at which corresponding value of each parameter leads to stable or unstable jetting for all formulations F1-F14.	112
Figure 4. 4: SEM ((i) low magnifiaction); ((ii) images at higher or equal magnifications); (iii) EDS analysis; (iv) particles size distribution histogram using (ii) SEM images of all formulations F1-14. (A) F1; (B) F8; (C)AMX in DCM and acetone; (D)F2; (E)F9; (F)F3; (G)F10; (H)F4; (I)F11; (J)F5; (K)F12; (L)F6; (M)F13; (N)F7; (O) F14.	126
Figure 4. 5: ATR-FTIR spectra of raw materials PLGA and AMX.....	129
Figure 4. 6: ATR-FTIR spectra of formulation F1-F7 using the solvent acetone.	129
Figure 4. 7: ATR-FTIR spectra of F8-F14 using the solvent DCM.	130
Figure 4. 8: DSC thermograms of raw material.	132
Figure 4. 9: DSC thermograms of formulations without metallic nanoparticles.....	132
Figure 4. 10: DSC thermograms of formulations containing metallic nanoparticles in DCM.....	132

Figure 4. 11: DSC thermograms of formulations containing metallic nanoparticles in acetone.	132
Figure 4. 12: TGA thermograms showing weight loss of raw materials AMX and PLGA	134
Figure 4. 13: TGA thermograms showing weight loss of formulations F1-F7 in the solvent acetone.	134
Figure 4. 14: TGA thermograms showing weight loss of formulations F8-F14 in the solvent DCM.	135
Figure 4. 15: XRD diffractograms of raw materials PLGA and AMX.....	137
Figure 4. 16: XRD diffractograms of formulations F1-F7 in the solvent acetone.	138
Figure 4. 17: XRD diffractograms of formulations F8-F14 in the solvent DCM.....	138
Figure 5. 1: UV-vis curve of AMX.....	151
Figure 5. 2: Calibration curve of AMX from 12.5 µg/mL to 125 µg/mL.....	151
Figure 5. 3: Cumulative drug release curves for formulations F2-F7.....	158
Figure 5. 4: Disk diffusion zones against <i>E. coli</i> and <i>S. aureus</i> at varying volumes of metallic nanoparticles with the control as AMX. (i) <i>S. aureus</i> and 5 µL of metal suspension; (ii) <i>E. coli</i> and 5 µL of metal suspension; (iii) <i>S. aureus</i> and 10 µL of metal suspension; (iv) <i>E. coli</i> and 10 µL of metal suspension. (A) AgNP; (B) AgNW; (C) AgP; (D) AuNP; (E) CuNP; (F) AMX control.	165
Figure 5. 5: Size of disk diffusion zones against <i>E. coli</i> and <i>S. aureus</i> at varying volumes of metallic nanoparticles with the control as AMX.....	165
Figure 5. 6: Disk diffusion zones against <i>E. coli</i> and <i>S. aureus</i> at varying volumes of formulations F2-F7 (i) <i>S. aureus</i> and 15 µL of metal suspension; (ii) <i>E. coli</i> and 15 µL of metal suspension; (iii) <i>S. aureus</i> and 30 µL of metal suspension; (iv) <i>E. coli</i> and 30 µL of metal suspension. (A) F2; (B) F3; (C) F4; (D) F5; (E) F6; (F) F7.	172
Figure 5. 7: Size of disk diffusion zones against <i>E. coli</i> and <i>S. aureus</i> at varying volumes for formulations F2-F7.....	172
Figure 5. 8: SEM/EDS analysis of <i>S. aureus</i> cell death. (i) SEM image; (ii) EDS analysis.	174
Figure 5. 9: General bacterial growth curve.	175
Figure 5. 10: Optical density curves of metallic nanoparticles against <i>S. aureus</i> at 5 µL.	178
Figure 5. 11: Optical density curves of metallic nanoparticles against <i>S. aureus</i> at 10 µL.	179
Figure 5. 12: Optical density curves of metallic nanoparticles against <i>E. coli</i> at 5 µL.....	179
Figure 5. 13: Optical density curves of metallic nanoparticles against <i>E. coli</i> at 10 µL.....	180
Figure 5. 14: Optical density curves of the formulations F2-F7 at 15 µL against <i>S. aureus</i>	183
Figure 5. 15: Optical density curves of the formulations F2-F7 at 30 µL against <i>S. aureus</i>	184
Figure 5. 16: Optical density curves of the formulations F2-F7 at 15 µL against <i>E. coli</i>	184
Figure 5. 17: Optical density curves of the formulations F2-F7 at 30 µL against <i>E. coli</i>	185
Figure 5. 18: Cell viability graph of AgNP formulations at different concentrations.	189

Figure 5. 19: Cell viability graph of AgNW formulations at different concentrations. 190

Figure 5. 20: Cell viability graph of AgP formulations at different concentrations. 191

Figure 5. 21: Cell viability graph of AuNP formulations at different concentrations. 192

Figure 5. 22: Cell viability graph of CuNP formulations at different concentrations. 193

List of tables

<i>Table 3. 1: Zeta potential values of spherical AgNP.</i>	95
<i>Table 3. 2: Zeta potential values of AgNW.</i>	96
<i>Table 3. 3: Zeta potential values of AgP.</i>	96
<i>Table 3. 4: Zeta potential values of AuNP.</i>	97
<i>Table 3. 5: Zeta potential values of CuNP.</i>	97
<i>Table 4. 1: General composition of all formulations.</i>	101
<i>Table 4. 2: Table of characterisation displaying values for viscosity (mPa.s), surface tension (γ) and electrical conductivity ($\mu\text{s/cm}$) of solvents DCM and Acetone, and all formulations F1-F14. All experiments performed in triplicate.</i>	107
<i>Table 4. 3: Zeta potential values of F1. Table 4. 4: Zeta potential values of F2.</i>	140
<i>Table 4. 5: Zeta potential values of F3. Table 4. 6: Zeta potential values of F4.</i>	140
<i>Table 4. 7: Zeta potential values of F5. Table 4. 8: Zeta potential values of F6.</i>	140
<i>Table 4. 9: Zeta potential values of F7. Table 4. 10: Zeta potential values of F8.</i>	141
<i>Table 4. 11: Zeta potential values of F9. Table 4. 12: Zeta potential values of F10.</i>	141
<i>Table 4. 13: Zeta potential values of F11. Table 4. 14: Zeta potential values of F12.</i>	141
<i>Table 4. 15: Zeta potential values of F13. Table 4. 16: Zeta potential values of F14.</i>	142
<i>Table 5. 1: Drug loading and encapsulation efficiency values for formulations F2-F7.</i>	158
<i>Table 5. 2: Table of reagents in each well for AgNP.</i>	189
<i>Table 5. 3: Table of reagents in each well for AgNW.</i>	190
<i>Table 5. 4: Table of reagents in each well for AgP.</i>	191
<i>Table 5. 5: Table of reagents in each well for AuNP.</i>	192
<i>Table 5. 6: Table of reagents in each well for CuNP.</i>	193

Abbreviations

AFM – atomic force microscopy

AgNO₃ – silver nitrate

AgNP – silver nanoparticles

AgNW – silver nanowires

AgP – polygonal silver nanoparticles

AIDS – acquired immune deficiency syndrome

AmK – amikacin

AMX – amoxicillin

API – active pharmaceutical ingredient

ATR-FTIR – attenuated total reflection Fourier-transform infrared spectroscopy

AuNP – gold nanoparticles

Cm – chloramphenicol

CuNP – copper nanoparticles

CuSO₄ – copper sulphate

D.I – deionised water

DCM – dichloromethane

DMSO – dimethyl sulfoxide

DSC – differential scanning calorimetry

E. coli – *Escherichia coli*

EDS - Energy-dispersive spectroscopy

EE% - encapsulation efficiency

EG – ethylene glycol

EHDA – electrohydrodynamic atomisation

FDA – Food and Drug Administration

FTIR – Fourier-transform infrared spectroscopy

H₂AuCl₄ · 3H₂O – gold (III) chloride hydrate

HEPA – high efficiency particulate air

HGT – horizontal gene transfer

HIV – human immunodeficiency virus

HUS – haemolytic uremic syndrome

ICDD – International Centre for Diffraction Data

LPS – lipopolysaccharides

MBC – minimum bactericidal concentration

MIC – minimum inhibitory concentration

MRSA – Methicillin resistant *Staphylococcus aureus*

MTP – multiple twinned particles

MTT - 3-[4, 5dimethylthiazol-2-yl]-2, 5diphenyltetrazolium bromide

NA – nutrient agar

Na₃C₆H₅O₇ – sodium citrate

NaBr – sodium bromide

NB – nutrient broth

NMR – nuclear magnetic resonance

PBS – phosphate-buffered saline

PEO – poly(ethylene oxide)

PLGA – poly(lactic-co-glycolic acid)

PVA – poly(vinyl alcohol)

PVP – polyvinylpyrrolidone

RMS – root-mean square

ROS – reactive oxygen species

S. aureus – *Staphylococcus aureus*

SEM – scanning electron microscope

SERS – surface enhanced Raman spectroscopy

TEM – transmission electron microscope

TGA – thermogravimetric analysis

TiO₂ – titanium dioxide

TSS – toxic shock syndrome

TSST-1 – toxic shock syndrome toxin

UTI – urinary tract infection

UV-vis – ultraviolet-visible spectroscopy

Van – vancomycin

vRNA – viral RNA

vRNP – viral ribonucleoprotein complexes

WHO – World Health Organisation

XRD – X-ray diffraction

Chapter 1 - Literature Review

1.1 Microorganisms

Bacteria and fungi are both friends and enemies of humans and mammals alike. They have the ability to protect and boost the immune system and purify living environments, whilst having the potential to cause disease, death and epidemics (Hu et al, 2018, Fischbach and Walsh, 2009, Lin et al, 2013, Richter et al, 2017.). After the body is exposed to an infectious agent, the body will generate antibodies or other means of resistance. Bacteria, fungi and viruses start an infection by firstly infecting a cell or a tissue causing a subsequent spread around the body into more cells or tissues, which can cause severe consequences in many cases. A shared symptom of bacterial, fungal and viral infections is fever (Cole and Kramer, 2016). Therefore, it is important to have selective and sensitive identification of the microorganisms in order to prevent and treat infections (Hu et al, 2018).

1.1.1 Bacteria

Bacteria is a large group of prokaryotic microorganisms which can be found in various shapes, most commonly bacilli (rod shaped), cocci (spherical) and spirochaetes (spiral shaped), in the microscale range (Zikalala et al, 2018).

Bacteria is found ubiquitously in the environment; air, soil, water, land and food (Zikalala et al, 2018, Irvani, 2014). Bacteria are generally commensal organisms (bacteria living in harmony with the host; where the bacteria benefit whilst the host is neither harmed nor left unbenefited) allowing cutaneous homeostasis or immune competence (Parlet et al, 2019). Bacteria adapt easily to their surroundings, even in severe conditions whilst multiplying and growing rapidly. They are inexpensive to cultivate and easy to manipulate (Zikalala et al, 2018) and therefore often selected for their use in industry, as growth conditions i.e. temperature, oxygenation and incubation can all be easily controlled (Pantidos, 2014).

Bacteria are responsible for many of the most serious infections and foodborne illnesses worldwide, especially in developing countries where medical resources and general hygiene is poor (Zhang et al, 2018). Morbidity and mortality rates and the cost of healthcare is increased as a result of bacterial infections (Xia et al, 2019). Rapid detection and identification of the

bacteria is very important in order for treatment to be given and control measures to be put in place (Zhang et al, 2018).

Bacteria produce toxins (usually infectious and poisonous), which are generally heat-resistant and subsist even when the bacterium itself is killed by heat (Fleurot et al, 2014). Toxins also tend to be resistant to low pH, drying and freezing (Hennekinne et al, 2012, Kadariya et al, 2014). Therefore toxin-producing bacteria are a significant threat to food industries as they can survive the production process (Rubab et al, 2018).

These infections can be treated well with antibiotics, however the emergence of resistant strains of bacteria have outpaced the development of new antibiotics (Xia et al, 2019). Resistance to the first line antibiotics complicates the treatment of the infections (Schindler and Kaatz, 2016). Metal based nanoparticles are now being thoroughly investigated as possible antibacterial agents due to their large antimicrobial activity (Xia et al, 2019).

Most metal ions are toxic to bacteria, to which bacteria has a defence mechanism. Many bacteria have the capability of manufacturing specialised inorganic nanostructures (Zikalala et al, 2018). Bacteria convert metal ions to nanoparticles to overcome the toxicity. Bacteria then secretes proteins which are used to stabilise the nanoparticles. The ability for bacterial strains to perform this defence mechanism is due to intracellular proteins and enzymes (Iravani, 2014). The advantages of using mediated bacterial synthesis to produce metal oxide nanoparticles is that it reduces the use of toxic and expensive chemicals and produces nanoparticles without additional impurities. This method can also be scaled up without difficulty (Agarwal et al, 2017). The disadvantages are however, due to the screening of the bacteria it means the process is prolonged. Careful handling and inspection of bacteria is required in order to prevent contamination. Also, there is always difficulty in controlling the morphology and crystallinity of the nanoparticles (Zikalala et al, 2018, Agarwal et al, 2017).

1.1.1.1 Bacterial controlled synthesis of metal oxide nanoparticles

In this synthesis, bacteria synthesise iron oxide nanoparticles which are entrapped in phospholipid membrane-bound vesicles (magnetosome). Ferric iron is reduced on the cell surface and transported into the magnetosome, the ferrous ions are then oxidised and precipitated to produce iron oxide nanoparticles which are crystallised. The iron oxide nanoparticles are of high chemical purity, obtain a narrow size distribution and have similar

morphologies. Only iron-reducing bacteria (magnetotactic bacteria) can carry out this type of synthesis (Zikalala et al, 2018).

1.1.1.2 Bacterial induced synthesis of metal oxide nanoparticles

In this synthesis, bacteria alter to their environment and generate conditions suitable for extracellular synthesis of nanoparticles in order to degenerate the toxicity. The bacteria modify the solubility by changing their redox state, complexation and precipitation of the metal ions (Zikalala et al, 2018). Jha et al, 2009 synthesised titanium dioxide (TiO₂) nanoparticles using *Lactobacillus* cells whilst heating on a steam bath at 60 °C for 10-20 minutes. **Figure 1.1** shows the TiO₂ nanoparticles and aggregates.

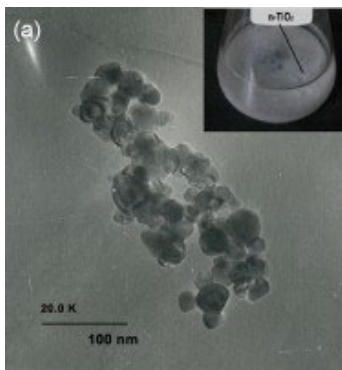


Figure 1. 1: TiO₂ nanoparticles synthesised by *Lactobacillus* cells (Jha et al, 2009).

1.1.1.3 Gram-positive bacteria

The key difference between gram-positive and gram-negative bacteria is the cell wall composition and thickness. The cell walls of gram-positive bacteria have thicker peptidoglycan layers (Zyoud et al, 2019). Gram-positive bacteria have one cytoplasmic membrane with a cross linked 20-80 nm thick peptidoglycan layer with acidic residues on the exterior (Hu et al, 2018). Irrespective of the thickness of the peptidoglycan layer, due to its relative porosity it doesn't act as a permeability barrier (Agel et al, 2019, Maisch et al, 2004).

Gram-positive bacteria are responsible for many devastating worldwide infections with high morbidity and mortality rates (Hu et al, 2018). Bacterial infections caused by gram-positive bacteria can lead to sepsis, bacteraemia, pneumonia, osteomyelitis and endocarditis (Xia et al, 2019).

Commonly known gram-positive bacteria important to human medicine include: *Staphylococcus aureus*, *Staphylococcus epidermis*, *Staphylococcus haemolyticus*, *Enterococcus faecalis*, *Enterococcus faecium*, *Streptococcus pneumoniae* and *Clostridium difficile* (Schindler and Kaatz, 2016).

1.1.1.3.1 *Staphylococcus aureus* (*S. aureus*)

S. aureus is a commensal gram-positive round-shaped bacterium (**Figure 1.2**) found commonly in the upper respiratory tract and on the skin (El-Shahawy et al, 2018, Seyyed Mousavi et al, 2017, Argudín et al, 2012.).

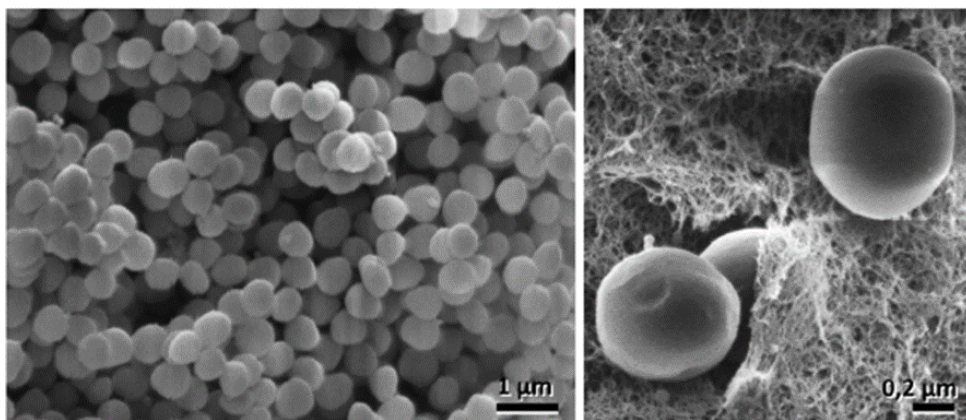


Figure 1. 2: SEM images of *S. aureus* grown on agar at low and high magnifications (Zubair et al, 2015).

S. aureus also frequently exists in perineum, rectum, axilla and genitals (Miao et al, 2017). The bacterium also naturally exists in the anterior nares of animals and likewise humans (Yadav et al, 2018). It is a facultative anaerobe, non-spore-forming (Rubab et al, 2018) which can grow without oxygen and is capable of surviving in hot, dry and saline environments (Chaibenjawong and Foster, 2010, Shahbaz et al, 2015). *S. aureus* has a round shape and approximately 1 µm. *S. aureus* is often a cause of skin infections (e.g. abscesses), respiratory infections (e.g. sinusitis, pneumonia), food poisoning (El-Shahawy et al, 2018.) osteomyelitis, endocarditis (Seyyed Mousavi et al, 2017, Rubab et al, 2018) and can lead to the development of septicemia (Fluit, 2012). Toxic shock syndrome and staphylococcal scarlet fever is a result of the toxic shock syndrome toxin (TSST-1) produced by *S. aureus* which is often fatal (Seyyed Mousavi et al, 2017, Otto, 2014). Several stains can cause infections by producing virulence factors (potent protein toxins) which are expressed on the cell surface to bind and activate antibodies (El-Shahawy et al, 2018.). *S. aureus* is a major burden in both communities and

hospitals but also a serious problem regarding animals and farming. Dairy cows are known to develop mastitis due to *S. aureus* outbreaks and it is also a detriment to chickens (Fluit, 2012).

S. aureus is generally the most problematic bacterium of the *Staphylococcus* genus (Parlet et al, 2019, Miao et al, 2017). *S. aureus* is responsible for a greater number of deaths than acquired immunodeficiency syndrome (AIDS), tuberculosis and viral hepatitis combined (Yang et al, 2019, van Hal et al, 2012). There are more than 40 antimicrobial resistant genes located on plasmids and transposons have been identified which plays an important role in making non-resistant bacteria resistant (Yadav et al, 2018).

S. aureus is an easily adaptable bacterium and can gain strong antibiotic resistance quickly (Pantosti et al, 2007, Yadav et al, 2018). World Health Organisation (WHO) reports *S. aureus* is a major threat to both human animal health (Hu et al, 2018, Nordmann et al, 2007, Zhang et al, 2014, O'Connell et al, 2013). Therefore, fast detection of this bacterium is vital in order to avoid major outbreaks and widespread infections (Yang et al, 2019) and reduce the threats regarding public health and food safety (Rubab et al, 2018).

The largest and most exposed organ of the human body is the skin. The organ is densely populated with bacteria which compete with each other for survival. The skin is predominantly occupied by members of *Staphylococcus*, *Corynebacterium*, *Streptococcus*, and *Propionibacterium* (Parlet et al, 2019, Christensen and Brüggemann, 2014, Grice and Segre, 2011, Byrd et al, 2018).

S. aureus produces virulence factors both inside and out of the cell, leading to damage to the hosts biological membranes and ultimately cell death (Rubab et al, 2018). Many virulence factors are encoded on mobile genetic elements e.g. plasmids or prophages which can be transferred between strains by horizontal gene transfer (HGT) (Otto, 2014).

S. aureus withholds many adhesins (surface-bound proteins which adhere to other cells/tissues) and thus can attach and persist on a multitude of the hosts tissues (e.g. heart tissues and bones) and also implant materials (e.g. catheters, prosthetic joints and pacemakers) and thus cause detrimental infections (Raafat et al, 2019, Miao et al, 2017).

1.1.1.3.1.1 Membrane-damaging toxins

The cytoplasmic membrane is a target for bacterial toxins. The toxins initiate pore formation in the membrane causing the efflux of vital molecules and metabolites. Membrane-damaging toxins can be split into receptor mediated and non-receptor mediated. Receptor mediated has high target cell specificity, where the lysis is dependent on initial receptor interaction. Non-receptor mediated is less specific and relies only on interacting with the membranes (**Figure 1.3**).

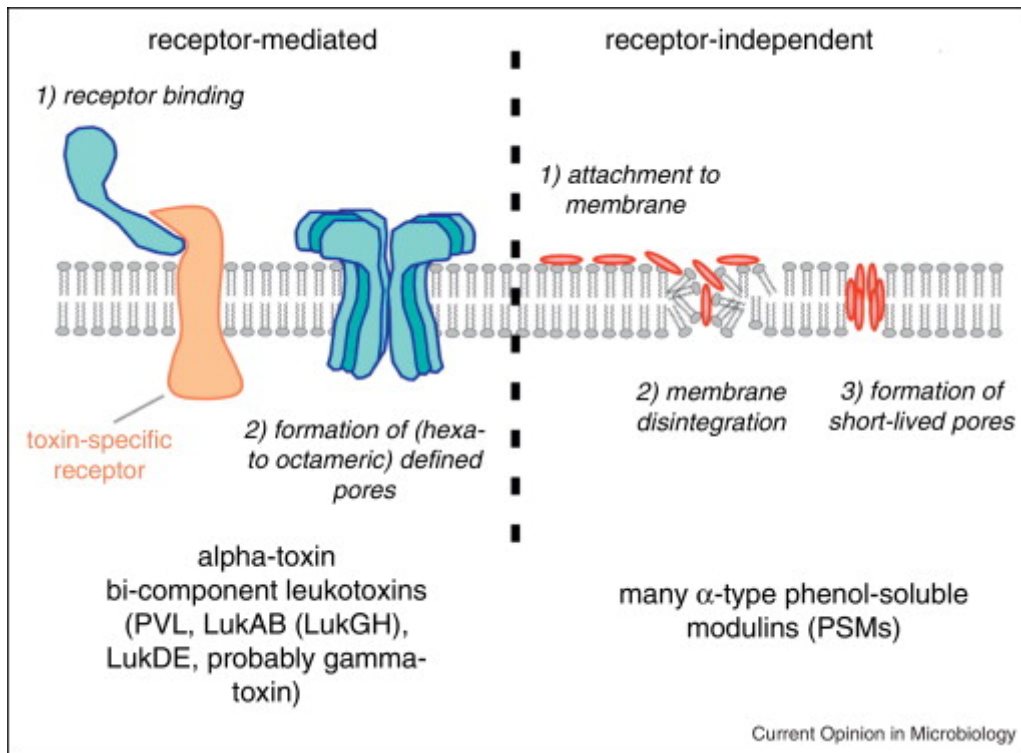


Figure 1. 3: Membrane damaging toxin mechanisms (Otto, 2014).

1.1.1.3.1.2 Enzymes

There are many enzymes that are secreted by *S. aureus* which degrade host molecules or interfere with the hosts metabolic or signalling pathways. Proteases are often secreted to break down the hosts proteins which ultimately leads to tissue destruction. Secreted staphylokinase activates plasminogen to plasmin, which breaks down fibrin networks, therefore deteriorating the function of the fibrin network which is meant to keep the staphylococcal infection localised. Although staphylokinase allows bacterial penetration through the skin barrier, it actually reduces the severity of skin lesions by promoting the opening and draining of skin lesions (Otto, 2014, Kwiecinski et al, 2013).

1.1.1.3.2.1 Methicillin-resistant *S. aureus* (MRSA) outbreak

During the pre-antibiotic era, the mortality rate of invasive *S. aureus* was intense. Penicillin was introduced onto the market and the treatment of infections was greatly successful. However, shortly after *S. aureus* became resistant to penicillin due to the production of β -lactamase (enzyme which destroys the β -lactam ring of penicillin). Methicillin (a semi-synthetic penicillin) was then developed and first used in the early 1960's against penicillin-resistant *S. aureus* (Miao et al, 2017). In 1961, reports suggest that penicillin-resistant *S. aureus* had now acquired resistance to methicillin (methicillin-resistant *S. aureus*, (MRSA)) (Rubab et al, 2018, David et al, 2017). Outbreaks of MRSA were predominantly a problem confined within hospitals and immunocompromised patients (Ibelings and Bruining, 2003), however recent outbreaks have emerged into communities and caused pandemic infections amongst immunocompromised populations and increasingly into populations of healthy individuals (Parlet et al, 2019, Chambers and DeLeo, 2009, Otto, 2010, DeLeo et al, 2010). It has now become increasingly difficult to treat MRSA associated infections due to the strength of resistance the bacteria has to a wide spectrum of antibiotics (Rubab et al, 2018, Stevens, 2003). MRSA has been present in a variety of animals, from pets to farmed animals (typically found in meat, fish and dairy products) which therefore directly affects any humans who has consumed or been in close with these animals (van Loo et al, 2007, Leonard and Markey, 2008). MRSA is currently associated with skin and soft tissue infections more than respiratory infections (Zetola et al, 2005, Crago et al, 2012). Since 2013, a few number of new antimicrobial agents have been developed and approved by North American and European regulatory agencies for the treatment of MRSA. However, these drugs have been generally approved for the treatment of complicated soft-tissue infections rather than more complicated infections such as bacteraemia, osteomyelitis or endocarditis (David et al, 2017).

1.1.1.3.2.2 Toxic shock syndrome (TSS)

TSS is a rare (Biglari et al, 2019.), multi-system, toxin-mediated and potentially deadly disease. It is a severe illness that results in fever, hypotension, shock and multiple organ failures (Gottlieb et al, 2018). TSS is mostly concerned with women of childbearing age, long-term use of tampons and the subsequent bacterial growth, in particular of *S. aureus* (Sada et al, 2017, Lappin et al, 2009). The heat resistant (Biglari et al, 2019) toxic shock syndrome toxin (TSST-1) is produced by very few strains of *S. aureus* (Wilson et al, 2011). The TSST-1 toxin induces the mass production of cytokines which is believed to be the key in the pathogenesis of TSS

(Kum et al, 2001, Lappin et al, 2009). The toxins interfere with leukocyte receptors to prevent recognition and subsequent activation of the immune system (Otto, 2014). Repetitive cycles of cell stimulation and cytokine release results in tissue damage and organ dysfunction.

TSS was first reported in 1978 with the association of highly absorbent tampons in young women and found high percentages of vaginal cultures yielding *S. aureus*. Therapy requires early identification of the disease, control of the source and administration of the relevant antibiotics and drugs to suppress toxin production (Lappin et al, 2009). Although the disease is quick to be lethal it is usually treatable (Gottlieb et al, 2018).

Non-menstrual TSS can still result from a primary staphylococcal infection or colonisation of a toxin producing strain of *S. aureus*. This can occur after disruption to skin or mucous membranes (skin abscesses/burns or after surgical procedures) (Lappin et al, 2009).

Recent changes in the manufacturing and use of tampon has led to a significant decline in the frequency of menstrual-related TSS, however the incidences of non-menstrual TSS has increased (Gottlieb et al, 2018, Chuang et al, 2005, Reingold et al, 1989, Hajjeh et al, 1999).

1.1.1.4 Gram-negative bacteria

Gram-negative bacteria's cell envelope is comprised by two membranes; an inner membrane and an outer membrane which are separated by a periplasmic space containing peptidoglycan (Zheng et al, 2017). Gram-negatives withhold a thinner peptidoglycan layer than gram-positive bacteria (Hu et al, 2018).

This second membrane has a strong negative charge due to the presence of lipopolysaccharides (LPS) and porins (Agel et al, 2019, Maisch et al, 2004, Malik et al, 1992). The LPS in the outer membrane of a gram-negative bacteria is a key component and can be used to identify the bacteria due to its unique pathogen-associated molecular pattern (Zhang et al, 2018, Ramachandran, 2013, Ulevitch and Tobias, 1999). The LPS is recognised by macrophages (Mathison et al, 1992), granulocytes (Fang et al, 2013) and dendritic cells (Barrientos et al, 2014) which triggers the intracellular signal transduction and therefore activates the host defence against the invasion of gram-negative bacteria (Zhang et al, 2018).

It is known that gram-negative bacteria are harder to kill than gram-positive bacteria, due to the presence of two cytoplasmic membranes, when compared to the single cytoplasmic membrane that gram-positive bacteria withhold; hence making it more difficult for

antibacterials to cross the membranes and cause an inhibitory effect (Agel et al, 2019). Gram-negative bacteria are normally found in the environment (Zhang et al, 2018, Kaye and Pogue, 2015).

1.1.1.4.1 *Escherichia Coli* (*E. coli*)

E. coli is the most common commensal aero-anaerobic gram-negative rod-shaped bacterium of the gut (Tenailon et al, 2010), where it is found in the intestinal flora (Ahmadian-Fard-Fini et al, 2018).

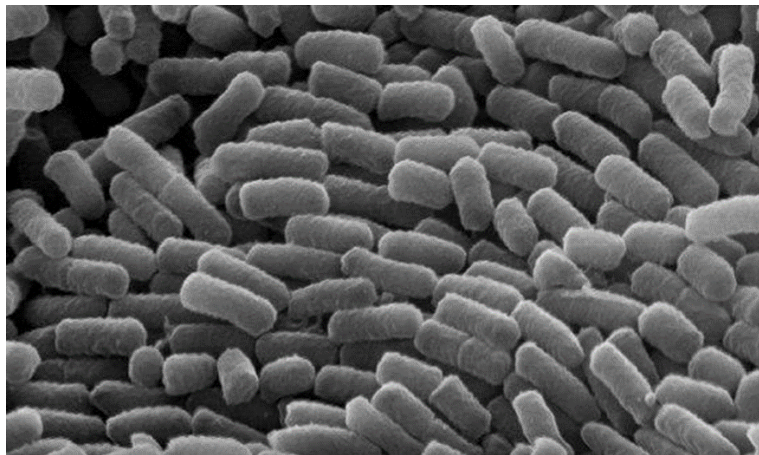


Figure 1. 4: SEM image of *E. coli* grown on agar (Keerthana, 2016).

If the bacterium reaches any tissues outside the intestinal flora, the bacterium becomes pathogenic and infections may arise. These infections often occur within the urinary tract, biliary tract and can even spread to the bloodstream, prostate gland, lungs, bones and eyes (El-Shahawy et al, 2018). Many food and water borne diseases are a consequence due to the exposure of *E. coli* strains (Gupta et al, 2019, Mathelié-Guinlet et al, 2017). *E. coli* is passed into the environment through faecal matter leading to water-related diseases where waste water and drinking water are not treated effectively. Therefore, *E. coli* is used as a faecal indicator which monitors the quality of recreational water at freshwater beaches (Shrestha, A. and Dorevitch, S., 2019).

E. coli was first discovered by German bacteriologist Theodor Escherich in 1885 in the human colon (Feng et al, 2002). *E. coli* has a cytoplasmic membrane and a peptidoglycan layer and holds an outer membrane composed of a phospholipid bilayer containing lipopolysaccharide (LPS) molecules and proteins (Mathelié-Guinlet et al, 2017). *E. coli* has become one of the greatest host organisms for metabolic engineering and synthetic biology due to its rapid growth

(short replication time), easy culture conditions and its ability to thrive under various growth conditions, metabolic manipulability and due to the immense knowledge in the biochemical and physiological properties of the bacterium. *E. coli* can be genetically manipulated easily which allows new phenotypes to be developed and its physiology to be explored. Numerous molecular cloning and genetic tools have been developed using *E. coli* (Pontrelli et al, 2018, Meyer and Schmidhalter, 2012).

Although *E. coli* is selected a one of the greatest host organisms there are also disadvantages which accompany *E. coli* as a host organism. *E. coli* is unable to be cultured at high (Tao et al, 2005) and low pH (Wernick et al, 2016) and also at high temperatures (Hasunuma and Kondo, 2012, Bhalla et al, 2013) due to the rise of contamination resistance (Tao et al, 2005, 11). *E. coli* is incapable of producing glycosylated biopharmaceutical products, proteins that require complex assembly or proteins with a high number of disulphide bonds (Meyer and Schmidhalter, 2012). The use of *E. coli* or bacteria in general in industry will always present as a threat to production, due to phage contamination where used in non-sterile conditions (de Melo et al, 2018, Samson and Moineau, 2013).

E. coli strain K-12 is classified into Risk Group 1 which suggests there is no threat of to a healthy human adult. This is due to the lack of O-antigens, virulence factors, colonisation factors. Therefore, these strains are useful in the productions of pharmaceuticals, food, chemicals and fuels (Pontrelli et al, 2018).

Chest and blood infections can result from the exposure of *E. coli* strain MRE 162. Mathelié-Guinlet et al, 2017 used MRE 162 in their work to understand the interaction between silica nanoparticles and the *E. coli* strain to mimic real biological attacks and to see how populations exposed to the strain are at risk of contracting infections.

1.1.1.4.1.1 Urinary tract infections (UTI)

A UTI refers to any infection in the urinary tract; in the urethra (urethritis), bladder (cystitis) or more severely kidneys (pyelonephritis) (Sheerin, 2011). The infection causes frequent and painful urination (Foxman, 2013), and although brings about distress they rarely present a threat to life (Sussman, 2013). UTIs are a result of pathogenic bacteria (most commonly faecal bacteria) colonising the urethra and moving to the bladder to multiply due to the lack of protective flora present. The virulence factors of the bacteria and host defence mechanisms determine the development of a UTI. *E. coli* has the ability to bind to specific receptors on the

epithelial cells in the urinary tract mucosa using surface adhesins in order to overcome the flow of urine (Sheerin, 2011). Whilst the host defence mechanism includes the production of glycosaminoglycans to coat the uroepithelium to provide a barrier against bacterial attachment (Zimmel, 2014). Women are more susceptible to contracting a UTI than men, which is due to the periurethral area (the area surrounding the urethral opening) in women providing more places for bacterial growth than in men, in combination with the shorter distance from the urethral opening to the bladder which fortifies the risk in women (Norrby, 2010). UTIs are easily treatable with a short course of antibiotics for an acute UTI; which means the chance for selecting antibiotic resistance in an individual is low. However due to the large number of women being treated for a UTI with antibiotics (e.g. nitrofurantoin and fosfomycin), there is a high chance that resistance can arise and spread. UTIs tend to reoccur; after the first seemingly cured UTI, about 20% of women will contract another within 6 months. The rise of resistance to antibiotics has pushed to the research of alternative treatments for UTIs which include the use of cranberry products (Foxman, 2013). UTIs rank among the most common infections in humans along with respiratory and gastrointestinal infections (Sussman, 2015).

1.1.1.4.1.2 *E. coli* O157:H7

Although many strains of *E. coli* are generally harmless (Pontrelli et al, 2018), several strains can produce toxins. For example, strain O157:H7 produces a potent toxin known as Shiga toxin which is detrimental to the lining of the small intestine (El-Shahawy et al, 2018) which can cause lethal effects (Pennington, 2010). The *E. coli* bacteria adhere to the epithelial cells and create lesions therein through producing these Shiga toxins (Mead and Griffin, 1998). The first outbreak of *E. coli* O157:H7 was observed in 1982 when it was isolated from individuals who developed bloody diarrhoea and abdominal cramps after consuming hamburgers from a restaurant. *E. coli* O157:H7 is the most common cause of haemolytic uremic syndrome (HUS) and therefore early diagnosis is essential. Once infection has been established, the development of HUS cannot be prevented. An infection of *E. coli* O157:H7 must be considered for any person who reports bloody diarrhoea. Faecal to oral transmission can occur through many routes and therefore many barriers are needed to prevent infection (Pennington, 2010).

1.1.2 Fungi

Fungi are ubiquitous eukaryotic microorganisms (Bartemes and Kita, 2018) which includes yeasts and moulds (Zikalala et al, 2018, Jeevanandam et al, 2016). Fungi are heterotrophs and therefore are unable to make their own nutrients so depend on other organisms to provide their food (Twaroch et al, 2015). Fungi extracellularly digest their food by secreting enzymes and then take it up as nutrients once broken down (Bartemes and Kita, 2018). Fungi are encased in thick cell walls (Limon et al, 2017) largely made up of proteins (Hu et al, 2018).

Fungal products are biological molecules produced by fungi either associated with the fungal cell wall or secreted extracellularly (Bartemes and Kita, 2018). Fungi produce spores which remain dormant until they are ready to germinate, through doing this they swell and send out hyphae (branching, filamentous body of fungus) (Templeton et al, 2010). Fungal growth depends majorly on temperature; *Alternaria* and *Cladosporium* species grow well in moderate climates around 20-30°C; because they do not grow well at body temperatures, they rarely cause infections in humans. However, their airborne fragments and secreted fungal products can cause respiratory allergies (i.e. asthma) (Bartemes and Kita, 2018). Thermotolerant fungi; *Candida*, *Penicillium* and *Aspergillus* species have the capability of growing at human body temperature and serves as part of the microbiome and as a cause of infections (37°C) (Rodrigues et al, 2016.).

Fungal spores are greatly variable in size; they can range between less than 2 µm to 250 µm in diameter (Bartemes and Kita, 2018). Spores that are larger than 10 µm (i.e. *Alternaria species*) deposit in the upper airways – where the temperature is less than 37°C; however, spores that are less than 10 µm can reach the lower airways (i.e. *Aspergillus* and *Penicillium*). *Aspergillus* species is the most prominent fungus to infect the lungs and they have the ability to colonise and germinate in the respiratory mucosa, unlike other respiratory allergens which are unable to grow within the host (grass and tree pollens) (Rick et al, 2016). Fungi can be found at all levels of the respiratory tract (Limon et al, 2017). Fungi are naturally present in the intestinal tract (Bartemes and Kita, 2018, Iliev et al, 2012), intestinal fungal dysbiosis influences the development of gastrointestinal diseases (Leonardi et al, 2018), this fungal can then go on to cause inflammation of the lungs (Wheeler et al, 2016).

Humans are at constant exposure to environmental fungal spores, often at levels 1000-fold greater than grass or tree pollen (Bartemes and Kita, 2018, Peay et al, 2016, Denning, 2006). Healthy hosts are often unaffected and resistant to fungal spores as a close relationship and

immunity has been established between the host and fungi at barrier surfaces (Casadevall, 2012). However, fungi can stimulate immune responses and cause pathologic changes in organs. In immunocompromised hosts, fungi often colonise and infect the lungs and other organs, leading to an increase in morbidity and mortality rates (Bartemes and Kita, 2018). Commonly known fungal genera which are related to allergies in humans are *Alternaria*, *Cladosporium*, *Penicillium* and *Aspergillus* (Mari et al, 2003).

Although numerous environmental factors are involved in developing asthma and allergies, exposure to airborne allergens from animals, arthropods and moulds is considered a risk factor (Knutsen et al, 2012). An association between developing allergic asthma and fungal exposure has been found in human subjects, especially regarding the *Alternaria* and *Aspergillus* species (Denning, 2006). Downs et al, 2001 found an association between severe asthma with an increase exposure of the *Alternaria* species in their study.

Water damage can lead to an increase in the growth of fungi, for example *Stachybotrys chartarum*, which affects the air quality and can often lead to airway inflammation (Chung et al, 2010).

Fungi can be found on the skin. Lipophilic fungus *Malassezia* is a dominant fungal found on the skin in adults (Findley et al, 2013, Paulino et al, 2006). The *Malassezia* species require long chain fatty acids for optimal growth; they are commonly found on most skin areas however are more commonly found with lipid-rich sebum secreted from the sebaceous glands (Gaitanis et al, 2012). In children where there is less sebaceous gland activity, the fungal communities are more diverse, including species of *Aspergillus*, *Epicoccum* and *Phoma* (as well as *Malassezia*) (Jo et al, 2016). The role of *Malassezia* is unknown regarding the benefits on the skin, however it has been studied that the aryl hydrocarbon receptor ligands they produce may encourage epithelial cell health and protecting cells from UV radiation (Velegraki et al, 2015).

Fungi has been used in food and drink production since the ancient times, especially regarding the production of alcoholic beverages and breads. Moulds and yeasts are used today for large scale fermentation or synthesis of many other ingredients (e.g. enzymes, organic acids, vitamins, pigments and fatty acids). Fungi that are used in fermentation processes to convert solid or liquid substrates into various products. Key points for the fermentation processes include producing the desired bioproduct with the highest consistent yield at the fastest rate in the cheapest and possible way (Copetti, 2019).

1.1.3 Viruses

Viruses are the most abundant entities on Earth, withholding a large reservoir of genetic diversity (Paez-Espino et al, 2016). Depending on the environment, bacterial activity and colonisation results in the abundance and diversity of the viruses (Lima et al, 2019).

The human gut harbours a complex microbial ecosystem which includes the presence of viruses (virobiota) (Lima et al, 2019).

Viruses can be transmitted in many ways, but predominantly through the mucosal surfaces. The virus can be transported through the gastrointestinal tract during faecal-oral transmission. The virus can be transported through the genital mucosa during sexual transmission. The virus can be transported through infected aerosol particles which is inhaled and deposited in the upper airways by a vulnerable person during aerosol transmission. Blood-borne viruses require arthropod vectors (e.g. mosquitoes, flies, fleas) to carry and disseminate the virus into the host during feeding on blood (Wilks et al, 2013).

The host's microbiota can influence viral infections. The presence of microbiota could be neutral, hinder viral infections or it could promote viral infection (Wilks et al, 2013).

1.1.3.1 Influenza virus

Influenza viruses are from the family *Orthomyxoviridae*. Influenza A and B viruses are held responsible for epidemics which cause up to half a million deaths globally each year. Influenza C viruses are less common and cause only mild infections. Influenza D viruses are not known to infect humans (Walker and Fodor, 2019, Krammer and Palese, 2013).

Vaccines against influenza viruses are available, however many vaccines are often ineffective due to the variation in surface proteins on the virus (Houser and Subbarao, 2015, Krammer and Palese, 2015).

Influenza viruses have a genome consisting of eight viral RNA (vRNA) segments, each encoding one or two major viral proteins. Each genome segment is packaged with viral ribonucleoprotein complexes (vRNPs). Influenza virions must contain full set of vRNPs to be actively infectious (Walker and Fodor, 2019).

The illness is characterised by the sudden onset of respiratory symptoms, including fever, myalgia, headache, malaise, non-productive cough, sore throat and rhinitis. Acute influenza

typically resolves after 3-7 days, however, the cough and malaise can persist for more than 2 weeks (Nichols and LeDuc, 2009). The majority of influenza illnesses are acute but in immunocompromised patients severe infections which can last multiple months can occur (Nichols et al, 2004, Vigil et al, 2010, Memoli et al, 2013). In these immunocompromised hosts, their immune responses are either weakened or absent (Xue et al, 2018) and these infections are treated with a long course of antiviral drugs (Nichols et al, 2004, Vigil et al, 2010, Memoli et al, 2013.). Due to the much longer viral infection in chronic influenza, the influenza viruses can replicate and quickly mutate and therefore generate genetically diverse populations simultaneously. The influenza virus is usually found co-occurring with other respiratory pathogens (Xue et al, 2018) and in most severe cases associated with pneumonia which is induced by bacterial co-infection (Wilks et al, 2013).

1.1.3.2 Human Immunodeficiency Virus (HIV)

HIV is an RNA retrovirus that infects T-lymphocytes in human hosts. The virus is transmitted through contaminated bodily fluids. The virus remains dormant for a period of 5-10 years before it diminishes the immunological function of the body it manifests to AIDS (Weledji, 2013).

HIV is a sexually transmitted organism which can affect the anorectum. Other viral organisms include herpes simplex virus and cytomegalovirus which can also arise due to the suppressed immune system. Symptoms caused by the presence of one or more of the organisms often results in fever, diarrhoea, rectal bleeding and even visible lesions in the anus and perineum (Weledji, 2013, Beck and Wexner, 1990).

Injecting drugs has created international public-health problems, especially regarding the transmission of blood-borne viruses (Hladik and McElrath, 2008). HIV can be transmitted through sharing needles to inject drugs (Des Jarlais, 2013) and contributes to the morbidity and mortality of illicit drug use (Hladik and McElrath, 2008). In order to reduce the transmission of HIV through needle sharing, it is imperative that clean injection equipment is available for drug users (Des Jarlais, 2013).

There is currently no cure for HIV/AIDS but highly active antiretroviral treatment prolongs the survival in many patients (Weledji, 2013) and some achieve near-normal life expectancy (Bloomfield et al, 2015, Johnson et al, 2013, Sabin, 2013).

1.1.3.3 Dengue virus

Dengue virus are the cause of dengue fever in humans (Gubler, 1998). There are four antigenically distinct dengue virus serotypes (DENV1, DENV2, DENV3 and DENV4) which are part of the family *Flaviviridae* (Yacoub and Farrar, 2014). This virus is largely transmitted by the *Aedes aegypti* mosquito. The virus is taken up by the mosquito through dengue laden blood, which firstly infects the mosquito gut tissue and migrates to the salivary gland where it will transmit to another host during feeding (Gubler, 1998).

Currently, there are no available antiviral drugs or vaccines for dengue, and the management relies solely on fluid replacement of the severe cases (Yacoub and Farrar, 2014). The main strategy currently is vector control to reduce the incidence of dengue fever, which will potentially reduce medical costs, productivity losses and premature deaths (Undurraga et al, 2016).

Dengue fever can range from a mild form of illness to severe dengue, which is characterised by capillary leakage, leading to hypovolaemic shock, organ impairment and bleeding complications (Yacoub and Farrar, 2014).

Dengue fever is presented by 3-5 days of high fever, intense headache, myalgia, nausea, vomiting, muscle joint pain, seizures and rashes (Qureshi, 2016, Naides, 2012, Tulchinsky and Varavikova, 2014). Severe dengue fever is a lethal complication causing fluid accumulation, plasma leakage, respiratory problems, severe bleeding or organ impairment and this is often presented by symptoms of continuous vomiting, rapid breathing, severe abdominal pain and bleeding gums (Tulchinsky and Varavikova, 2014).

1.2 Antibacterial Agents

An antibacterial agent is a chemically enhanced natural substance with the potential to kill (bactericidal effect) or slow down the growth or multiplication (bacteriostatic effect) of a bacterial organism without affecting the host functions (Hajipour et al, 2012). The latter working synergistically with the host's own immune system to control and eradicate an infectious bacterial population. Almost all of the different antibiotics available currently on the market are based on the structure of antibacterial agents naturally found in environmental microorganisms; with many of these antibiotics being synthetic derivatives of these discovered microorganisms (e.g. the discovery of penicillin) (Qiao et al, 2018).

At the beginning of the last century, the major cause of death worldwide was mainly attributed to infectious diseases e.g. tuberculosis (Huh and Kwon, 2011), in 1928, Sir Alexander Fleming discovered the natural antibacterial agent 'penicillin' which came into use in the 1940s (Conly and Johnston, 2005). Since the introduction of antibiotics onto the drug market, considerable improvement on the health and wellbeing of the mass population in many major countries has been observed, as well as the dramatic rise in the population's life expectancy and improved general health.

Antibacterial agents have been used in industries, from house hold products, to agricultural use as well as in livestock and farming. In livestock they play a therapeutic role to treat bacterial infections in animals, as well as having a prophylactic use when there is risk of infection and finally, added in small quantities in feed and water to promote the growth of the animal (Marshall and Levy, 2011).

From the 1950's to the 1970's, new classes of antibiotics were developed (Abed and Couvreur, 2014) e.g. tetracyclines, rifamycins, nitroimidazoles, quinolones and trimethoprim. However, for the majority of the years after 1985 there has been a severe drop in novel antibiotic drug discovery (oxazolidinones and lipopeptides were discovered in 2000 and 2003, respectively) (Conly and Johnston, 2005). Moreover, with the increase in cases regarding bacterial resistance and with the rise of disease-causing organisms, increased effort is needed in the discovery of new and potent antibacterial agents.

For further development in the discovery of novel antibacterial agents, understanding the mechanism of action is paramount, listed are some of the modes of action of antibacterial agents: (I) inhibition of cell membrane function and permeability (e.g. polymyxins); work best against gram-negative bacteria due to increased number of lipopolysaccharides (LPS) in the outer cell membrane. The mode of action involves disrupting the LPS in the cell membrane, hence increasing the permeability to antibacterial agents. (II) interfere with ribosome function (e.g. aminoglycosides and chloramphenicol); aminoglycosides achieve irreversible inhibition of bacterial protein synthesis, this is achieved through interfering with the translation of mRNA. (III) block folate synthesis and metabolism (e.g. sulphonamides); these are structural analogues of para-amino benzoic acid, in bacterial cells act as antagonists and block synthesis of folic acid. (IV) inhibit nucleic acid synthesis (e.g. nitroimidazoles). (V) inhibit the cell wall synthesis (e.g. penicillin's and cephalosporin's); penicillin's inhibit cell wall synthesis, through

inhibition of the enzyme transpeptidase, leading to the prevention of peptidoglycan forming and therefore cell wall synthesis (Byarugaba, 2010).

1.2.1 Antibiotic Resistance

The discovery and benefits of antibiotics have led to improved healthcare worldwide over the past century, however the inappropriate and lack of infection controlled resources of the antibacterial agents (Santos et al, 2013), and some mutations in the pathogens have stimulated the rise in resistance to antimicrobial drugs. Antimicrobial resistance itself has been around for a very long time.

Antibacterial resistance itself can be acquired or inherent (characteristic of all species of that isolate), an example of inherent resistance is the resistance of *Pseudomonas aeruginosa* to a wide range of antibiotics, acquired bacterial resistance is where bacteria gain the genes encoding resistance, through a mutation or due to the transfer of genetic material from other bacteria (MacGowan and Macnaughton, 2013). Mutations cause changes to the gene target of the antibiotic, causing it to no longer have an effect on the targeted bacteria. Genetic material transferring from bacteria to bacteria (I) prevents entry of an antibiotic; (II) allows the removal of an antibiotic once it has entered the cell; (III) neutralises the antibiotic. These processes are labelled horizontal gene transfer (HGT). HGT is defined as the uptake of DNA into the genome of the bacteria through transfer from its surrounding area. This can be achieved through, transformation uptake of the DNA from the environment, transduction transfer of DNA through the use of a bacteriophage (a bacterial virus that replicates inside a cell and incorporates bacterial DNA and conjugation direct cell to cell transfer through a plasmid).

Furthermore, the overuse and misuse of antibacterial agents has led to the emergence of antibiotic resistant genes, which further reduce the therapeutic effect of an antimicrobial agent, and renders it ineffective. Some examples include the resistance of all gram-positive organisms to colistin, and the resistance of *Enterobacteriaceae* to glycopeptides and linezolid (MacGowan and MacNaughton, 2013).

Bacterial resistance has now reached pandemic levels as various bacteria have developed resistance to many antibacterial agents (e.g. *Staphylococcus aureus* is resistant to Methicillin and *Staphylococci* is resistant to vancomycin) (Kandi and Kandi, 2015). Illnesses develop when bacteria enters the human body and is not treated properly, ranging from mild to life threatening conditions such as wound infections, abscess infections, endocarditis or blood stream infection

(Muñoz-Bonilla and Fernández-García, 2012). The increasing evolution of antibacterial resistant strains of pathogenic bacteria has enforced the need to discover alternative and effective approaches, which can fight microbial resistance and treat infectious diseases (Allahverdiyev et al, 2011).

Along with mutation's and HGT another reason for the rise in bacterial resistance is the insufficient understanding of the numerous bacteria and their antimicrobial susceptibility patterns, for patients with bacterial infections this poses a risk, as knowledge of bacteria is deficient, to counter this the overuse and misuse of broad spectrum antibacterials occurs.

Bacteria have evolved and developed several mechanisms of bacterial resistance which include (I) producing degradable enzymes to antibacterial agents (including cephalosporin's and penicillin's); in this case the bacteria (e.g. *E-coli*) release the enzyme β -lactamase, which cleaves of the lactam ring in penicillin causing it to become ineffective; (II) reducing the bacterial membrane permeability to antibiotics (including chloramphenicol and quinolones); chloramphenicol (Cm) is a broad spectrum antibacterial, inhibition of bacterial protein biosynthesis by Cm is largely due to the prevention of peptide chain elongation. Its bacteriostatic action is centred on a reversible binding to the peptidyltransferase centre at the 50S ribosomal subunit of 70S ribosomes; however bacteria since have developed resistance to Cm through acetylation of the drug and through the use of different chloramphenicol acetyltransferases enzymes (Schwarz et al, 2004); (III) alteration of an antibiotic target protein (including penicillin binding protein) (Dever and Dermody 1991). Other mechanisms of resistance include increased efflux of drug particles out of the cell and altering drug binding sites on the bacterial cell surface. Some conventional antibacterial agents have encountered bacterial resistance due to the inaccurate or even high dosage administered which also leads to adverse side effects and intolerable toxicity.

The lack of discovery of novel antibiotics are partially due to the insufficient resources available in discovering new antibacterial agents. However, a larger responsibility lies on pharmaceutical companies, for not finding investments into new synthetic antimicrobials research, financially rewarding. Furthermore the rise in the number of antimicrobial resistant strains, has led to a need of an alternative formulation to common antimicrobials, it is known that over 70% of bacterial infections are resistant to one or more of the antibiotics that are commonly used to eliminate the infection, which can in severe cases lead to death, in the US over 2 million people contract an infection resistant to antibiotics yearly, leading to the death

of around 23,000 people (Akova 2016), therefore now more than ever advancements in novel and effective antimicrobial agents are of great importance (Dizaja et al, 2014).

Some of the antibacterial agents are hydrophilic in nature leading to absolute restriction to cellular penetration for such drugs (e.g. aminoglycosides). However, other hydrophobic antibacterial agents (e.g. macrolides) suffer from low intracellular retention (Conly and Johnston, 2005). Beta-lactams are considered acidic by nature, allowing them to diffuse to the infection site but not accumulate to give the antibacterial action (Tulkens 1991). With so many antibacterial agents available with varying properties, it is essential when developing a novel antibacterial formulation to consider targeting the intracellular bacteria, this includes intracellular penetration, accumulation and distribution (Kandi and Kandi 2015).

1.3 Nanotechnology

With the introduction of nanotechnology involving the development, management and application of structures in the nanometer size range, it allows for the new advances in scientific fields including molecular treatment and rapid detection of diseases (Farokhzad and Langer, 2006). Nanosized drug delivery systems can overcome biological barriers and instead direct the drug to the specific targets. Nanotubes, nanoparticles and nanofibers have already proven to be effective drug delivery systems (Faraji and Wipf, 2009, Brandelli et al, 2017).

1.3.1 Nanoparticles

Nanoparticles have attracted a lot of attention due to their unique physical and chemical properties, which derives from the high area to volume ratio they possess and large quantity of surface atoms, which makes them ideal candidates for biomedical applications as many biological processes occur at the nanometer level (Sharma et al, 2009). Heavy metals such as copper, silver and gold have been widely used for centuries for the control and treatment of infectious diseases. Silver in particular, has been recognised for its antimicrobial properties and use as an antimicrobial agent. Silver also shows potential activity against antibiotic-resistant microorganisms, which is a frontline concern for the public healthcare (Prabhu and Poulose, 2012).

1.3.2 Metal nanoparticles as antibacterial agents

Recent years has seen resistance to antibiotics ever increasing. Many organic antimicrobial agents are toxic to humans and other animals and therefore inorganic antibacterial agents have attracted interest for bacterial control due to their known safety, sustainability, heat tolerance and stability (Rajawat and Qureshi, 2012, Hossain et al, 2015). Studies have shown that metal oxide nanoparticles exhibit bactericidal action against both gram-positive and gram-negative bacteria (Ravishankar and Jamuna, 2011). The biochemistry of all organisms is pivotal on the essential metal ions; however, an excess of these ions or the presence of non-essential ions can be lethal to cells due to oxidative stress and membrane damage (Lemire et al, 2013).

1.3.3 Silver nanoparticles

Due to silver nanoparticles possessing a low cytotoxicity, it has been used against gram-positive and gram-negative bacteria. The bactericidal action of silver nanoparticles is not completely understood, however considerable amounts of research is reviewing the mechanism (Ravishankar and Jamuna, 2011). It is thought that the high affinity of silver towards sulphur and nitrogen can disrupt the protein structure through binding to the thiol and amino groups, thus affecting the bacterial cell viability (Beyth et al, 2015). The silver ions from the nanoparticles interact with the phosphorus fraction of DNA which results in the inactivation of DNA replication (León-Silva et al, 2016). Silver compounds with or without combination of antibiotics provide broad spectrum antimicrobial activity against *Escherichia coli*, *Staphylococcus aureus*, *Staphylococcus epidermis*, *Salmonella typhi*, *Klebsiella pneumoniae* and many others (Chopade et al, 2014, Wang et al, 2014). Silver nanoparticles have already been incorporated into systems including bandages, surgical dressings and catheters to control bacterial colonisation to prevent infections (Maiti et al, 2014, Franci et al, 2015). The antimicrobial properties of silver nanoparticles mean they are being selected and incorporated into household items; bedding, toothpaste, shampoo, deodorant and paints (Ravishankar and Jamuna, 2011). The use of silver in food items is restricted, but through washing fruit and vegetables with suspensions containing silver nanoparticles, there may be residual silver contents. Silver nanoparticles have the ability to extend shelf life of foodstuffs, however due to inconclusive reports on toxicity, their use in food packaging is regulated in the EU and US and should be used cautiously (Carbone et al, 2016). Faria et al, 2015, incorporated silver nanoparticles into graphene nanosheets to measure the antibacterial activity against

Pseudomonas aeruginosa. The results shown a minimum inhibitory concentration range from 2.5 to 5 µg/mL and a 100% inhibition rate towards the bacterial cells adhered to the surface.

1.3.4 Gold nanoparticles

Gold nanoparticles are considered safe to human cells. Gold nanoparticles can be used to kill multi-resistant pathogens and cancer cells when combined with photosensitisers (León-Silva et al, 2016). Tuning the gold nanoparticles so that they can absorb near-infrared radiation (NIR) allows them to cause irreparable cell damage once attached to bacterial cells, through the transfer of heat from the NIR irradiation (Norman et al, 2008, Beyth et al, 2015). Gold nanoparticles have a high antibacterial activity which can be used in combination with antibiotics such as vancomycin, ampicillin and cefaclor for both gram-positive and gram-negative bacteria (Zhang, 2015, Payne et al, 2016). Ravishankar and Jamuna, 2011, studied the mode of action of cefaclor when combined with gold nanoparticles; cefaclor inhibits the synthesis of the peptidoglycan layer itself however when bound to gold nanoparticles, holes are produced in the cell wall leading to the leakage of the cell contents and cell death. Gold has been used for many applications for thousands of years; for the treatment of mental disorders, syphilis, lepra, epilepsy and diarrhoea. Gold nanoparticles in recent years have been used in many medical and hygiene applications, including sensitizers in radiotherapy, targeted drug delivery systems and detection of cancer cells (Dykmana and Khlebtsov, 2012, Zhang, 2015). Lima et al, 2013, dispersed gold nanoparticles onto zeolite and found it was an effective antimicrobial agent against food pathogens *Escherichia coli* and *Salmonella typhi*.

1.3.5 Copper nanoparticles

Copper compounds are often toxic to some organisms and can cause environmental concerns, however using copper nanoparticles can reduce the hazard (Ingle et al, 2014). Copper nanoparticles are cheap and can readily mix with polymers (Gawande et al, 2016). Although copper nanoparticles antimicrobial efficacy is inferior to silver, it is still effective against many bacterium's including, *Escherichia coli*, *Staphylococcus aureus* (Cubillo et al, 2006), *Bacillus subtilis* (Ruparelia et al, 2008). It is shown that copper nanoparticles have a high antimicrobial activity against *Bacillus subtilis* and *Bacillus anthracis* due to the profusion of amines and carboxyl groups on the cell surface which has a high affinity for copper. The exact mechanism for the antimicrobial activity is not fully understood, however it is thought that it occurs through

membrane disruption and reactive oxygen species (ROS) production (Beyth et al, 2015). Lemire et al, 2013, found that with an increase of copper uptake into bacterial cells there was a decrease in cell viability, whilst the production of ROS increased. Ingle et al, 2014, found that copper nanoparticles have the ability for drug loading and photoluminescence and therefore can be used in the delivery of anticancer drugs. Although copper nanoparticles can be used for a variety of applications, their use is restricted by copper's inherent instability of oxidising under atmospheric conditions (Gawande et al, 2016). The oxidation issue can be overcome through using inert gas such as argon or nitrogen or through using reducing or capping agents (Umer et al, 2014).

1.4 Electrohydrodynamic atomisation (EHDA)

Electro hydrodynamic atomization (EHDA) is a multipurpose approach to fabricate materials for numerous applications especially in the pharmaceutical industry. Since the 1990s, this process has gained the attention of researchers to produce nano- and micro-structured fibers and particles (Xie et al, 2015). The main principle for the EHDA process utilises a high voltage applied to a capillary filled with solution. The resultant fibers or particles are collected on a grounded collector plate which is often covered by a material (i.e. paper, fabric, microscope slides) to make collection easier (Frenot and Chronakis, 2003). EHDA is a very simple, one-step process for fabricating highly functional nanofibers and nanoparticles which can be used for a wide range of applications. EHDA processes are practicable at room temperature with atmospheric conditions (Bhardwaj and Kundu, 2010).

1.4.1 EHDA process

The EHDA process is very simple and requires few apparatuses (Frenot and Chronakis, 2003, Bhardwaj and Kundu, 2010). A medical syringe is filled with the solution and fitted into the syringe pump which controls the flow rate of the solution. Here, the solution flows through to the capillary needle where the solution is held at the nozzle by its surface tension. An electric field is applied to the nozzle which induces a charge on the surface of the liquid (Frenot and Chronakis, 2003). The charge repulsion causes a force to act directly opposite to the surface tension (Doshi and Reneker, 1995). The intensity of the electric field is increased and the solution forms a Taylor cone (hemispherical surface of the fluid elongates to form a conical shape). Increasing the intensity further till the critical value is reached, where the repulsive electrostatic force overcomes the surface tension and a charged jet of fluid is ejected from the

tip of the Taylor cone. The jet is broken during electrospinning to form fine droplets. Whereas the jet stretches and undergoes a whipping process in electrospinning. In both of these processes the solvent evaporates leaving behind solid droplets or fibers respectively on the grounded collector plate (Frenot and Chronakis, 2003, Bhardwaj and Kundu, 2010, Sill and von Recum, 2008).

The parameter determining whether electrospinning or electrospaying will occur is the concentration of the polymer solution. When the solution concentration is high, the jet from the Taylor cone is stabilized and elongation takes place by whipping instability mechanism. If the solution concentration is low, the jet is destabilized due to the varicose instability and fine particles are formed (Anu Bhushani and Anandharamakrishnan, 2014).

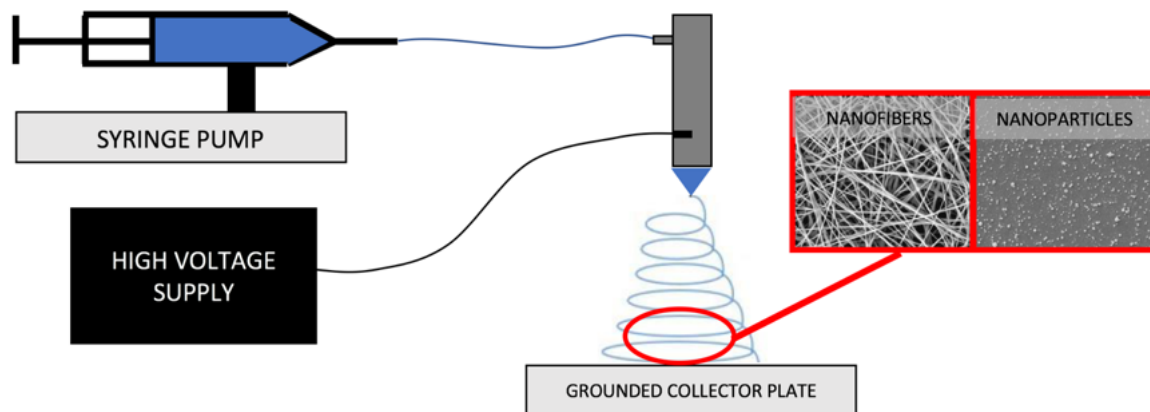


Figure 1. 5: Schematic representation of EHDA set-up.

1.4.2 Electrospaying

Electrospaying is the liquid atomisation by an applied electric field. It is a simple, versatile and cost-effective one-step process used for the fabrication of micro and nanoparticles (Anu Bhushani and Anandharamakrishnan, 2014, Zong et al, 2018).

The principle of electrospaying is based on the theory of charged droplets. An electric field applied to a liquid droplet exiting a capillary is able to deform the interface of the droplet (Min et al, 2004). An electrostatic force inside the droplet competes with the surface tension of the droplet, forming the Taylor cone (characteristic of a charged droplet). When the electrostatic force overcomes the surface tension, excess charge needs to be dissipated and small charged

droplets are ejected from the initial droplet which are of micro and nano-scale; this reduces the charge without significantly reducing its mass (Bock et al, 2012). The particles are self-dispersing in space due to the Coulomb repulsion of the charges which therefore reduces agglomeration and coalescence of the particles. The evaporation of the solvent results in contraction and solidification of the droplets which result in polymeric particles deposited on the grounded collector (Anu Bhushani and Anandharamakrishnan, 2014).

1.4.2.1 Processing parameters of electrospaying

1.4.2.1.1 Electrical conductivity

Electrospaying depends on the electrostatic attraction of charged particles to the grounded collector plate and therefore the electrical conductivity of the solution is an important parameter for optimising the process (Bock et al, 2012). An increased conductivity of a solution means that more charge can be carried by the electrospaying jet. A low electrical conductivity is preferred as a higher conductivity favours elongated particles and even fibers if the polymer concentration is high enough. Changes to the electrical conductivity can be altered by changing the solvent (Meng et al, 2009). When the electrical conductivity of the solution is lower than $0.01 \mu\text{S/m}$, current flow is insufficient, and it is likely electrospaying cannot occur. However, an electrical conductivity too high can lead to unstable electrospaying (Ding et al, 2005). The deposition pattern of the particles are dependent on the electrical conductivity; with a higher electrical conductivity, the Coulombic repulsion forces are higher and compete with the viscoelastic forces of the solution and unravelling the polymeric network and allowing the solution to be broken up into smaller droplets (Bock et al, 2012).

1.4.2.1.2 Flow rate

Flow rate influences the morphology and particle size and must be selected depending on the anticipated particles (Boda et al, 2018). A suitable flow rate should be selected to allow for complete solvent evaporation, this is not possible with flow rates that are too high. If the particles land on the collector plate partially solvated it can lead to deformed and non-consistent morphologies (Xie et al, 2006). In order for spherical morphologies and monodispersity to be fabricated, it is important for sufficient polymeric chain entanglements to occur, which can only occur if the flow rate is low (Bock et al, 2012).

1.4.2.1.3 Applied voltage

Applied voltage does not significantly affect the size of the resultant particles; it has only been found to slightly decrease the particle size when the applied voltage is increased (Hong et al, 2008). Shenoy et al., found that as the voltage increased, the morphology of the particles changed from spherical to elongated or even beaded fibers, if the polymer concentration is high enough (Shenoy et al, 2005). With an increased applied voltage there is more charge acting on the droplet which leads to the stretching and elongation of the droplet (Bock et al, 2012, Boda et al, 2018).

1.4.2.1.4 Capillary tip to collector distance

The distance between the capillary tip and collector plate influences the particles morphology. If the distance is too small, there will be insufficient evaporation of the solvent and therefore wet droplets will result on the collector plate; this leads to collapsing and coalescing of the droplet which therefore leads to large size distributions (Arya et al, 2009, Boda et al, 2018). Through increasing the distance, more spherical particles are formed due to the ability of the polymer chains to diffuse sufficiently in the droplet before they land. An increased distance also allows sufficient time for the solvent to evaporate from the droplets exterior (Bock et al, 2012).

1.4.2.1.5 Temperature

Temperature affects the vaporisation of the solvent from the liquid droplets which are fabricated during electrospinning. A higher temperature speeds up the drying and solidification of the electrospun particles, but also enhances the mobility of the polymeric chains within the droplets which decreases the particle size (Nguyen et al, 2016, Boda et al, 2018).

1.4.2.1.6 Humidity

A high relative humidity can change the morphology of the nanoparticles from solid to porous. This results from the from condensation, adsorption and diffusion of water from water vapour into the particle and then followed by a phase separation between the solvent and non-solvent phases during the drying process (Ikeuchi et al, 2011).

1.4.2.2 Applications of electrospaying

Electrospaying has presented itself as a novel and appreciable technique for the synthesis of nanoparticles at a lab scale and now up-scaling to major production (Nguyen et al, 2016). Electrospaying has the advantage over other conventional techniques which includes easy instrumental set up, utilising fewer resources, ability to produce a wide range of particle sizes with a narrow size distribution and low chance of particle aggregation. A wide range of materials can be used for electrospaying which might not work with other processes, including thermally sensitive and labile materials because of the ambient conditions needed (Pawar et al, 2018).

1.4.2.2.1 Antibacterial drugs

Curcumin is an anti-septic, analgesic and anti-inflammatory molecule (Sood and Nagpal, 2013). Mai et al, 2017, loaded curcumin into poly-lactic (PLA) microcapsules. The composite electrospayed microparticles exhibited broad spectrum antibacterial activity against gram-positive *S. aureus* and gram-negative *E. coli*, which didn't affect the viability of human dermal fibroblasts or induce haemolysis and was shown to have excellent biocompatibility. Ghayempour and Mortazavi, 2014, used coaxial electrospay to encapsulate peppermint essential oil which withholds broad spectrum antibacterial activity. The peppermint was emulsified with polyoxyethylene sorbitan monolaureate surfactant in the core and sodium alginate in the sheath. These nanocapsules lead to the complete eradication of *S. aureus* and *E. coli* colonies in comparison to the empty sodium alginate capsules (Boda et al, 2018).

1.4.2.2.2 Anti-inflammatory drugs

Inflammation of the tissues is caused by the over-oxidation and the generation of free radicals (Pham-Huy et al, 2008). Alpha-lipoic acid is a naturally occurring antioxidant and free radical scavenger which has been studied for their anti-inflammatory properties in diseases like type II diabetes and neurodegenerative diseases (Packer et al, 1995). Bai and Hu, 2014, loaded ALA into chitosan with polyethylene oxide (PEO) plasticiser to form composite nanoparticles using electrospaying. Confocal microscopy results proved that the uptake of the composite nanoparticles by LPS treated RAW 264.7 macrophage cells and initiated an anti-inflammatory effect by the alpha-lipoic acid due to the sustained release from the composite nanoparticles (Boda et al, 2018).

1.4.2.2.3 Food coatings

Food coatings enhance the shelf life through acting as a barrier for the food product. Spray coating is commonly used as the method for food coating, however electrospraying can also be employed due to the coating uniformity on large areas of food surfaces with sufficient control on the deposition rate and film thickness (Anu Bhushani and Anandharamakrishnan, 2014). For example, chocolate coating is used in the snack and confectionary industry. The complexity of chocolate coating is due to the rheological properties of the chocolate solution having a direct effect on the processing and ultimate quality of the product. Electrospraying chocolate has been studied and it is found that parameters including the viscosity and electrical conductivity play a significant role on the spray quality. Through manipulating the fat content, temperature and quantity of added lecithin these values can be decreased and thus droplet size decreases and which provides a more uniform coating to the product. Gorty and Barringer, 2011, achieved good quality of chocolate electrospraying through using samples with high fat content and an addition of less than 1.5% lecithin concentration. Marthina and Barringer, 2012, also studied these parameters with three different types of fats, cocoa butter, cocoa butter equivalent and lauric butter to determine the effect of the lecithin content on the viscosity and the electrical conductivity and how it affects the droplet size and overall coverage of the product. With an increase in lecithin content, the named parameters decreased providing fine droplets of a narrow size distribution which created a more even coverage than conventional methods which ultimately would be beneficial to the confectionary industry. For circumstances where the coating is essential for the protection of the product, electrospraying for thin film coating can be employed over the use of conventional spray coating methods. Electrospraying is a one step, low-energy and low-cost processing method and produces products with unique characteristics, which can benefit the confectionary industry (Anu Bhushani and Anandharamakrishnan, 2014).

1.4.3 Electrospinning

Electrospinning process is a fiber fabrication process utilised by applying an electrostatic field onto a liquid (polymeric solution). This approach has gained much attention because of its capability and feasibility in the fabrication of large quantities of fibres to be used in tissue engineering, filtration, drug delivery, biosensors, and wound dressings (Bhardwaj and Kundu, 2010). Their high surface area, small pore size and possibility of fabricating three dimensional

structures for the development of advanced technologies is very attractive to current research in many fields (Frenot and Chronakis, 2003).

The electrospinning process fabricates polymeric nanofibers (often with a diameter of less than 100 nm) which is produced by an electrostatically driven jet of polymeric solution. The alignment of the electrospun nanofibers can construct unique and highly functional nanostructures. The deposition of the nanofibers can be controlled and aligned through manipulating the electrospinning process, in order to form complex and continuous three-dimensional structures (i.e. nanowires and nanotubes). Nanofibers can also be laced together to create ultrathin layered polymeric fibrous sheets. Small insoluble particles can be incorporated in the polymeric solutions so they are encapsulated within the electrospun nanofibers. Likewise, soluble drugs or bacterial agents can also be incorporated (Frenot and Chronakis, 2003). A variety of cross-sectional shapes and sizes can also be fabricated using the electrospinning process. Koombhongse et al, 2001 used electrospinning to produce a variety of shapes and structures including branched fibers, flat ribbons and bent ribbons. Their research on the properties of these structures indicated that the selected polymer and solvent used affected the fluid mechanics, electrical properties of the solution and evaporation of the solvent which therefore contributed to the resultant structure of the nanofibers.

Research on the fundamental aspects of the process and the correct conditions is at the forefront to understand nanofiber morphology, structure, surface functionality and strategies to assemble the nanofibers, for their applications as multifunctional membranes, biomedical structures (i.e. scaffolding in tissue engineering, wound dressings, artificial organs or vascular grafts), filter media, fabrication of speciality fabrics etc (Frenot and Chronakis, 2003).

Conventional fiber spinning methods, (i.e. wet spinning, dry spinning, melt spinning and gel spinning) typically only produces fibers down to the microscale. However, electrospinning has the ability to produce fibers of the nanoscale. The nanofibers are solid fibers exhibiting a diameter of less than 100 nm and therefore noted for their large surface area per unit mass and small pore size (Frenot and Chronakis, 2003, Bhardwaj and Kundu, 2010).

Porosity is a geometric parameter and the porosity and pore size of the nanofibers are important considerations for the applications for which the nanofibers will be used for; i.e. filtration, tissue engineering etc (Zussman et al, 2002, Schreuder-Gibson et al, 2002., Li et al, 2002). The

porosity can easily be manipulated through changing process parameters (Bhardwaj and Kundu, 2010).

Nanofibers obtained currently are only found in non-woven form, which is useful for many applications such as filtration (Gibson et al, 1999), tissue engineering (Fertala et al, 2001) and wound dressings (Jin et al, 2002). It is a very difficult target to achieve a continuous single nanofiber due to the polymer jet trajectory in the complicated ‘whipping’ motion. If this target were to be achieved the applications for these nanofibers would be endless (Huang et al, 2003). However, approaches to achieving a continuous single nanofiber are being researched through different techniques; a cylinder collector with high rotating speed (Boland et al, 2001), an auxiliary electric field (Bornat, 1987) and an electrostatic field-assisted assembly collector (Theron et al, 2001).

1.4.3.1 Processing parameters for electrospinning

The electrospinning process relies on numerous parameters, which are classified into solution parameter, process parameter and ambient parameters. Solution parameters include solution concentration, polymeric molecular weight, viscosity, surface tension, electrical conductivity. Process parameters include applied voltage, flow rate and capillary tip to collector plate distance. Ambient parameters include temperature and humidity. Each of these parameters have an effect the fibers morphology, and through manipulating these parameters fibers of desired morphology can be collected (Chong et al, 2007).

1.4.3.1.1 Solution concentration

A minimum solution concentration is required in order for the electrospinning process to happen and consequently fiber formation to occur. When the solution concentration is low, a mixture of beads and fibers is attained. With increasing the solution concentration, the shape of the beads alters from spherical to spindle-like and then ultimately to uniform fibers with increased diameters due to the increase in viscosity. At too high concentrations it is difficult to form continuous fibers due to the failure to maintain the flow of solution and therefore unstable large average diameter fibers are formed. The concentration of the solution inevitably effects the solution surface tension and viscosity (Bhardwaj and Kundu, 2010).

1.4.3.1.2 Molecular weight

The molecular weight of the polymer has a significant effect on the rheological (viscosity, surface tension) and electrical properties (electrical conductivity and dielectric strength) of the solution. At too low a molecular weight, beads are typically formed rather than fibers; and at too high a molecular weight fibers with large average diameters are formed. The molecular weight of the polymer affects the number of entanglements of the polymer chains, which is an important aspect of the electrospinning process. However, it is observed that high molecular weights are not always essential if there are sufficient intermolecular interactions which substitutes chain entanglements (Bhardwaj and Kundu, 2010).

1.4.3.1.3 Viscosity

The viscosity of a solution is an important parameter in determining fiber size and morphology of the electrospun fibers. An optimum viscosity is required in order for the electrospinning process to happen and consequently fiber formation to occur. When there is very low viscosity, there is a high generation of beads and no continuous fiber formation. When the viscosity is too high, it is too difficult for the ejection of jets from the polymeric solution. The viscosity of the solution plays a significant role in determining the range of concentrations in which continuous fibers can be fabricated (Bhardwaj and Kundu, 2010).

1.4.3.1.4 Surface tension

The surface tension of a solution tends to be a function of the selected solvent and plays a critical role in the electrospinning process. There is no conclusive correlation between surface tension and the fiber morphology. A solution with a high surface tension tends to inhibit the electrospinning process due to the instability of jets and therefore large sprayed droplets are formed. Using a solution with a low surface tension allows the electrospinning process to occur at a lower electric field but doesn't always confirm stability of the jets (Bhardwaj and Kundu, 2010).

1.4.3.1.5 Electrical conductivity

The solution conductivity is a combination of the selected polymer, solvent and the availability of ionisable salts which are all vastly influential in the jet formation. With an increase in electrical conductivity there is a decrease in the fiber diameter, however with a low electrical conductivity there is insufficient elongation of the jet and thus non-uniform fibers withholding

beads. Adding salts to the formulation increases the uniformity of fibers and decreases the presence of beads (Bhardwaj and Kundu, 2010).

1.4.3.1.6 Applied voltage

The applied voltage is a crucial parameter for electrospinning. Only after the threshold voltage has been reached, fiber formation occurs through inducing the necessary charges on the solution. Through manipulating the applied voltage, experimentally the shape of the initial drop changes; from dripping mode to stable Taylor cone to unstable jetting mode (Bhardwaj and Kundu, 2010, Sill and von Recum, 2008). Although most research shows that with increasing the applied voltage causes greater stretching of the solution due to greater columbic forces in the jet and in turn reduces the fiber diameter, some research suggests a conflicting statement. Reneker and Chun, 1996, suggest that there was no correlation on the effect of the electric field with the fiber diameter of their PEO fibers. Zhang et al, 2005, suggests that with an increase in applied voltage, polymer ejection is greater and therefore facilitating fibers of a larger diameter. It is also shown that at a higher applied voltage there is a greater probability of bead formation (Buchko et al, 1999).

1.4.3.1.7 Flow rate

The flow rate is another important process parameter as it influences the jet velocity and material transfer rate. A lower flow rate is more desirable as it allows the solvent in solution enough time to evaporate from the jet before reaching the collector plate. It is observed that the morphology of the fiber and pore diameter increases with an increase in flow rate for polystyrene fibers. High flow rates often result in beaded fibers due to the incomplete drying prior to reaching the collector plate (Bhardwaj and Kundu, 2010, Sill and von Recum, 2008).

1.4.3.1.8 Capillary tip to collector distance

The distance between the capillary tip and the collector plate influences the fiber morphology and diameters, however is not as significant as other parameters. A minimum distance is required in order to provide the fibers with enough time to dry (solvent evaporation) prior to reaching the collector plate. When the distance is too small, beads are observed on the resultant fibers (Bhardwaj and Kundu, 2010, Sill and von Recum, 2008). (Buchko et al, 1999) observed that the fibers produced at closer distances are flatter than the fibers produced at increased distance which had a rounder morphology.

1.4.3.1.9 Temperature

It has been found that with an increase in ambient temperatures there has been a decrease in the resultant fiber diameter. Mit-Uppatham et al, 2004, investigated the effect of temperature on electrospun polyamide-6 fibers ranging from 25-60°C, the results concluded that with the increase in temperature there is a decrease in the yielded fiber diameters. The researchers credited this finding to the decrease in viscosity of the polymer solution at increased temperatures (Bhardwaj and Kundu, 2010).

1.4.3.1.10 Humidity

Baumgarten, 1971, found that their electrospun fibers dried faster at very low humidity's, which is due to the ability of the solvent to evaporate faster than at higher humidity's. If the evaporation rate of the solvent is too fast, evaporation of the solvent would take place at the end of the needle and the electrospinning process would only take place for a few minutes before the needle tip is clogged up (Bhardwaj and Kundu, 2010). Therefore, the choice of solvent is an important parameter as it strongly influences whether fibers are capable of forming as well as affecting fiber porosity. A volatile solvent is often selected in order for sufficient solvent evaporation to occur between the capillary tip and the collector plate and therefore for solid polymeric fibers or particles to be deposited (Sill and von Recum, 2008).

1.4.3.2 Applications of electrospinning

Use of electrospun nanofibers are very attractive due to their advantageous high surface area to volume ratio, high porosity and capability to manipulate the fibers into achieving desirable attributes, through changing solution and process parameters. Therefore, electrospun fibers are increasingly being used in a wide variety of applications, including biomedical applications, wound healing, drug delivery, filtration and cosmetics (Bhardwaj and Kundu, 2010).

1.4.3.2.1 Tissue engineering applications

Tissue engineering is about the restoration, maintenance or improvement of tissue (cartilages, dermal tissue, bones, blood vessels, heart, nerves) function (Bhardwaj and Kundu, 2010). Electrospinning as a means of producing fibrous scaffolds is a simpler and more cost-effective procedure when compared to other fiber forming processes such as self-assembly and phase separation and meets all the essential design criteria of an ideal tissue engineered scaffold. Scaffolds for cellular growth, proliferation and new tissue formation in three-dimensions are a

crucial element for tissue engineering. Electrospinning is now the most extensively used fabrication method for the preparation of nanofibrous scaffolds due to the positive promotion of cell-matrix and cell-cell interactions with the cells possessing a normal phenotypic shape and gene expression (Frenot and Chronakis, 2003). The diameter of the electrospun fibers is of similar diameter of the fibrils in the extracellular matrix and therefore mimics the environment of the natural tissue (Friess, 1998). However, the pore size of the nanofibrous scaffolds are often very low and often cell infiltration is inhibited. Natural polymers are often selected for nanofibrous scaffold due to their enhanced biocompatibility. Biopolymers such as collagen, alginate, silk, hyaluronic acid, fibrinogen and starch have all been used to fabricate scaffolds and their ability to blend with synthetic polymers can improve the cytocompatibility of the scaffold (Park et al, 2006, Almany and Seliktar, 2005, Wayne et al, 2005, Yoo et al, 2005).

1.4.3.2.2 Wound dressings

An ideal dressing for wound healing is to have haemostatic ability, efficiency as a bacterial barrier, absorption ability of excess exudates (wound fluid and pus), suitable water vapour transmission rate, suitable gaseous exchange ability, ability to conform to the contour of the wound area, adherence to healthy tissue and non-adherent to wound tissue and inexpensive (Bhardwaj and Kundu, 2010, Huang et al, 2003). The use of electrospun nanofibrous materials for wound dressings are still in their infancy, however they meet most of the requirements for an effective dressing due to their desirable nanofibrous structure and reports of cytocompatibility (Huang et al, 2003). Jia et al, 2007, used electrospinning to prepare an antibacterial polyvinyl alcohol (PVA) membrane using silver loaded zirconium phosphate nanoparticles for use as a wound dressing. Antimicrobial tests demonstrated the efficacy of the nanofibers against tested strains.

1.4.3.2.3 Drug delivery

Nanofiber mats have been used as drug carriers in drug delivery systems. These drug delivery systems are fabricated using a biocompatible delivery matrix of polymer and biodegradable polymers and the particular active pharmaceutical ingredient (API) (Kost and Langer, 2001). There are various fabrication methods to develop the drug delivery systems; 1) API as particles attached to the surface of the carrier (nanofibers); 2) both API and carrier are in nanofiber form and interlace each other; 3) blend of API and carrier materials integrated into the nanofiber; 4) API is encapsulated in the carrier material using coaxial electrospinning. It relies on the

principle that the dissolution rate of a particulate drug increases with increasing surface area of the drug and corresponding carrier. Their large surface area allows for fast solvent evaporation which provides limited time for the incorporated drug to recrystallize which then favours the formation of amorphous dispersions or solid solutions (Verreck et al, 2003). The release rate of the API can be designed as rapid, intermediate, delayed or modified dissolution, all depending on the chosen polymeric carrier used. Many researchers have successfully encapsulated APIs within an electrospun fibrous mat (Zeng et al, 2003, Zong et al, 2002, Luu et al 2003, Kenawy et al 2002). Many APIs have been successfully electrospun; lipophilic drugs such as ibuprofen (Jiang et al, 2004), cefazolin (Katti et al, 2004) and hydrophilic drugs such as mefoxin (Kim et al, 2004, Zong et al, 2002) and tetracycline hydrochloride (Kenawy et al, 2002). Coaxial electrospinning to develop drug loaded polymeric nanofibers and has been successful using two medically pure drugs Resveratrol and Gentamycin sulphate (Huang et al, 2006).

1.4.3.2.4 Filtration

For over a decade, polymeric nanofibers have been used in air filtration applications. The channels of the filtration device must match the scale of the particles or droplets that are to be captured in the filter. The nano-sized fibers produced by electrospinning provide an advantage for use as filtration membranes. The very large surface area to volume ratio and high surface cohesion allow small particles in the order of $< 0.5 \mu\text{m}$ to be easily trapped in the nanofibrous membranes (Bhardwaj and Kundu, 2010). Non-woven mats produced by electrospinning have already been successfully used as high-performance air filters which demonstrates an extremely effective removal of airborne particles with diameters between $1 \mu\text{m}$ and $5 \mu\text{m}$ (approximately 100% removal) (Kattamuri et al, 2005, Ramakrishna et al, 2006). Filtration efficiency is closely associated with fiber fineness and is an important concern for filter performance. Ahn et al, 2006 evaluated the filtration efficiency of nylon 6 nanofilters using nanofibers with diameters between 80 and 200 nm and found an efficiency of 99.993% greater than commercialised high efficiency particulate air filter (HEPA) (Frenot and Chronakis, 2003). Jeong et al, 2007, synthesised polyurethane cationomers containing different amounts of quaternary ammonium groups into nanofiber mats for use as antimicrobial nanofilters applications. The results showed there were successful antimicrobial activities against *Staphylococcus aureus* and *Escherichia coli*. Charged fibers can also be produced from

electrospinning and this can be used for filtration media; the charge retention characteristics can be modified through the polymeric material selected (Tsai and Schreuder-Gibson, 2001).

1.4.3.2.5 Cosmetics

Electrospun polymeric nanofibers have been utilised as a cosmetic skin care mask with the addition of skin-revitalising factors for skin healing treatments, skin cleansing and other therapeutic and medical properties. The skin mask has the advantage of a high surface area and very small interstices which facilitates the transfer and transfer rate of additives to the skin (Huang et al, 2003, Smith et al, 2001). The skin mask can be applied gently and painlessly and can provide a three-dimensional topography of the skin (Huang et al, 2003).

1.4.4 Polymer choice

The selection of the polymer is an important parameter as it is able to influence the strength, weight, porosity and surface functionality of the resultant nanofiber or particles (Frenot and Chronakis, 2003). Selected polymers for the EHDA process are dissolved in the solvent forming a polymeric solution. Many polymers emit unpleasant or toxic smells and therefore a fume chamber must be used for the process (Bhardwaj and Kundu, 2010). The use of a variety of polymers are applicable for the electrospinning process, like those used in conventional spinning (i.e. polyamides, polyester, acrylic as well as biopolymers like proteins, DNA and polypeptides) (Frenot and Chronakis, 2003, Bhardwaj and Kundu, 2010).

Depending on the electrical properties of the selected polymer, the resultant polymeric nanofibers may dissipate or retain electrostatic charges. These charges can be manipulated by electric fields and the electrical polarity of the fibers are influenced by the polarity of the applied voltage (Frenot and Chronakis, 2003). The charges can be removed however through the presence of ions carried in the air or neutralised through contact with the collector plate (Reneker, and Chun, 1996). Tsai and Schreuder-Gibson, 2001, have researched the effect of electrospinning material and conditions upon the residual electrostatic charge of polymeric nanofibers; polymers including PEO, polycarbonate and polystyrene where evaluated on their charge induction and retention properties and ranked by their inherent polarity (Frenot and Chronakis, 2003).

Natural polymers often display better biocompatibility and low immunogenicity and therefore typically selected for biomedical applications (Bhardwaj and Kundu, 2010). Proteins of collagen, gelatin, elastin and silk fibroin have all been used previously for the electrospinning process (Li et al, 2005, Li et al, 2006a, Li et al 2006b, Zhang et al, 2006, Zhong et al, 2006). The fabrication of electrospun scaffolds using natural polymers provide better clinical functionality, however the main concern is the partial denaturation of the natural polymers. For example, Zeugolis et al, 2008, found that through the production of nanofibers by the electrospinning process the properties of collagen are often affected (i.e. the denaturation temperature and the loss of the triple helical structure).

Synthetic polymers are often selected over natural polymers due to their ability to be fabricate materials with a wider range of properties; including mechanical properties like strength and viscoelasticity and withhold a desirable degradation rate.

Copolymers enhance the properties of polymeric materials including the thermal stability, mechanical strength and barrier properties. The electrospun scaffolds fabricated from copolymers rather than homopolymers are often significantly better regarding their performance as desirable properties (mechanical, morphology, structure, pore size and distribution, biodegradability) can be tailored.

The chosen polymer for electrospaying can influence the particles size and morphology. It has been found that the particles diameter increases with increasing polymer concentration. Increased polymeric concentration leads to an increase in the viscosity and surface tension of the solution, this can form an unstable jet from the capillary tip (Pawar et al, 2018, Shao et al, 2015). Choosing a polymer with a high molecular weight can cause the formation of larger particles due to the increase of viscosity (Felder et al, 2003, Tapia-Hernández et al, 2003, Hazeri et al, 2012). A polymer with a high molecular weight can also increase the surface tension which can cause unstable jetting at the capillary tip and therefore a higher voltage would need to be applied for electrospaying to occur (Pawar et al, 2018).

1.4.5 Solvent choice

The chosen solvent for electrospraying can affect the particles morphology and size and also the surface morphology. If the solvent is not volatile it can lead to the formation of ribbon-like fibers and even fuse the fibers together, due to the solvent retention. A solvent with too high volatility can cause an increase to the diameter of the particles and affect the surface morphology and porosity as the evaporation rate is too high (Chakraborty et al, 2009). Electrospraying solvents which are too volatile are also a problem as they may clog the capillary, as they begin to evaporate at the Taylor cone itself, this creates a problem with the spraying (Pawar et al, 2018).

1.4.6 Physical characterisation

Physical characterisation is associated with the structure and morphology of the nanofibers which contributes to the physical and mechanical properties. Geometric properties include the fiber diameter, diameter distribution, fiber orientation and fiber morphology (cross-section shape and surface roughness). Scanning electron microscopy (SEM), transmission electron microscopy (TEM) and atomic force microscopy (AFM) are all techniques that can be used to show these geometric properties (Huang et al, 2003, Bhardwaj and Kundu, 2010). SEM is a quick method for detecting fiber diameters and morphologies with only a small sample size required. TEM also obtains fiber diameters but for extremely small fibers (< 300 nm). AFM is also used to measure fiber diameters but is more difficult to obtain an accurate measurement due to tip convolution. However, AFM is the best technique to observe surface morphology and descriptions of the fiber surface (Bhardwaj and Kundu, 2010).

1.4.7 Chemical characterisation

Details of the molecular structure of the nanofiber can be collected from Fourier transform infrared (FTIR) and nuclear magnetic resonance (NMR). The configuration of the macromolecules in the nanofiber can be characterised by X-ray diffraction (XRD) and differential scanning calorimeter (DSC). The surface chemical properties of the nanofibers can be assessed by its hydrophilicity through using water contact angle analysis (Huang et al, 2003, Bhardwaj and Kundu, 2010).

1.4.8 Coaxial EHDA

Coaxial EHDA is a nozzle configuration which allows for the simultaneous coaxial electrospinning or electro spraying of two different solutions. Two separate solutions flow through two capillary needles which are coaxial with a smaller capillary inside a larger capillary (Sill and von Recum, 2008). The materials used for this configuration are immiscible in order to be encapsulated. This technique is useful for materials that are susceptible to degradation as the shell can protect the contents of the core as well as releasing the contents of the core as when needed; i.e. through drug delivery systems.

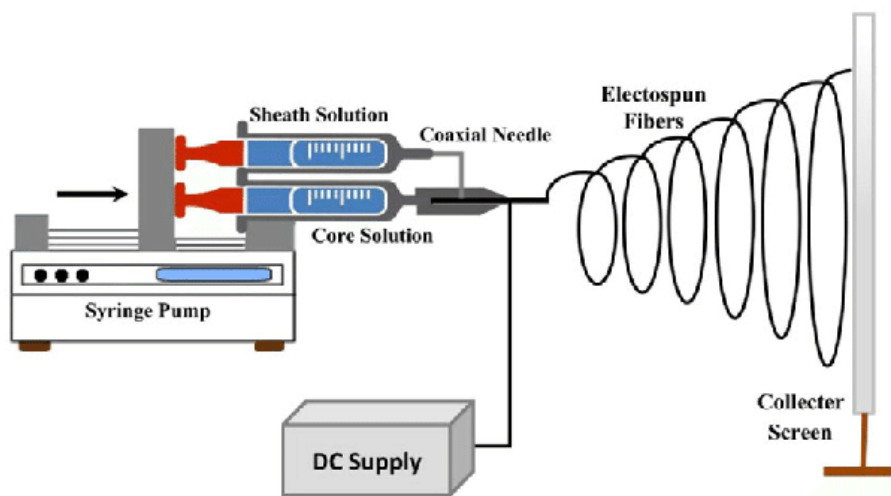


Figure 1. 6: Schematic representation of coaxial EHDA set-up (Alharbi et al, 2016).

1.4.8.1 Coaxial electro spraying

Using the coaxial configuration during electro spraying allows for the one-step encapsulation of APIs inside a polymeric shell, producing a defined shell with a defined core. This configuration still produces particles with a narrow particle size distribution in the micro and nanometer range (Sill and von Recum, 2008). These multi-layered nanoparticles have been utilised for many applications due to high encapsulation efficiency, uniform size distribution and effective protection of the core (Pawar et al, 2018).

1.4.8.2 Coaxial electro spinning

Using the coaxial configuration during electro spinning, a smaller fiber can essentially be encapsulated within a larger fiber, leading to a core-shell morphology. Coaxial electro spinning is particularly useful for materials that cannot be spun (i.e. non-conductive materials); the material can flow through the inner capillary needle to be encapsulated by a polymeric shell to

produce a core-shell nanofiber (Sill and von Recum, 2008). Townsend-Nicholson and Jayasinghe, 2006, successfully encapsulated living cells within a poly(dimethylsiloxane) (PDMS) fiber; cell viability remained high throughout the process with approximately 67.6% of cell surviving the electrospinning process. The electrospun cells were reported to show no observable difference in cell morphology or rate of growth with the control cells over a period of 6 days.

1.4.9 History

This technique was first observed in 1897 by Rayleigh; Zeleny further studied the electrospaying process in 1914 and was patented by Formhals in 1934 (Frenot and Chronakis, 2003, Bhardwaj and Kundu, 2010), in which he described the experimental set-up for the production of polymer filaments using an electrostatic force. In 1969, Taylor focussed on electrically driven jets as the groundwork for electrospinning (Bhardwaj and Kundu, 2010). In 1934, Formhals patented the experimental set-up and process that used an electrostatic force to spin polymeric nanofibers. Formhals used a movable thread-collecting device, which collected fibers in a stretched state which allowed for the collection of aligned fibers. Formhals spun cellulose acetate fibers using acetone/alcohol as the solvent. However, there were some issues with the electrospinning method; due to the close proximity between the collector plate and the tip of charged polymer solution, there was not enough time for the solvent to completely evaporate by the time the fiber jet reached the collector plate, which resulted in a loose web structure. These fibers were sticking to the collector plate as well as to each other which made the removal of fibers difficult. In Formhals second patent, a new process was detailed where there is a greater distance between the tip of the charged polymer solution and the collector plate, allowing enough time for evaporation and therefore relieving the issues Formhals had observed prior. Formhals also detailed the use of multiple nozzles for simultaneous spinning of the polymer solution as well as directing the jets towards the collector plate. In 1940, Formhals patented another process to create composite fibers by electrospaying directly onto a moving base. In 1969, Taylor published his work on the jet forming process, which examines the polymer droplet at the end of the capillary needle and how it behaves when an electric field is applied. When the surface tension is balanced by electrostatic forces the Taylor cone is formed. Taylor also established that the fiber jet is emitted from the apex of the cone, which generates fibers of a significantly small diameter. In 1971, Baumgarten investigated the relationship between varying solution and processing parameters and the resulting fiber

morphology. Baumgarten used a high-speed camera to allow him to determine that a single fiber was being drawn from the electrically charged drop at the end of the processing needle. Baumgarten also found that there was a relationship between solution viscosity and the fiber diameter; the higher the viscosity, the larger the resulting fiber diameter. He also found that the fiber diameter does not decrease with increasing the electric field, however it decreases initially to a minimum with an increase in applied voltage, however the fiber diameter increases further when the applied voltage increases further. Through varying the solution and processing parameters Baumgarten was able to produce fibers of varying diameters (Sill and von Recum, 2008). Reneker and Chun, 1996, revived the interest in the EHDA process in the early 1990's through electrospinning various polymers to produce nanofibers of various diameters.

Chapter 2 – Materials and methods

2.1 Materials

2.1.1 Polymer

2.1.1.1 Poly(lactic-co-glycolic acid) (PLGA)

PLGA is a synthetic copolymer comprised of monomers of glycolic acid and lactic acid (**Figure 2.1**). The degradation rate is affected by the sequence of monomers; random PLGA shows rapid degradation in comparison with sequenced PLGA. Sequenced PLGA are considered valuable for controlled drug delivery due to their release kinetics caused by the degradation. The ratio between the monomer components in the polymer chain influences the PLGA degree of crystallinity, mechanical strength, glass transition temperature and its ability to hydrolyse. PLGA with 50:50 ratio of the two monomers hydrolyse much faster in comparison with PLGA containing a higher ratio of either two monomers. PLGA terminal groups are either an acid or an ester - an ester terminal group allows resistance to hydrolysis. Many solvents can be used to dissolve PLGA depending on their composition. Higher lactide polymers can be dissolved using chlorinated solvents, however higher glycolide materials require the use of fluorinated solvents. The ester linkages of PLGA degrade with the presence of water. PLGA undergoes hydrolysis in the body which produces the original monomers. The body can metabolise the two monomers and therefore there is minimal systematic toxicity with using PLGA for biomaterial applications (Mir et al, 2017).

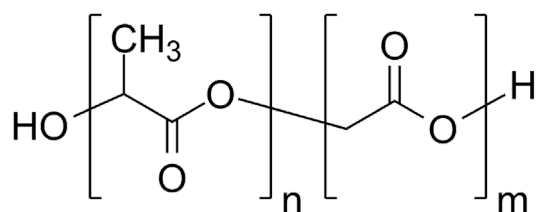


Figure 2. 1: Structure of PLGA 50:50 ester.

2.1.2 Drug

2.1.2.1 Amoxicillin (AMX)

AMX is a semi-synthetic, penicillin-derived, broad spectrum, bactericidal, β -lactam antibiotic used for the treatment for various bacterial infections (**Figure 2.2**). It is most commonly taken orally and thereafter it is well absorbed in the intestinal tract with the possession of very low toxicity. AMX has bactericidal actions against a wide variety of gram-positive and a fewer variety of gram-negative microorganisms (*E. coli* is highly resistant to AMX (Kibret and Abera, 2011)) through inhibiting the biosynthesis and repair of the bacterial cell wall (owing to the β -lactam ring (**Figure 2.3**)), leading to bacterial death. AMX has excellent diffusion capability into infected tissues (Resnik and Cillo, 2018, Karaman, 2015.). Prevalence studies suggest that the rate of resistance to AMX in humans is very high (Riley and Lizotte-Waniewski, 2009). Semi-synthetic β -lactam antibiotics like AMX are mostly produced through chemical synthesis. Although this process has successfully high yields, it is often criticised for its costly steps, toxic organic solvents and high volumes of waste and by-products which is harmful to the environment making the process undesirable (Wegman et al, 2001).

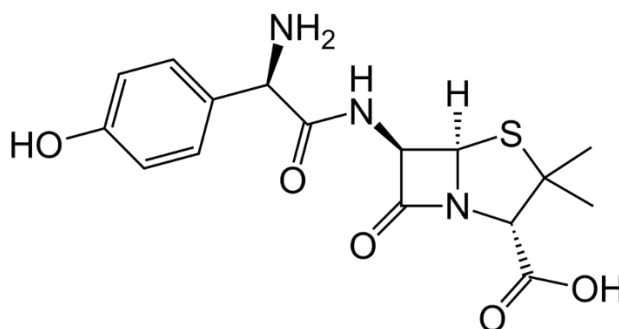


Figure 2. 2: Structure of AMX.

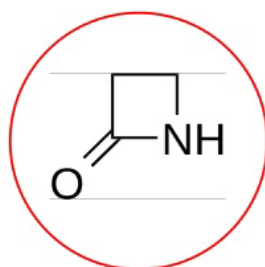


Figure 2. 3: β -lactam ring of AMX.

2.1.3 Solvent

2.1.3.1 Dichloromethane (DCM)

DCM is an organochloride compound (**Figure 2.4**). It is a colourless, volatile liquid withholding a mildly sweet aroma. DCM is widely used as a solvent. It is not miscible in water, however due to its polarity it is miscible in many organic solvents. DCM is produced through the treatment of methane or chloromethane with chlorine gas at 400-500°C where it undergoes a series of reactions to produce more chlorinated products i.e. DCM. DCM is a useful solvent for many chemical processes due to its volatility and its capability to dissolve many organic compounds. DCM is commonly used as a paint stripper and is the main component of plastic welding adhesives due to its ability to chemically weld plastics. Of all the simple chlorohydrocarbons, it is the least toxic – however due to its high volatility, it is an acute inhalation hazard. DCM can also be absorbed through the skin in which long contact can lead to the dissolving of some fatty tissues in the skin. Medical studies in the 1980's suggest that exposure to DCM has the potential to cause cancer, however research does not suggest to what level of exposure is carcinogenic (Hahn et al, 2019, Monette, 2009, Hurst and Martin, 2017).

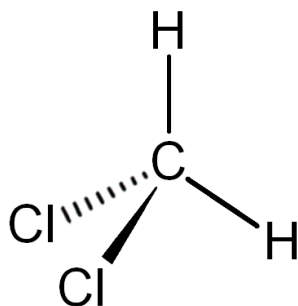


Figure 2. 4: Structure of DCM.

2.1.3.2 Acetone

Acetone is an organic compound (**Figure 2.5**). It is a colourless, volatile and an extremely flammable liquid, which is the simplest ketone. Acetone is miscible in water and is widely used as a solvent; it is a good solvent for many plastics and many synthetic fibers. It is also an excellent solvent for alcohols due to the lone pair of electrons on the carbonyl groups, which act as hydrogen bond acceptors. It is commonly used for cleaning purposes in laboratories and as the active ingredient in nail polish remover and paint thinner. Acetone is naturally produced and disposed of in the human body through regular metabolic processes. It is often present in the blood and urine; diabetics produce it in larger measures. Acetone has been studied extensively regarding health concerns and is found to have low toxicity regarding normal use and safety precautions are followed. With prolonged use, acetone can cause mild skin irritations and up to severe eye irritations. The high vapor concentrations can depress the central nervous system. Acetone is not currently recognised as a carcinogen (Ouellette and Rawn, 2014, Bradberry, 2007).

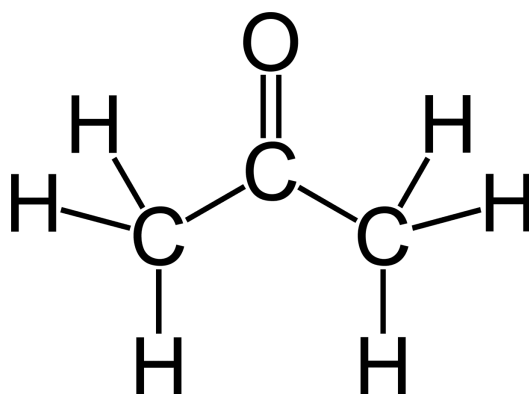


Figure 2. 5: Structure of acetone.

2.1.4 Precursor materials

2.1.4.1 Silver nitrate (AgNO_3)

AgNO_3 is an inorganic compound and is a versatile precursor for many silver compounds (Figure 2.6). In the 13th century, nitric acid was used to separate gold from silver, leaving behind a solution of AgNO_3 which was found to blacken skin. AgNO_3 is the least expensive salt of silver, it non-hygroscopic and relatively stable to light. AgNO_3 readily dissolves in many solvents which also includes water. AgNO_3 is often used for silver staining in histology, presenting proteins and nucleic acids, and is also used as a stain in scanning electron microscopy. AgNO_3 is effective against many strains of *Staphylococcus* and against many Gram-negative aerobes which can colonise wounds. Due to silver's antimicrobial activity there has been a lot of research evaluating the ability of the silver ion to inactivate *Escherichia coli* and was used for many applications prior to modern antibiotics. One-half percent AgNO_3 solution was commonly used as an effective topical agent in the 1960's for wounds and warts. Although AgNO_3 is often used in low concentration, it is still very toxic and corrosive. Brief exposure may only leave purple/black stains on the skin, but through constant exposure to high concentrations, skin burns and eye damage may occur. AgNO_3 is not currently recognised as a carcinogen (Bessey, 2007, Kunio and Schreiber, 2013).

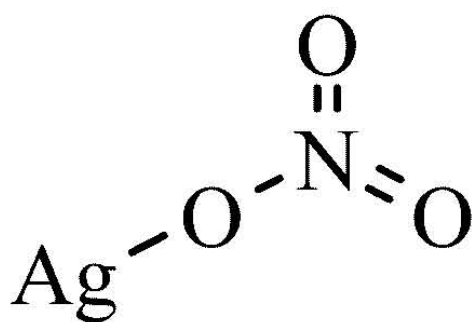


Figure 2. 6: Structure of AgNO_3 .

2.1.4.2 Gold (III) chloride trihydrate (HAuCl₄ x 3H₂O)

HAuCl₄ x 3H₂O is a precursor for the synthesis of gold nanoparticles (**Figure 2.7**). It exhibits a very high catalytic activity. Gold nanoparticles are often studied due to their unique synthetic properties, chemical inertness, high electron density and compatibility with living tissues. Gold possesses many effective properties against diseases and were used historically to cure various infections. Gold nanoparticles have been used in microorganism control, drug delivery, genomics, clinical chemistry, vaccine development and cancer-cell imaging. The Turkevich method is a routine protocol for synthesising gold nanoparticles; this is through the reduction of HAuCl₄ x 3H₂O with sodium citrate (Jazayeri et al, 2016, Ahmad et al, 2017).

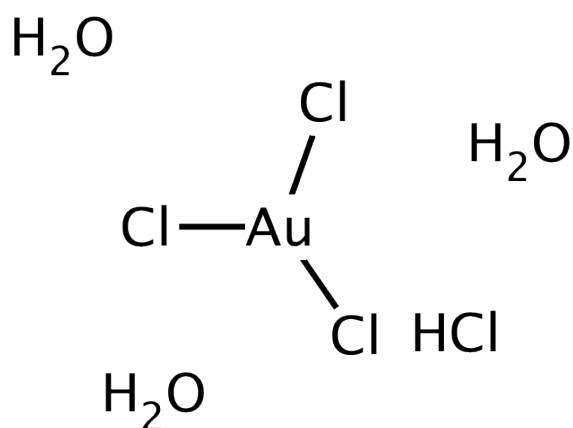


Figure 2. 7: Structure of HAuCl₄ x 3H₂O.

2.1.4.3 Copper (II) sulphate (CuSO₄)

CuSO₄ is a bright blue, inorganic compound, used as a precursor to make copper nanoparticles (**Figure 2.8**). It is highly soluble in water. CuSO₄ has shown potential as an antibacterial agent; for thousands of years CuSO₄ has been used to prevent wound infections and in recent years, the use of copper as an antimicrobial in hospital has amplified and in which can reduce the burden of antibiotic use. Copper nanoparticles are described as more active and more economical compared to bulk copper. Through the release of copper ions, bacterial membranes and DNA can be damaged due to the disruption of vital charge transports within the cells leading to cell death. Many chemical tests utilise CuSO₄; Fehling's solution to test for reducing sugars, Biuret reagent to test for proteins and to test blood for anaemia. It is often used as a fungicide; however, some fungi are able to adapt to elevated levels of copper ions. Due to its bright blue colour, CuSO₄ is often used as a colourant in artworks and also used in firework manufacturing. Previously, CuSO₄ was used as an emetic, however it is now considered too toxic for this use due to its irritating effect on the gastrointestinal tract. CuSO₄ is an irritant to the skin and eyes; prolonged skin contact can lead to itching or eczema and eye contact can cause conjunctivitis and inflammation to the eyelid lining (Betts et al, 2018, Ramos et al, 2019).

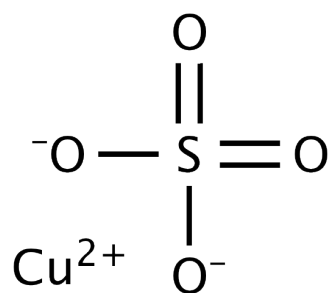


Figure 2. 8: Structure of CuSO₄.

2.1.5 Capping agents

2.1.5.1 Trisodium citrate ($\text{Na}_3\text{C}_6\text{H}_5\text{O}_7$)

$\text{Na}_3\text{C}_6\text{H}_5\text{O}_7$ is largely used as a food additive often seen as E number, E331 (**Figure 2.9**). It possesses a saline and mildly tart flavour. In food, it is used as a flavouring agent in beverages and also ice creams, yoghurt and cheeses. It can also be used as an emulsifier in cheese production to allow the cheese to melt without becoming greasy. $\text{Na}_3\text{C}_6\text{H}_5\text{O}_7$ has been used as an anticoagulant in blood transfusions in 1915, and is still used today for the preservation of blood in blood banks. The citrate ion chelates calcium ions in the blood to form calcium citrate complexes to disrupt the natural blood clotting mechanism. $\text{Na}_3\text{C}_6\text{H}_5\text{O}_7$ acts as a capping agent during the synthesis of nanoparticles. Capping agents are used to control the growth rate and particle size of the nanoparticles and prevent uncontrollable growth and particle aggregation.

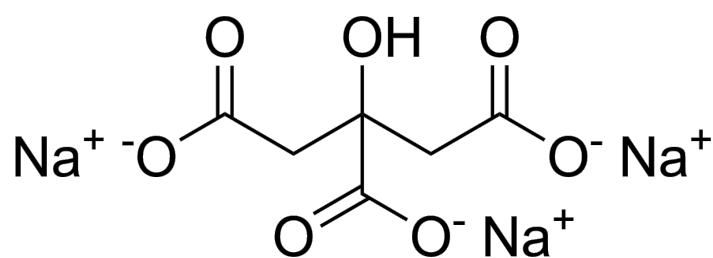


Figure 2. 9: Structure of $\text{Na}_3\text{C}_6\text{H}_5\text{O}_7$.

2.1.5.2 Polyvinylpyrrolidone (PVP)

PVP is a water-soluble polymer, made from the monomer N-vinylpyrrolidone (**Figure 2.10**). PVP is also soluble in other polar solvents such as alcohols and urea. Dry PVP is a light flaky hygroscopic powder able to readily absorb up to 40% its weight in atmospheric water. It has admirable wetting properties and can readily form films thus making it ideal for use as coatings. Due to these admirable properties, PVP was used as a blood plasma expander for trauma victims. PVP is also used as a binder in many pharmaceutical tablets in wet granulation or used to stabilise an amorphous API in a solid dispersion application. PVP is used as a lubricant or wetting agent in contact lenses and their packaging in order to reduce friction. PVP has been approved by the US Food and Drug Administration (FDA) for many uses and generally considered safe (Kariduraganavar et al, 2014, Narang et al, 2017).

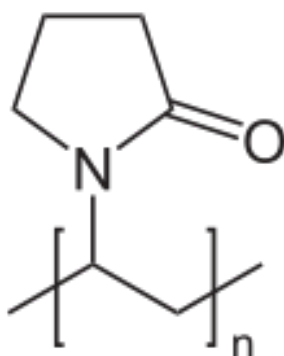


Figure 2. 10: Structure of PVP.

2.1.5.3 Sodium bromide (NaBr)

NaBr is an inorganic compound usually encountered as a white microcrystalline powder. It is effectively used as a reducing agent, with its relatively low cost and ease of handling contributing to its popularity. NaBr is soluble in water (although it slowly hydrolyses), alcohols and some ethers. It is a salt and exists in three polymorphs; α , β and γ , which changes upon changes in pressure. NaBr reduces many organic carbonyls depending on the conditions; typically used to convert ketones and aldehydes into alcohols. NaBr reacts with water and alcohols to produce hydrogen gas (Kabalka and Varma, 1991, Szekely and Didaskalou, 2016).

2.1.6 Reducing agent

2.1.6.1 Ascorbic acid

Ascorbic acid, also commonly known as vitamin C, is an essential nutrient found in various fruits and vegetables (citrus fruits, kiwi, broccoli, raw bell peppers) (**Figure 2.11**). It is required for the repair of tissues and enzymatic production of many neurotransmitters. Ascorbic acid also functions as an antioxidant due to its high reducing potential. It has been shown that ascorbic acid is an efficient reductant of CuSO_4 (along with other metal ions) and often used for the synthesis of copper nanoparticles. The hydroxyl groups of ascorbic acid are responsible for the antioxidant activity of the molecule, donating hydrogen atoms to other molecules. This reaction is reversible forming dehydroascorbic acid which is relatively stable (Luty-Błocho et al, 2013, Rucker et al, 2008, Duncan and Chang, 2012, Avendaño and Menéndez, 2008).

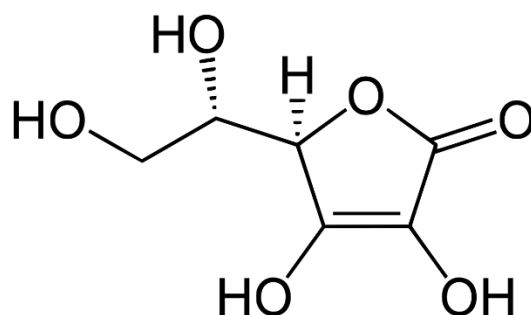


Figure 2. 11: Structure of ascorbic acid.

2.1.7 Vehicles

2.1.7.1 Ethylene glycol (EG)

EG is a non-volatile, colourless, organic compound found as a viscous liquid (**Figure 2.12**). Ethylene is mainly used for two purposes; starting material for the manufacture of polyester fibers or used in antifreeze formulations due to its low melting point and high boiling point. EG is toxic. Children and animals often consume large amount due to its sweet taste leading to EG toxicity. EG is non-volatile and odourless and thus inhalation exposure is not considered a health hazard. However, absorption of EG through the skin is considered a health hazard especially if there are any skin lesions. EG is rapidly and completely absorbed from the intestinal tract upon ingestion. It is oxidised to glycolic acid and then into oxalic acid which is toxic, affecting the central nervous system, the heart and then the kidneys. It is fatal if left untreated (Roy, 2016, Pohanish, 2017, Carney, 2011, Dasgupta and Klein, 2014, Dasgupta and Wahed, 2014).

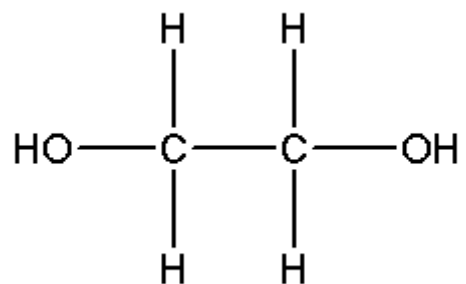


Figure 2. 12: Structure of EG.

2.1.7.2 Deionised water (D.I water)

D.I water is natural water which has had all of its mineral ions removed. The ions include: sodium, calcium, iron, copper, chlorides and sulphates. D.I water is used for chemical processes where the minerals present may interfere with the chemicals, therefore D.I water has a low chemical reactivity. Pharmaceuticals are made with D.I water for this reason. To create D.I water, natural water is exposed to electrically charged resins which attract and bind to the mineral ions and thus they are removed from the water. Although D.I water is deemed highly pure, it still may contain bacteria or viruses. In microbiology and fields where sterile water is required, the D.I water is cooked in an autoclave prior to use to kill of the bacteria and viruses within.

2.2 Methods

2.2.1 Determination of Material Properties

2.2.1.1 Viscosity

Viscosity is a property of a liquid relating to the resistance of flow. A sine-wave vibro viscometer is used to quantify the viscosity of all formulations (**Figure 2.13**). The mechanism for the viscometer involves determining the driving current to resonate two gold-plated sensors maintained at constant frequency of 30 Hz. The driving current is determined as the difference in the viscous drag between the two plates and the sample.

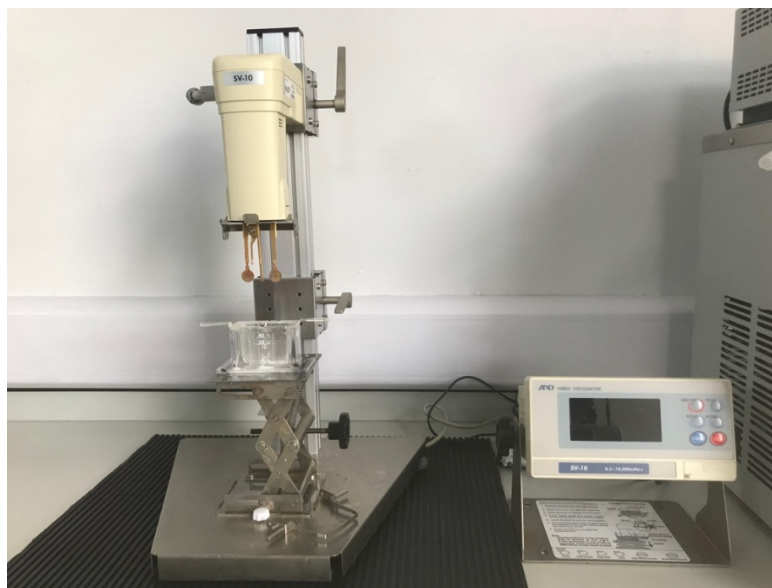


Figure 2. 13: Digital image of an A&D SV-10 sine wave vibro viscometer.

2.2.1.2 Surface tension

The surface tension of the formulations was measured using the DuNuoy ring method (**Figure 2.14**). It is measured by the force required to remove the platinum ring from the surface of the liquid phase into the gas phase.

The ring is placed onto the surface of the liquid and upon external forces, the ring is lifted up off the liquid surface. The amount of force required to remove the ring from the liquids surface correlates to the surface tension of the liquid using the equation:

$$\sigma = \frac{F}{L \cos \theta}$$

Where:

σ = surface tension (N/m)

F = force (N)

L = wetting length of the ring (m)

$\cos \theta$ = contact angle between the liquid and the ring

Equation 2. 1: Equation for surface tension.



Figure 2. 14: Digital image of a White Electrical Instrument Co. OS torsion balance.

2.2.1.3 Electrical conductivity

An electroconductivity meter is used to measure the ability of a liquid to pass an electrical current through itself (**Figure 2.15**). The electroconductivity meter is a probe withholding four electrodes. An alternating current is initiated by the probe once placed in the sample and the current is passed between the four electrodes.

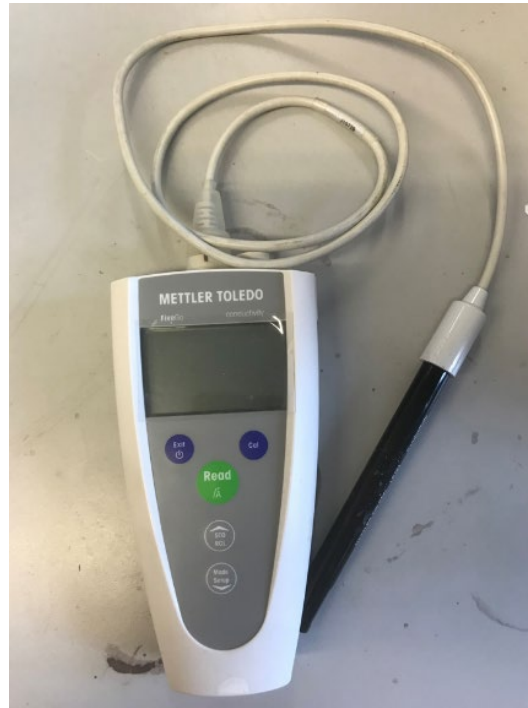


Figure 2. 15: Digital image of a Mettler Toledo FiveGo electrical conductivity meter.

2.2.2 Electrohydrodynamic atomisation (EHDA)

The EHDA technique is a simple set-up consisting of 5 components; syringe filled with the formulation, syringe infusion pump, stainless steel processing needle, high voltage supply and a grounded collector plate (**Figure 2.16**).

The formulations are filled into the syringe and the infusion pump controls the flow rate of the formulation throughout the procedure. The formulation is fed through a silicon tube and into an electrically conducting processing needle. A high voltage is applied across the processing needle where the formulation is held by its surface tension inducing a charge. When the intensity of the electric field overcomes the repulsive electrostatic force of the surface tension of the formulation a charged jet of fluid is ejected from the Taylor cone. The solvent within formulation evaporates as the fluid is ejected causing the production of particles or fibers. The resulting particles or fibers are collected on a grounded plate.

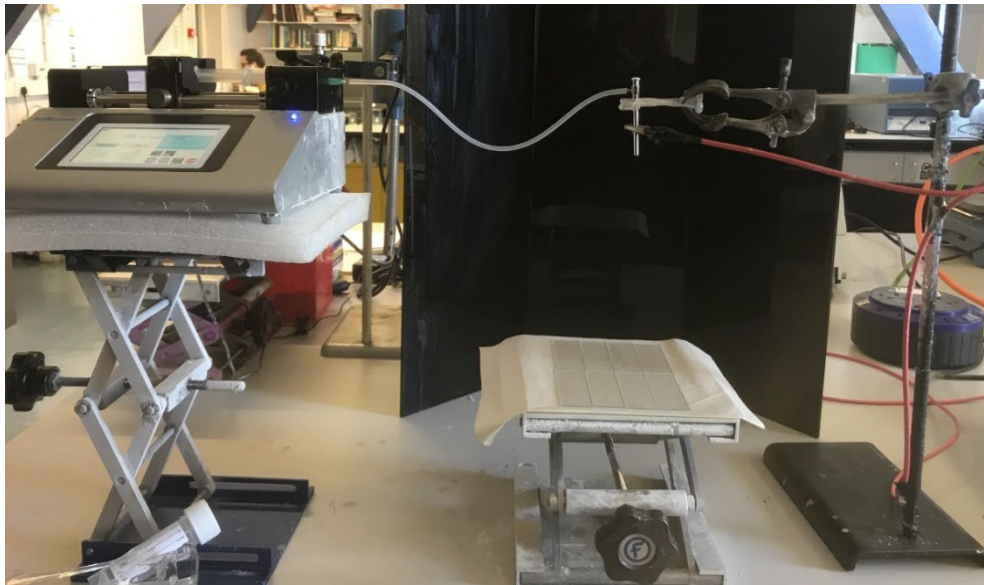


Figure 2. 16: Digital image of the EHDA set up.

2.2.3 Scanning electron microscope (SEM)

SEM is a microscopic technique used to reveal information about the surface morphology, chemical composition, structure and the alignment of the materials making up the sample (**Figure 2.17**). SEM uses beams of electrons to image a surface, which are of high energy with a very small equivalent wavelength. The resolution of the SEM is better than one nanometer and the interaction of the electron beam with the surface of the sample can give rise to X-ray emission which can allow chemical characterization of the materials making up the sample. By using SEM, highly detailed images over a wide range of magnifications from the samples surface can be produced. The interaction between the surface of the sample and the electron beam forms an image which is created by the electrons emitted from the surface – either secondary electrons or backscattered electrons. Secondary electrons are emitted by the atoms on the samples surface when they become excited and withhold sufficient energy to leave the surface. Secondary electrons within the top 10 nm of the surface are likely to escape and be detected. These electrons have a high resolution and carry information about the samples surface which are used to create the images in SEM. Backscattered electrons are high energy electrons which originate from the electron beam and are reflected and provides contrast reflecting differences in rough composition within the sample. This is due to the atomic mass of the nuclei – the greater the atomic mass, the greater the scattering which appears brighter than lighter elements. Different detectors collect either secondary or backscattered electrons. Typically, the sample is coated with a thin layer of gold which makes the sample conductive. The sample is then affixed onto aluminum stubs by copper tape and then mounted onto the stage in the chamber.



Figure 2. 17: Digital image of Carl Zeiss Evo 15 SEM.

2.2.4 Differential scanning calorimetry (DSC)

DSC is a thermal analytical method used to measure the energy changes within a sample upon heating and establishes the thermal stability of the sample (**Figure 2.18**). DSC measures the difference in the amount of heat required to increase the temperature of a sample and reference measured as a function of temperature. Upon the application of the heat, the sample may undergo chemical (hydrolysis) or physical (melting) changes, which may emit energy (exothermic) or require energy to take place (endothermic), which can be seen in the thermogram of the DSC.



Figure 2. 18: Digital image of a Jade differential scanning calorimeter.

2.2.5 Thermogravimetric analysis (TGA)

TGA is thermal analytical technique used to observe the physical mass changes of a sample when subjected to heating at a constant rate (**Figure 2.19**). It determines the materials thermal stability and its fraction of volatile components through monitoring the mass change. The sample is placed in an inert atmospheric chamber typically with nitrogen and the changes in mass is measured as a function of temperature. Loss of mass can be due to decomposition (bonds breaking) or due to evaporation of volatile solvents. However, weight gain can be due to oxidation or absorption, which can be seen on the thermogram of the TGA.



Figure 2. 19: Digital image of a PerkinElmer Pyris 1 TG analyser.

2.2.6 Attenuated total reflection Fourier transform infrared spectroscopy (ATR-FTIR)

FTIR spectroscopy is used to identify or confirm the samples compositional molecules based on the samples unique infrared absorption spectrum (**Figure 2.20**). The samples can be either solid, liquid or gas. The FTIR spectrometer collects high spectral resolution data over a wide spectral range simultaneously. The infrared beam passes through a sample and parts of the spectrum is absorbed and some is transmitted. The absorbed radiation by selective molecules and then causes changes in dipole moments of the sample. The vibrational energy level of the sample transitions to an excited state. The transfer to excited state from ground state is shown as an absorption peak of the sample and the intensity is correlative to the change in the dipole moment and this is presented as the molecules unique fingerprint. Attenuated Total Reflection (ATR) is a technique conjugated with FTIR which uses a dense crystal. The beam of infrared light is passed through the ATR crystal and the internal reflectance causes an evanescent wave which passes through the sample and reflection radiation is returned to the detector as it exits the crystal, establishing a unique fingerprint for the sample.



Figure 2. 20: Digital image of Bruker FTIR Platinum-ATR spectrophotometer.

2.2.7 X-ray diffraction (XRD)

X-ray diffraction (XRD) is a non-destructive technique which uses large area X-ray detectors which are capable of probing deep into the lattice structures in order to characterise micro-crystalline materials (**Figure 2.21**). This method provides information on the crystal structure, orientation (texture), average grain size, crystallinity, strain, stress, multilayer composition, morphology, phase identification and any structure defects.

X-rays are produced from the sudden deceleration of high-speed electrons as they collide with a metal target. During the deceleration process, most of the electron energy is converted into heat and about less than 1% is converted into X-rays. X-ray diffraction occurs as incident beams of monochromatic X-rays constructively interfere with the atomic planes at specific angles as they leave the crystal. X-rays excite atoms at different positions along a time period – this excitement introduces secondary X-rays which form interference patterns.

The sharper the peaks on the peak graph the more crystalline the material. However, amorphous materials like glass do not produce sharp peaks. The peak intensity presents the distribution of atoms within the lattice. Therefore, the X-ray diffraction pattern is the unique fingerprint which combines the presence and intensity of the atomic elements that make up a material. In order to identify an unknown sample, a database of X-ray diffraction patterns in the ICDD (International Centre for Diffraction Data) is available for the phase identification. XRD is advantageous as it is a non-destructive technique and provides quantitative measurements of phase and texture orientation. There is little sample preparation required prior to the use of XRD and ambient conditions are acceptable for analysis.



Figure 2. 21: Digital image of a Bruker 2nd Generation D2 Phaser.

2.2.8 Raman spectroscopy

Raman spectroscopy is a technique used to provide highly chemical specific information about the samples based on their fundamental vibrations of the molecules (**Figure 2.22**). Through the absorption of light (using a laser), the molecules get excited causing them to vibrate and through measuring the inelastic scattering of photons information is presented regarding the properties of the molecules. The interactions provide information on the functional groups, chain orientation and structural changes (Rinke-Kneapler and Sigman, 2014, Goh et al, 2017, Gomes et al, 2018).

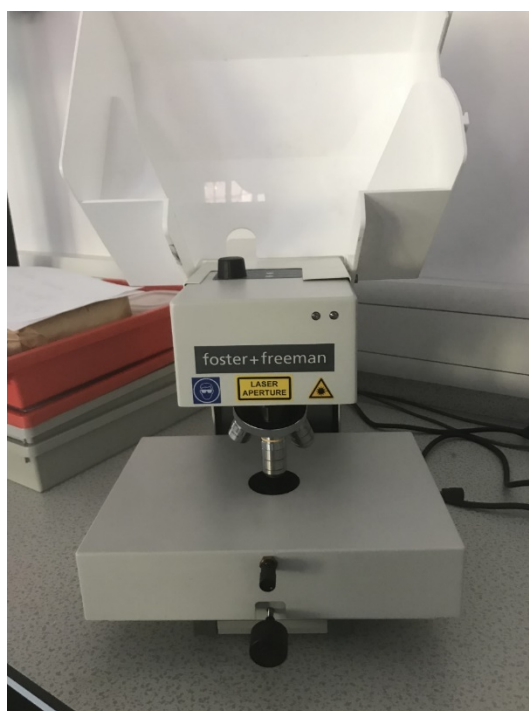


Figure 2. 22: Digital image of a Foster+Freeman Foram-2 Raman spectrometer.

2.2.9 Zeta potential

Zeta potential is the surface charge of the particle (**Figure 2.23**). Most liquids contain ions which are attracted to the surface of the suspended particle. Ions close to the surface of the particle are bound strongly, however ions further away are loosely bound forming a diffuse layer. When the particle moves in the medium, any ions in this boundary will move with the particle, however particles outside this boundary will remain stationary. Through measuring the velocity of the particle moving in a cell under the influence of an applied electric field allows the zeta potential to be obtained. It is the potential difference between the moving dispersion medium and the stationary layer of the dispersion medium attached to the dispersed particle. The pH of the medium strongly affects the zeta potential, along with the ionic strength, concentration, temperature and any additives (Harmata and Guelcher, 2016, Krstić et al, 2018, Lu and Gao, 2010).



Figure 2. 23: Digital image of a Brookhaven NanoBrook Omni zeta potential analyser.

2.2.10 In-vitro drug release

In-vitro refers to tests carried out in a controlled laboratory environment to mimic physiological conditions. In-vitro drug release measures the release of the API released from the carrier in an environment stimulating physiological conditions. The dosage form is subjected to a set of conditions that would induce drug release and quantitating the amount of drug released under those conditions. The typical conditions for this test to be carried out is in a water bath at 37°C with a pH of 7.1-7.4 (**Figure 2.24**). Personalised dosage forms may require elevated or dropped temperature and/or pH. Samples are taken in intervals over an extended period of time and measured using ultraviolet-visible spectroscopy to calculate the concentration of drug released at that time point (Singhvi and Singh, 2011) (**Figure 2.25**).



Figure 2. 24: Digital photo of a Stuart SBS40 Shaking water bath.

2.2.11 Ultraviolet–visible spectroscopy (UV-vis)

UV-vis spectroscopy is a simple, fast and low-cost analytical technique (Tuhkanen and Ignatev, 2018) (**Figure 2.25**). It refers to the absorption spectroscopy which relies on the sample containing species that absorbs light within the near-UV (180-390 nm) and visible (390-780 nm) spectral regions in solution or in gas phase. A beam of light excites the species from a grounded state to an excited state, undergoing an electronic transition (Holmes-Hampton, 2014). However, UV-vis is not a technique commonly used for identification purposes. Although all species have their own unique fingerprint region, it is not sufficient enough to show fine structures, therefore, it is mainly used for quantitative analysis (Worsfold and Zagatto, 2017). The concentration of the analyte in the sample can be calculated through measuring the absorbance at the selected wavelength and applying the Beer-Lambert law (Hameed et al, 2018, Mäntele and Deniz, 2017).

$$A = -\log T = \log_{10} \frac{I_0}{I_1} = \epsilon cd$$

Where:

A = absorbance

T = transmission

I_0 = intensities of the incident light

I_1 = intensities of the transmitted light

ϵ = molar absorption coefficient

c = concentration

d = path length of the sample

Equation 2. 2: Beer-Lambert law equation.

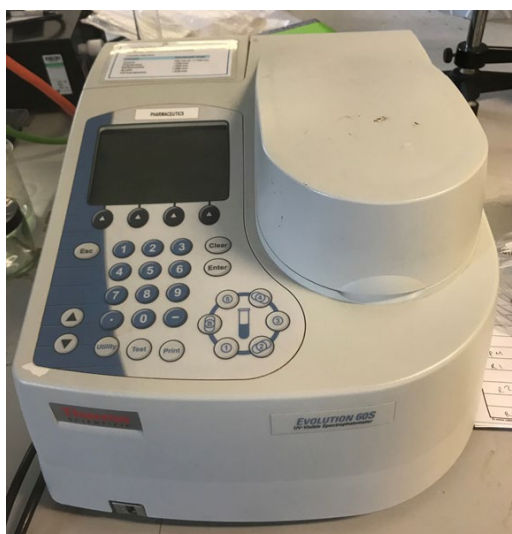


Figure 2. 25: Digital image of a UV-Vis spectrophotometer

2.2.12 Disk diffusion testing

The disk diffusion test is the test of antibiotic sensitivity of bacteria. Antibiotic disks are placed on an agar plate where bacteria has been spread; the plate is then incubated. The test measures the extent to which bacteria are affected by the antibiotics. If the antibiotic is successful and stops the bacteria from growing or kills the bacteria, there will be no colonies of bacteria growing in the area around the disk; this is the zone of inhibition. The diameter of the zone depends on multiple factors; 1) how effective the antibiotic is at stopping the growth of the bacterium; 2) diffusion of the antibiotic in the agar medium depending on the molecular configuration of the antibiotic; 3) the concentration of antibiotic in the dose. The concentration of antibiotic will be highest next to the disk and decrease as the distance increases (Christenson and Korgenski, 2012, Sandle, 2016).

2.2.13 Ex-vivo cell culture

Cell culture is the reproduction and survival of cells in an controlled artificial environment (Uysal et al, 2018). The cells of interest are isolated from living tissue and then maintained under carefully controlled conditions. Conditions vary for varying cell types but it generally consists of a suitable vessel filled with a medium which supplies essential nutrients (amino acids, carbohydrates, vitamins, minerals), growth hormones, gases (oxygen, carbon dioxide) and regulates the physiochemical environment (pH buffer, osmotic pressure and temperature). The growth of the cells can be characterised by cell division or through processes such as differentiation, where the cells can change into specific types which are capable of functions equivalent to tissues or organs in the whole organism (Lynn, 2009). The cell culture laboratory must be a sterile environment. Contamination is the most common issue in the cell culture studies which can lead to serious loss of samples and wasted time. Good cell culture practice occurs when necessary appropriate conditions are met and contamination factors are removed. Using macroscopic and microscopic techniques to follow-up the culture environment is important. The reproduction of the cells is reliant on the free space in the culture vessel and the amount of nutrients in the medium to support growth (Singhvi and Singh, 2011).

2.2.14 Optical density

The optical density measurement is the intensity ratio between the light falling onto a material to the light being transmitted through a material, governed by:

$$A(\lambda) = -\log_{10} \frac{I_0}{I_1}$$

Where:

A = absorbance

I_0 = intensities of the incident light

I_1 = intensities of the transmitted light

Equation 2. 3: Equation for optical density.

The absorption spectra provides an array of information of the sample including concentration, geometry and size of particles and biological activities. The absorbance is reliant on the incident wavelength. An optical density measured at a wavelength of 600 nm (OD600) is commonly used for estimating the concentration of bacteria in a liquid. This concentration can be correlated to signpost the stage in the bacterial growth curve; log phase, exponential phase, stationary phase or death phase. Optical density (**Figure 2.26**) is preferred to UV spectroscopy as UV light has the ability to kill or damage the cells of interest (Zhang and Hoshino, 2019).



Figure 2. 26: Digital image of a SpectraMax Plus 384 Microplate Reader.

Chapter 3 – Synthesis of metallic nanoparticles

3.1 Introduction

In this new age of antibiotic resistance, it is imperative that research is carried out to discover new materials with broad spectrum antibacterial activity. Poor intracellular bioavailability and a non-target specific mode of action reduces efficacy of antibiotics. Of the many materials that can be used as antibacterial agents those most promising (based on already published experimental data) are metallic particles, these are easy to synthesise and readily reproducible (Rai et al, 2012). Discoveries from experimental data have shown metallic nanoparticles display antibacterial activity, combining such materials with an antibacterial active drug can only augment efficacy and overcome resistant strains. Research into this combined drug therapy is now being explored. Major application for these formulations is the antibacterial activity, they decrease bacterial growth through blockage of the food source or can kill bacteria through disruption of cell wall (Wang et al, 2017).

The synthesis and use of metallic nanoparticles as antibacterial is on the rise due to the numerous advantages including, the increased surface area to volume ratio and crystalline structure of the nanoparticles leading to them being more effective than their ionic counterparts, as well as being significantly less toxic to surrounding cells (Chatterjee et al, 2014), furthermore, the different types of metallic compounds that can be synthesised, including gold, silver and copper nanomaterials, also different shapes of these metals can be synthesised and each variation in morphology may influence efficacy against bacteria.

The mechanism related to metallic nanoparticles efficacy however, is still under investigation, probable mechanisms have been proposed: (I) dissolution of the metal molecules from the surface of the nanoparticles that lead to increase in the free metal ion toxicity and (II) generation of a reactive oxygen species on the surface of the nanoparticles stimulate an oxidative stress leading to the antimicrobial effect (Besinis et al, 2014, Dizaja et al, 2014).

Moreover, accumulation and dissolution of the nanoparticles at the cell membrane changing its permeability, uptake of the metallic ions derived from nanoparticles into cells followed by depletion of ATP production, generation of ROS and corresponding ions from nanoparticles with subsequent oxidative damage to cell structure. (Chatterjee et al, 2014)

Inorganic materials such as metals and metal oxides have demonstrated antimicrobial activity toward various microbes. Metallic nanoparticles are effective as growth inhibitors for different microorganisms. Accordingly, they have the advantage to be used in medical devices and antimicrobial control systems against multi-drug resistant bacteria (Kim et al, 2007). For example; gold nanoparticles and silver nanoparticles are frequently used for their antimicrobial activity. For instance, 2 nm core cationic monolayer protected gold nanoparticles are able to interact with both gram-negative and gram-positive bacteria cell membrane inducing blebbing, distinct aggregation patterns and lysis of bacterial cell wall (Li et al, 2014). Silver is a broad-spectrum antibiotic with high toxicity toward microorganisms due to the generation of free radicals of silver nanoparticles (Kim et al, 2007) that attack the lipid membrane on the bacteria accordingly breaking down its functions (Mendis et al, 2005). For example, the minimal inhibitory concentrations (MIC) of silver nanoparticles (13.5 ± 2.6 nm) against *E. coli* and yeast are estimated in the range of 3.3 to 6.6 nM and 6.6 and 13.2 nM, respectively (Kim et al, 2007).

Other examples of metallic nanoparticles are zinc oxide (Xie et al, 2011), titanium dioxide (Santhoshkumara et al, 2014), copper oxide (Meghana et al, 2015) and iron oxide (Behera et al, 2012). These nanoparticles have better efficiency against resistant bacteria and have a selective toxicity toward bacteria, however demonstrating less efficacy upon mammalian cells (Reddy et al, 2007), when compared to conventional antibiotics.

Copper nanoparticles are also popular, due to acquisition and synthesis of these nanoparticles being financially viable, as well as being effective. Furthermore, due to the increased surface area to volume ratio at the nano size range, greater interactions with bacteria was demonstrated. A study by (Bogdanović et al, 2014) demonstrated the antibacterial activity of copper nanoparticles, after 2 hours of contact with bacteria, a 98% reduction of tested strains was seen, at high copper nanoparticle concentration (32 ppm). *E. coli* was completely eradicated and almost full inhibition against *C. albicans* at this concentration of copper nanoparticles.

Moreover, a study conducted by (Jahangiri and Jamshidi, 2014), has demonstrated that after 2 hours of incubation, almost all treated bacteria cells of *E. coli* were severely inhibited when a concentration of $150 \mu\text{g mL}^{-1}$ copper nanoparticles were used. This study used varying concentrations of copper and showed that varying concentrations vary in efficacy against bacteria, with higher concentrations of the copper nanoparticles more bacterial death was seen at a much faster rate.

Data has been published on the effect of copper nanoparticles upon gram-negative bacterium *E. coli* K12 and the gram-positive bacteria *Bacillus subtilis* and *Staphylococcus aureus*. Results from this study showed that when $12.0 \mu\text{g mL}^{-1}$ of the copper nanoparticles were added to the bacterial species, 18h after incubation no *E. coli* was present, the initial concentration before incubation of *E. coli* was 3×10^7 . Besides *E. coli*, the antibacterial properties of copper nanoparticles were also studied on the bacterial species *B. subtilis* and *S. aureus*. From the viability assay of cells in the presence of different concentrations of copper nanoparticles, the MIC and minimum bactericidal concentration (MBC) values of copper nanoparticles for *B. subtilis* were determined to be 3.0 and $9.0 \mu\text{g mL}^{-1}$, respectively, whereas for *S. aureus* the values were $4.5 \mu\text{g mL}^{-1}$ and $9 \mu\text{g mL}^{-1}$, respectively. Moreover, as in the case of *E. coli*, copper nanoparticles-induced cell filamentation was also observed in *B. subtilis*. This then proves the ability of copper nanoparticles to kill both gram-negative and gram-positive bacterial cells at such low concentration, meaning further investigation of copper nanoparticles as potential antibacterial agents is needed (Chatterjee et al, 2012).

Metallic nanoparticles synthesis can be controlled, to produce varying sizes and morphologies, silver nanoparticles have been synthesised, as nanorods or wires, triangular and octahedral, the synthesis of a specific shape depends on the reaction conditions. Kanwal et al, 2019 synthesised varying sizes and shapes of nanoparticles through the citrate reduction method, to test efficacy against bacteria, in their study they synthesised three different types of silver nanoparticles, larger diameter, smaller diameter and triangular shaped nanoparticles, results showed the smaller sized spherical particles to be more antiseptic, than those shaped triangularly, as for the larger particles they were found to be less efficient in bactericidal action than the triangular shaped nanoparticles. Data collected confirms that with an optimized size and shape of silver nanoparticles, and with a higher surface area, action as potential antibacterial agents is possible.

3.2 Aims & Objectives

With the increase in antibacterial resistance, novel methods of antibacterial drug delivery are being researched and tested, one such method is the use of antibacterial metallic nanoparticles.

In this chapter synthesis of metallic nanoparticles, varying in their morphology and size, was attempted. Shapes of the metallic nanoparticles included spherical silver nanoparticles (AgNP), silver nanowires (AgNW), polygonal silver nanoparticles (AgP), spherical gold nanoparticles (AuNP) and spherical copper nanoparticles (CuNP). Upon synthesis characterisation was

required to determine the identity and chemical properties of synthesised nanoparticles, the characterisation techniques used included SEM/EDS, ATR-FTIR, Raman, UV-Vis, XRD and Zeta Potential.

3.3 Materials and methods

3.3.1 Materials

Metallic nanoparticles were synthesised in-house.

All of the chemicals used in this work were of analytical grade and used as they were without any additional purification. The precursors used for synthesis of the metallic nanoparticles included AgNO₃, CuSO₄, HAuCl₄ x 3H₂O, Na₃C₆H₅O₇ and PVP M_w 40,000. NaBr was used as a reducing and capping agent in many of the silver nanomaterials synthesis, moreover ascorbic acid was used for the CuNP synthesis and help prevent rapid oxidation of copper particles. D.I water and ethylene glycol (EG) were used for the preparation of all the solutions in the capacity of a vehicle.

3.3.1.1 Silver nanoparticles (AgNP)

AgNP were prepared through a citrate reduction method (Frost et al, 2017), a 1 % w/v solution of Na₃C₆H₅O₇ was prepared, 42.5 mg of AgNO₃ was added to 50 mL D.I water, this solution was brought to the boil, to this the reducing agent was added dropwise, after certain amount of time the final colour of solution observed was yellow indicating the end point of synthesis (Gakiya-Teruya et al, 2018). Upon synthesis nanoparticles were centrifuged at speed of 4600 rpm and washed with acetone once and D.I water three times to eradicate any impurities and unreacted precursors.

The particles were produced through the following reaction:



Equation 3. 1: Equation showing the synthesis of spherical AgNP.

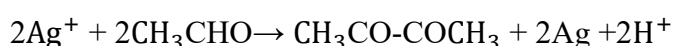
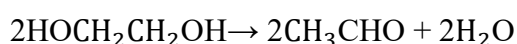
3.3.1.2 Silver nanowires (AgNW)

AgNW synthesized by reducing AgNO₃ with EG in the presence of PVP as the capper agent. Two solutions, 127 mg of AgNO₃ in 7 mL of EG and 127 mg of PVP in 7 mL of EG were

added concurrently, to 5 mL of EG refluxed for an hour at 160 °C. Colour changes observed were from a darkish black colour to a final colour cloudy grey indicating end point of the synthesis. Upon synthesis nanoparticles were centrifuged at speed of 4600 rpm and washed with acetone once and D.I water three times to eradicate any impurities and unreacted precursors (Sahin Coskun et al, 2011).

3.3.1.3 Polygonal silver nanoparticles (AgP)

The name polygon is attributed to any 2-dimensional shape formed with straight lines, hence why these nanoparticles were called AgP. To synthesize AgP or non-spherical silver nanoparticles with edges, 3 mL of two EG solutions were added, first contained 144 mM of PVP with 0.11 mM NaBr, the second contained 94 mM AgNO₃, these were added dropwise via a two-channel syringe pump to 5 mL of EG refluxed in a condenser at 160 °C one after the other. An additional 30 µL drop of 10 mM NaBr was added to the pre-heated EG. The solution turned yellow in a few seconds upon the addition of AgNO₃ and PVP which confirmed the formation of AgNPs. After 10 minutes, the yellow colour faded in intensity due to oxidative etching and remained a light-yellow colour for approximately 10 minutes before turning to brown and then to darker grey as the nanoparticles increased in size. Upon synthesis nanoparticles were centrifuged at speed of 4600 rpm and washed with acetone once and D.I water three times to eradicate any impurities and unreacted precursors.



Equation 3. 2: Equation showing the synthesis of AgP.

The presence of mediating species such as NaBr, play a role in the etching of the particle seeds, enabling the formation of particles with edges. The PVP also works as a shape-control agent encouraging the reduction of AgNO₃ onto specific crystal faces while stopping reduction onto others.

3.3.1.4 Gold nanoparticles (AuNP)

For preparation of the AuNP, 2.2 mM sodium citrate of 150 mL D.I water was placed in a beaker over hot plate for 20 minutes under continuous stirring. After boiling (100 °C) 1 mL

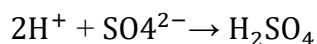
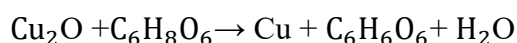
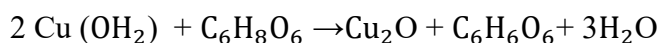
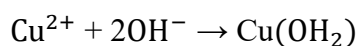
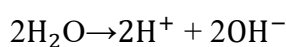
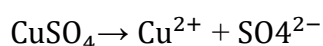
drop of 25 mM of $\text{HAuCl}_4 \times 3\text{H}_2\text{O}$ was added to the solution. The colour of the solution changed from yellow to dark wine red after a few minutes, indicating the end point. Upon synthesis nanoparticles were centrifuged at speed of 4600 rpm and washed with acetone once and D.I water three times to eradicate any impurities and unreacted precursors.

3.3.1.5 Copper nanoparticles (CuNP)

The CuNP were prepared, through formulation of a solution by adding 1.59 g of CuSO_4 , 1 g PVP and 4.36 g of ascorbic acid all in 100 mL of D.I water. PVP was used as a surfactant and ascorbic acid as a reducing agent. It was then mixed with the use of a stirring magnetic bar and maintained at 80 °C. CuNP are highly unstable as they oxidise rapidly but this can be inhibited by the use of ascorbic acid. The formation of CuNP was confirmed with the presence of nanoparticles brick red in colour formed and could be seen, the colour changes observed were from blue to dark green and then brick red. Upon synthesis nanoparticles were centrifuged at speed of 4600 rpm and washed with acetone once and D.I water three times to eradicate any impurities and unreacted precursors.

CuSO_4 primarily dissociates to Cu^{2+} and SO_4^{2-} in water, and Cu^{2+} ions are hydrolysed into $\text{Cu}(\text{OH})_2$ as a precursor.

Moreover, further reduction of $\text{Cu}(\text{OH})_2$ takes place in the presence of ascorbic acid to form Cu_2O . Lastly, Cu_2O is further reduced to form Cu. The reaction can be represented as the following.



Equation 3. 3: Equation showing the synthesis of CuNP.

3.3.2 Methods

3.3.2.1 Morphological observation through scanning electron microscopy (SEM)

Imaging of samples was done using a Zeiss Evo HD15 SEM (Carl Zeiss, Cambridge, UK). Samples after centrifugation were pipetted on to microscope slides and allowed to dry, these were then analysed to study the size and morphology of the structures produced. Prior to assessing coated microscope slides; the samples were sputter coated with gold (S150B, Edwards, Crawley, West Sussex UK) under vacuum to prevent charging. SEM images were captured at a working distance of 12 mm at varying low and high magnifications.

3.3.2.2 Elemental analysis through energy dispersive spectroscopy (EDS)

EDS analysis indicated the key elements present making up the synthesised material. The microstructural characterization was conducted with SEM-EDS in backscattering electron imaging mode using a scanning electron microscope with a conventional tungsten filament (Zeiss DSM 962). This equipment has an energy dispersive spectrometer Oxford Instruments INCAx-sight. The analyses were performed at a working distance of 25 mm, with an accelerating voltage of 20 kV, a filament current of approximately 3A and an emission current of 70 μ A. In order to obtain the EDS spectra peaks, samples were not sputter-coated with gold.

3.3.2.3 Particle size analysis through size distribution

Size distribution histograms were plotted, SEM related software smart tiff was used, the particles displayed in the images measured using the tools available from the smart tiff software, giving exact measurements of size in nm or μ m. Particle size recorded and a histogram displaying frequency in numbers of particle size was plotted.

3.3.2.4 Attenuated total reflectance Fourier transform infrared spectroscopy (ATR-FTIR)

ATR-FTIR spectrums collected confirmed through vibration or excitation the bonds present within samples, through analysis of peaks at certain wavenumbers, which in turn help confirm the identity of the material based on previous literature. The metallic nanoparticles were collected upon drying as powder samples and analysed over a scanning range of 400–

4000 cm^{-1} using FTIR Platinum-ATR fitted with Bruker Alpha Opus 27 FT-IR at an average of 10 scans at resolution 4 cm^{-1} at ambient temperature.

3.3.2.5 Raman spectroscopy

Raman spectra were collected using a FORAM® Raman spectrometer equipped with a 785 nm laser, using 30 scans at a resolution of 4 cm^{-1} . Raman spectra were collected between 200 cm^{-1} to 3300 cm^{-1} . The samples were prepared on glass slides, spectra were generated through laser hitting part of the sample, the part of the sample to be analysed appears through an optical microscope image at certain magnification. Thereafter, the spectra were produced. Similar to ATR-FTIR the peaks at different wavenumbers represent bonds present within the samples, which in turn identify the metallic particles. This technique was used to further confirm the ATR-FTIR results for the samples.

3.3.2.6 Ultraviolet-visible spectroscopy (UV-Vis)

UV-vis spectroscopy is an analytical technique where the absorbance of material is studied as a function of wavelength. The near-ultraviolet region of the spectrum falls in the wavelength region of about 200 nm, while the visible region of the spectrum falls in the wavelength of between 380 nm (violet) to 740 nm (red). Therefore, in material characterization, the UV-visible spectrophotometer analyses in a wavelength range of between 200 nm and 900 nm. Samples after centrifugation were suspended in water, then pipetted into a glass quartz UV high precision cuvette to be analysed in a UV-Vis spectrophotometer.

3.3.2.7 X-Ray diffraction (XRD)

Sample crystallinity was evaluated using XRD analysis performed on a Bruker D8-Advance diffractometer, operating at 40 kV and 40 mA whilst using Cu Ka1. A scanning rate of 0.20 s/step was used. Spectra were collected in 2θ from 20° to 80°. Samples were used after drying, the powder samples collected were placed upon powder specimen holders, and run at set operating parameters.

3.3.2.8 Zeta potential

Zeta potential values play a crucial role in deciding the colloidal suspension stability of prepared nanoparticles or nanocomposites. Higher level of stability for colloidal suspension of nanoparticle depends on the value of zeta potential ranging from -25 mV to $+25$ mV. A nano-brook omni zeta sizer was used, samples were prepared as a suspension, placed in plastic cuvettes a probe was inserted into the sample, readings were taken in triplicate and data tables collected.

3.4 Results and Discussion

3.4.1 Synthesised metallic nanoparticle images

Figure 3.1 displays the end point colours of each of the synthesised metallic nanoparticles, which were then centrifuged at 4600rpm three times and washed with D.I water to remove any impurities and unreacted precursors. For **Figure 3.1Ai** the end point is indicated by the cloudy yellow colour this is in correlation with literature for the end point of silver nanoparticle synthesis as beyond this no further colour change was observed (Dong et al, 2009). For **Figure 3.1Bi** the colour observed is a cloudy grey colour this signifies the end point for nanowire synthesis through the polyol method (Guo et al, 2015), **Figure 3.1Ci** the colour of final solution can be described as a dark cloudy grey colour similar to that of **Figure 3.1Bi** but darker as the synthesis method the polyol method is similar, moreover literature for polygon shaped or edge shaped silver particles show similar colour. **Figure 3.1Di** shows the distinct dark wine-red colour indicating the synthesis of AuNP (Tyagi et al, 2016), as for **Figure 3.1Ei** CuNP presence is confirmed through the appearance of particles brick red in colour (Khan et al, 2016). Thereafter, the samples were centrifuged at 8000rpm for 5 minutes, the nanoparticles sedimented to the bottom, as can be seen by **Figure 3.1(Aii-Eii)** they were then extracted, dried and used for further characterisation.

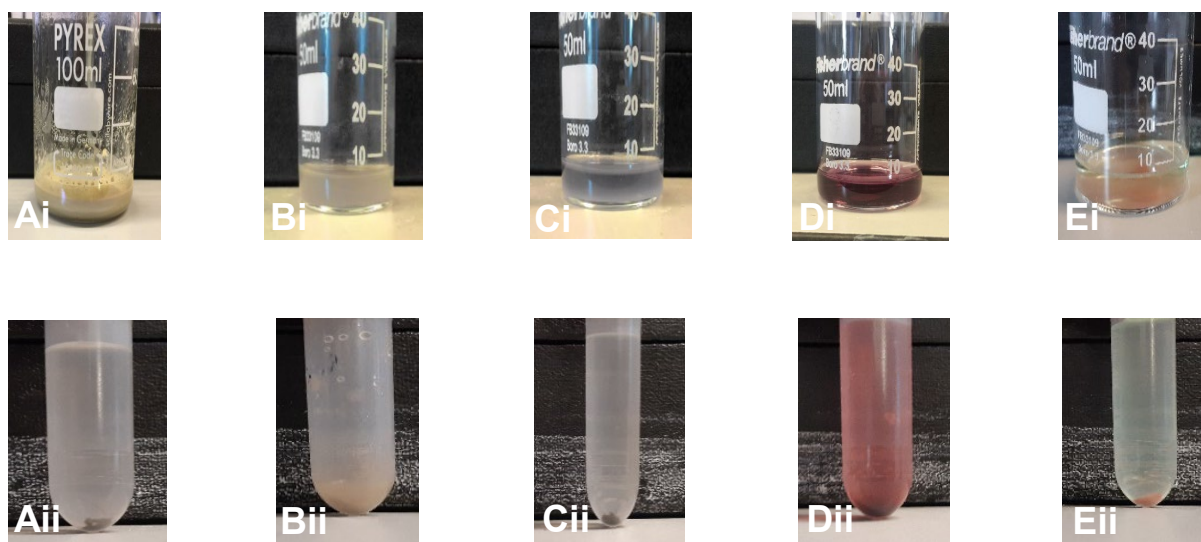


Figure 3. 1: digital images of end-point synthesis of metallic nanoparticles and their respected centrifuged nanoprecipitates. (Ai) synthesised AgNPs (Aii) collected precipitate of centrifuged AgNPs (Bi) synthesised AgNWs (Bii) collected precipitate of centrifuged AgNWs (Ci) synthesised AgPs (Cii) collected precipitate of centrifuged AgPs (Di) synthesised AuNPs (Dii) collected precipitate of centrifuged AuNPs (Ei) synthesised CuNPs (Eii) collected precipitate of centrifuged CuNPs.

3.4.2 SEM/EDS

Figure 3.2 shows the SEM images of the samples, at high and low magnifications, the corresponding EDS spectrums generated and the size distribution histograms for each metal synthesised.

Figure 3.2Ai shows the spherical AgNP, the particles present at x5 kV have similar morphologies and appear monodispersed but quite sparse, at high magnification **Figure 3.2Aii** x50 kV this is confirmed as particles appear uniform with some slight differences in size and morphology, overall size of particles can be said is increasing, this leads to particles with a variable size distribution shown in **Figure 3.2Aiv**. The average particle size was 69.4 nm, from the histogram it can be seen many of the particles were between 61-70 nm and 71-80 nm in size.

Ranoszek-Soliwoda et al, 2017 reported synthesis of spherical AgNP using a single reagent in this case sodium citrate results in a broader size range of particles, with variations in morphology. As sodium citrate is a weak reducing agent it does not allow the control of the AgNP morphology, changes in the reaction temperature where the synthesis occurs at 100 °C still does not produce uniform AgNP. EDS analysis on this sample **Figure 3.2Aiii** confirmed the presence of silver. Pillai and Kamat, 2004 confirmed the variation in morphology and larger particle size (50-100 nm) is due to the use of sodium citrate as the reducing agent. Gakiya-Teruya et al, 2018, has also shown that AgNP produced through the regular Turkevich citrate reduction method produces particles with a wider size distribution.

Successful synthesis of nanowires is observed in image **Figure 3.2Bi**, at low magnification x5 kV nanowires are surrounded by colloidal silver particles, the size and morphology of the wires varies, with some longer in length and wider in diameter than others. The presence of colloidal silver particles is due to the synthesis method, as (Sun et al, 2002) report if during synthesis the AgNO₃ and PVP solutions are added simultaneously then a mixture of silver wires with colloidal particles will occur. Prabukumar and Bhat, 2018, determined centrifugation alone may not be enough to remove the particles attached to the nanowires. The polyol method has shown to be one of the easiest and efficient ways to produce nanowires of such high yield and with similar morphologies.

AgNWs displayed an average particle diameter size of 317.4nm and an average length of 1138.4nm. The histogram **Figure 3.2Biv** shows in blue the diameter sizes (nm) of the particles and in red the size (nm) in length of particles, most particles measured showed a diameter size

between 301-400 nm and a length between 1101-1200 nm. Chen et al, 2008, produced nanowires with an average diameter of 400 nm through utilization of the polyol method. Findings published showed similar results in nanowire sizes, when using the same polyol synthesis method used here. Coskun et al, 2011 described the effects of temperature on size and morphology of nanowires produced, the particle diameter at around 160 °C is around 350-400 nm which is similar to the particle diameter of the nanowires synthesized in **Figure 3.2Bi**. Nghia et al, 2012, explained that a low amount of PVP and a medium amount of silver seeds gives rise to nanorod or nanowire structures. Silver seeds form through the small amounts of precursor material added e.g. NaBr or NaCl. Gebeyehu et al, 2017, explained the final morphologies of AgNWs at the end of the polyol process are strongly dependent on the PVP to AgNO₃ ratio and the molecular weight of PVP originally used.

Jang et al, 2018, describe the steps involved in the polyol synthesis of nanowires in steps, an initial seeding step producing octahedral silver seed crystals and a growth step producing pentagonal wires, this is followed by a nucleation step where Ag⁺ ions are reduced by EG acting as the reducing agent. These silver nuclei grow and function as Ag seed crystals. In the presence of AgNO₃ PVP acts as a capping agent kinetically controlling the growth rate of Ag. The capping process leads to the growth of wires, through selective absorption of PVP onto different crystal faces, hence showing control of the silver seed crystal structure is key to controlling size of the wires formed. EDS spectra **Figure 3.2Biii** confirms the presence of silver.

Figure 3.2Ci is that of the polygonal shaped particles, as can be seen the shape of these particles differ to those in **Figure 3.2Ai** (spherical in shape), with clear edges observed in many of the particles at high magnification x25 kV **Figure 3.2Cii** but varying in number of sides. The morphologies of the particles observed are similar, the average particle size is around 427.6 nm much larger than the spherical AgNP synthesised. The histogram **Figure 3.2Civ** shows a larger number of particles between 401-500 nm in size, and the overall range of particles between 201-600 nm, which suggests a wider size distribution. The shape in particles size and morphology is highly dependent on the synthesis method, as described the polyol method was utilised with concentrations of precursors altered.

The morphology of the particles observed arises through the growth of multiple twinned particles (MTP), these are best described by (Wiley et al, 2006), who have shown that before growth into fully fledged nanowires, MTP's form shaped as polygonal particles, as the method

of synthesis is similar, the end morphology varies by controlling the crystal structures of the seeds. **Figure 3.3**, shows that the presence of EG helps reduce the silver ions, which form clusters that are fluctuating in their structure, as growth continues fluctuation decreases, until it evolves into a single-crystal, single twinned, or multiple twinned seed. The presence of the multiple twinned seed is before the synthesis of the wire and can be seen with a shape similar to that of a polygon with closed sides. Xiao-Yang Zhang et al, 2018, explain the formation of five twinned pentagonal seeds occurs before the growth of nanowires, and if the size of these seeds can be controlled size of nanowires can also be.

These five twinned pentagonal seeds are similar to the shape of particles observed in **Figure 3.2Cii**, and forms before the formation of the nanowire, (Sun et al, 2002) also confirm nanowires form through the evolution of multiple twinned silver particles. Al-Thabaiti et al, 2013, described the precursors needed for the development of AgP, it was found that the presence of PVA led to the synthesis of polygonal shaped particles, it was reported that PVA may act as PVP does in binding to crystal faces and yielding different shape growth. Cuya Huaman et al, 2018, synthesised copper nanowires using a similar polyol method, what was observed showed that the copper ions are reduced to copper seeds, which lead to the formation of copper nanowires, these seeds take the polygonal shape, similarly here the silver seeds have the shape of a polygon and form before the eventual nanowire formation.

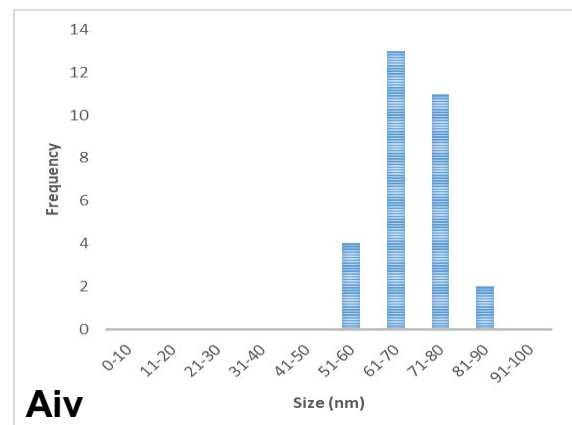
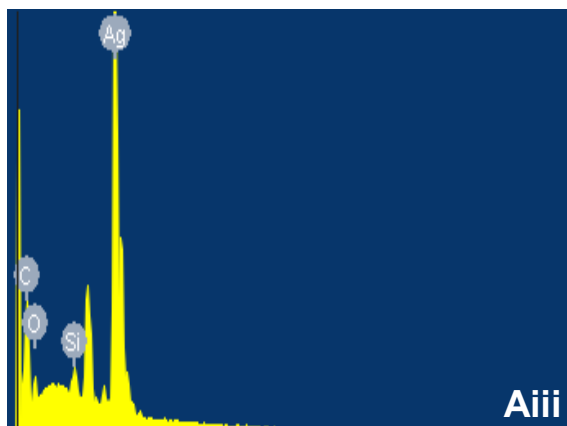
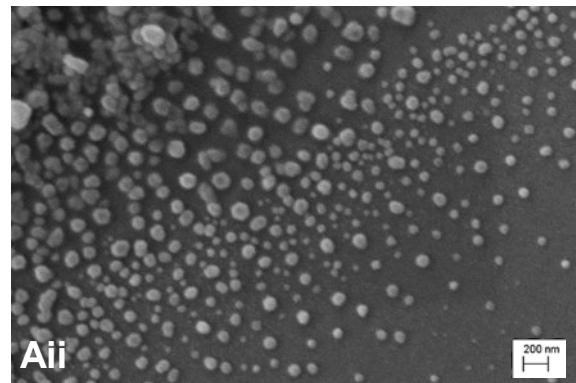
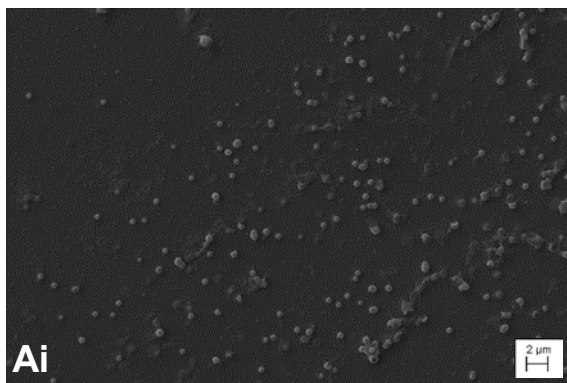
EDS analysis **Figure 3.2Ciii** again confirms the presence of silver, however the element arsenic (As) can also be detected on the EDS spectrum, as this does not appear in any of the other spectra's this can be noted as an anomaly.

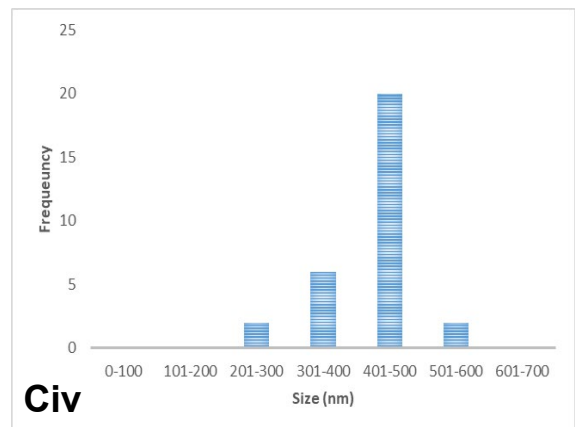
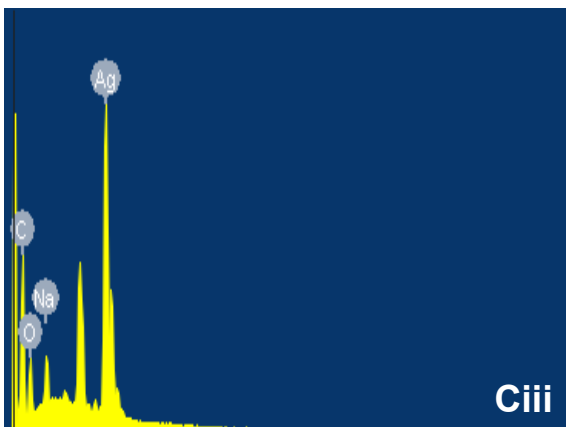
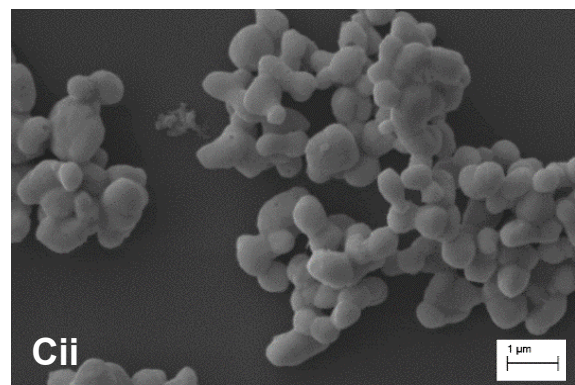
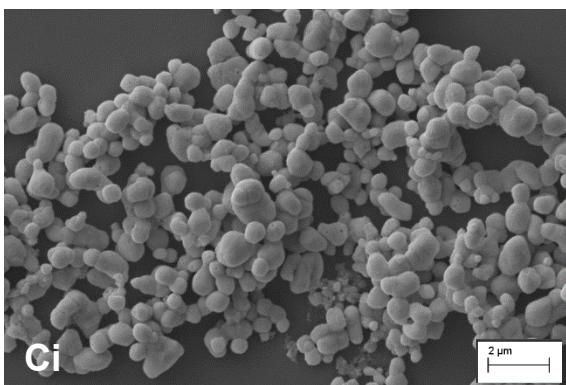
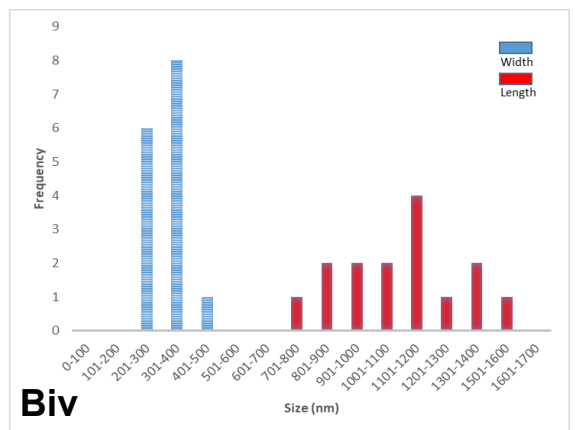
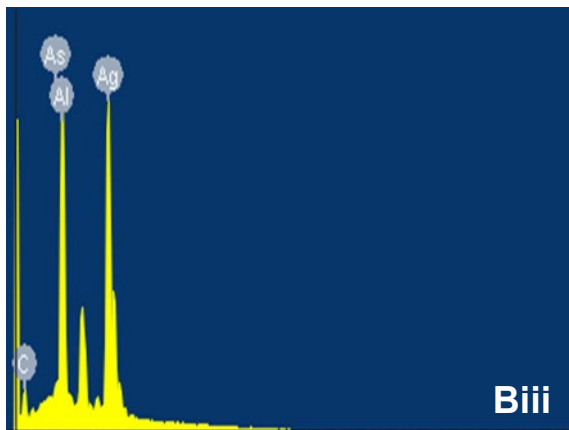
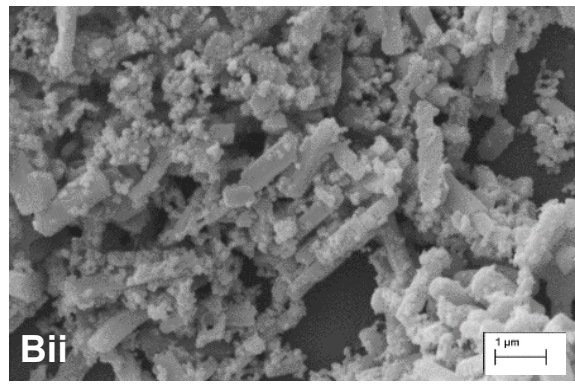
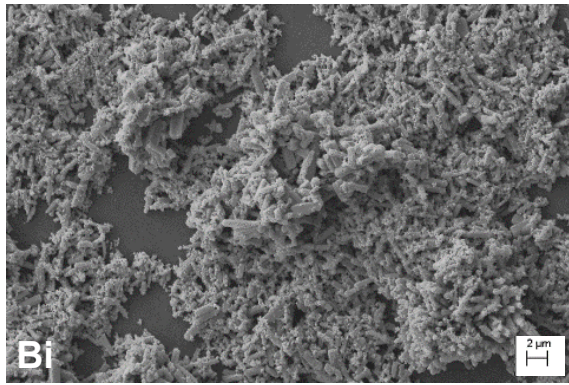
Figures 3.2Di and **Dii** are of the synthesised AuNP, at low and high magnification respectively. At low magnifications x5 kV the particles appear spherical and similar in morphology, at a higher magnification the particles can be seen clumped together in a colloidal arrangement with many of the particles appearing charged throughout. The average particle size was 104.7 nm, with **Figure 3.2Div** showing that a larger number of particles are observed between 101-120 nm. Kumar et al, 2007, confirm the coagulation of nanoparticles occurs due to higher presence of citrate ions as well as the existence of salts. The precursor $\text{HAuCl}_4 \times 3\text{H}_2\text{O}$ is a salt that is reduced by sodium citrate, together this may have led to increased coagulation of particles. Ji et al, 2007, found that the relationship between the gold salt and sodium citrate is key, with increased amounts of gold salt the particle size increases, however when reducing gold salt concentration and increasing sodium citrate concentration particle size reduces and becomes

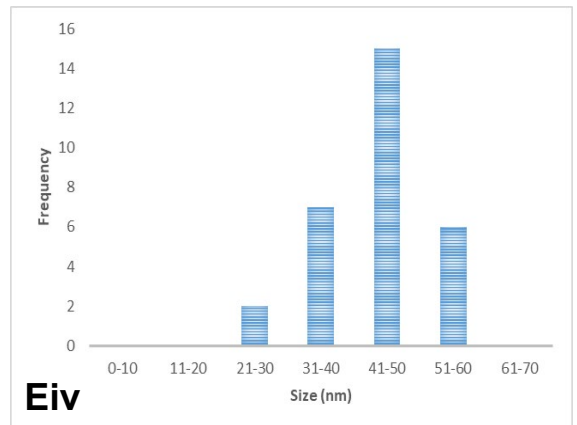
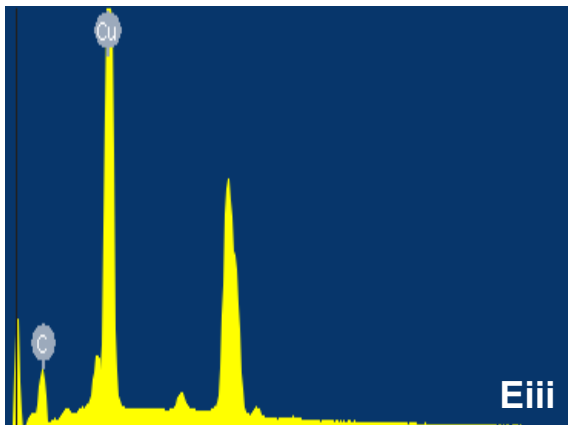
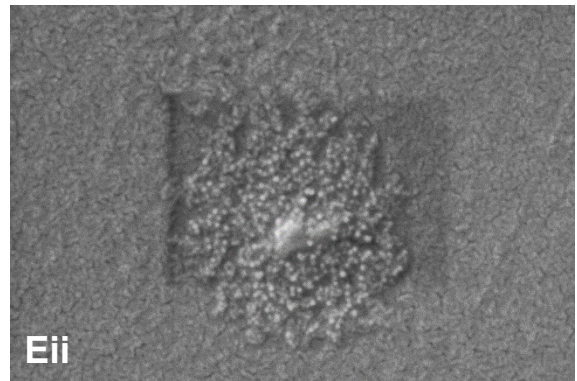
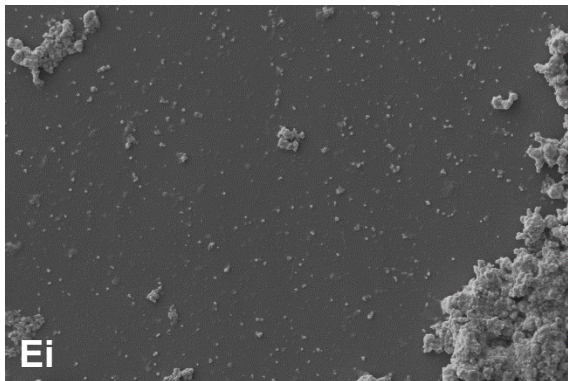
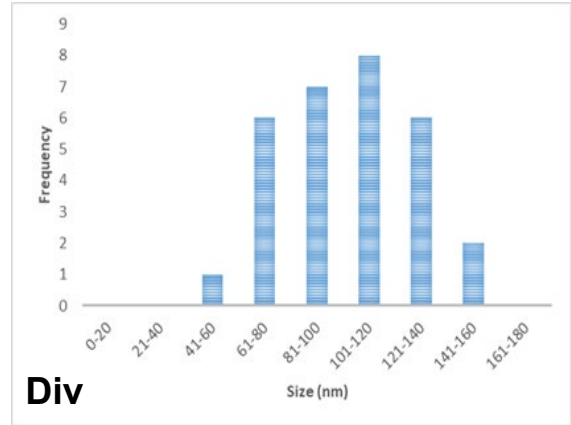
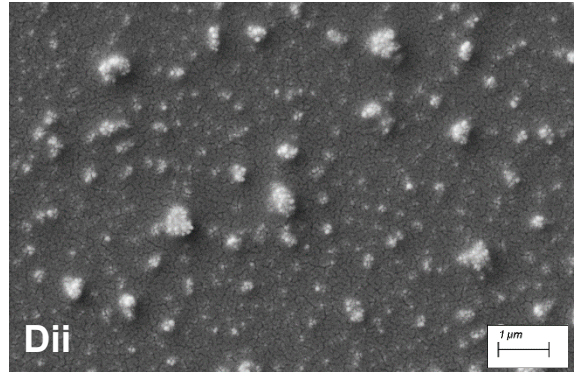
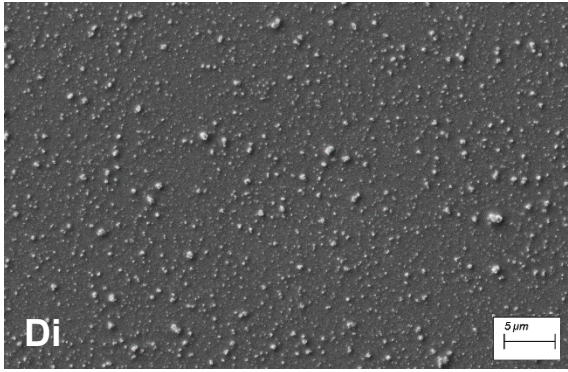
more uniform, furthermore, they found that the pH has a key part to play in aggregation of gold particles, and that as well as being a reducing and stabilizing agent sodium citrate can also alter reaction pH, hence deciding if coagulation occurs or not.

Spherical CuNP are observed at high magnification x50 kV **Figure 3.2Eii**, particles appear similar in size and morphology, they appear monodispersed. An average particle size of 44.8nm, with many of the particles between 41-50 nm. Khan et al, 2015, demonstrates the CuNP synthesised tend to coagulate and form clusters, moreover the presence of ascorbic acid not only helps in preventing rapid oxidation but also in reducing particle size and maintaining narrow size distribution. EDS spectrum **Figure 3.2Eiii** confirms the presence of copper.

Figure 3.2 Fi, shows the successful synthesis of hexagonal shaped particles, with 6 clear sides, the particles were synthesised following a method described by (G. Cynthia Jemima Swarnavalli et al, 2011), the size of the particles however is too large, as shown in **Figure 3.2Fiv** the size is above 1 micron, and continues to rise above 2 micron, EDS spectrum in **Figure 3.2Fiii** confirms the presence of silver, however these particles were not used due to not appearing at the nano-size range, also with the larger size and increased density, formulations formed in future chapters became too viscous and unable to spray, hence why the synthesis was abandoned.







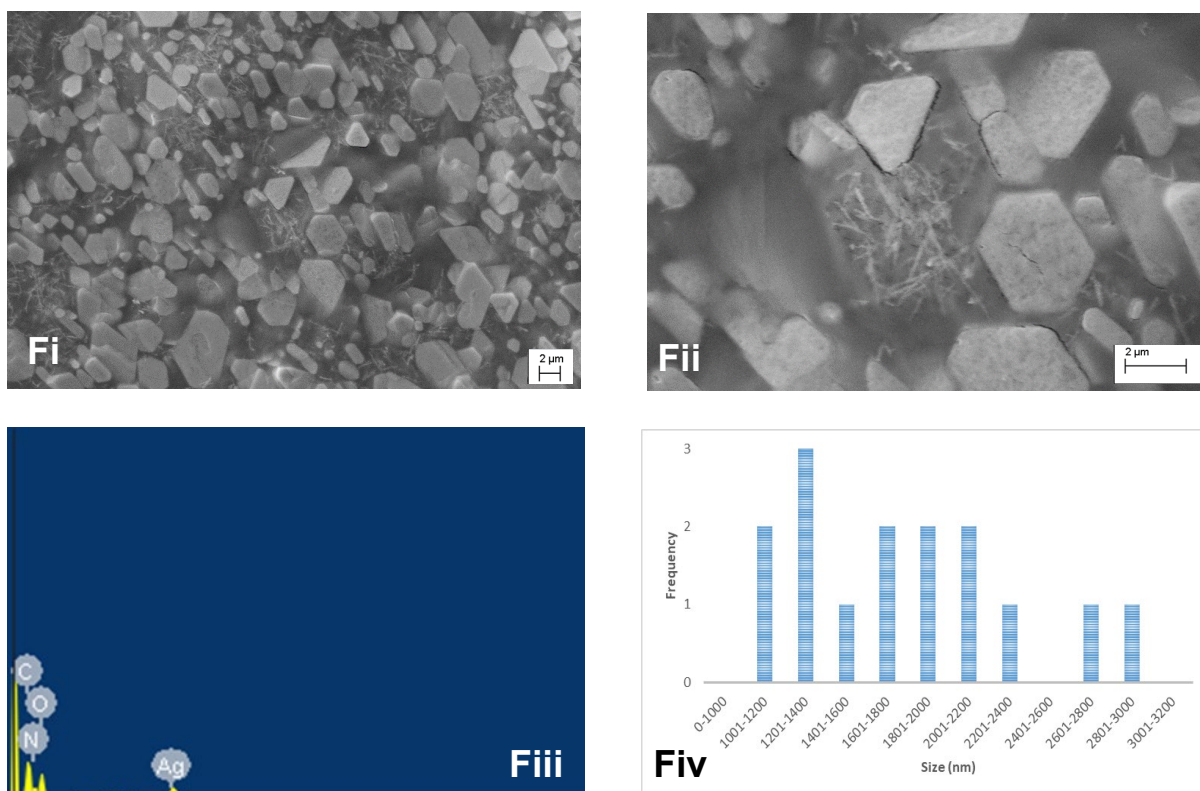


Figure 3. 2: SEM ((i) images at low magnification); ((ii) images at higher or equal magnifications); (iii) EDS analysis; (iv) particles size distribution histogram using (ii) SEM images. (A) AgNP; (B) AgNW; (C) AgP; (D) AuNP; (E) CuNP; (F) hexagonal silver nanoparticle not used.

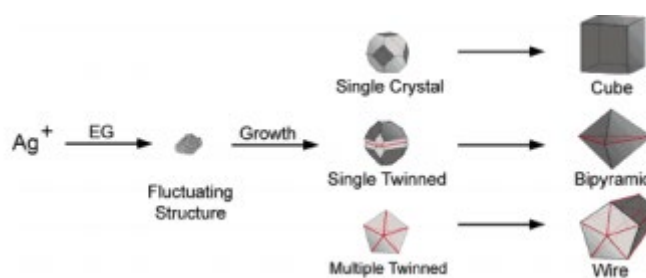


Figure 3. 3: Pathway describing the growth multiple twinned seed particles prior to nanowire formation.

3.4.3 ATR-FTIR

Evidence of the surface functionalisation of AgNP and AuNP by citrate ions was obtained through FTIR measurements **Figure 3.4**. The peaks at 1388 cm^{-1} for AgNP and 1372 cm^{-1} for the AuNP correspond to the symmetric and anti-symmetric stretching of COO. As there are no peaks at 1417 cm^{-1} which is the peak for free citrate molecules this indicates citrate molecules are bound to the surface of AgNP and AuNP. Additionally, there is an O-H stretch present in both spectra, indicated through a broad spectrum from 3321 cm^{-1} to 3373 cm^{-1} for AuNPs and between 3184 cm^{-1} to 3396 cm^{-1} (Frost et al, 2017).

Ranoszek-Soliwoda et al, 2017, synthesised AgNP through citrate reduction mechanism and FT-IR analysis of the sample showed characteristic peaks at 1196 cm^{-1} , 1397 cm^{-1} , 1583 cm^{-1} and 1690 cm^{-1} . AgNP shown in **Figure 3.4** shows peaks at similar wavenumbers, 1137 cm^{-1} , 1388 cm^{-1} , 1537 cm^{-1} and 1638 cm^{-1} . The peak at 1583 cm^{-1} indicates a C=O stretch, and the signal at 1397 cm^{-1} indicates COO- peak, these values are characteristic for free citrate molecules, in **Figure 3.4** the spectrum for AgNP shows slight peak shifts at these wavenumbers indicating citrate molecules are no longer free and now attached to the surface of the metallic nanoparticles.

The spectrum shown in **Figure 3.4** for AuNP displays, a small broad peak at 1238 cm^{-1} , a broad but sharper peak at 1389 cm^{-1} and a sharp peak at 1628 cm^{-1} , which are all similar to those in literature reported by (Yadav and Jyoti, 2018) who shows AuNP synthesised through the citrate reduction method have similar characteristic peaks at 1231 cm^{-1} 1474 cm^{-1} and 1637 cm^{-1} .

FT-IR spectra for AgNW and AgP, display peaks at very similar wavenumbers but at different intensities. AgP spectra shows sharp peaks at 1035 cm^{-1} and 1083 cm^{-1} indicative of a C-O stretch, the sharp peak at 1638 cm^{-1} describing a C=O stretch and two shoulder peaks around 2878 cm^{-1} and 2937 cm^{-1} displaying CH₃ stretch. As for the AgNW the spectra show peaks in similar areas 1034 cm^{-1} , 1076 cm^{-1} , and 1623 cm^{-1} , and a slight broad peak at around 2941 cm^{-1} , both spectra again show a broad peak between $3100\text{--}3400\text{ cm}^{-1}$ indicating presence of an O-H group (Zhijie Zhang et al, 2017). The intensity in peaks between these two spectra may vary due to the concentration of precursors used to synthesise the metallic particles or because of the amount of material used during analysis.

As for the spectra of CuNP, it shows a small broad peak between 1020 cm^{-1} and 1140 cm^{-1} , and a sharp peak at 1630 cm^{-1} indicating a (C=C) bond, a larger broader peak between 3132

cm^{-1} and 3447 cm^{-1} , indicating the presence of an (O-H) group, the broadness of the peak is due to the increase in hydrogen bonding, this spectrum is in correlation with previous literature (Zafar et al, 2015). All metallic particle spectra's show variation, due to synthesis method utilised which can be visualised through peak differences, as peaks for shaped silver nanoparticles are not present in spectra of AgNP, AuNP and CuNP, as stated metallic particles are synthesized through a chemical reduction method and shaped AgNP are formulated through the polyol synthesis method.

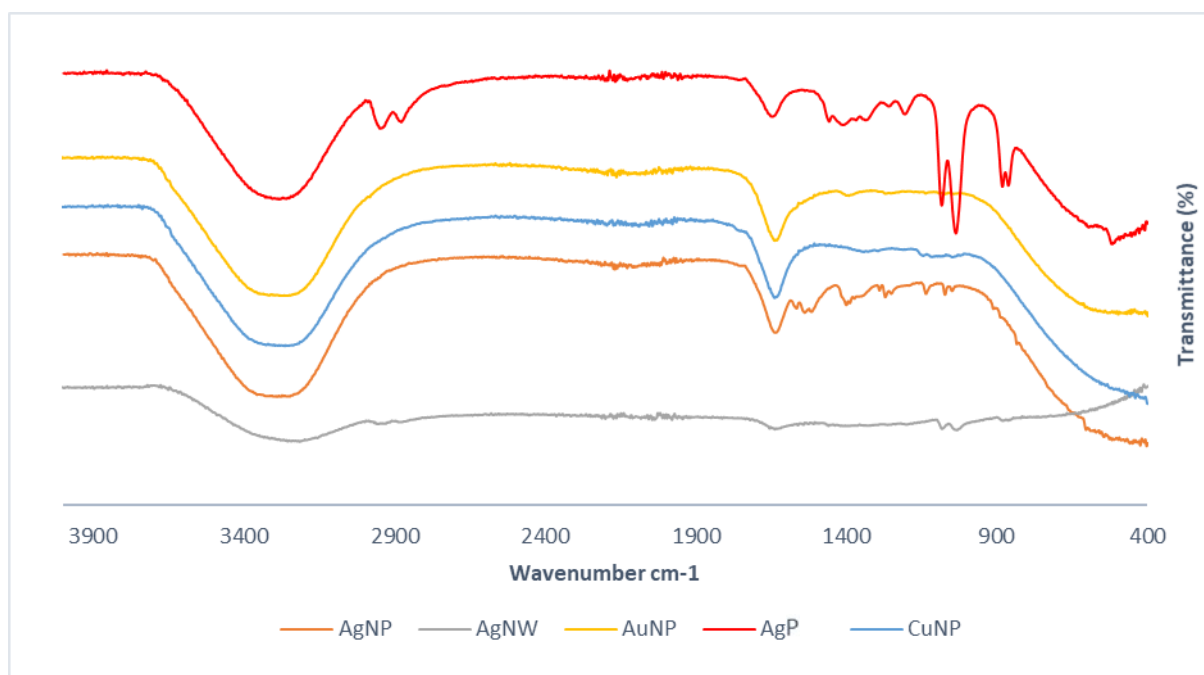


Figure 3. 4: ATR-FTIR spectra of synthesised metallic nanoparticles; AgNP, AgNW, AuNP, AgP and CuNP.

3.4.4 Raman spectroscopy

Figure 3.5 shows the Raman spectra for synthesised metallic nanoparticles. AgNPs have numerous small shoulder peaks between 200 and 862 cm^{-1} indicative of C-H peaks, there are two sharp peaks at 922 cm^{-1} showing deformation of C-O-H and at 1410 cm^{-1} which shows CH_3 and CH_2 deformations. The sharpest peak appears at 3102 cm^{-1} indicating an aromatic compound (benzene ring). Interestingly, the surface enhanced Raman spectroscopy (SERS) intensity of the analyte increases gradually with the increase of the size of the AgNPs.

AgNW have a sharp peak at 1386 cm^{-1} indicating CH_3 and CH_2 deformations, and the sharpest peak at 3100 cm^{-1} . A broad sharp peak at 1902 cm^{-1} and the sharpest intensity peak at 3100 cm^{-1} displaying an aromatic ring. AgP spectrum results follow a similar pattern to that of the silver nanowires, which again may be due to similarity in the synthesis method, peaks are observed at 1386 cm^{-1} again indicating CH_3 and CH_2 deformations, a broad peak at 1902 cm^{-1} and the peak of highest intensity at 3100 cm^{-1} displaying an aromatic ring. Furthermore, just as shown in related FT-IR spectra the peak intensity for the AgP particles is much higher than that of AgNW.

The AuNP spectrum shows peaks at 1390 cm^{-1} related to CH_3 and CH_2 deformations, with the peak at 3104 cm^{-1} indicating an aromatic ring. The CuNP show a very different spectra, may be due to the difference in precursor materials used, as it has no sharp peaks until 3100 cm^{-1} indicating an aromatic ring, and shows small broad peaks between 320-1220 cm^{-1} mainly suggesting presence of CH groups.



Figure 3. 5: Raman spectra of synthesised metallic nanoparticles; AgNP, AgNW, AuNP, AgP and CuNP.

3.4.5 UV-vis spectroscopy

Figure 3.6 displays the UV-Vis analysis of the synthesised nanoparticles illustrates differing results between the types of metal synthesised. Displaying differences in wavelengths and sharpness of peaks related to size and shape of nanoparticles synthesised as well as synthesis method utilised, between the citrate reduction method and the polyol synthesis method, generating particles varying in shape.

The AuNP and AgNP solutions prepared by the citrate reduction method displayed characteristic absorption spectra with LSPR absorbance maxima at values of 523 nm and 415.5 nm respectively (Frost et al, 2017). Synthesised AuNP show a sharper band at the maximum absorbance in comparison to the spherical AgNP which display a broader band from 370 to 470 nm, this may be due to a decrease in particle size in correlation with size quantum theories, whereas the sharper peak area is related to aggregation of particles, and a reduced amount of space between particles leading to larger particle size (Desai et al, 2012). The AuNP synthesised show broad sharp peak between 517-532 nm and in correlation with literature, (Huang et al, 2018) synthesised AuNP with a maximum absorbance at around 523 nm. The AgNP show a broad peak between 380-446 nm which correlates with data found by (Ranoszek-Soliwoda et al, 2017).

As for the synthesised AgNW, a broad but short band with a maximum absorption at 311nm correlates with previous literature (Prabukumar and Bhat, 2018), the similarity between this maximum and to that of the AgP which has a maximum at 325nm may be due to the similarity in synthesis method. The CuNP UV-vis curve is not displayed as the metallic nanoparticles present sedimented to the bottom of the cuvette therefore any attempt at creating a curve was ineffective. From literature it was found copper nanoparticles display a maximum wavelength between 550-600 nm (Thi My Dung Dang et al, 2011).

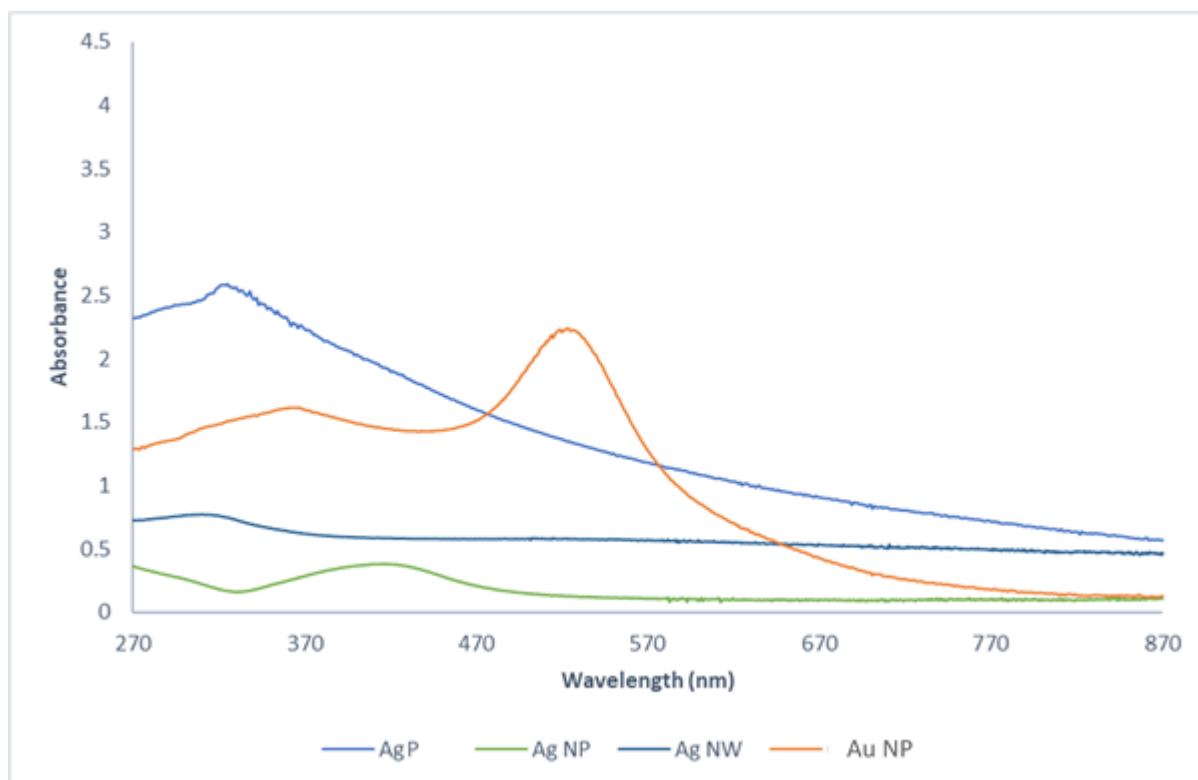


Figure 3. 6: UV-vis spectra of synthesised metallic nanoparticles; AgNP, AgNW, AuNP and AgP

3.4.6 XRD

Diffraction patterns displayed in **Figure 3.7** confirm the crystallinity of synthesised nanoparticles. CuNP display the sharpest intensity peaks, sharp peaks observed at the 2θ values of 36.44, 29.74, 43.17, 50.38, 61.45 and 74.04. Peaks observed at 2θ values of 43.17, 50.38 and 74.04 correspond to (111), (200) and (220) planes of metallic copper (Khan et al, 2015). These three peaks were quite consistent with those of the standard JCPDS Card No. 04-0836 for the standard spectrum of the pure face centred cubic (FCC) metallic copper. Besides the metallic copper peaks, several other diffraction peaks appeared at 2θ values of 29.74, 36.44, 61.45 indicating the formation of copper (I) oxide nanocrystals.

The spectrum of AgPs displayed, peaks similar to those of AgNWs a sharp peak at the 2θ value of 43.65 (111), with further smaller peaks at the 2θ values of 37.45 (200) and 64.11 (220). From the spectra for AgNWs numerous peaks were observed, at 2θ of 37.80, 43.55, 64.15, 77.11, two diffraction peaks at 37.80 (111) and 43.55 (200) are matching with standard diffraction data for silver (JCPDS 04-0783). The relative intensity of (111) with that of (200) plane is attributed to preferred (111) plane growth of silver nanowires (Prabukumar and Bhat, 2018), the use of a capping agent promotes this preferred growth. Moreover, peaks at 64.15 and 77.11 correspond to planes (220) and (311) as shown in previous literature in accordance with JCPDS card 04-0783 (Lin et al, 2015). XRD diffraction patterns published by (Guo et al, 2015) further confirm the peaks seen in **Figure 3.7**, correlate with synthesised AgNWs. Gao et al, 2005, also published an AgNW diffraction pattern with similar peak positions and intensities.

Peaks for AuNPs show the sharpest peak at 2θ value of 37.21 further peaks were seen at 2θ values of 43.89 63.76 and 77.23. Peak at 2θ values of 37.21 corresponds to the (111) plane, 43.89 63.76 and 77.23 correspond to the planes at (200), (220), (211) respectively. (Krishnamurthy et al, 2014) (Mohamed et al, 2017).

Spherical AgNPs exhibited peaks at 2θ values of 38.26, 44.01, 64.39 and 77.33. These values correspond to planes at (111), (200), (220) and (311) respectively, the intensity of the peak at the plane (111) indicates this is preferred plane of growth, similar to the findings of other silver nanoparticles synthesised (Raza et al, 2016) (Wang et al, 2018).

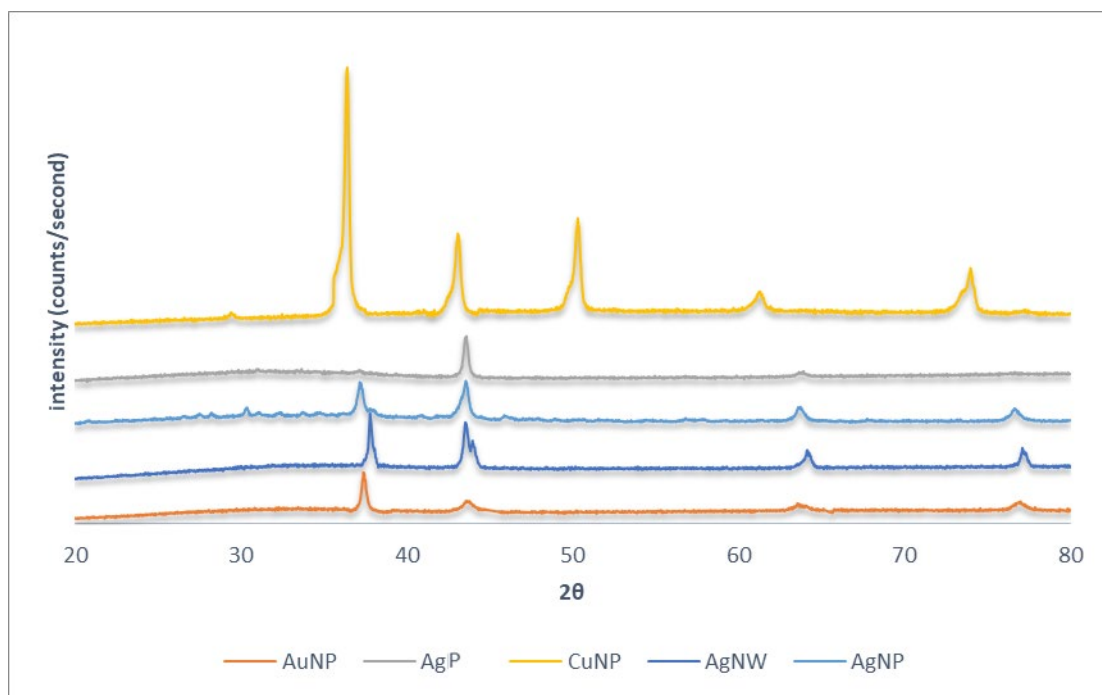


Figure 3. 7: XRD diffractograms of synthesised metallic nanoparticles; AgNP, AgNW, AuNP, AgP and CuNP.

3.4.7 Zeta Potential Values

Zeta potential values are used as a measure of colloidal suspension stability, the higher the value either negative or positive means greater stability of nanomaterials synthesised within a suspension, the stability of these nanoparticles in colloidal suspensions is important based on further analysis. Zeta potential values cannot be obtained directly, it is calculated through experimental data such as the electrophoretic mobility of particles, this in turn helps determine values of zeta potential, as the rate at which a charged particle moves in response to an electric field is recorded. Particles that possess a zeta potential will migrate toward the opposite-charged electrode. Root mean squared (RMS) residual is displayed as a measure of how spread out data points are and allows for verification of results.

From **Table 3.1** it can be observed that synthesised AgNPs have an average zeta potential value of -31.38 mV, a value high enough to indicate colloidal stability, also indicating that the particles are less likely to aggregate (Haider and Mehdi, 2014), **Table 3.2** for the AgNWs show a higher mean value at -36 mV showing colloidal stability, **Table 3.3** with the AgPs at -31.03mV also indicating stability in a suspension, **Table 3.4** AuNPs show a decrease in zeta potential values which may be due to aggregation of particles (Saeb et al, 2014) also observed in **Figure 3.2Dii**. **Table 3.5** for CuNPs the zeta potential value is again higher at -29.47mV indicating good colloidal suspension stability, and less likely to agglomerate.

Table 3. 1: Zeta potential values of spherical AgNP.

Sample ID	Zeta Potential (mV)	Mobility (μ/s)/(V/cm)	RMS Residual
AgNP - 1	-34.96	-2.73	4.81E-02
AgNP - 2	-35.91	-2.81	5.14E-02
AgNP - 3	-23.27	-1.82	1.05E-01
Mean:	-31.38	-2.45	6.82E-02
Std Err:	4.06	0.32	1.84E-02
Std Dev:	7.04	0.55	3.18E-02

Table 3. 2: Zeta potential values of AgNW.

Sample ID	Zeta Potential (mV)	Mobility (μ/s)/(V/cm)	RMS Residual
AgNW - 1	-20.46	-0.04	1.02E-02
AgNW - 2	-41.50	-0.08	9.85E-03
AgNW - 3	-46.03	-0.09	2.58E-02
Mean:	-36.00	-0.07	1.53E-02
Std Err:	7.88	0.02	5.25E-03
Std Dev:	13.65	0.03	9.09E-03

Table 3. 3: Zeta potential values of AgP.

Sample ID	Zeta Potential (mV)	Mobility (μ/s)/(V/cm)	RMS Residual
AgP - 1	-31.39	-2.45	5.21E-02
AgP- 2	-33.46	-2.61	1.86E-02
AgP - 3	-28.24	-2.21	3.71E-02
Mean:	-31.03	-2.42	3.59E-02
Std Err:	1.52	0.12	9.68E-03
Std Dev:	2.63	0.21	1.68E-02

Table 3. 4: Zeta potential values of AuNP.

Sample ID	Zeta Potential (mV)	Mobility (μ/s)/(V/cm)	RMS Residual
AuNP - 1	-23.86	-1.86	7.54E-02
AuNP - 2	-11.08	-0.87	7.39E-02
AuNP - 3	-12.45	-0.97	5.78E-02
Mean:	-15.80	-1.23	6.90E-02
Std Err:	4.05	0.32	5.64E-03
Std Dev:	7.01	0.55	9.76E-03

Table 3. 5: Zeta potential values of CuNP.

Sample ID	Zeta Potential (mV)	Mobility (μ/s)/(V/cm)	RMS Residual
CuNP - 1	-11.71	-0.92	3.73E-02
CuNP - 2	-35.12	-2.74	1.84E-01
CuNP - 3	-41.59	-3.25	1.21E-01
Mean:	-29.47	-2.30	1.14E-01
Std Err:	9.07	0.71	4.25E-02
Std Dev:	15.72	1.23	7.37E-02

3.5 Conclusion

In this chapter, five different metallic nanoparticles have been successfully synthesised, spherical silver nanoparticles, silver nanowires, polygonal silver nanoparticles, spherical gold nanoparticles and spherical copper nanoparticles. EDS analysis confirmed the presence of each metal synthesised, and size distribution confirmed the nano-size range of all metallic nanoparticles. The smallest size metallic nanoparticles were the CuNPs with an average size distribution of 44.8 nm, followed by the AgNPs with an average size of 69.4 nm, then the AuNPs with an average size of 104.7 nm, thereafter the AgPs with an average size distribution of 427.6 nm and finally the AgNWs which had an average diameter of 317.4 nm and an average length of 1138.4 nm. ATR-FTIR confirmed the molecular bonds present within each type of metallic nanoparticle, results varied depending on the synthesis method, between the chemical reduction method and polyol synthesis method. Raman data further confirmed the data from ATR-FTIR and peak intensities gave an indication of nanoparticle size. UV-Vis analysis displayed results that are characteristic of the metallic nanoparticle synthesised, AgNPs displayed a maximum at 415.5 nm, the AuNPs with a maximum at 523 nm, the AgNWs with a small broad peak, the maximum at 311 nm and AgP with a sharp peak point at 325 nm. The XRD diffractograms presented sharp peaks for each metallic nanoparticle, peaks at positions which correlated to the metallic nanoparticle synthesised based on previous literature. The zeta potential results were all greater than -25 mV indicating good colloidal stability, apart from AuNPs with an average value at -15.80 mV.

Chapter 4 – Synthesis of polymeric composites

4.1 Introduction

Antibiotic resistance has now reached an epidemic level. A wide variety of bacterial pathogens have developed resistance their antibacterial agents and thus render them ineffective. The WHO has advised that if the issue of antibiotic resistance is not effectively addressed and controlled, the phenomenon has the capability to change the health care systems as we know them today. The potential for an array of infectious diseases to have no feasible antibiotic therapy is an ever looming and an impending reality. Various conventional drug dosage forms have been developed and used to overcome such resistance synergistically with the use of APIs. However, limitations arise with many of these drug dosage forms, additionally at the same time, the growth in resistant bacterial strains continues into epidemic proportions. Today, there is more need for continued research into novel antibacterial drug delivery methods than ever before. One novel method withholding numerous advantages compared to its traditional drug delivery approach is the EHDA process which allows the manufacture of formulations holding antibacterial properties. Through this method, API particles are encapsulated within a polymeric matrix, and the antibacterial effect augmented further through the addition of metallic nanoparticles. EHDA also permits for the encapsulation of insoluble drugs, an easy fast one-step process means it is relatively low-cost.

Drug-loaded microspheres fabricated with biodegradable polymers typically form a matrix structure in which the drug is theoretically molecularly dispersed, which results in amorphous properties. Drug distribution within the microspheres depends on the miscibility of the drug with the polymer and the drug loading of the particles.

In biodegradable microparticle systems, the drug-release kinetics can be controlled partly by altering the polymer composition such as molecular weight or the ratio monomers for copolymer systems. Also, several studies have shown that the properties of the microparticles such as size, morphology and porosity as well as drug loading are important factors in determining the drug-release profile of these particles (Adam Bohr et al, 2012).

Microparticles made from biodegradable polymers for pharmaceutical applications, is an area extensively studied, as an alternative for the common antibacterial agents, as active agents are continuously released from the particles over time. Electrohydrodynamic atomization technique, commonly referred to as electrospraying has many advantages when creating

particles in the nano and micro scale, such as improved dissolution rates of poorly water-soluble drugs, reproducibility, ease of set up and encapsulation of active agents. Moreover, multi-pharmacy or poly pharmacy can be achieved by loading different drugs into multi-layered particles via electrospraying, and the controlled release of these ingredients has been made possible (Muhammet Emin Cam et al, 2019).

Polymeric nanoparticles with intrinsic antimicrobial properties have gained interest for treating infections. Polymers are available in natural and synthetic state. Some of these polymers demonstrate an antimicrobial potency by themselves e.g. chitosan nanoparticles (Rampino et al, 2013), others need some chemical modification to their conferred antimicrobial activity e.g. nanoparticles of polyvinyl caprolactam–polyvinyl acetate–polyethylene glycol graft copolymer (Soluplus®) modified with chitosan (Takahashi et al, 2015) or to incorporate organic or inorganic compounds with antimicrobial activity e.g. AgNPs.

4.2 Aims & Objectives

In this chapter, the synthesis of polymeric composites was attempted; these were loaded with an insoluble drug amoxicillin (AMX) and the metallic nanoparticles synthesised in the previous chapter. The EHDA process was used. Upon synthesis, characterisation was carried out to determine polymer-drug interactions and the presence of metallic nanoparticles within the composites. For this, the methods used were SEM/EDS, ATR-FTIR, DSC, TGA, XRD and zeta potential.

The experiments carried out within this chapter were novel, no previous work has been published related to using the electrospraying system to generate such antibacterial composites as possible alternatives to overcome the rise in bacterial resistance. All data collated from the characterisation techniques used, have not been found in any previously published literature related to this research.

4.3 Materials and Methods

4.3.1 Materials

Materials purchased from Sigma Aldrich UK included PLGA resomer RG 503 H, lactide: glycolide 50:50, M_w 24,000-38,000; AMX with a potency ≥ 900 μg per mg; and acetone with a purity $\geq 99.9\%$. DCM $\geq 99\%$ was purchased from Fisher Scientific UK. The metallic nanoparticles; AgNP, AgNW, AgP, AuNP and CuNP used were synthesised in-house as detailed in the previous chapter.

4.3.2 Methods

4.3.2.1 Formulation preparation

Several preliminary experiments were performed in order to govern the optimal concentrations of excipients. All formulations follow the same concentration of excipients whilst only the type of vehicle and metallic nanoparticle used changes amongst them (**Table 4.1** shows the formulation compositions). The formulations were stirred with the US152D magnetic stirrer (Stuart, Staffordshire, UK) for 1 hour in an ambient environment (23 °C at 45% relative humidity) to allow for the homogenous distribution of particles throughout. The formulation was covered with parafilm ‘M’ laboratory film (Bemis, Lincolnshire, UK) to prevent the evaporation of the vehicles during the stirring process. Images of all formulations were taken.

Table 4. 1: General composition of all formulations

	Composition			
	Polymer (% w/v)	Drug (% w/w of the polymer)	Vehicle (mL)	Metal nanoparticles (% w/w of the drug)
	5	5	10	5
Excipient alternatives	PLGA	AMX	<ul style="list-style-type: none">• Acetone• DCM	<ul style="list-style-type: none">• AgNP• AgNW• AgP• AuNP• CuNP

4.3.2.2 Formulation characterisation

The viscosity of the formulations was measured using the SV-10 sine-wave vibro viscometer (A&D, Oxfordshire, UK). The surface tension of the formulations was measured using the OS torsion balance (White Electrical Instrument Co. Ltd, Worcestershire, UK) using the 4 cm diameter platinum DuNuoy ring. The electrical conductivities of the formulations measured using the FiveGo electrical conductivity meter (Mettler Toledo, Leicestershire, UK) which was standardised using a calibration medium. All measurements were done in triplicate in an ambient environment (23 °C at 45 % relative humidity).

4.3.2.3 EHDA set-up

Figure 2.18 shows the set up for the single needle electrospraying system. A BD Medical™ Plastipak™ Plastic Concentric Luer-Lock syringe (Fisher Scientific, Loughborough, UK) contained 5 mL of formulation and was mounted on to an SP100IZ infusion pump (WPI, Hertfordshire, UK) to control the flow rate of the formulation through the EHDA system. The syringe was connected to a BD Microlance™ 3 needle (Fisher Scientific, Loughborough, UK) and inserted into a silicon tubing of known length. From preliminary testing it was found using a longer length of tubing could lead to evaporation of solvent before reaching the capillary needle exit, therefore tubing of a shorter length 8cm was used. The silicon tubing was attached to an electrically conducting processing capillary needle (size 330 µm). A high voltage power supply (Glassman High Voltage Supply, New Jersey, USA) was attached to the capillary needle for the atomisation of the formulation. The collector plate was covered with greaseproof paper and microscope slides to collect the samples for analysis. A depth of 9 cm was maintained between the capillary needle tip and the collector plate. All procedures were carried out in an ambient environment (23 °C at 45 % relative humidity).

Optimising the spraying of the formulation was achieved through recording the effect of varying the flow rate and applied voltage. Each known formulation was sprayed at flow rates 15, 20, 25, 30 and 40 µL/min, with an applied voltage between 10-17 kV in order create a stable jet for each formulation. Jetting maps for each formulation to show the areas of dripping mode, stable jet and unstable jet can be plotted from this.

4.3.2.4 Scanning electron microscopy (SEM)/ Energy dispersive spectroscopy (EDS)

Particle size and morphology were measured using the Zeiss Evo HD15 SEM (Carl Zeiss, Cambridge, UK). Samples collected onto glass microscope slides were coated with 15 nm gold using the Q150RS gold coater (Quorum Technologies, Sussex, UK). Images were taken at low and high magnification from x5,000 and upwards at an accelerated voltage of 10 kV, along different points on the coated microscope slide.

EDS analysis indicated the elemental composition of the synthesised material, and the components present within. The microstructural characterization was conducted with SEM-EDS in backscattering electron imaging mode using the SEM.

4.3.2.5 Attenuated total reflectance Fourier transform infrared spectroscopy (ATR-FTIR)

For the study of interactions between PLGA and AMX, along with the metal nanoparticles ATR-FTIR was used. FTIR Platinum-ATR (Bruker, Coventry, UK) spectrophotometer and Bruker Alpha Opus 27 software was used for the analysis of the formulations. Spectra was generated over the range 400-4000 cm^{-1} for both raw materials and full formulations.

4.3.2.6 Differential scanning calorimetry (DSC)

Thermograms were generated using the Jade Differential Scanning Calorimeter (PerkinElmer, USA). Both raw materials and full formulations were analysed to understand the interactions of the materials used. Samples of 5-10 mg were added and sealed into aluminium pans. A heating range of 20-300 °C with a heating rate of 20 °C per minute was used.

4.3.2.7 Thermogravimetric analysis (TGA)

Thermograms presenting the weight loss (%) of both the raw materials and full formulations were analysed using the Pyris 1 TGA Thermogravimetric analyser (PerkinElmer, USA). Samples of 5-15 mg were added and sealed into aluminium pans. A heating range of 20-600 °C with a heating rate of 10 °C per minute was used.

4.3.2.8 X-ray diffraction (XRD)

Sample crystallinity was measured of both the raw materials and full formulations, to determine the nature of the sample using the 2nd Generation D2 Phaser (Bruker, Warwickshire, UK), operating at 20 kV and 5 mA. The diffraction pattern was collected between 5-40° with a step size of 0.04° changing steps every 0.4 seconds. Samples were scraped of microscopic glass slides and loaded into powder specimen holders.

4.3.2.9 Zeta potential

Measurements for zeta potential were carried out using a Brookhaven NanoBrook Omni Particle Size and Zeta-Potential Analyser with Microrheology (Brookhaven, New York, USA). Measurements were carried out at the 15° detection angle minimising diffusion broadening. Known weight of samples were placed in a cuvette, suspended in water for analysis. Analysis was undertaken at neutral pH of 7.4 with a temperature of 25°C.

4.4 Results and Discussion

4.4.1 Formulation characterisation

Physical properties of liquids have a paramount effect on the size and morphology of particles that are produced from the EHDA system and hence they can be predicted and manipulated based on the properties of the formulation used. Moreover, the choice of vehicle is crucial in the EHDA process as it influences the jetting and stability of the spray, hence the reason viscosity, surface tension and electrical conductivity are important parameters. Particles fabricated through the EHDA process are a result of the interplay between viscosity, surface tension and electrical conductivity (Browne et al, 2019, Wahyudiono et al, 2019).

4.4.1.1 Viscosity

Table 4.2 displays the viscosity results of the solvents and formulations F1-F14. The viscosity results of both vehicles acetone and DCM matched values found in literature (Mohammadi and Hamzehloo, 2019). Formulations, F1 and F8 show similar viscosities as they consist of only polymer in solvent forming a solution. Upon the addition of the drug AMX F2 and F9 the viscosity increased accordingly as it is now formed a suspension. General trend showed formulations F9 to F14 were apparently more viscous which is due to the solvent DCM, in comparison to the F2 to F7 formulations which use acetone as the solvent. The formulations containing the metallic particles also increased in viscosity, as there is a higher concentration of material within the suspensions. Ghozatloo, 2015, described that the increase in concentration increases viscosity, but also the morphology of particles, as the metallic nanoparticles are shaped differently this can also lead to variation in viscosity. From **Table 4.2** it can be seen that formulations F4 and F11 both have the highest viscosity values, these formulations contain the metallic nanowires, which indicates these may have a higher density leading to overall increase in viscosity.

The effects the viscosity differences have on the electrospaying system are observed through SEM images. Too high a viscosity can lead to fibres forming or spraying of particles clumped together, whereas a lower viscosity allows for good flow of sample through syringe and good shaped particles forming. It is known that viscosity can differentiate between the types of spraying between electrospinning and electrospaying, as well as the stability of the spray. A viscosity too high can lead to blockage or impede the flow of the formulation within the syringe causing no spray to occur (Ardila et al, 2018).

4.4.1.2 Surface Tension

Surface tension results for all formulations F1-F14, are displayed in **Table 4.2**. For electro spraying to occur, atomisation must occur, this is when the electrical field applied overcomes the surface tension of the formulation, moreover, the cone jet breaks into small charged droplets by the electrostatic forces. The values for the surface tension remained low for all formulations F1 to F14, and hence it can be determined that it had no significant effect on the type of spray or morphology of particles. A lower surface tension of liquid can allow the flow rate to be reduced therefore yield smaller particles, however reducing the surface tension too low has its pit falls, as it prevents a stable cone from forming (Marin et al, 2012).

4.4.1.3 Electrical Conductivity

A sizeable difference in electrical conductivity values of the two vehicles is observed in **Table 4.2**, with acetone being highly conductive, many more times more conductive than DCM (Jahangir et al, 2017). All formulation utilised in the EHDA system must be electrically conductive as the main element of EHDA is the use of an electric field. The electrical conductivity of the formulations varied; overall the formulations which contained acetone were more electrically conductive and further increased with the addition of metallic nanoparticles, whose electrical conductivity increases with a decrease in particle size (Yuliza et al, 2014). F7 contains copper nanoparticles which had the smallest average in particle size when compared to other metallic nanoparticles synthesised and thus the result correlates with the literature. F4 and F5 contain metallic nanoparticles of a larger particle size and it reflects in electrical conductivity values when compared to F7. Similar patterns are observed for formulations F10 to F14, at lower overall electrical conductivity values. Electrical conductivity influences the particle size in electro spraying; moreover, a stable spray is dependent on the electrical conductivity, formulations with a higher electrical conductivity lead to the production of more uniform particles. (Ardila et al, 2018) (Faraji et al, 2017).

Table 4. 2: Table of characterisation displaying values for viscosity (mPa.s), surface tension (γ) and electrical conductivity ($\mu\text{s/cm}$) of solvents DCM and Acetone, and all formulations F1-F14. All experiments performed in triplicate.

Material	Viscosity (mPa.s)	Surface Tension (γ)	Electrical Conductivity ($\mu\text{s/cm}$)
ACETONE	0.35 \pm0.03	0.041 \pm0.020	1.48 \pm0.05
PLGA+ACETONE (F1)	0.51 \pm 0.02	0.037 \pm 0.003	4.71 \pm 0.01
PLGA+ACETONE+AMX (F2)	0.67 \pm 0.02	0.042 \pm 0.002	10.63 \pm 0.77
PLGA+ACETONE+AMX+ AGNP (F3)	1.41 \pm 0.07	0.024 \pm 0.002	54.71 \pm 0.74
PLGA+ACETONE+AMX+AGNW (F4)	1.76 \pm 0.10	0.044 \pm 0.002	61.41 \pm 0.78
PLGA+ACETONE+AMX+AGP (F5)	1.62 \pm 0.15	0.055 \pm 0.005	48.93 \pm 0.75
PLGA+ACETONE+AMX+AUNP (F6)	1.16 \pm 0.01	0.041 \pm 0.002	6.71 \pm 0.12
PLGA+ACETONE+AMX+ CUNP (F7)	1.31 \pm 0.02	0.038 \pm 0.004	84.01 \pm 1.47
DCM	0.41 \pm0.01	0.015 \pm0.002	0.13 \pm0.02
PLGA+DCM (F8)	0.64 \pm 0.02	0.038 \pm 0.003	7.97 \pm 0.05
PLGA+DCM+AMX (F9)	1.54 \pm 0.07	0.022 \pm 0.001	2.97 \pm 0.03
PLGA+DCM+AMX+AGNP (F10)	2.47 \pm 0.03	0.043 \pm 0.002	0.62 \pm 0.02
PLGA+DCM+AMX+AGNW (F11)	2.85 \pm 0.06	0.037 \pm 0.002	1.59 \pm 0.05
PLGA+DCM+AMX+AGP (F12)	2.13 \pm 0.02	0.034 \pm 0.002	1.77 \pm 0.07
PLGA+DCM+AMX+AUNP (F13)	1.95 \pm 0.04	0.029 \pm 0.002	3.94 \pm 0.11
PLGA+DCM+AMX+CUNP (F14)	1.66 \pm 0.02	0.047 \pm 0.003	13.21 \pm 0.22

4.4.2 Images of solution and suspension preparations

The appearance of solutions and suspensions remained the same for both solvents used acetone and DCM, for this reason in **Figure 4.1** acetone was used as the solvent for all images. As can be seen in **Figure 4.1A** is the polymer solution beaker appears clear, as the polymer is dissolved. In **4.1B** the appearance of the liquid becomes cloudy, as a suspension with PLGA and AMX has now formed, **Figure 4.1C** with the introduction of AgNPs the suspension becomes darker in colour as suspension concentration has increased, concurrent with AgNPs present in **Figure 3.1Aii**, as for **4.1D** the colour turns lighter and more light grey similar to the AgNW centrifuged image from **Figure 3.1Bi**, with the AgPs added the formulation turns darker grey in correspondence with the colour of centrifuged AgP particles in **Figure 3.1Cii**, with addition of AuNP **Figure 4.1F** the suspension becomes more red characteristic of the AuNP colour, the colour also indicates better dispersity of the AuNP throughout the suspension, and with the addition of CuNP the suspension turns yellow to red with brick red nanoparticles suspended within the centre of the beaker seen in **Figure 4.1G**.

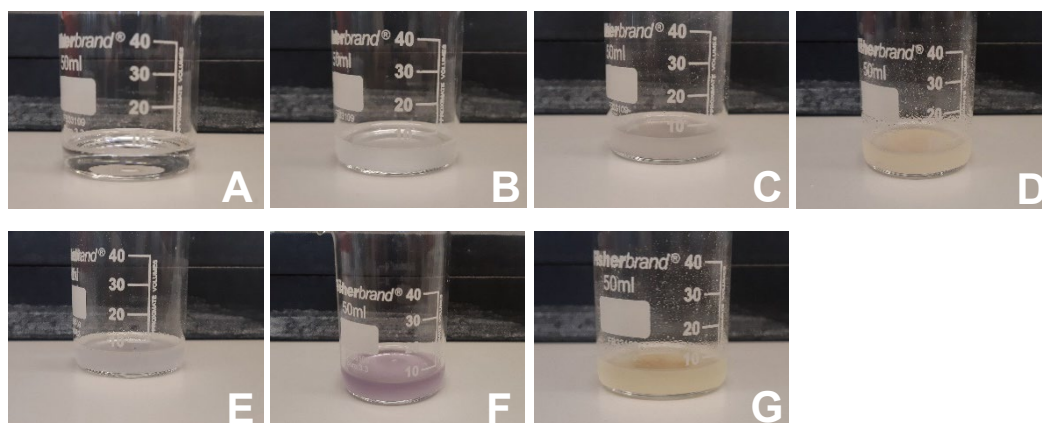


Figure 4. 1: Digital images of solution and suspension preparations in acetone; A) F1, B) F2, C) F3, D) F4, E) F5, F) F6, G) F7.

4.4.3 Jetting modes

Figure 4.2A shows the formation of a droplet at the end of the capillary needle. **Figure 4.2B** is when a low voltage has been applied and the jet is in dripping mode. **Figure 4.2C** shows the formation of a Taylor cone, the jetting is stable and particles will be collected, this is achieved when all parameters and conditions related to the liquid characteristics and the relationship between voltage and flow rate are favourable. However, with further increase in voltage or the optimum altering, the spray will become unstable (as seen in **Figure 4.2D**)

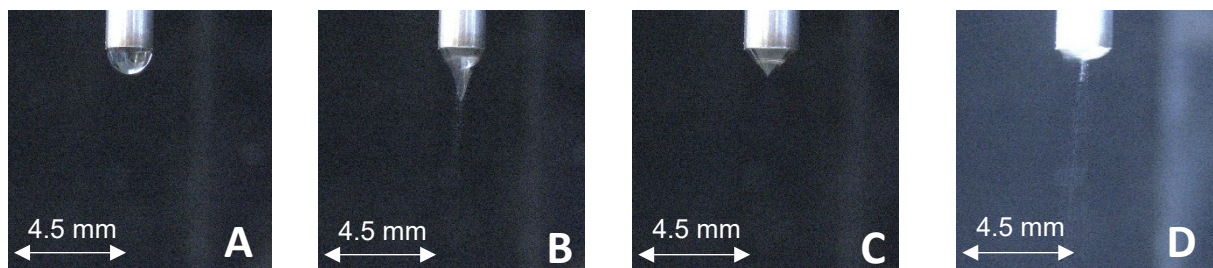


Figure 4. 2: Digital images of jetting modes through electrospaying. (A) initial droplet with no voltage applied, (B) dripping mode, (C) stable jetting mode, (D) unstable jetting mode.

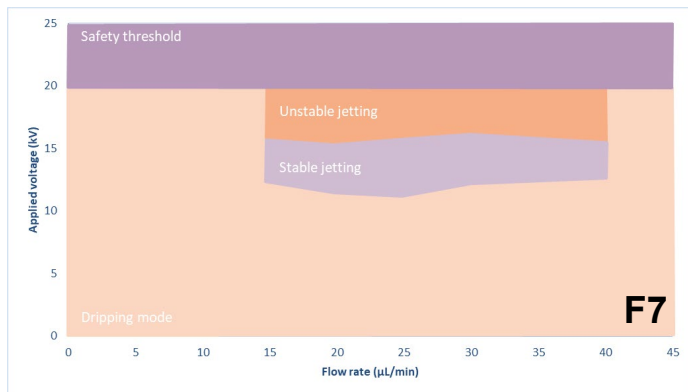
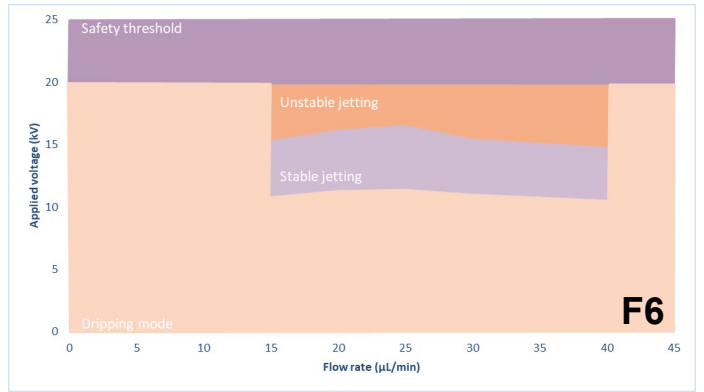
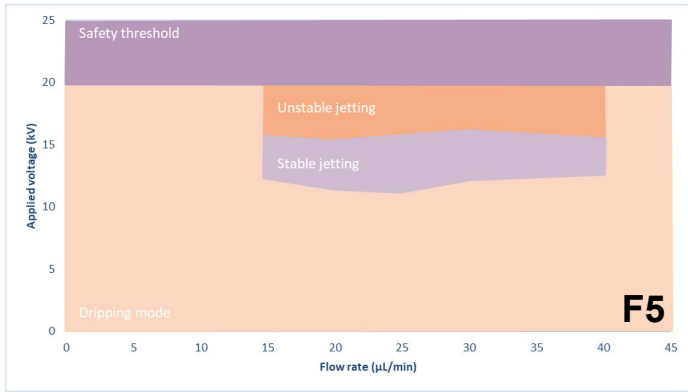
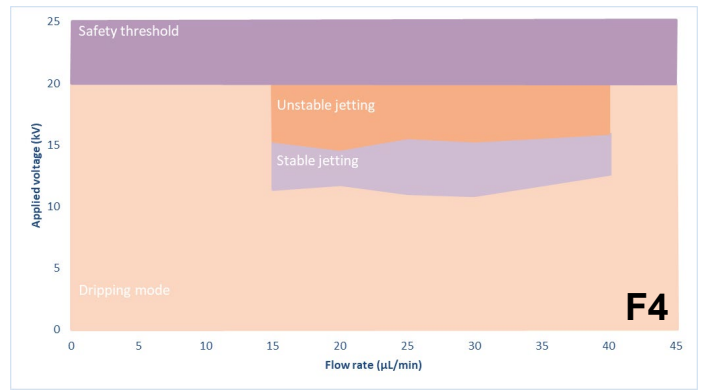
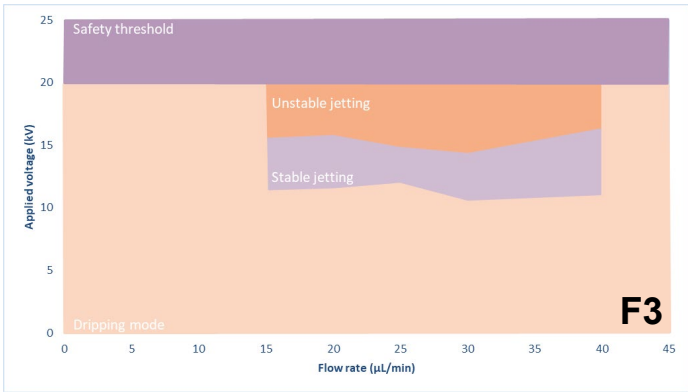
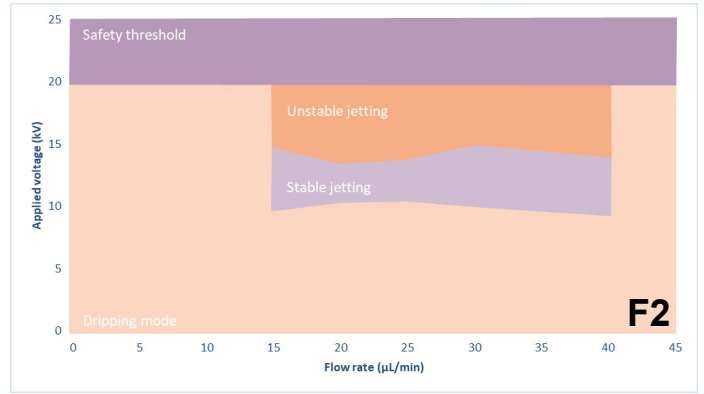
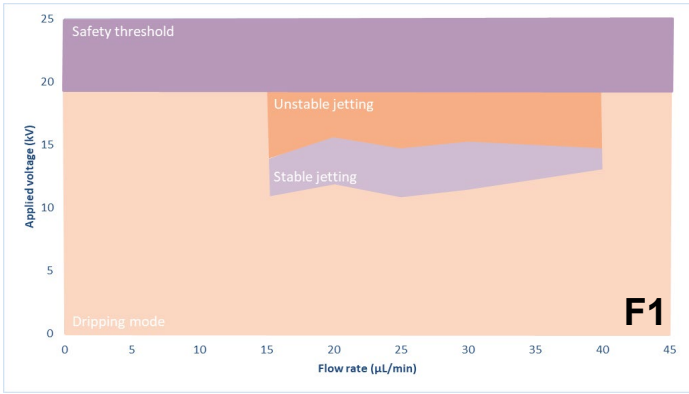
4.4.4 Jetting maps

The type of jetting mode created through the EHDA system is determined by the way in which the liquid formulation leaves the capillary needle. Different combinations of parameters have a paramount effect on the type of spray and material collected (i.e. particles or fibers). Upon setting up the formulation in the EHDA system, liquid is emitted from the capillary needle in the 'dripping mode' (**Figure 4.2A**). Upon applying electrostatic forces to the dripping mode, a Taylor cone arises to provide a stable spray.

To give rise to a stable Taylor cone, conditions have to be at an optimum, this relates to the relationship between the voltage and flow rate. When conditions are at an optimum you enter into 'stable jetting mode'. However, if you were to increase the flow rate further past this point, the spray enters into 'unstable jetting mode' as the formulation is flowing faster through the system, and therefore insufficient voltage is applied to the system preventing a stable cone from forming and non-uniform particles are produced. Increasing the voltage beyond this point can cause a more unstable spray, however voltage should not be increased beyond 20 kV for safety reasons.

Jetting mode maps for each formulation were plotted to determine the ideal conditions for 'stable jetting mode' and the creation of the Taylor cone **Figure 4.3**. Each formulation was synthesised and tried through the EHDA system; voltage values and flow rates were varied to find the ideal conditions for stable jetting. Each formulation has to be assessed individually due to the differences in solvents, insolubility of AMX, as well as type of metallic nanoparticles added, as differing shapes led to differing viscosity and electrical conductivity values.

The flow rates used ranged from 15 to 40 $\mu\text{L}/\text{min}$, below 15 $\mu\text{L}/\text{min}$ all the formulations were in dripping mode regardless of voltage applied. The voltage applied ranged from 10-17 kV, as this was sufficient for a stable spray; any higher led to an unstable spray in correlation with the flow rate used. As well as this, another important parameter was the working distance between the capillary needle and the collector plate, a distance too high meant a percentage of the created particles are lost and are not landing on the collector plate; a distance too short prevents the solvents from evaporating sufficiently. Moreover, the morphology of particles can change depending on distance used. Upon experimental work alongside the jetting mode maps, it was determined that 9 cm is the ideal distance to use between the capillary needle and the collector plate.



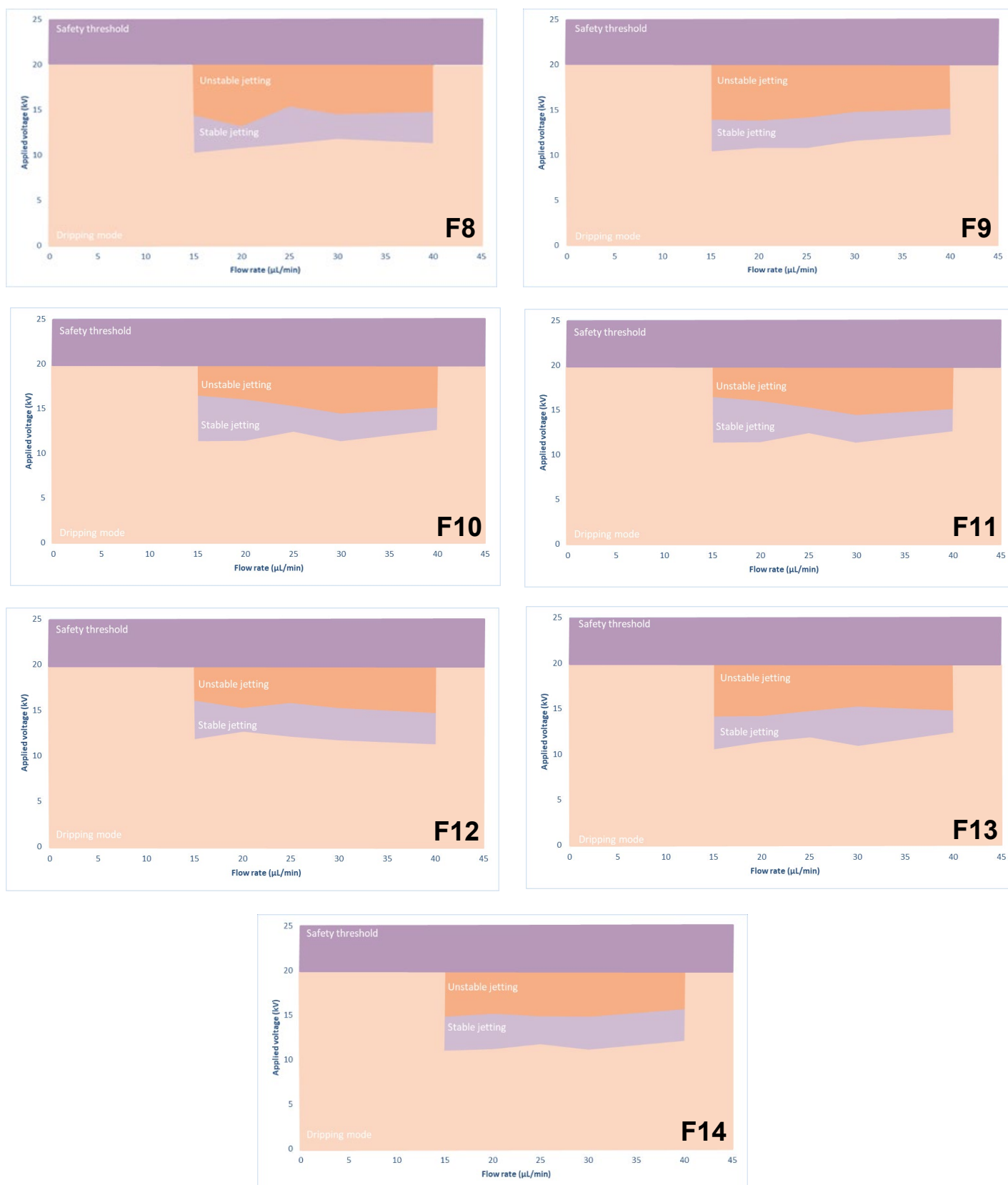


Figure 4. 3: Jetting maps of electro spraying process to show the relationship between flow rate and applied voltage, at which corresponding value of each parameter leads to stable or unstable jetting for all formulations F1-F14.

The mode maps for formulations from F1-F7, overall showed larger zones of stable jetting, which is attributed to the use of acetone, when characterised it shows high electrical conductivity therefore leading to easier spray. The suspensions F3-F7 and F10-F14 were a lot harder to spray, as the metallic nanoparticles sedimented to the bottom of the syringe due to difference in densities, so re-suspending the particles was important and had to be carried out regularly to ensure uniform spray of all particles present. Individually it was found that formulation F6 formed a stable cone quickly and held a stable uniform spray, this may be due to the electrical conductivity or viscosity, but more so with how well the AuNP particles dispersed within the formulation during synthesis as observed in **Figure 4.1F**. For formulations F8-F14 the spraying was a lot harder, stable jetting zones were a lot smaller, this is relative to the poor electrical conductivity value of DCM and the slightly higher viscosity. Furthermore, the differences between sprays of formulations can be analysed through the SEM images, as stability of spray effects morphology and size of particles. For formulations F4 and F11 which displayed the highest viscosity, it can be noted the zones of stable jetting are smaller in comparison to other formulations using metallic nanoparticles.

4.4.5 SEM

Formulations synthesised were then sprayed, using optimum flow rate and voltage as shown in the mode maps above, the particle size and morphology of samples collected was then analysed using SEM.

The SEM images of the electrosprayed formulations, are shown in **Figure 4.4** at both low and high magnification and at different points along the same sample. One issue related to magnification was the electron beam, at high magnifications particles would break up and deform due to intensity of the electron beam, this was a common theme for most of the samples using DCM as the solvent, moreover some of the metallic formulations would be disrupted at higher magnifications, this may be due to the charge these particles carry already.

Figure 4.4Ai shows the production of PLGA particles in acetone. The particles are large in size, show a uniform donut shape and correlate to images of PLGA found in literature (Parhizkar et al, 2017). Particles exhibit a collapsed porous structure due to rapid evaporation of solvent (Ahmad et al, 2008). The size distribution histogram shows the majority of particles were 3-4 micron in size, the average particle size was 3.3 micron. (Bock et al, 2011), has shown that morphology of particles sprayed at 5 % w/v is flat and donut shaped, for more spherical particles a higher concentration of around 9-10 % w/v is required. Furthermore, flat shaped particles with irregular morphologies also form due to incomplete solvent evaporation, this occurs more often with polymers used at low concentrations as solvent content is higher. As for **Figure 4.4Bi** spherical particles of polymer in DCM, particles have similar morphologies and appear spherical, corresponding to similar images observed by (Nath et al, 2013). The particle size varies between 2.5 to 6 microns, with an average particle size of 3.4 micron.

Particles observed in **Figures 4.4 Ci** and **Cii** are for the drug AMX electrosprayed in solvents DCM and acetone respectively, from observation particles appear brighter and more charged, as oppose to polymer particles, this may be due to the increased crystallinity of the drug particles. The particles appear monodispersed and spherical in shape, particle size varies between 200-400 nm, with an average particle size of 236 nm.

Figures 4.4Di and **Ei** are of PLGA and AMX electrosprayed in both acetone and DCM respectively, the drug (AMX) was insoluble in both solvents used, so images may show AMX particles embedded upon PLGA, or complete encapsulation of AMX. **Figure 4.4Di** shows particles with a smaller size range from 1.2-2 microns, with an average particle size of 1.6 micron, this may be due to the addition of excipients to the formulation, as incorporating more

excipients leads to an overall particle size reduction (Prabhakaran et al, 2015). (Kumari et al, 2010) explained encapsulation by biodegradable materials occurs through entrapment of drug within the polymeric matrix, or adsorption onto the surface of the polymer. This is observed in **Figure 4.4Ei** were smaller drug particles can be seen embedded on to the polymeric matrix. As for **Figure 4.4Di** it is assumed particles have been encapsulated as particle size has reduced and particles appear more charged. Smaller fibres can also be observed in **Figure 4.4Di** this may be due to the increased viscosity as a suspension has formed. The particle size in **Figure 4.4Ei** is a recurring theme throughout the SEM images for all formulations F8-F14 as these contain the solvent DCM, larger particles are observed with no clear morphology, this may be due to the difficulty of spraying a suspension using DCM as the vehicle, as electrical conductivity is lower and viscosity higher. This also may be attributed to the incomplete solvent evaporation.

EDS analysis was introduced, seen in **Figures 4.4Diii** and **Eiii**, these samples contained no metallic nanoparticles which is shown in the related EDS spectra, the reason for this was to compare and confirm the presence of metallic nanoparticles in the following EDS spectra to come. Moreover, for **Figure 4.4Ei** the solvent used DCM which is made up of two chlorine groups, Cl groups are present in **Figure 4.4Eiii**.

Figures 4.4Fi and **Fii**, are high and low magnification images of F3, the particles again appear donut shaped, some appear more spherical. The particle size ranges from 800 nm to 2 microns, with an average particle size of 1.3 micron. Some of the particles appear charged this may be due to drug encapsulation or metallic nanoparticles. The presence of metallic nanoparticles runs in tandem with an increase in electrical conductivity of the suspension **Table 4.2**, allowing for easier spray, which may be responsible for the better morphology of the particles and more uniform size distribution observed, this may also lead to more successful encapsulation of drug and metal present. EDS **Figure 4.4 Fiii** confirms the presence of silver within the sample, confirming successful electrospaying of the suspension formulated. Detecting the presence of metallic nanoparticles through SEM images has proven to be difficult, hence why EDS is utilised as the spectra generated is more of an indicator than the SEM images themselves, as (Almajhdi et al, 2013) electrospun PLGA and AgNP, but the metallic particles upon the surface of the fibres were only observed through TEM images. (Abdelrazek Khalil, 2013) also show that confirmation of silver presence occurs through EDS, to visually see the metallic particles TEM analysis is required.

For the formulation F10 SEM images in **Figure 4.4Gi** and **Gii**, display smaller particles settled upon larger particles, these smaller particles may be drug particles, or metallic nanoparticles embedded upon the surface of the polymeric matrix, (Chaubey et al, 2014) displayed TEM images of interactions between PLGA and AgNPs, in this case AgNPs were deposited upon the surface of the polymer, this indicated dispersity of the AgNPs throughout the polymeric matrix. The larger spherical particles which appear charged upon the surface of the polymer may be AMX particles or the metallic nanoparticles, due to them appearing charged. EDS analysis confirms the presence of silver as well as chlorine. The size of particles ranges from 1.2-2.2 micron with the larger sized particles being the polymeric composite particles. Average particle size was shown as 1.7 micron. The morphology of the larger particles again may be due to the use of DCM which as mentioned has its drawbacks including incomplete evaporation.

For the formulation F4 the key was to spray the AgNWs alongside the polymeric composites, as is shown in **Figure 4.4Hi** and **Hii** both images were at low magnifications, the AgNWs were successfully sprayed, the morphology and size varies from the AgNWs shown in **Figure 3.1Bi**, the AgNWs appear more 3D like and layered, this may be due to the conditions applied during synthesis of suspension or the electrospaying process, from **Figure 4.4Hi** it can be seen that polymeric composite particles have deposited upon the AgNW, and some embedded within, there also appears to be coating of the AgNW by the polymeric composites. The related EDS spectra confirms the presence of silver, which also confirms successful electrospaying of the AgNW. Size distribution here was carried out for the particles and nanowire separately, the particle size varies between 800 nm to 2.4 micron, the nanowire width is recorded at around 4.1 micron.

For the formulation F11 in **Figure Ii** AgNWs are formulated here using DCM as the vehicle, **Figure 4.4Ii** and **Iii** show the morphologies of sprayed particles as well as the AgNW, here results are more interesting, the AgNW seem to be present embedded within the polymeric matrix, as no clear present nanowire is present, instead particles observed exhibit an elongated morphology as oppose to spherical, and the topography upon the surface of these particles appears to be coated with polymeric composite particles. (Homan et al, 2011) synthesised colloidal star shaped AgNP upon PLGA via a facile two-step reduction process, SEM images showed the star shape of silver-polymer composites, where polymeric particles were deposited and coated the star shaped AgNPs particles.

As for **Figure 4.4Iii** the nanowire is clearly present, from the image polymeric composite particles can be seen wrapping around the nanowire, indicating encapsulation of the nanowire is possible, polymer drug particles can be seen surrounding the nanowire, smaller particles can be seen deposited upon the larger polymeric particles this may be the drug particles embedded onto the polymer. EDS analysis again confirms the presence of silver meaning successful electrospaying of the AgNW, and as F11 was formulated with DCM as the vehicle EDS spectrum displays the presence of chlorine within the sample. The particle size of the particles was taken as well as the width of the elongated microparticles present. The size of particles was roughly between 1-3 micron but the width of the elongated particles was higher between 4.5-7 micron, this may indicate encapsulation of metal within polymeric composite.

Figure 4.4Ji and **Jii** for F5 taken at similar magnifications, show highly charged particles, this may be due to the encapsulation of drug and metallic nanoparticles, or due to the intensity of the electron beam. The presence of smaller charged particles upon the polymeric particles is again evidence of drug and metallic nanoparticles being embedded within the polymeric matrix, which also indicates successful electrospaying of the suspension. The particles appear to have similar spherical morphologies and a narrow size distribution, and in correlation with previous images using acetone as the vehicle having the donut or ring-shaped appearance. The particle size varies from 1.2-2 micron, with an average particle size of 1.6 micron. EDS spectrum confirms the presence of AgNP.

Formulation F12 displayed in **Figures 4.4Ki** and **Kii** are at different magnifications, the SEM images show polymeric composite particles of varying shapes and sizes. Charged particles are present which again may validate the presence of the drug and silver particles, which is further confirmed by the EDS analysis results as well as the presence of chlorine. The particle size ranges from 600nm to 2.2 micron, with an average particle size of 1.3 micron. A similar average particle size to from **Figure 4.4Kii** particles with more defined edges can be seen, these may be the polygonal shaped nanoparticles present within the sample, or encapsulation of these within the polymeric matrix. However, to have full confirmation of AgNPs presence within all samples visually then TEM images are required.

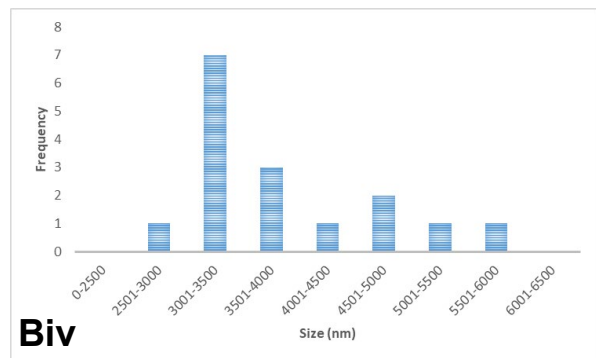
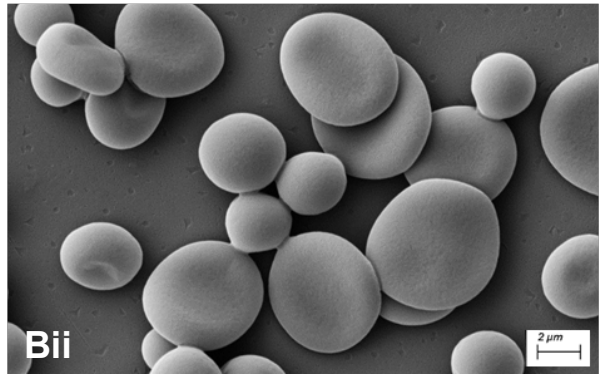
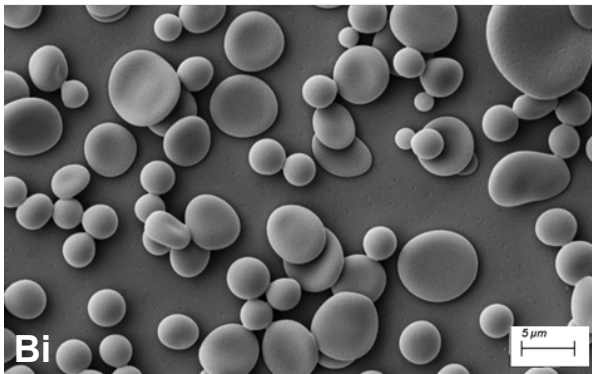
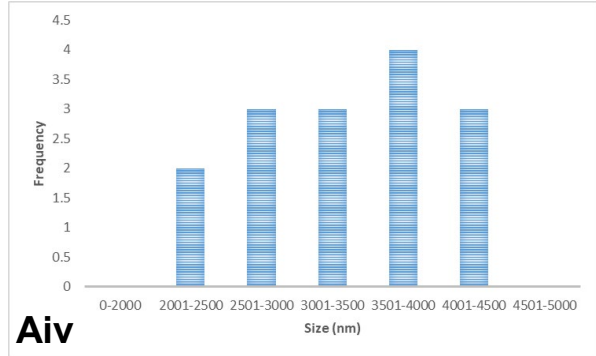
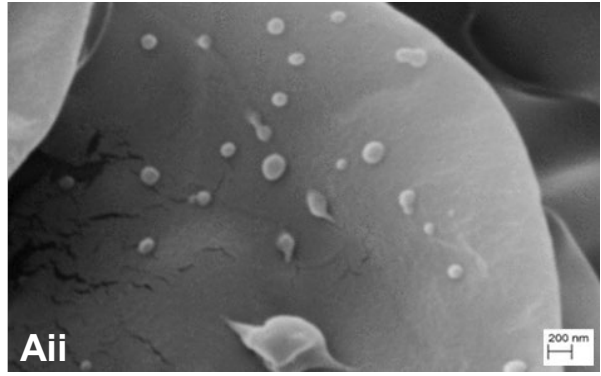
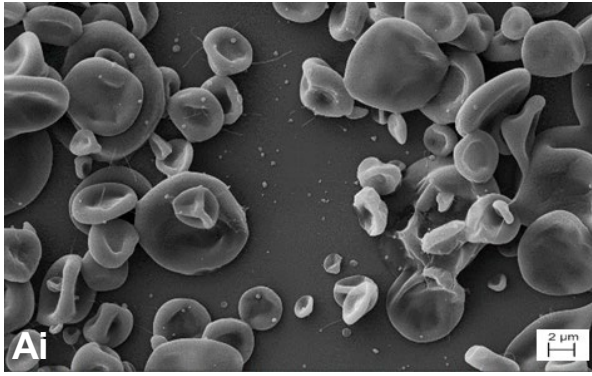
Figure 4.4Li and **Lii** for formulation F6 show uniform spherical particles monodispersed, the SEM image shows uniform spherical particles, which also exhibit charge which may indicate the presence of drug and metallic nanoparticles. The size range of particles varied between 400 nm to 1.1 micron, the particles appear smaller and more uniform which may be due to the

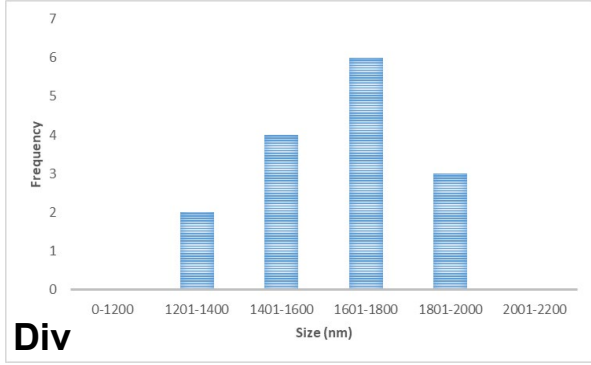
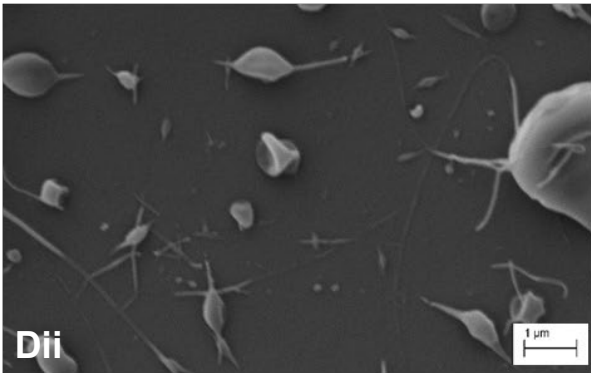
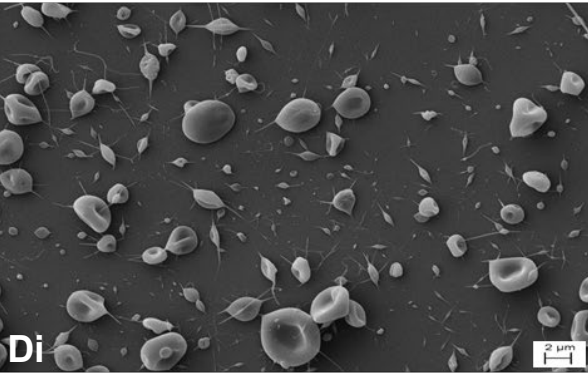
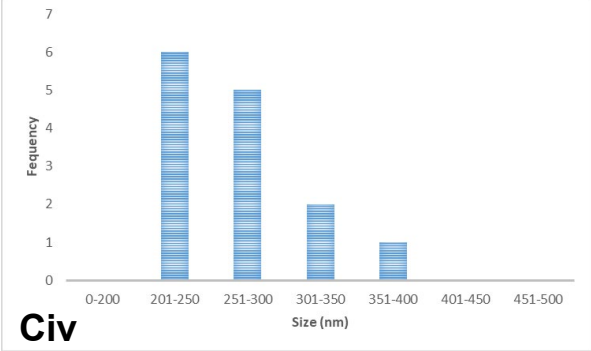
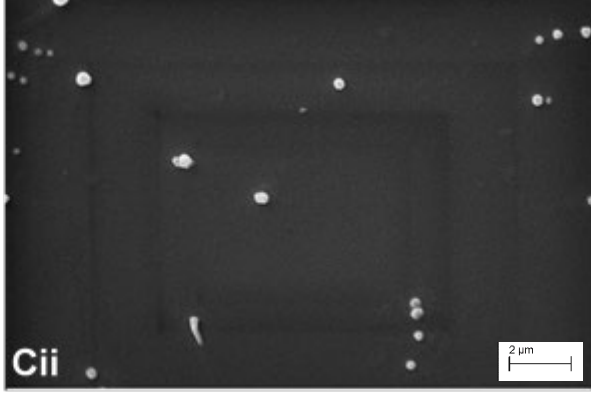
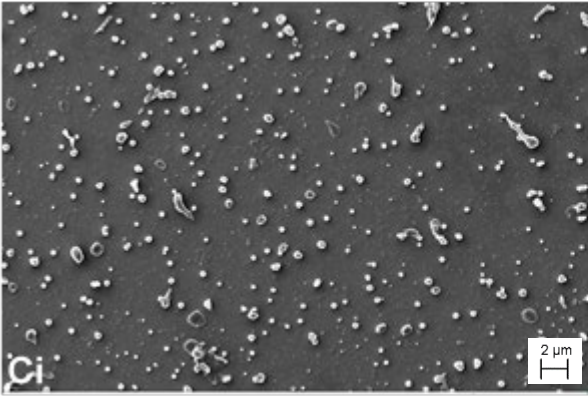
uniform polydispersity of particles observed in **Figure 4.1F**. (Alkilany et al, 2018) showed it is possible to completely encapsulate AuNP within the PLGA matrix, also described PLGA as being one of the few biodegradable polymers capable of encapsulating metallic material. Moreover, (McKeon-Fischer and Freeman, 2010) displayed SEM images and explained detection of metallic particles was through spotting brighter spots in SEM images. EDS analysis confirms the presence of gold within the sample.

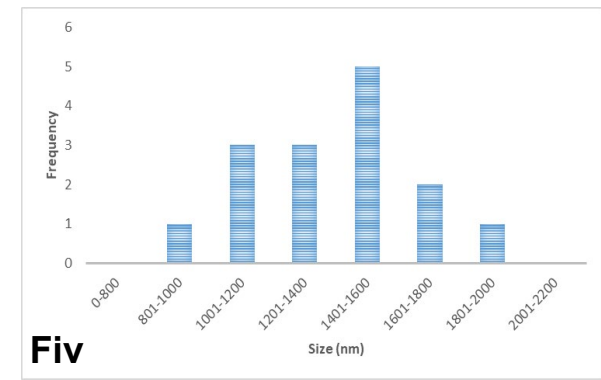
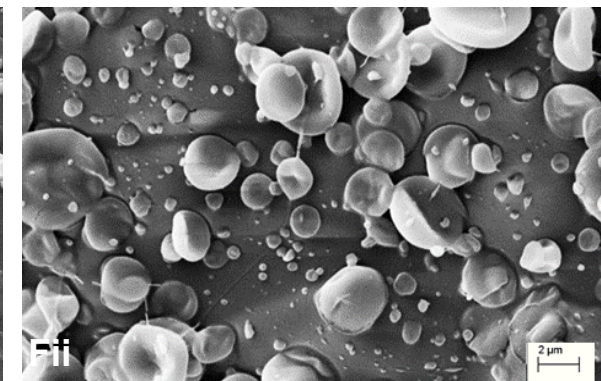
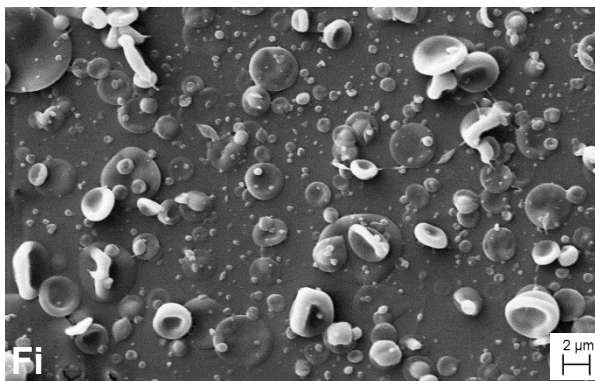
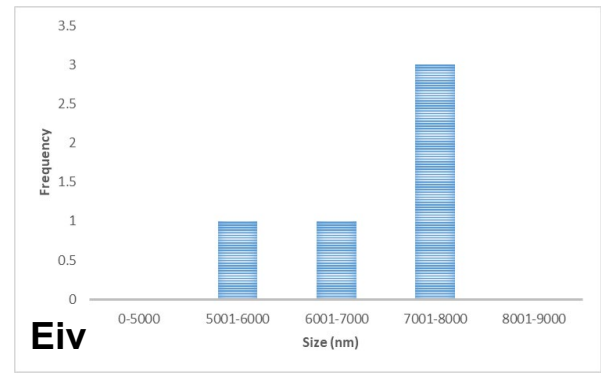
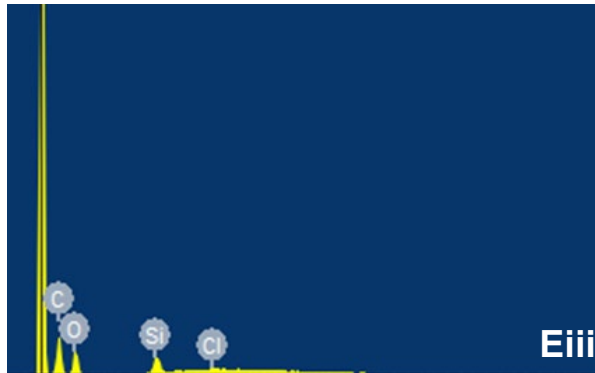
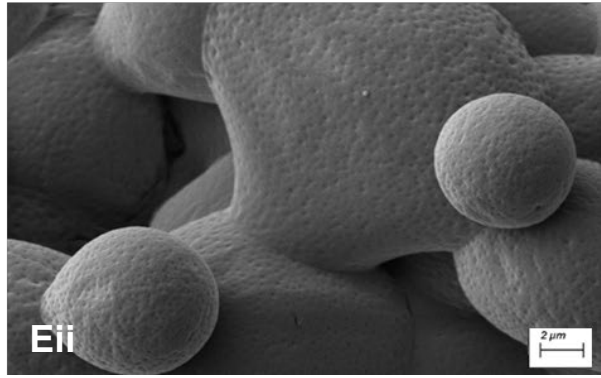
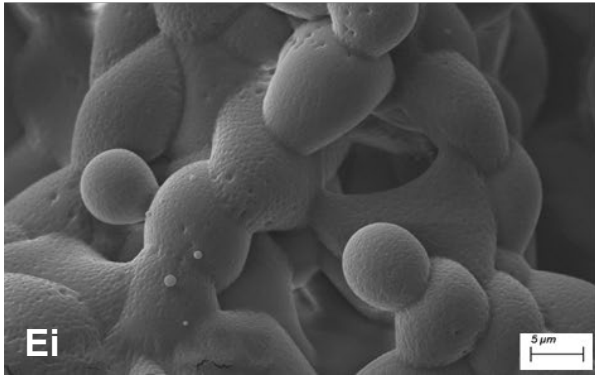
Figure **4.4Mi** for F13 displays larger particles with spherical morphologies, upon which many smaller particles have deposited, particles appear charged, a lot of fibres are also visible indicating a highly viscous formulation. When comparing the morphologies with F6, particle size is a lot bigger, no uniform dispersity of nanoparticles, instead particle size ranges from 1-2 micron. The reasons for the differences in morphologies is associated with choice of solvent, as the AuNPs dispersed well in formulation preparation seen in **Figure 4.1F**, this led to very uniform spherical particles in **Figure 4.4Li**, however this was not the case here. EDS analysis confirms the presence of AuNPs and chlorine. (Corbierre et al, 2001) synthesised polymer stabilised gold nanoparticles and showed complete dispersion of AuNP throughout the polymer matrix.

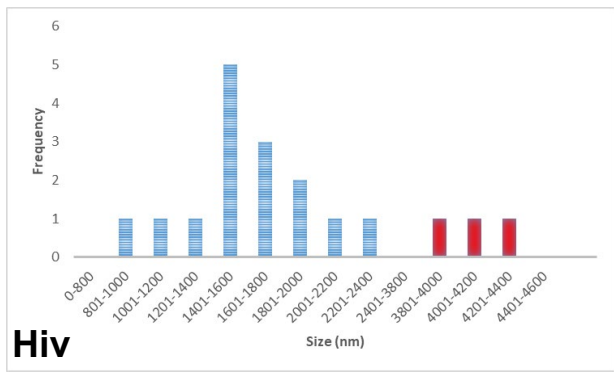
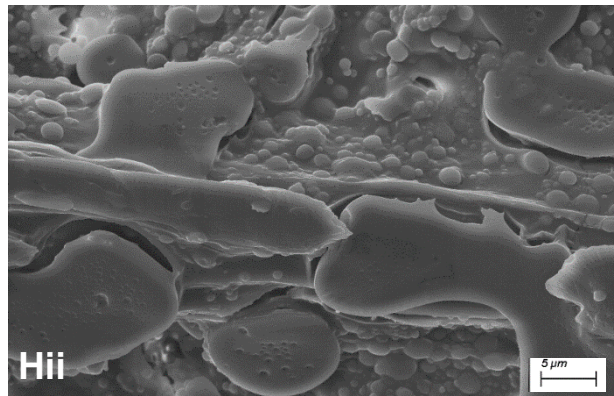
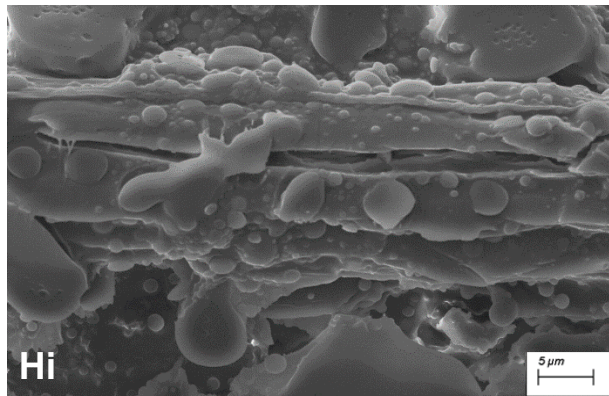
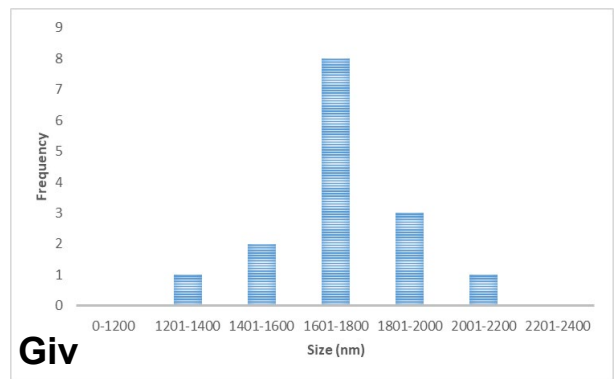
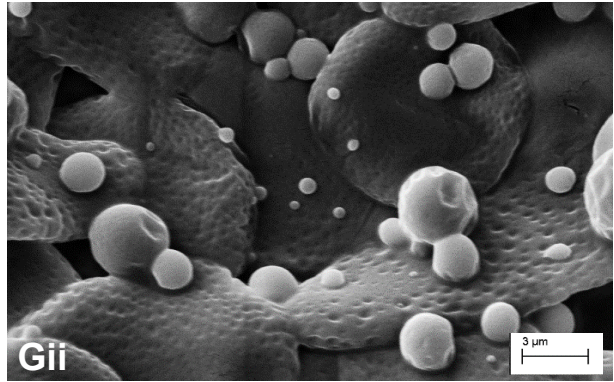
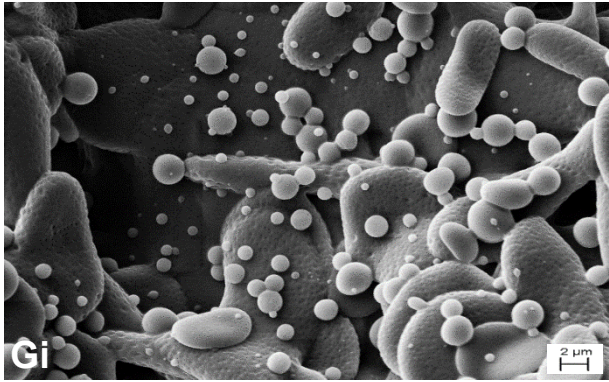
Figure 4.4Ni and **Nii** for F7, particles appear flatter, may be due to insufficient solvent evaporation, more spherical with similar morphologies. This may be due to the high electrical conductivity this formulation demonstrates. EDS spectra confirms the presence of copper. Particle size varies between 1.2-2.2 micron with an average particle size of 1.7 micron. (Prabhakaran et al, 2015) showed at higher concentrations of polymer around 10% w/v in DCM the particles appear more spherical and uniform, with a smaller size distribution, however in this case this was not possible as the formulation would become too viscous to spray.

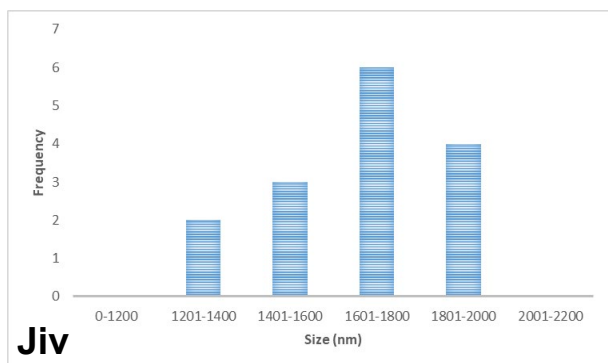
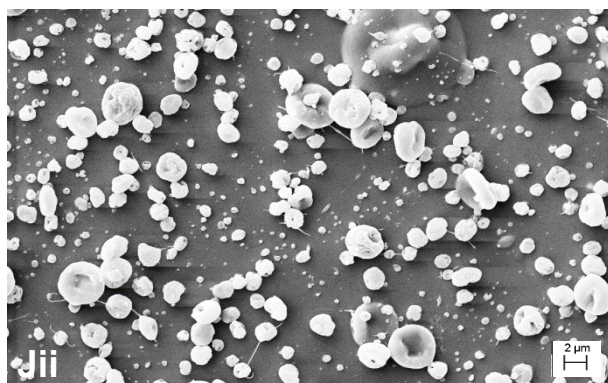
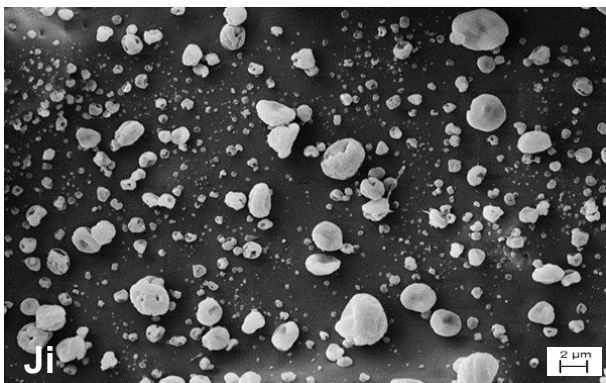
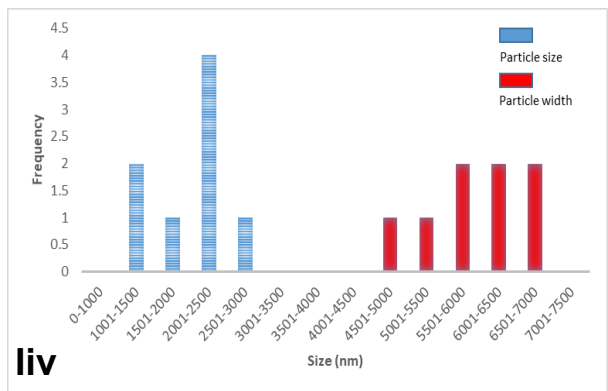
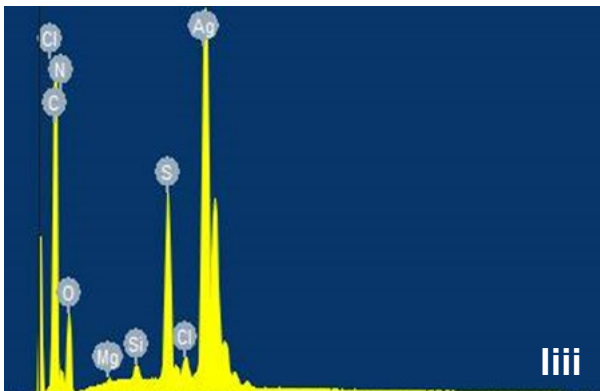
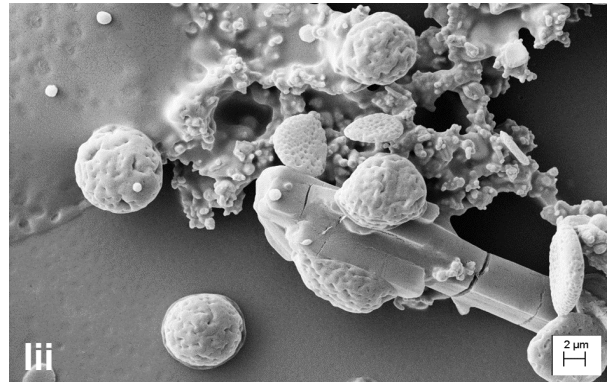
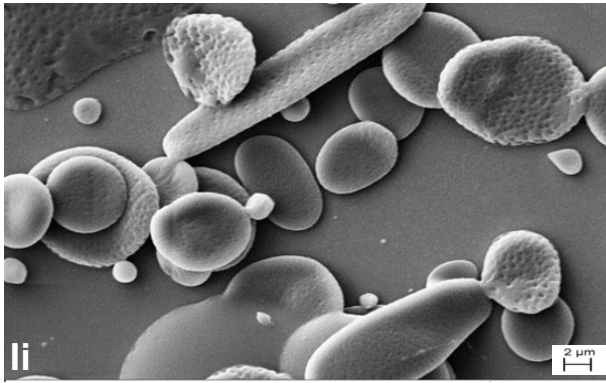
The corresponding formulation F14, displayed in **Figure 4.4Oi** and **Oii**, display smaller sized particles deposited upon larger particles, the smaller particles appear embedded within the polymeric matrix and appear charged, seen better in **Oii**, in correlation with previous formulations using DCM as the vehicle the morphology of the larger particles is hard to make out, therefore size distribution was carried out on the spherical particles present. Size range of particles was between 300-700 nm, with an average particle size of 420 nm. EDS analysis confirms the presence of copper and chlorine. (Kampuri and Dolui, 2010) synthesised copper-polystyrene nanocomposite particles and showed complete dispersion within the polymeric matrix.

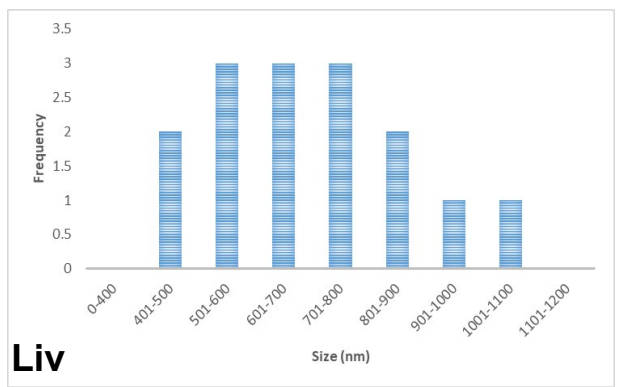
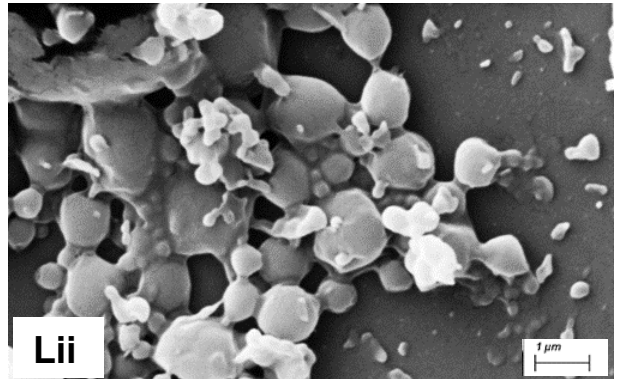
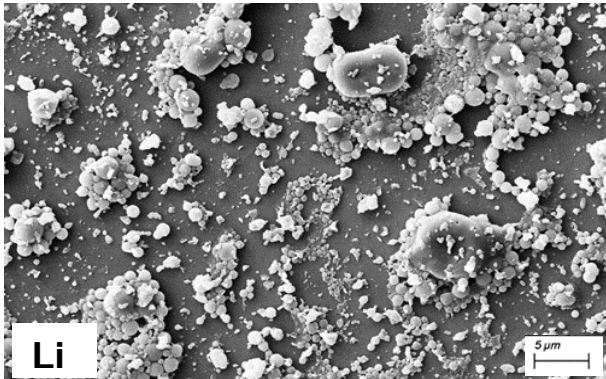
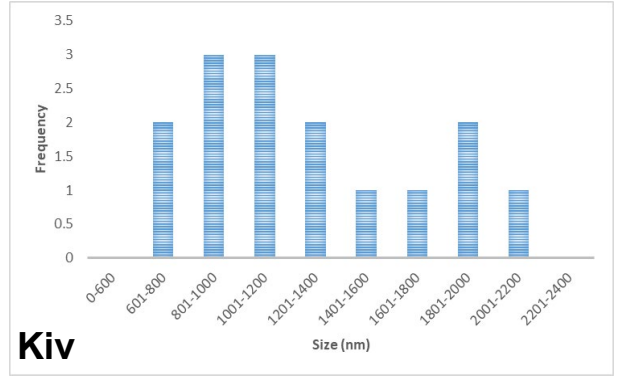
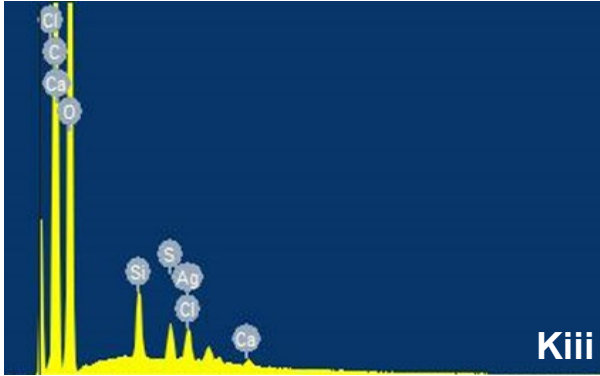
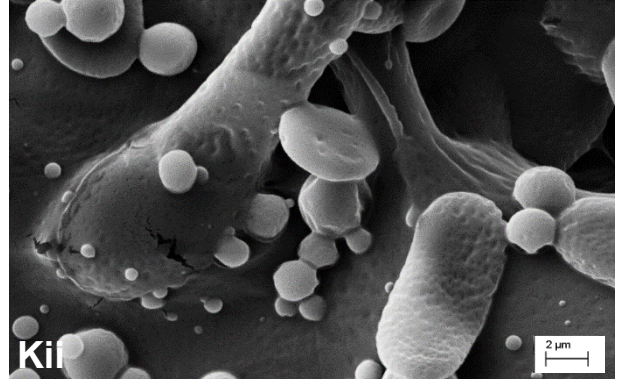
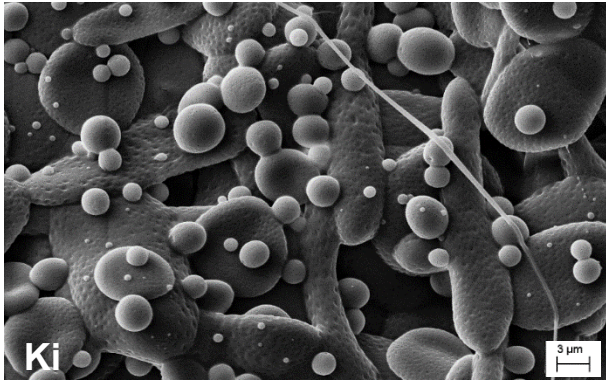


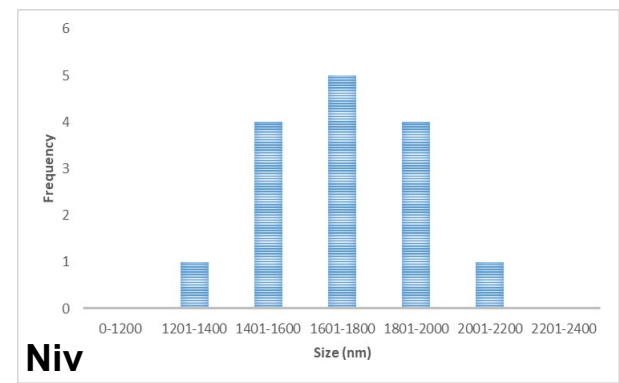
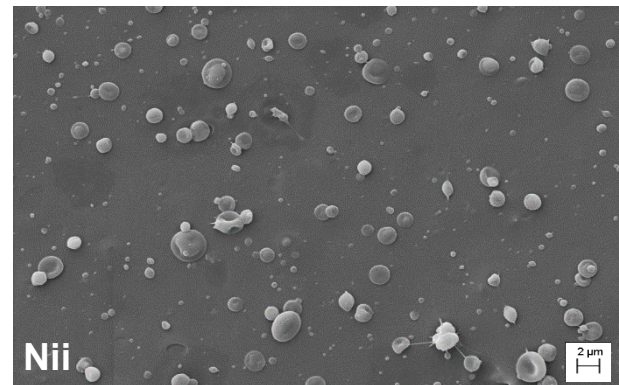
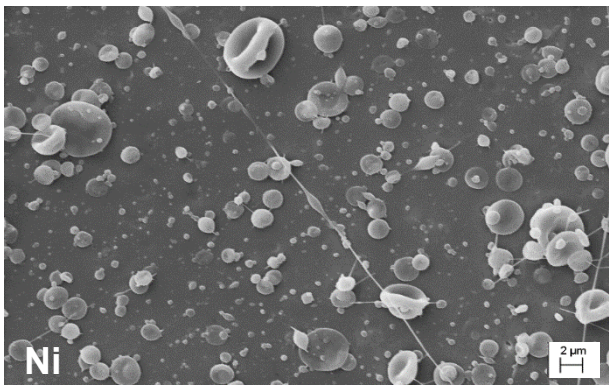
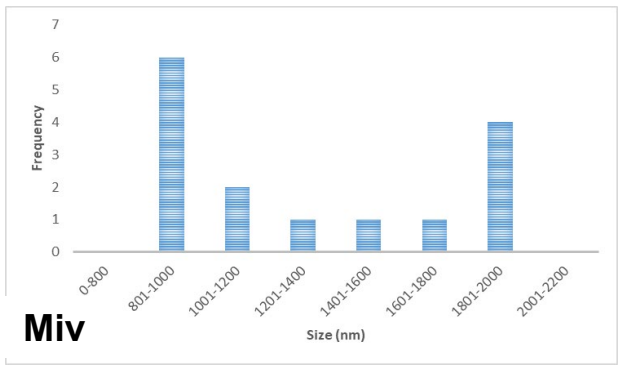
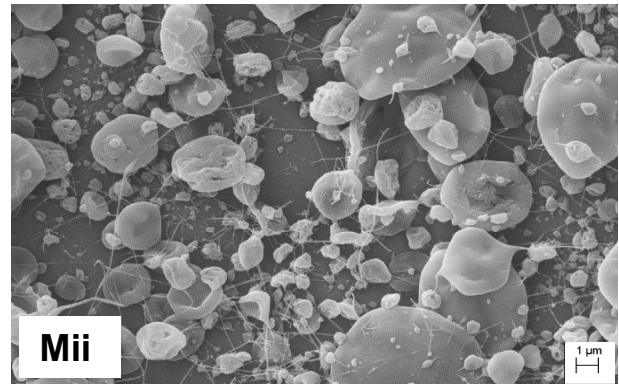
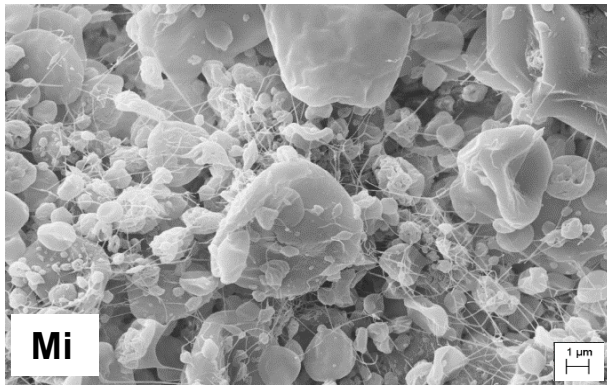












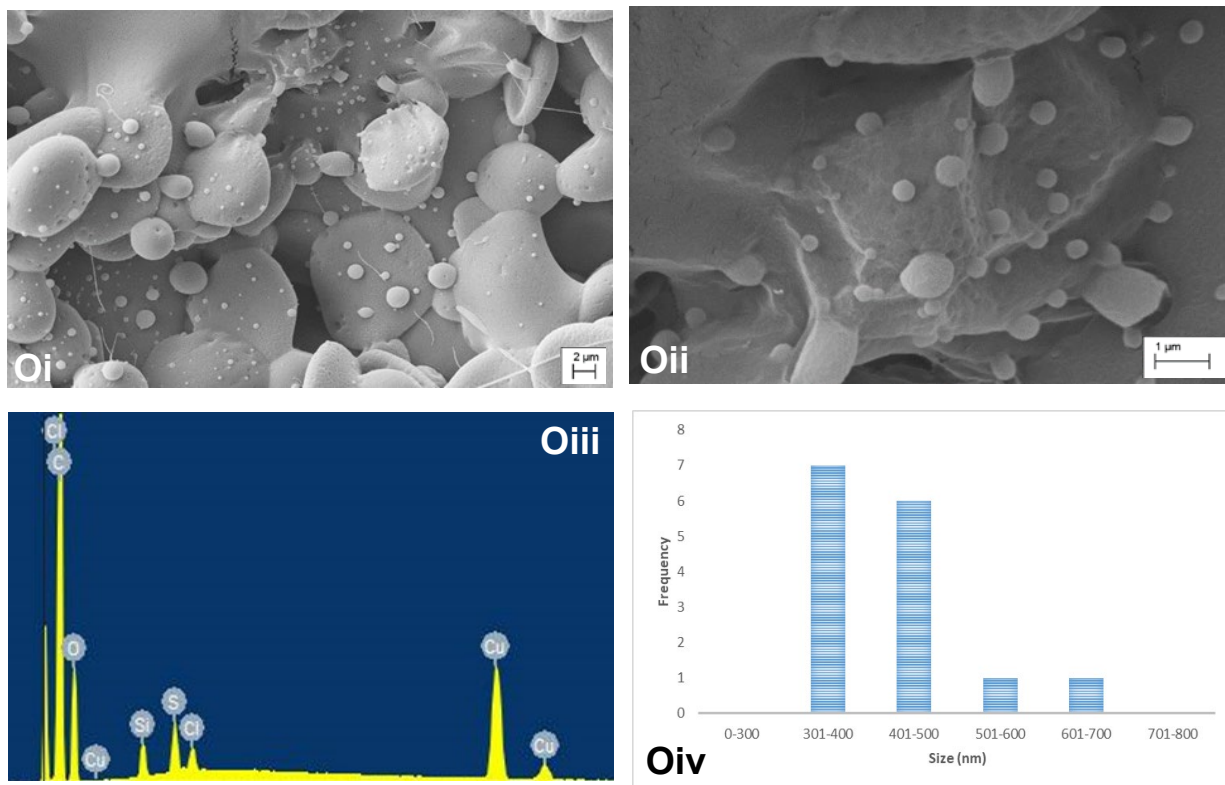


Figure 4. 4: SEM ((i) low magnification); ((ii) images at higher or equal magnifications); (iii) EDS analysis; (iv) particles size distribution histogram using (ii) SEM images of all formulations F1-14. (A) F1; (B) F8; (C) AMX in DCM and acetone; (D) F2; (E) F9; (F) F3; (G) F10; (H) F4; (I) F11; (J) F5; (K) F12; (L) F6; (M) F13; (N) F7; (O) F14.

4.4.6 ATR-FTIR

The FTIR spectra for PLGA in **Figure 4.5** show sharp peaks at 1088 cm^{-1} and 1168 cm^{-1} which correspond to a C-O stretch, a sharp peak at 1750 cm^{-1} for a C=O stretch, further smaller peaks can be seen between $2949\text{-}2963\text{ cm}^{-1}$, relating to CH-CH₂-CH₃ stretches (Nath et al, 2013, D'Avila Carvalho Erbetta, 2012). The FTIR spectra of AMX in **Figure 4.5** shows sharp peaks at 1519 cm^{-1} and 1686 cm^{-1} assigned to the two amide bonds of AMX, peaks at 1022 cm^{-1} , 1585 cm^{-1} and 1766 cm^{-1} can be attributed to the stretching vibration of C-S group, absorption band of benzene ring and the vibration of a carboxyl group respectively (Zheng et al, 2013, Abdelmalek et al, 2018).

Figures 4.6 and **4.7** show all spectrums for the final formulations, F1-F7 utilising the vehicle acetone and F8-F14 synthesised with DCM as the vehicle. F1 and F8 are for the polymer in solvent formulations, both spectra have peaks similar to the spectrum described in **Figure 4.5** for the PLGA material, sharp peaks at 1080 cm^{-1} , 1158 cm^{-1} and 1746 cm^{-1} show similar intensity. The difference between F1 and F8 is described through a sharp peak at 730 cm^{-1} , this indicates the presence of a C-CL bond (Deepashree et al, 2013), bonds present in the molecular formula of DCM, furthermore, this is a recurring theme for all formulations F8-F14, with all spectra showing sharp peaks at around 730 cm^{-1} . The presence of this peak indicates the solvent has not fully evaporated, and may be one of the reasons as described above, for the SEM images to not have clear, defined morphologies.

Results differ however for F2 and F9 with the inclusion of the antibacterial agent AMX, peaks can be seen at similar positions but with less intensity. For F2, some variations are present; there is no peak at 563 cm^{-1} and between 705 cm^{-1} - 738 cm^{-1} , the small broad peak at 901 cm^{-1} is no longer present, there is no longer a dip at around 936 cm^{-1} and the sharp drop from 992 cm^{-1} to 1042 cm^{-1} is not so prominent. The decrease in peak intensities indicates interactions between components within the sample. Moreover, at 1746 cm^{-1} and 3000 cm^{-1} the peaks seem to have become flatter and wider indicating hydrogen bond enhancement (Sun et al, 2015).

Spectrums for F3 and F10, show peaks at similar positions with similar intensities, peaks appear with more intensity at 1079 cm^{-1} , 1158 cm^{-1} and 1743 cm^{-1} , moreover the peak at 2949 cm^{-1} appears broader and more defined. These spectra follow similarly to the spectra of F6 and F13 respectively, this may be due to similarity in synthesis of the metallic nanoparticles included in these formulations.

In comparison with F4 and F5, peaks appear with less intensity, perhaps indicating more interactions between compounds present, moreover, peaks appear at 1642 cm^{-1} and at 1539 cm^{-1} , representing a C-O stretch and C=C stretch respectively. These peaks are only observed in F4 and F5 as well as F11 and F12. These formulations all contain shaped AgNP synthesised through a similar polyol method. As for F7 and F14 spectra follow a similar pattern to that of PLGA, with no real differences, aside from intensity of peaks. Zhang et al, 2017, synthesised AgNW-PVA nanofibers; results suggest that at increasing concentrations of nanowires within the fibers did not change ATR-FTIR spectra significantly.

The spectra overall from F1-F14, show peak positions at similar positions, in comparison to raw PLGA with the only major difference being in peak intensities, and the presence of C-CL peak in formulations F8-F14, (Abdelrazek Khalil, 2013) electrospun PLGA with AgNP, plotted FTIR spectra showed no real difference between raw PLGA and PLGA with silver formulations, with the only difference in transmittance intensity. Furthermore (Shams et al, 2018), electrospayed drug encapsulated microparticles, FTIR peaks for the synthesised formulations, showed spectrums similar to the raw polymer used, indicating drug polymer interactions.

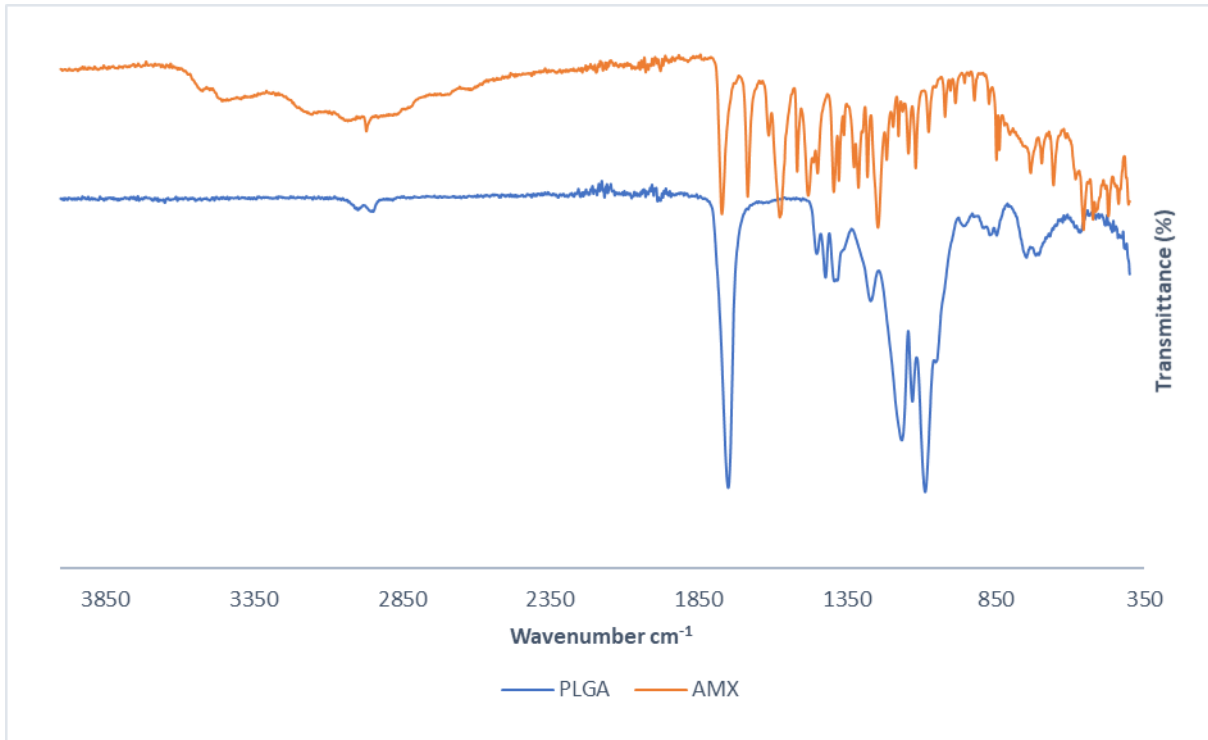


Figure 4. 5: ATR-FTIR spectra of raw materials PLGA and AMX.

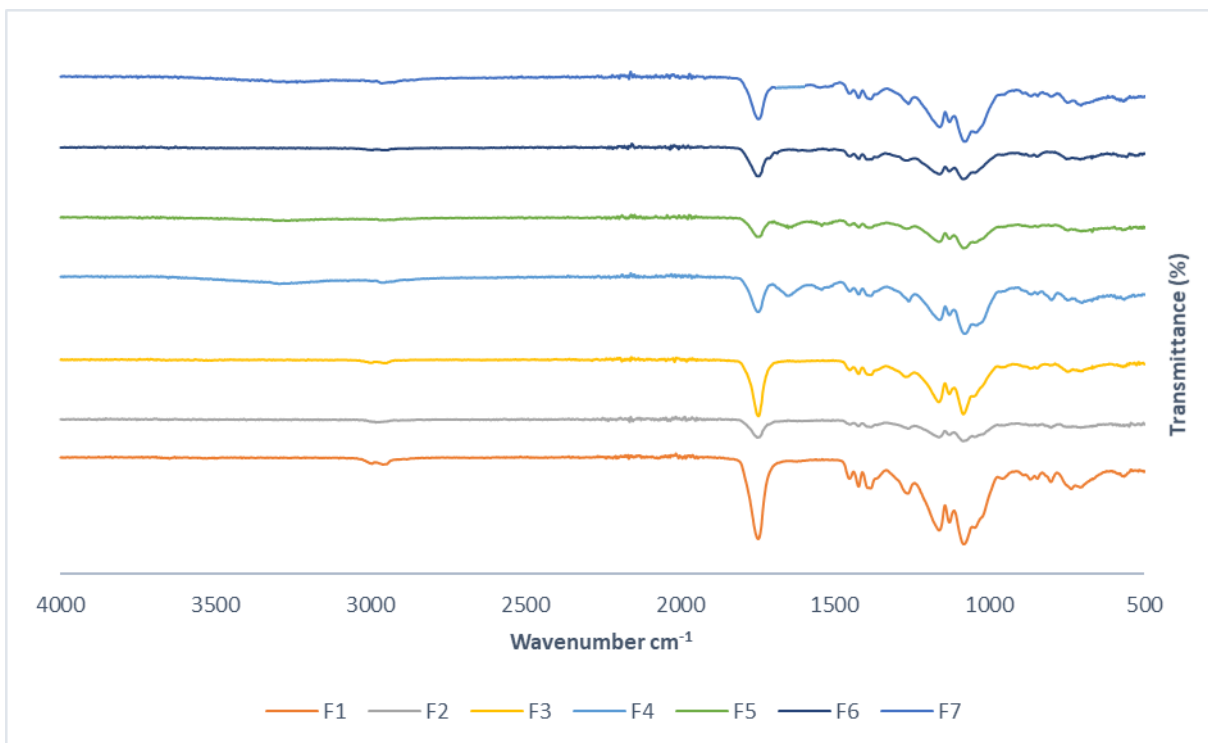


Figure 4. 6: ATR-FTIR spectra of formulation F1-F7 using the solvent acetone.

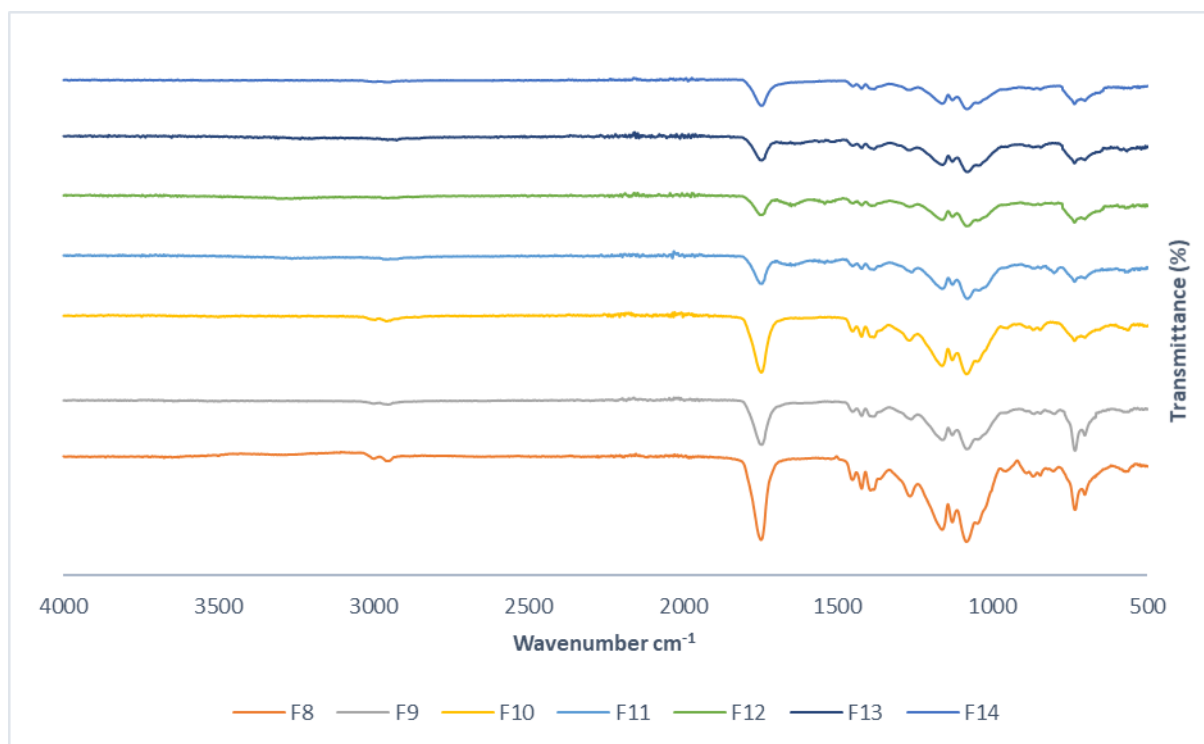


Figure 4. 7: ATR-FTIR spectra of F8-F14 using the solvent DCM.

4.4.7 DSC

DSC thermograms of all formulations including the raw materials are presented. Thermal stability analysis is important to determine if the electrospraying technique has an effect on the physical stability of the actives used as well as further confirming interactions between the drug and polymer. **Figure 4.8** displays thermograms for raw materials, AMX shows a melting peak at 160 °C, with PLGA showing a glass transition temperature at 56.5 °C (Yandrapu and Kompella, 2013); the polymer being amorphous doesn't exhibit a melting point. For the synthesised formulations F2 and F9 in **Figure 4.9**, there is no endothermic peak at 160 °C suggesting incorporation of the drug within the polymeric matrix, hence crystallinity of the drug has been reduced to a more amorphous state within the polymeric matrix (Sun et al, 2015). Moreover, when comparing the glass transition peak size, between F1 and F2 as well as F8 and F9, peaks decrease in intensity for F2 and F9, (Abdelrazek Khalil, 2013) reported the reason for this may be due to increased interactions between polymer chains and drug particles. Furthermore, (El-Houssiny et al, 2016) described the interactions between drug and polymer through DSC thermograms, the endothermic peak for the drug at 218.65 °C indicating crystallinity, was no longer present in the diffractogram for polymeric microspheres containing the crystalline drug material, again suggesting entrapment or dispersion of drug material within the polymeric matrix.

As for formulations F3-F7 in **Figure 4.10**, the glass transition temperature for PLGA is observed, no sharp melting peak at around 160 °C is evident, indicating the drug is now embedded or encapsulated within the polymeric matrix, however the thermograms can be seen to continue rising beyond 200 °C, which is very different to formulations without metallic nanoparticles in **Figure 4.9**, therefore this may be due to the metals present within the formulation. From literature it has been established that the smaller the size of metallic nanoparticles, the lower the melting point; for silver particles nano in size the melting point is around 450 °C (Asoro et al, 2009, Luo et al, 2008). (Abdelrazek Khalil, 2013) published thermograms, of the raw polymer PLGA, electrospun PLGA and electrospun PLGA incorporated with AgNP, the data followed similar endothermic peak patterns to that of the raw PLGA, displaying the the capability of PLGA to encapsulate. DSC thermograms published by (Shams et al, 2018) showed similar results, for drug and polymer concentrations, to confirm interactions between drug and polymer used. Thermograms for F3-F7 and F10-F14 were similar, due to the concentration of materials used to make up the formulation being the same, with a higher concentration of polymer compared to the other excipients seen in **Table 4.1**.

The differences between solvents here are negligible, due to rapid evaporation at such high temperatures. The presence of metallic nanoparticles maybe the reason for the continued rise in the thermograms when compared to raw PLGA, successful encapsulation of drug within the polymeric matrix was shown as the melting peak for AMX at around 160°C was no longer present in the formulations with AMX present.

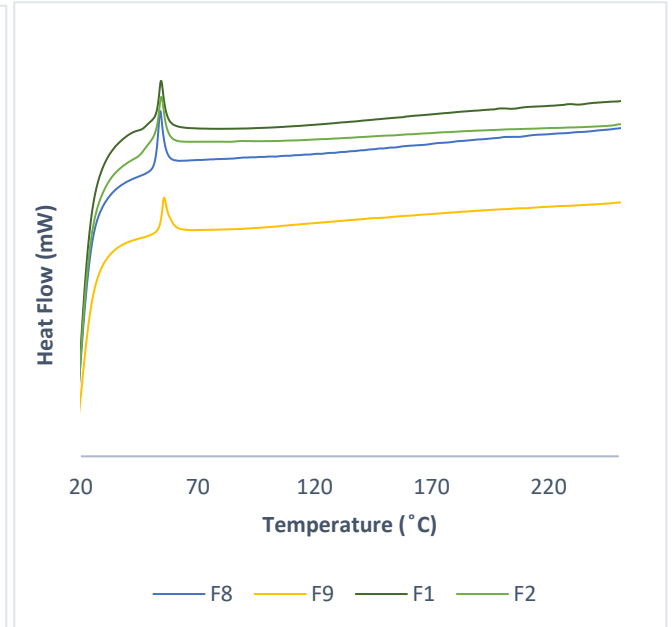
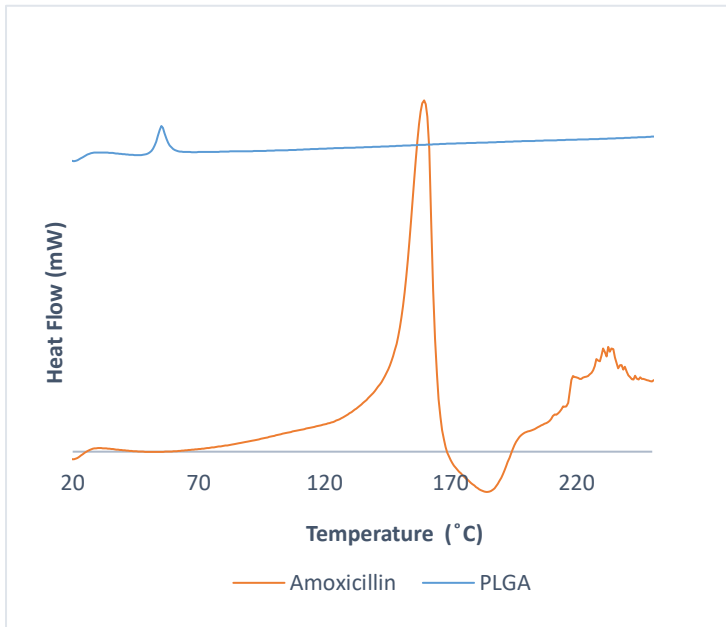


Figure 4. 8: DSC thermograms of raw material.

Figure 4. 9: DSC thermograms of formulations without metallic nanoparticles.

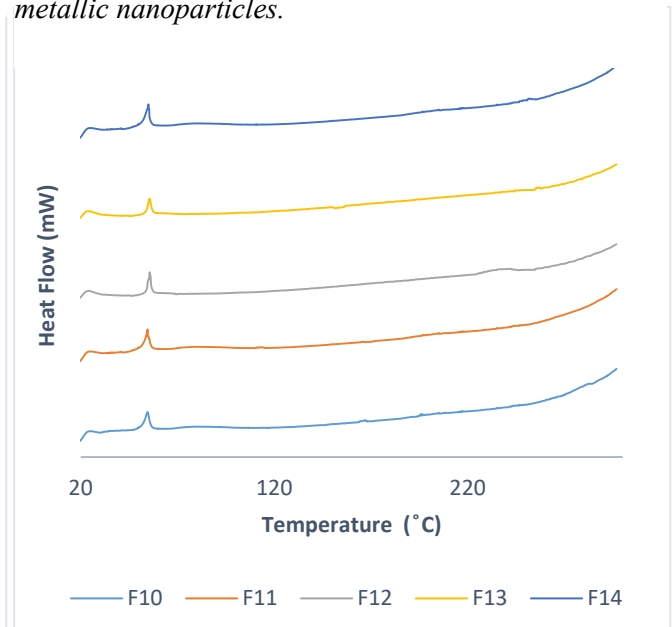
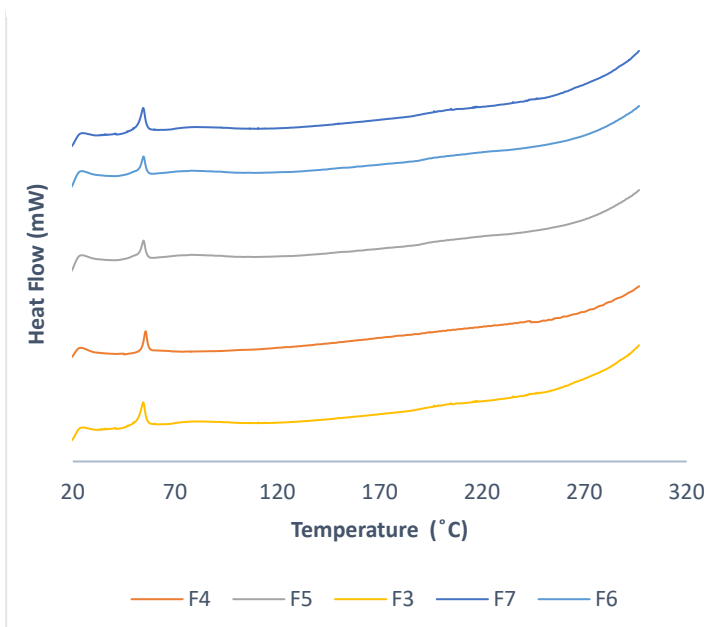


Figure 4. 11: DSC thermograms of formulations containing metallic nanoparticles in acetone.

Figure 4. 10: DSC thermograms of formulations containing metallic nanoparticles in DCM.

4.4.8 TGA

Figure 4.12 shows the TGA thermograms for the raw materials. The thermogram for PLGA shows a sharp endothermic weight loss peak from 242.4 °C to 412.6 °C between which around 96.1 % of weight is lost, the thermogram follows those found in previous literature (Silva et al, 2015). As for AMX two different phases of endothermic weight loss can be observed, the first begins at temperatures of 86.7 °C to 122.9 °C, may be due to water loss, where weight loss is around 10 %, the second phase is from 182.6 °C to 600 °C where the percentage weight lost is around 58 % attributed to degradation of material (Roy Biswas et al, 2014).

Figures 4.13 and 4.14 presenting the weight loss of all formulations F1-F14, display similar thermograms to that of PLGA in **Figure 4.12**, encapsulation of drug material within polymeric matrix has been successful through presence of a single endothermic weight loss peak. F1 shows a very similar weight loss thermogram to that of pure PLGA, whereas the following formulations to F7, start weight loss at slightly lower temperatures. This may be due to more interactions between polymer and excipients, as more drug particles may be present within the polymeric matrix. Moreover, F8 and F9, show more weight loss (%), when compared to the AMX weight loss thermogram, this also suggests the drug particles have become dispersed within the polymeric matrix. As AMX reduced to 29% weight loss overall, after reaching the maximum temperature, however all formulations fall below this value, similar to that of PLGA, again demonstrating encapsulation and dispersity of AMX within PLGA.

TGA data published by (Gomathi et al, 2014) showed curves for the raw polymer, drug alone and drug loaded polymeric particles, the characteristic endothermic peak for the drug particles was not observed when analysing the drug loaded polymeric particles, which confirmed the amorphous nature of the composite sample. Broadening of the exothermic peak area also indicates loading of drug in polymer, overall this increases the amorphous nature of the polymeric composites which is important as it increases the efficiency of drug delivery and gives better stability.

The presence of metallic nanoparticles, may have slightly varied the thermograms, as in **Figure 4.13**, formulations F4, F5 and F7 display slightly higher weight loss (%) plateaus when compared to PLGA alone. A similar trend is observed for F12 in **Figure 4.13**, both F5 and F12 contain the AgPs, which may have had an effect on the final peak position for weight loss.

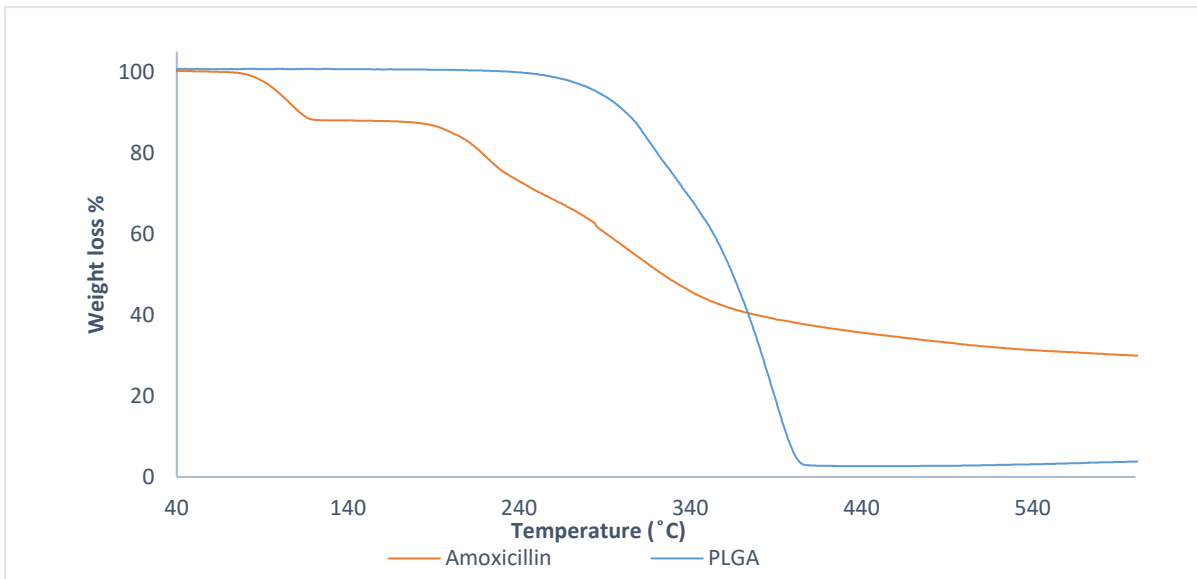


Figure 4.12: TGA thermograms showing weight loss of raw materials AMX and PLGA

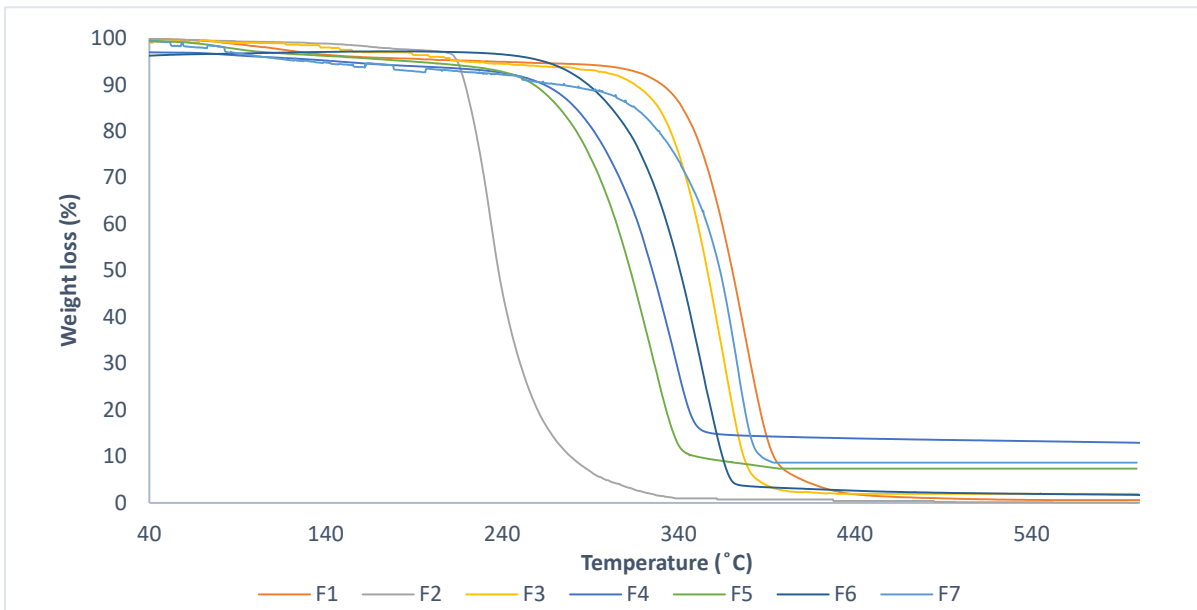


Figure 4.13: TGA thermograms showing weight loss of formulations F1-F7 in the solvent acetone.

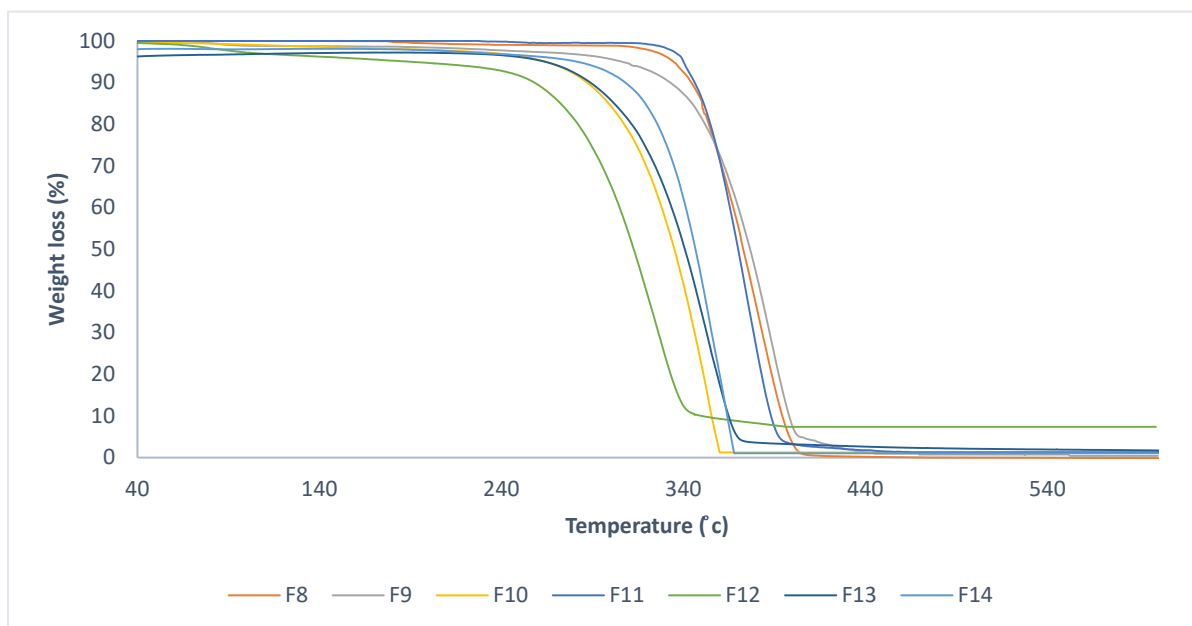


Figure 4. 14: TGA thermograms showing weight loss of formulations F8-F14 in the solvent DCM.

4.4.9 X-ray diffraction (XRD)

XRD spectra help us understand the properties of the raw materials (PLGA and AMX) as well as the interactions between these materials after electrospraying through diffractograms.

Figure 4.15 shows the diffractograms of the raw materials; pure AMX showed various intense peaks characteristic of the drug as it is crystalline (Awasthi et al, 2011), as for the polymer it is amorphous as previously known but confirmed through lack of peaks (Russo et al, 2016).

The absence of sharp peaks for the diffractograms of formulations F2-F7 and F9-F14 in **Figures 4.16** and **4.17** at the same 2θ values indicates an amorphous dispersion of the drug throughout the polymer. Vedha Hari et al, 2015, published diffractograms, of raw drug which showed crystallinity through numerous peaks, once introduced into the polymeric matrix peaks disappeared as drug has now become more amorphous, through reduction in particle size, this can lead to better dissolution and bioavailability in the body. Further evidence of drug polymer interactions shown through XRD diffractograms is published by (Vedha Hari et al, 2018) as peaks for polymer composite particles were no longer present compared to raw drug material.

Further evidence of drug polymer interactions is seen through intensity of broad peaks, formulations F1 and F8 display broad peaks with highest intensity between 2θ values of 15 and 22, when compared to F2 and F9 the intensity of the broad peak is lower, indicating interaction of the drug and polymer increasing the amorphous nature of the composites.

The introduction of metallic nanoparticles which themselves are highly crystalline had no real impact on the diffractograms, indicating metallic particles may be dispersed throughout the polymeric matrix. Although slight variations are observed, diffractogram for F3 in **Figure 4.16** shows a slight peak rise at 2θ of 38.78 (111), this is correlated with 2θ peak values of raw AgNPs in **Figure 3.7**, which may indicate complete encapsulation of metallic nanoparticles may not have been achieved. Similar differences can be observed for all formulations F3-F7 and F10-F14 as these composites contain metallic nanoparticles, which may indicate presence of metallic nanoparticles within the sample. Alexander S Pozdnyakov et al, 2016, synthesised polymeric composites containing silver nanoparticles, upon XRD analysis of the raw polymer and composites, small peaks appeared at the 2θ values characteristic of silver nanoparticles, at planes (111) and (200). Xiaoyi Xu et al, 2006, synthesised PLGA/AgNP composite nanofibers through electrospinning, XRD data showed at very high concentrations of AgNPs (32%), 2θ values characteristic of silver nanoparticles appear at all planes (111), (200), (220) and (300). At lower concentrations 8%, one of these peaks appear in the (111) plane similar to the peak

observed in **Figure 4.16**, the concentration of metallic nanoparticles used for formulations F3-F7 and F9-F14 was 5% of the polymer, hence why for some formulations small crystalline peaks did not appear and were not as sharp as those reported in literature.

Previous literature published supports results displayed, reduction in intensity of drug peaks and absence of sharp peaks, indicate interactions between drug and polymeric particles (Sun et al, 2015).

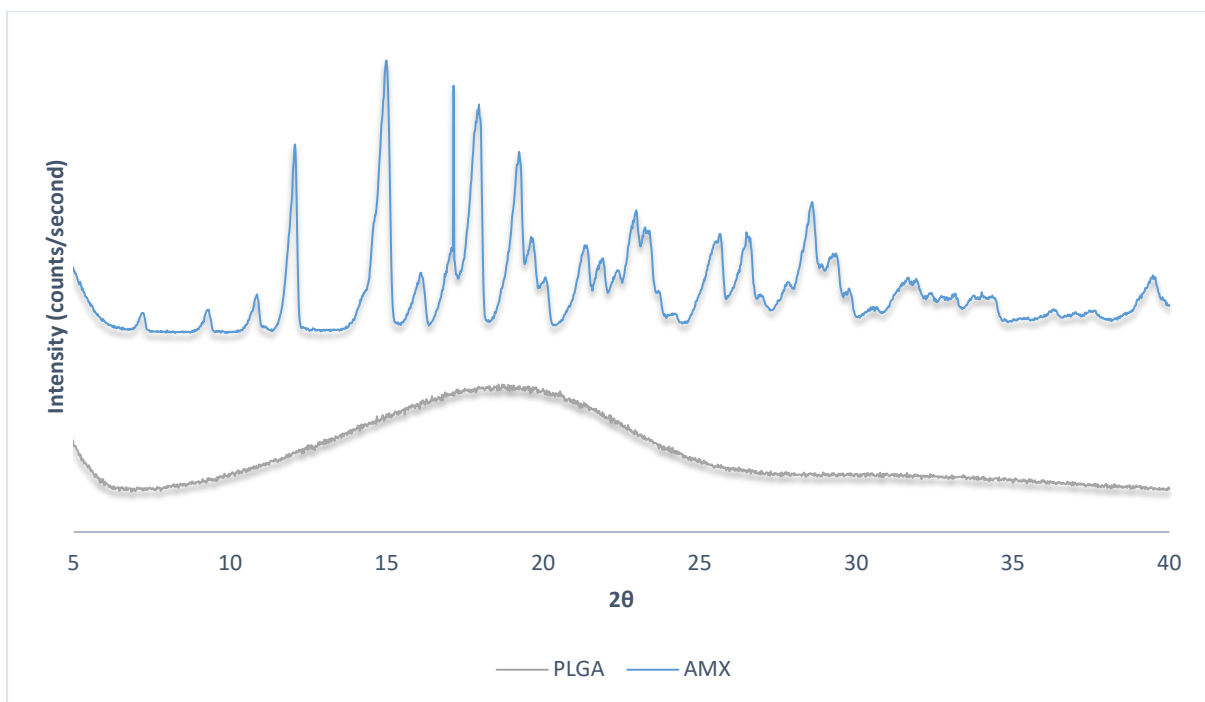


Figure 4. 15: XRD diffractograms of raw materials PLGA and AMX

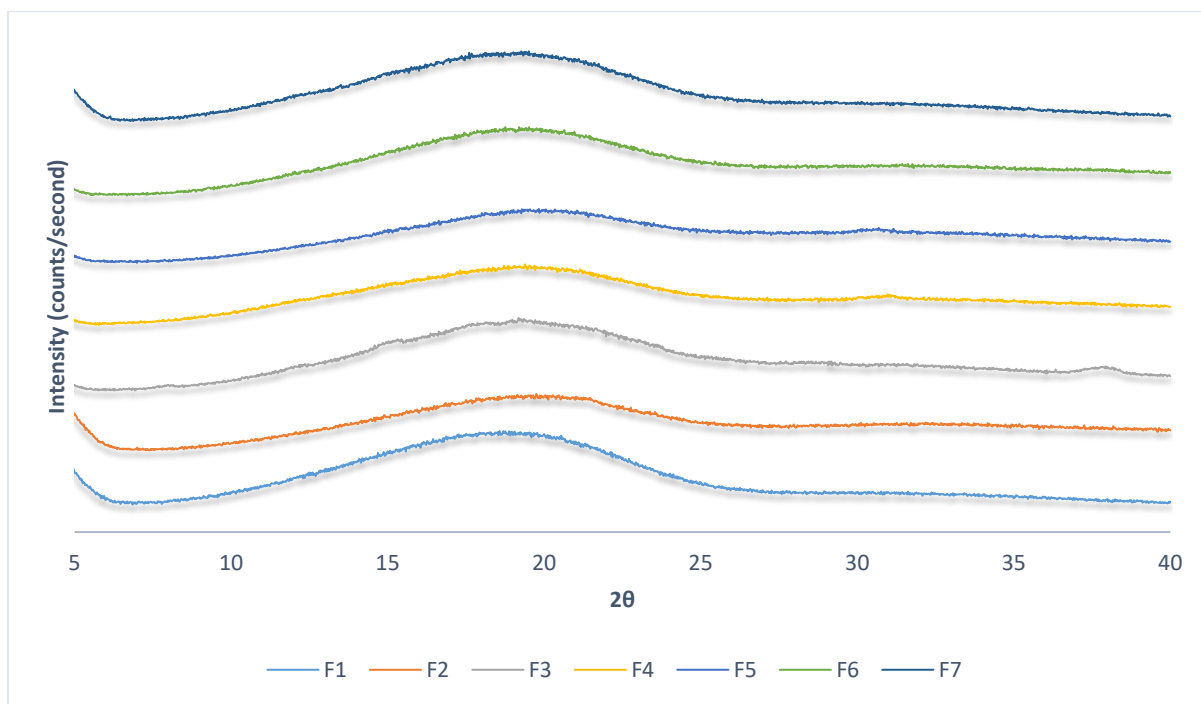


Figure 4. 16: XRD diffractograms of formulations F1-F7 in the solvent acetone.

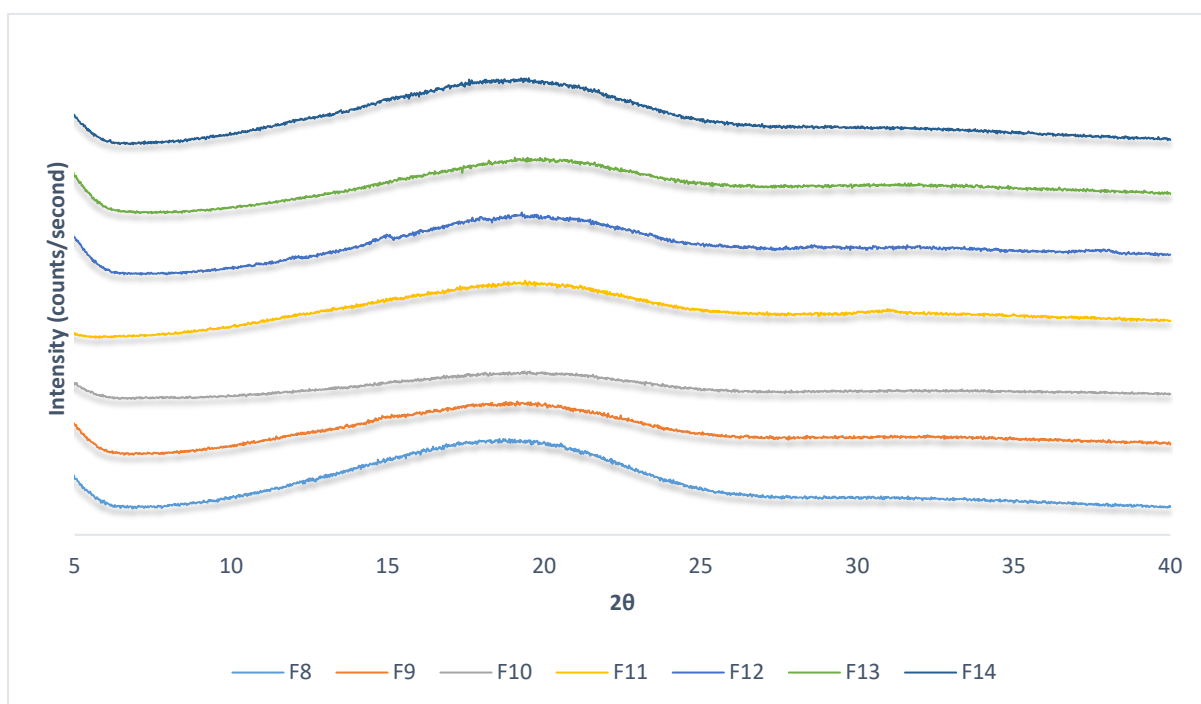


Figure 4. 17: XRD diffractograms of formulations F8-F14 in the solvent DCM.

4.4.10 Zeta potential values

Zeta potential (ζ) values give an indication of the surface charge of particles. The significance of zeta potential is that its value can be related to the short- and long-term stability of suspensions. Suspensions with high zeta potential (negative or positive) are electrically stabilized while suspensions with low zeta potentials tend to coagulate or flocculate, possibly leading to poor physical stability. In general, when the zeta potential of a suspension is high, the repulsive forces exceed the attractive forces, resulting in a relatively stable system.

For formulation F1 a zeta potential average value of -61.12 mV indicates excellent colloidal stability within suspensions, when compared to F8 with an average value of -18.90 mV the difference is quite high indicating the use of solvent may have had an effect on zeta potential values. The factors affecting zeta potential include the pH of the medium, ionic strength, the concentration of any additives, and temperature. The pH was maintained at 7.4 at the temperature set at 25 °C, the ionic strength may vary depending on the formulation analysed.

Therefore, differences in average zeta values may be due to concentration or nature of additives. The general trend observed shows the average zeta values for formulations F1-F7 were higher than F8-F14, this may be due to the use of solvent. Moreover, decrease in zeta potential values is observed with increase in excipients within the suspension, leading to lesser stability of particles. The difference in zeta potential values with addition of excipients may arise from adsorption of the added drug and metallic nanoparticles to the surface of the polymer resulting in increased thickness of the diffuse double layer and hence lowering zeta potential (Ali, 2014). Increase in concentration of suspension can lead to reduction of zeta potential values, as the metallic particles added vary in size and morphology this can lead to differences in suspension concentration therefore effecting zeta potential values (Giacomo Fontana et al, 2001).

F13 with an average zeta potential value of -2.72 mV indicates reduced stability, this may be due to the lesser zeta potential value of pure AuNPs, as shown in **Table 3.4**, due to increased agglomeration of synthesised nano-particles. F4 and F11 showed lower zeta potential values when compared to the other formulations containing silver particles, previous data has shown electrospaying of this formulation was difficult due to higher viscosity, this may have led to a reduced zeta potential value indicating lesser colloidal suspension stability.

Table 4. 3: Zeta potential values of F1.

Sample ID	Zeta Potential (mV)	Mobility (μ s)/(V/cm)	RMS Residual
F1	-51.41	-4.02	3.60E-02
F1	-64.09	-5.01	1.96E-02
F1	-67.87	-5.30	1.87E-02
Mean:	-61.12	-4.78	2.48E-02
Std Err:	4.98	0.39	5.62E-03
Std Dev:	8.62	0.67	9.73E-03

Table 4. 4: Zeta potential values of F2.

Sample ID	Zeta Potential (mV)	Mobility (μ s)/(V/cm)	RMS Residual
F2	36.85	2.88	5.22E-02
F2	36.45	2.85	3.08E-02
F2	40.56	3.17	1.69E-02
Mean:	37.95	2.97	3.33E-02
Std Err:	1.31	0.10	1.03E-02
Std Dev:	2.27	0.18	1.78E-02

Table 4. 5: Zeta potential values of F3.

Sample ID	Zeta Potential (mV)	Mobility (μ s)/(V/cm)	RMS Residual
F3	-35.03	-2.74	6.88E-02
F3	-43.15	-3.37	1.54E-02
F3	-43.68	-3.41	1.75E-02
Mean:	-40.62	-3.17	3.39E-02
Std Err:	2.80	0.22	1.75E-02
Std Dev:	4.85	0.38	3.03E-02

Table 4. 6: Zeta potential values of F4.

Sample ID	Zeta Potential (mV)	Mobility (μ s)/(V/cm)	RMS Residual
F4	-12.49	-0.98	2.83E-02
F4	-11.34	-0.89	1.67E-02
F4	-10.39	-0.81	2.25E-02
Mean:	-11.41	-0.89	2.25E-02
Std Err:	0.61	0.05	3.35E-03
Std Dev:	1.05	0.08	5.81E-03

Table 4. 7: Zeta potential values of F5.

Sample ID	Zeta Potential (mV)	Mobility (μ s)/(V/cm)	RMS Residual
F5	-35.49	-2.77	2.43E-02
F5	-36.28	-2.84	2.19E-02
F5	-38.16	-2.98	3.90E-02
Mean:	-36.65	-2.86	2.84E-02
Std Err:	0.79	0.06	5.34E-03
Std Dev:	1.37	0.11	9.24E-03

Table 4. 8: Zeta potential values of F6.

Sample ID	Zeta Potential (mV)	Mobility (μ s)/(V/cm)	RMS Residual
F6	-21.22	-1.74	1.93E-02
F6	-19.73	-1.54	2.07E-02
F6	-21.62	-1.77	2.22E-02
Mean:	-20.86	-1.68	2.07E-02
Std Err:	0.90	0.07	8.16E-04
Std Dev:	1.57	0.12	1.41E-03

Table 4. 9: Zeta potential values of F7.

Sample ID	Zeta Potential (mV)	Mobility ($\mu/s)/(V/cm)$	RMS Residual
F7	-22.51	-1.76	2.16E-02
F7	-17.30	-1.35	3.72E-02
F7	-23.34	-1.82	1.90E-02
Mean:	-21.05	-1.64	2.59E-02
Std Err:	1.89	0.15	5.69E-03
Std Dev:	3.27	0.26	9.86E-03

Table 4. 10: Zeta potential values of F8.

Sample ID	Zeta Potential (mV)	Mobility ($\mu/s)/(V/cm)$	RMS Residual
F8	-20.54	-1.60	2.57E-02
F8	-18.95	-1.48	1.49E-02
F8	-17.23	-1.35	2.61E-02
Mean:	-18.90	-1.48	2.22E-02
Std Err:	0.96	0.07	3.65E-03
Std Dev:	1.65	0.13	6.32E-03

Table 4. 11: Zeta potential values of F9.

Sample ID	Zeta Potential (mV)	Mobility ($\mu/s)/(V/cm)$	RMS Residual
F9	-18.20	-1.42	2.51E-02
F9	-16.36	-1.28	1.48E-02
F9	-18.93	-1.48	2.02E-02
Mean:	-17.83	-1.39	2.00E-02
Std Err:	0.76	0.06	2.97E-03
Std Dev:	1.32	0.10	5.14E-03

Table 4. 12: Zeta potential values of F10.

Sample ID	Zeta Potential (mV)	Mobility ($\mu/s)/(V/cm)$	RMS Residual
F10	-17.70	-1.38	2.91E-02
F10	-11.89	-0.93	2.10E-02
F10	-13.41	-1.05	2.79E-02
Mean:	-14.33	-1.12	2.60E-02
Std Err:	1.74	0.14	2.53E-03
Std Dev:	3.01	0.24	4.39E-03

Table 4. 13: Zeta potential values of F11.

Sample ID	Zeta Potential (mV)	Mobility ($\mu/s)/(V/cm)$	RMS Residual
F11	-11.34	-0.89	3.44E-02
F11	-11.66	-0.91	2.63E-02
F11	-11.56	-0.90	2.04E-02
Mean:	-11.52	-0.90	2.71E-02
Std Err:	0.09	0.01	4.06E-03
Std Dev:	0.16	0.01	7.03E-03

Table 4. 14: Zeta potential values of F12.

Sample ID	Zeta Potential (mV)	Mobility ($\mu/s)/(V/cm)$	RMS Residual
F12	-14.18	-1.11	2.37E-02
F12	-12.68	-0.99	2.94E-02
F12	-11.25	-0.88	6.39E-02
Mean:	-12.70	-0.99	3.90E-02
Std Err:	0.84	0.07	1.26E-02
Std Dev:	1.46	0.11	2.17E-02

Table 4. 15: Zeta potential values of F13.

Sample ID	Zeta Potential (mV)	Mobility ($\mu\text{s}/(\text{V}/\text{cm})$)	RMS Residual
F13	-3.67	-0.29	2.03E-02
F13	-3.24	-0.25	1.56E-02
F13	-1.24	-0.10	9.96E-03
Mean:	-2.72	-0.21	1.53E-02
Std Err:	0.75	0.06	3.00E-03
Std Dev:	1.30	0.10	5.19E-03

Table 4. 16: Zeta potential values of F14.

Sample ID	Zeta Potential (mV)	Mobility ($\mu\text{s}/(\text{V}/\text{cm})$)	RMS Residual
F14	-9.46	-0.74	1.80E-02
F14	-13.05	-1.02	3.91E-02
F14	-12.51	-0.98	2.46E-02
Mean:	-11.67	-0.91	2.73E-02
Std Err:	1.12	0.09	6.23E-03
Std Dev:	1.93	0.15	1.08E-02

4.5 Conclusion

In this chapter development of micro and nano particles made up of PLGA composites, which contained AMX and metallic nanoparticles was attempted through the EHDA process. Results obtained show the use of electrospaying to develop these microspheres was successful. SEM results displayed particles varying in morphology and size, but the key was to have successfully encapsulated the insoluble AMX drug particles. This was observed through presence of small charged particles embedded upon polymeric surface and within the matrix, as polymeric particles appeared charged themselves. Furthermore, metallic nanoparticles were successfully electrospayed, and were surrounded by polymeric composite particles, as seen in **Figures 4.4Hi and Ii**. Here silver nanowires were present submerged in polymeric composite particles. Literature did show however TEM analysis would better confirm the presence of metallic compounds.

EDS analysis was also used and confirmed, for each formulation the metallic compound present, including the differentiation between the solvent choice DCM and acetone. ATR-FTIR in **Figures 4.5 to 4.7** was then used to confirm interactions between PLGA and AMX, the variations in peak intensities and positions confirmed possible dispersion of AMX within PLGA. However, with the addition of metallic nanoparticles the spectrums did not show ample variation, this may have been due to the small concentration of metallic nanoparticles present, when compared to the concentration of PLGA. This could also be due to the use of EHDA process, as data from literature obtained when using the EHDA process to synthesise polymeric metallic nanocomposites, there were no variations between FTIR spectrums, aside from intensity of peaks.

Beyond this DSC analysis **Figures 4.8-4.11** confirmed the encapsulation of the drug AMX, as the endothermic melting peak for AMX no longer appeared on any of the electrospayed formulations. The presence of metallic nanoparticles may have been confirmed through the continued rise of the thermograms, as they exhibit melting points above 400 °C. TGA analysis **Figures 4.12-4.14** further confirmed the encapsulation and dispersion of the drug, AMX displayed two characteristic weight loss peaks, however the electrospayed formulations displayed a single weight loss peak at similar temperatures to PLGA. XRD data **Figures 4.15-4.17** was collected to indicate the crystalline or amorphous nature of AMX and PLGA, as well as describing the nature of the electrospayed formulations. As the electrospayed diffractograms now appeared amorphous, AMX had successfully been dispersed throughout the polymeric matrix. The presence of metallic nanoparticles did cause slight rises in the

diffractograms at the preferred plane of growth for each metallic particle, however this was not as clear due to the low concentration of metallic nanoparticles used. Zeta potential data in **Tables 4.4-4.15** gave an indication of the colloidal stability of the polymeric composites. Results showed an increase in number of excipients reduced the overall stability, metallic nanoparticles which tend to aggregate also reduced the zeta potential value. This was evident for AuNPs, which tend to agglomerate, hence why zeta potential value was much lower when compared to the other formulations.

Chapter 5 - Drug release kinetics, microbiological testing and cell culture studies

5.1 Introduction

5.1.1 Antibacterial agents

An antibacterial agent is a chemically enhanced natural substance with the potential to kill (bactericidal effect) or slow down the growth or multiplication (bacteriostatic effect) of a bacterial organism without affecting the host functions. Almost all of the different antibiotics available currently on the market are based on the structure of antibacterial agents naturally found in environmental microorganisms; with many of these antibiotics being synthetic derivatives of these discovered microorganisms.

5.1.2 Antibiotic resistance

Bacterial resistance itself can be acquired or inherent (characteristic of all species of that isolate), an example of inherent resistance is the resistance of *Pseudomonas aeruginosa* to a wide range of antibiotics, acquired bacterial resistance is where bacteria gain the genes encoding resistance, through a mutation or due to the transfer of genetic material from other bacteria. Mutations cause changes to the gene target of the antibiotic, causing it to no longer have an effect on the targeted bacteria.

The overuse and misuse of antibacterial agents has led to the emergence of antibiotic resistant genes (ARGs), which further reduce the therapeutic effect of an antimicrobial agent, and renders it ineffective. Some examples include the resistance of all gram-positive organisms to colistin, and the resistance of *Enterobacteriaceae* to glycopeptides and linezolid. The rise in bacterial resistance is also attributed to the insufficient understanding of the numerous bacteria and their antimicrobial susceptibility patterns, for patients with bacterial infections this poses a risk, as knowledge of bacteria is deficient, to counter this the overuse and misuse of broad spectrum antibacterial occurs. At present numerous antimicrobial agents are being synthesised through use of differing technologies, which offer a substitute to those currently available in drug therapy.

Development of nanotechnology has unlocked many avenues of further research into applications of nanoparticles. Increased efficiency and methods of manufacturing nanoparticles has also broadened the type of nanoparticles available. One such method is using composite

nano/micro particles in the transport of antibiotics. Of the many metallic nanoparticles available silver has shown strong antimicrobial and cytotoxic effects on the body, the physiochemical properties of silver such as shape, size and concentration can affect toxicity.

5.2 Aims & Objectives

Upon successful synthesis and characterisation of (nano/micro) polymeric composite particles, it was found that formulations containing acetone and DCM had similar results. However, formulations F8-F14 (DCM formulations) showed unstable morphology and large particle size distribution, in comparison to F1-F7, therefore were excluded from this chapter; furthermore, characterisation results from previous chapters showed the difference in solvents were negligible hence why F8-F14 were not used. Instead the focus for this chapter was on the effect different types of metallic nanoparticles have on drug release and antibacterial efficacy, as well as investigating differences in results generated through morphology variation.

In this chapter, the polymeric composites synthesised in the previous chapter were assessed for their drug loading, encapsulation efficiency, drug release data, bacterial efficacy and cell viability capabilities. Experimentally for this in-vitro drug release, bacterial disk diffusion tests, optical density kinetic reads and MTT assays were carried out.

5.3 Materials and methods

5.3.1 Materials

Amoxicillin with a potency ≥ 900 μg per mg, phosphate buffer saline (PBS) and DCM were used along with full formulations F2-F7. Mueller Hinton Agar grown and sterilised in-house. Gram-negative *E. coli* NCTC 13919 and a gram-positive *S. aureus* NCTC 12497 were purchased from Public Health England (UK). PBS was used as the vehicle for drug release kinetics, and also as a control in antibacterial testing. Whatman 1822-047 GF/C glass microfiber filters for disc diffusion.

Lymphoblastoid cells from the TK6 line, normal horse serum used for media with added L-glutamine, 3-[4, 5dimethylthiazol-2-yl]-2, 5diphenyltetrazolium bromide (MTT) reagent with stock concentration of 5 $\mu\text{L}/\text{mL}$, as well as dimethyl sulfoxide (DMSO) were all purchased from Sigma-Aldrich. All formulations were tested as well as the individual metallic nanoparticles at (AgNP, AgNW, AgP, AuNP and CuNP) 1 mg/mL stock; polymer PLGA and antibiotic AMX (P-Ab) at 1 mg/mL stock and metallic drug polymer composites (metal-P-Ab) at 1mg/mL. Hydrogen peroxide was used as a positive control, and just the cells as the negative control.

5.3.2 Methods

5.3.2.1 UV-vis and calibration curve

The UV-vis spectrum of AMX was plotted using a UV-vis spectrophotometer (Evolution 60S Thermo Scientific), the curve determines the maximum wavelength, this value was then used as the reference to calculate absorbance values.

For calibration curve of AMX, a stock solution of 5 mg AMX dissolved in fresh PBS at pH 7.4 was prepared. The stock solution was used to create a calibration curve with concentrations ranging from 12.5 $\mu\text{g}/\text{mL}$ to 125 $\mu\text{g}/\text{mL}$.

5.3.2.2 Drug content and encapsulation efficiency

Electrosprayed coatings 10 mg were weighed and dissolved in 1 mL DCM, and 2.5 mL PBS was added. The mixture was vortexed at 2500 rpm for 1 minute then centrifuged at 6000 rpm for a further 30 minutes. After centrifugation the supernatant was collected and analysed through a UV-vis spectrophotometer (Evolution 60S Thermo Scientific). Drug content (%) was

determined using the calibration curve of AMX. Equations used to calculate drug content and thereafter encapsulation efficiency (EE%) are shown (Xu et al, 2008).

Drug content in PLGA (%) = (weight of drug in microspheres/weight of microspheres) *100

Equation 5. 1: Formula for drug content percentage.

EE% = (actual drug encapsulated/theoretical drug encapsulated) *100

Equation 5. 2: Equation for encapsulation efficiency.

5.3.2.3 In-vitro drug release

Profiles of drug released from the formulations over 24 hours were plotted. 5 mg samples of the electrosprayed formulations were placed in eppendorfs containing 2 mL of PBS. This was followed for all formulations F2-F7. These eppendorfs were placed in a water bath at a temperature of 37 °C, mimicking that of the human body, at specific time points 1 min, 10 min, 30 min, 1 hour, 2 hours, 4 hours, 8 hours and 24 hours, 1.5 mL of sample was removed after centrifugation, making sure no particle aggregates were taken up. Drug release was quantified through the use of a UV-vis spectrophotometer (Evolution 60S Thermo Scientific) ($\lambda=229$). Experiments were carried out in triplicate for all formulations.

5.3.2.4 Bacterial testing

All investigations were carried out in triplicate on at least two separate occasions.

The antibacterial activities of the metallic nanoparticles and the full formulations was investigated using *E. Coli* (NCTC13919) resistant to penicillin and methicillin resistant *S. Aureus* (NCTC12497); these were used as models for gram-negative and gram-positive bacteria respectively. Bacteria strains were stored in Luria Bertani broth at -80°C; bacteria were then cultured in nutrient broth (NB) at 37 °C for 24 hours.

5.3.2.5 Disc diffusion

A disc diffusion method was used to determine the antibacterial activity of multi shaped silver nanomaterials, as well as gold and copper particles. The EUCAST standardised method was followed, as the zone diameter breakpoints are calibrated to the streamlined European MIC breakpoints. In order to produce reliable results, no changes were made to the method.

In brief, of overnight cultures (100 μ L) of *E. coli* and *S. aureus* were spread-plated on to nutrient agar (NA), a 6 mm paper disc was then impregnated with varying amounts (5 μ L and 10 μ L) of multi shaped silver nanoparticles, spherical shaped gold and copper nanoparticles. The metallic nanoparticles were dispersed in PBS at a concentration of 125 μ g/mL. The plates were then incubated at 37 °C for 24 hours. The efficacy of the metallic particles was determined through measurements of the zones of inhibition formed upon the agar plate surrounding the paper discs. The larger the zones, the more efficacy the nanoparticles showed.

For the full formulations, F2-F7, the efficacy was determined using similar methods. Overnight cultures of (100 μ L) of *E. coli* and *S. aureus* were spread-plated on to NA, a 2 cm paper disc was then impregnated with varying amounts (15 μ L and 30 μ L) of the formulations. To prepare the formulations, 20 mg of each of the formulations were placed in 2 mL freshly prepared PBS, these were then left in a 37 °C water bath over 24 hours. This allowed for release of drug and leaching of metallic ions into the liquid, this supernatant was then added in varying amounts to compare the antibacterial efficacy between formulations.

5.3.2.6 Scanning electron microscope (SEM)/ Energy dispersive spectroscopy (EDS)

SEM analysis was carried out on samples from the disc diffusion results. The samples used were from the metallic nanoparticle disc diffusion results, specifically the AgNP and AgP agar plates. Samples were prepared by cutting out 10 mm from the agar plate, and setting upon a metallic stub which was stored at 4 °C before analysis. The agar plates used all contained the bacteria *S. aureus*. The images were analysed at varying magnifications, and using both the normal scanning electron mode, as well as the secondary back scatter mode.

5.3.2.7 Growth kinetic curves (Optical Density (OD600))

The growth curves of *E. coli* and *S. aureus* in the presence of different volumes of metallic nanoparticles, and formulations F2-F7 was determined using optical density. To investigate the

growth kinetic curves of bacterial cells, varying volumes of metallic nanoparticles (5 μL and 10 μL) at a concentration of 125 $\mu\text{g}/\text{mL}$ were added, to 96-well plate cells containing aliquots of 100 μl of *E. coli* and *S. aureus*. Optical densities (OD) were measured every hour (from 0 to 24 hour) at 600 nm using a spectrophotometer (Spectra Max Plus 384). As for the formulations, preparation was carried out using the method stated previously, volumes of (15 μL and 30 μL) were added to 96-well plate cells containing aliquots of 100 μl of *E. coli* and *S. aureus* and the optical density values recorded over 24 hours, to determine the bacterial growth curve. Control wells contained bacteria only.

5.3.2.8 Ex-vivo cell culture studies (MTT assay)

For all cell culture studies target cell count was 40,000 for each well. The initial cell count of the culture was averaged at 102.5 via hemocytometry. Total cell count was 1×10^6 cells. To achieve 40,000 cells in each well for 50 wells a dilution factor of 5 was calculated. This required 2 mL of cells and 8 mL of media. Once prepared 200 μL of mixture was pipetted in to each well and the plate was incubated at 37 $^{\circ}\text{C}$ for 24 hours (5 % CO_2).

24 hours after incubation, 100 μL was removed out of each well and then 100 μL of MTT reagent at a concentration of 2 $\mu\text{L}/\text{mL}$ was pipetted into each well and the plate was incubated at 37 $^{\circ}\text{C}$ for 3 hours. Afterwards 150 μL of DMSO was added and then the plate was incubated at 37 $^{\circ}\text{C}$ for 2 hours. Once finished the absorbance values were read. From these values the cell viability was calculated for each formulation synthesised using the following formula:

$$\% \text{ viable} = \frac{\text{absorbance}_{\text{sample}} - \text{absorbance}_{\text{blank}}}{\text{absorbance}_{\text{control}} - \text{absorbance}_{\text{blank}}} \times 100$$

Equation 5. 3: Percentage cell viability calculation.

5.4 Results and Discussion

5.4.1 UV-vis and calibration curve

The UV-vis curve plotted in **Figure 5.1**, displays the λ_{max} at a wavelength of 229 nm, plotted using the most concentrated solution (125 $\mu\text{g/mL}$), correlating with previous literature for AMX (Chaturvedi and Chitlange, 2011). The calibration curve (**Figure 5.2**) was obtained by measuring absorbance values of AMX solutions in PBS, varying in concentration from 12.5 $\mu\text{g/mL}$ to 125 $\mu\text{g/mL}$. The solutions were measured, through UV-vis spectrophotometer at a fixed wavelength of 229 nm. Absorbance values were plotted against concentration, giving a calibration curve, with an (R^2) coefficient of 0.9975 indicating good linearity.

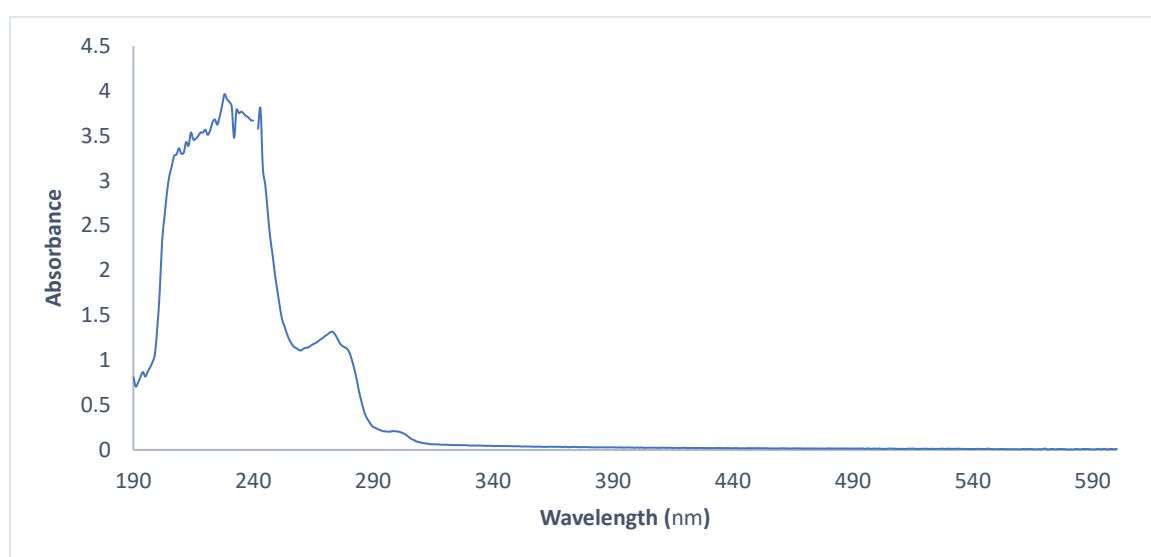


Figure 5. 1: UV-vis curve of AMX.

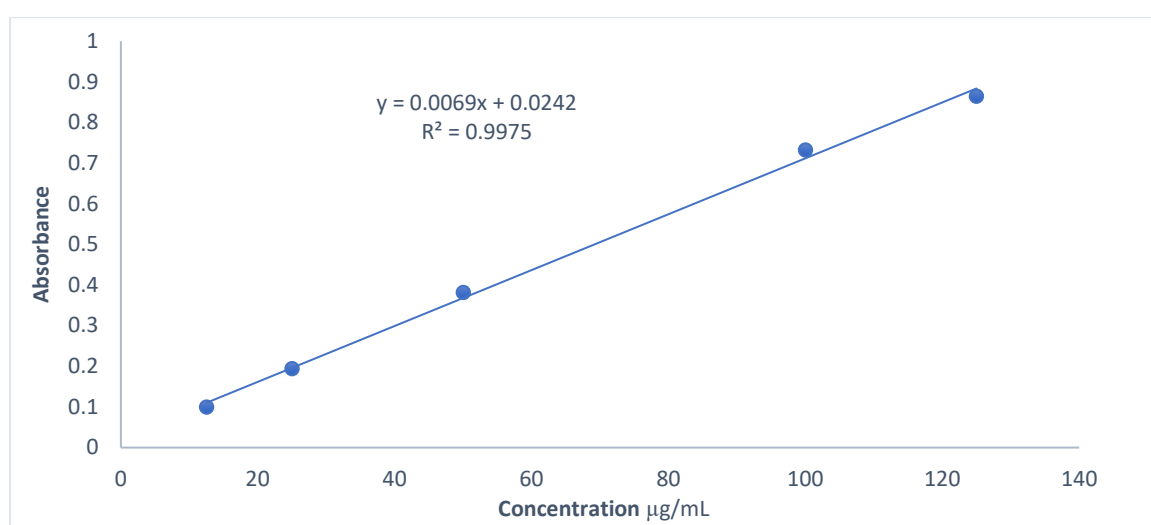


Figure 5. 2: Calibration curve of AMX from 12.5 $\mu\text{g/mL}$ to 125 $\mu\text{g/mL}$.

5.4.2 Drug content/encapsulation efficiency and drug release curve

Table 5.1 shows the drug loading (%) and EE% of the formulations. For F2 drug loading at 1.18 %, is very low, but expected as the drug is insoluble, with an EE% of 24.89 %, also lower than previously found literature, this may be due to the struggles found in electrospraying suspensions (Xu et al, 2008). Furthermore, (Sousa et al, 2010) synthesised AMX loaded PLGA microspheres using DCM, results from the study displayed similar drug loading and encapsulation values, as drug was insoluble so values remained low.

Previous data has studied the release from biodegradable polymer PLGA; data has shown PLGA is better used for sustained delivery of antimicrobial agents. Grayson et al, 2005, showed degradation of PLGA (Mw 24-38000) occurs best at 37°C, over a number of days. For sustained drug delivery, drug is released at a predetermined rate over a longer period of time. Traditional drug delivery methods are where the drug is circulated throughout the body, however in sustained drug delivery, drug is released mostly at the site of infection. Which can lead to an increase in therapeutic index as well as therapeutic efficacy (Prasanna and Venkatasubbu, 2018).

From **Figure 5.3** the release from F2 over 24 hours was very low compared to the other formulations, around 18% of drug was released over this period of time, correlating with previous literature. Zhang et al, 2018, electrospun PLGA and AMX fibres, at varying concentrations, for 5% PLGA AMX release data showed around 48% of drug was released from the polymeric fibres after 24 hours, this difference may be due to AMX forming a solution before electrospinning, hence more of the drug was encapsulated, however for F2, AMX was insoluble and therefore lower drug release was expected. Furthermore, PLGA is a hydrophobic polymer, and AMX is hydrophilic, as the drug was embedded and encapsulated within the polymer, this may have led to lower release of drug from the polymer and no burst release when compared to more hydrophilic polymers. Zheng et al, 2013, synthesised a 1% PLGA/AMX formulation, using electrospinning to generate fibres, release studies showed after 24 hours around 36% of AMX was released, however after 10 days 90% of AMX was released, hence showing PLGA is better for sustained release.

For formulations F3-F5 in **Table 5.1** the drug loading and EE% increased to 41%, 48% and 54% respectively, the reasons for this may be due to the presence of metallic nanoparticles, F4 and F5 were higher than F3 these formulations contained shaped metallic nanoparticles, which may have caused more degradation of polymer through scission, hence increasing the amount

of free drug particles in the supernatant. Chae and Kim, 2005, tested the effects of zinc oxide nanoparticles on polyacrylonitrile; results showed with increased amounts of zinc oxide the structure of the polymer weakened and toughness dramatically reduced. Weaker polymeric chains may have caused more release of drug particles into the surrounding environment. Furthermore, Gasaymeh, 2010, synthesised Ag/PVP composite particles and described chain scission of the polymer, as well as showed cross linking by the silver particles present improved optical properties.

Another reason for increased drug loading and EE% may be due to increased surface area. Particle size and morphology have an effect on drug release, the smaller the particles (nano-size) the larger the surface area to volume ratio, therefore enhancing drug content release (Rampersaud et al, 2016).

In the presence of metallic nanoparticles surface area to volume ratio increases, therefore more drug particles are present within the polymeric matrix, hence leading to higher loading and encapsulation. Moreover, the shapes of the nanoparticles vary, between spherical, polygonal and wire shaped silver. The surface area: volume ratio of a 100 nm sphere can be calculated using:

$$\text{Surface area} = 4 \times \pi \times \text{radius}^2 \qquad \text{SA} = 3.14 \times 10^5 \text{ nm}^2$$

Equation 5. 4: Equation for surface area of a sphere.

$$\text{Volume} = \frac{4}{3} \times \pi \times \text{radius}^3 \qquad \text{V} = 5.24 \times 10^6 \text{ nm}^3$$

Equation 5. 5: Equation for volume of a sphere.

$$\text{Surface area: volume} = 0.06$$

A polygonal shaped silver nanoparticle with varying sides, for this we assume the shape is more hexagonal as oppose to spherical. Working out the surface area: volume ratio of a 100 nm hexagonal particle using the equation below.

$$a = \text{edge length} = 33.33 \text{ nm} \quad b = \text{width} = 100 \text{ nm}$$

$$\text{Surface area} = 2\sqrt{3} * (3 + \sqrt{5}) * a^2 \quad \text{SA} = 2.02 \times 10^5 \text{ nm}^2$$

Equation 5. 6: Equation for surface area of a hexagonal particle.

$$V = 6 a^3 \quad V = 2.22 \times 10^6 \text{ nm}^3$$

Equation 5. 7: Equation for volume of a hexagonal particle.

$$\text{Surface area: volume} = 0.09$$

From the surface area: volume results, a hexagonal shape has almost a 50% increase in SA: V ratio than a sphere does. The surface area of the hexagonal shaped nanoparticles may be lower, but a higher surface area to volume ratio has shown that although a lower surface may affect rate of interaction, the ability to increase number of particles because of a smaller volume taken by each nanoparticle increases overall reactivity within the system. From this increased surface area of F5, drug content may also increase.

F4 contains nanowires; the increase in surface area again causes an increase in drug loading compared to spherical particles, the geometry of the wire shaped nanoparticles improves fluid mechanics, due to a smaller drag force and a higher surface area contact. The increased surface area contact can allow for more drug loading upon the nanowires, hence leading to higher values. Data published by (Loverde et al, 2011) analysed the differences between spheres and elongated worm like structures, similar to nanowires and found the worm like structures to increase the amount of drug delivered to target tumour sites; this is through the increased surface area as well as better movement through the blood stream within the body.

Drug release data presented in **Figure 5.3** for F3 shows a higher release of drug over the 24-hour time period, initially a burst release of drug was observed as after 60 minutes 29% of drug

had been released, beyond this the release steadied and after 24 hours around 34% of drug had released almost double the amount of drug release from F2. As for F4 the drug released was higher, an initial burst release showed after 60 minutes 38% of drug was released, and at 24 hours the release was at 41%. For F5 the release rate was the highest over the 24-hour time period, an initial burst release of 45% of drug released at 60 minutes, beyond this the drug release curve continued rising to 56% after 24 hours. The reason for continued rise, oppose to formulations F3 and F4 may be due to continued breakdown of the polymeric chains, or the increased amount of drug present as shown in **Table 5.1** for drug loading values. Moreover, as shown, drug release using PLGA occurs over many days, and will continue rising. Sofokleous et al, 2013, synthesised electropun PLGA AMX fibres for wound dressings, release data in PBS showed around 50% of drug was released after 21 days.

The release profiles for formulations F3-F5 in **Figure 5.3** shows a much higher release this can be attributed to the release of silver ions, as well as aiding and enhancing the degradation of the polymer, which further increases release rate of drug, this can be attributed as the reason for the initial burst release, and overall higher release of drug compared to F2. Long et al, 2017, published findings showing release of silver ions from AgNP; AgNP synthesised through differing methods, were all submerged in a 37 °C incubator. Results showed AgNP synthesised using the citrate reduction method released the most ions over 24 hours. This release of ions may have led to more break up within the polymeric chain, hence releasing more AMX. Liu and Hurt, 2010, prepared citrate reduced AgNP; data showed the release of silver ions occurs best at 37 °C, when compared to 4 °C and 20 °C, suggesting the metallic nanoparticles have become dispersed and embedded within the polymeric matrix. (Fortunati et al, 2011) synthesised PLGA/silver composites and explained release of ions can cause degradation of polymer through scission, at 37°C, the polymer is degrading causing the release of ions, as degradation increases AgNP becomes exposed, leading to the oxidation and increased ion formation. Alimohammadi et al, 2012, synthesised PLGA AMX composites coated with magnetic nanoparticles, data shows the release in PBS after 24 hours to be less than 60%. Increasing the hydrophilicity of the polymer however increased drug release to over 70%. The variation in shape and size had an impact on the drug released, particles with higher surface area: volume ratio led to increased amount of drug released. Steckiewicz et al, 2019, synthesised three different shapes of AuNPs, spheres, stars and rods which were synthesised using reduction method, results obtained show the shape of the particles had an impact on cell viability results, out of the three shapes star shaped AuNP exhibited the highest anti-cancer

potential but also was the most toxic. Li et al, 2012, synthesised five different multi-shaped nanoparticles and incorporated them into polyethylene forming nanocomposites, it was found that the octahedron shaped nanoparticles (2 nm) had the greatest interaction with the polymeric matrix, and decreased polymeric entanglement, through dispersion within the chains.

For F5 the shape of metallic nanoparticles, shown in **Figure 3.2Ci**, shows particles are no longer spherical, particles have sides and edges, this may have led to more contact with polymer oppose to spherical nanoparticles, increasing the breakdown of polymer enhancing the release of AMX. Rampersaud et al, 2016, synthesised spherical and caged shape iron oxide nanoparticles to determine whether shape has an effect on drug release; they found the shape of nanoparticles has a significant impact on drug release as well as efficacy, as drug release of cage shaped nanoparticle was three times higher than its spherical counterpart.

From **Table 5.1**, formulations F6 and F7 had similar encapsulation values at 33.03% and 33.43%, higher than F2 again this can be described by an increase in surface area: volume ratio overall, moreover, the presence of metallic particles within the polymer can reduce the interlinking between polymeric chains, allowing for more free drug particles, increasing drug loading and EE%. Wang et al, 2016, synthesised gold nanoparticles through citrate reduction, and stabilised them within PLGA matrix, furthermore, (Alkilany et al, 2018) encapsulated citrate reduced PLGA-GNPs composites into PLGA nanocarriers achieving a remarkable 100% encapsulation. Therefore, it seems AuNPs disperse better within the polymeric matrix, forming more stable composite particles, this was observed in **Figure 4.1F**, as the suspension formed showed good dispersion of AuNP throughout the formulation. This may have led to better encapsulation of AuNP in the polymeric matrix, this then can be observed through the drug release curve (**Figure 5.3**) for F6 as after 60 minutes only around 18% of drug had been released, no burst release was observed and after 24 hours drug release was at 24%. The increase in drug loading and encapsulation, therefore can be attributed to higher presence of AuNPs within the polymeric matrix, (Wang et al, 2016) also tested the inhibiting capability of PLGA-GNP and found over 24 hours cell viability of human breast cancer cells, reduced to below 20%. Furthermore, it was explained increasing AuNP concentration would adjust the polymer (50:50) composition, enhance effects of AuNP, as well as indicating the use of varying shapes of AuNP, nanorods or nano-shells can also enhance efficacy due to varying absorbances of infrared light.

Cioffi et al, 2005, synthesised CuNP encapsulated within three different types of polymer to investigate the release properties of copper ions and to assess antifungal properties, results showed when incorporated within a polymeric system, formation of the copper polymer suspension Cu-PVMK led to an increased release of copper, this was attributed to the rapid formation of copper oxide, in the suspension. Moreover, data showed it is possible to control the release of copper incorporated within a polymeric system, as once encapsulated oxidation of particles occurs a lot slower than it would in bulk. This can therefore sustain CuNP in the original form and reduce toxicity of copper ions. The release curve (**Figure 5.3**) of F7 shows the release of 33% drug after 60 minutes, which indicates a burst release effect, after 24 hours 39% of drug was released. The reasons for this release being higher than F3 may be due to the presence of copper ions, or oxidised copper particles as copper is known to rapidly oxidise. Furthermore, it may also be due to the leaching of colour from the CuNP embedded within the system, as CuNP are brick red in colour, upon successful electrospraying the red colour particles could be observed upon the glass slide coated over, but the slight tinge of red still present. When 5 mg of this sample was placed in 2 mL PBS and placed in the water bath, over time the colour of this leached out into the surrounding medium, which may have led to an increase in absorbance values, hence a higher cumulative release curve.

Table 5. 1: Drug loading and encapsulation efficiency values for formulations F2-F7.

Formulations	Drug Loading (%)	Encapsulation Efficiency (%)
F2	1.18 ±0.33	24.89 ±0.99
F3	1.99 ±0.25	41.97 ±1.63
F4	2.28 ±0.30	48.07 ±2.35
F5	2.57 ±0.32	54.12 ±2.82
F6	1.56 ±0.24	33.03 ±2.08
F7	1.58 ±0.17	33.43 ±2.79

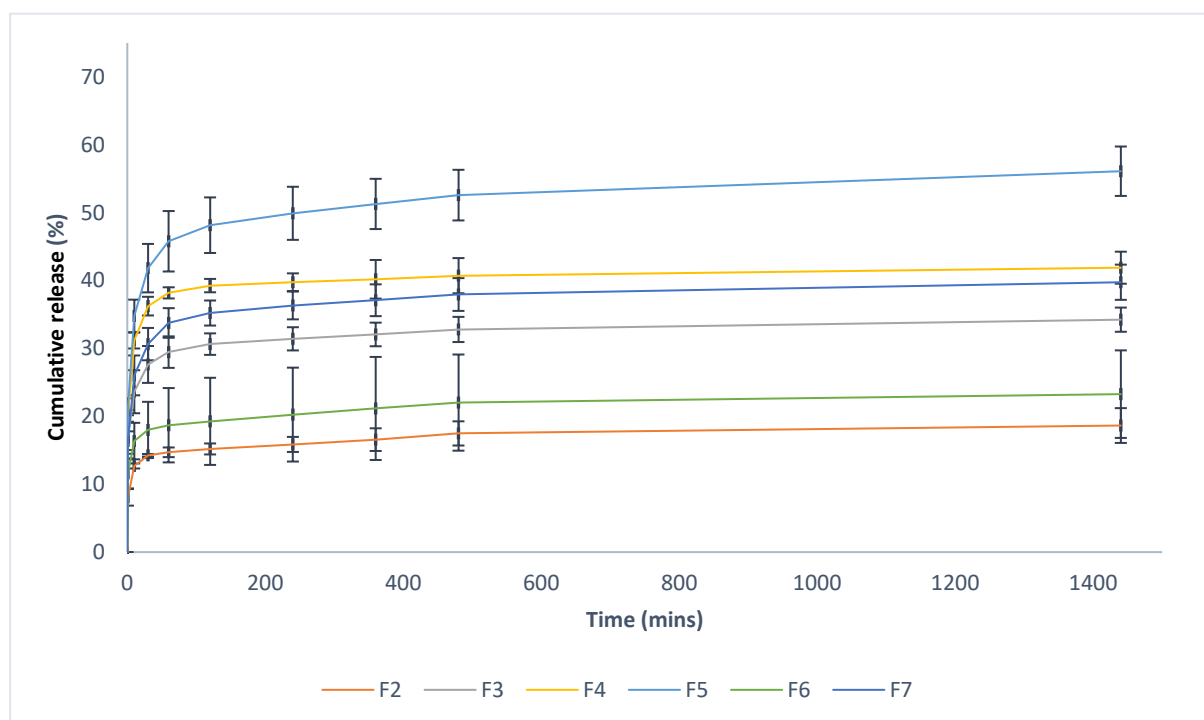


Figure 5. 3: Cumulative drug release curves for formulations F2-F7.

5.4.3 Microbiological testing

5.4.3.1 Disc diffusion results

5.4.3.1.1 Metallic nanoparticles

Results from the disc diffusion tests showed differences that arise from varying types of nanoparticles, and more importantly the differences between the type of shape the metallic nanoparticles have, as well as showing the differences in volume of suspension added (μL). When comparing results, images where 5 μL , of metallic suspension had been added will be discussed.

Results in **Figure 5.4** and **5.5** show all metallic nanoparticles synthesised show antibacterial efficacy, as clear zones are observed for all types and shapes of metallic nanoparticles used, as well as the increase in zone size with the increase in amount of suspension added. However, no zones were observed for the AuNP disk diffusion disks (**Figure 5.4Di-iv**), this is due to the inability of AuNP to diffuse through the disk and cause an antibacterial effect, (Kourmouli et al, 2018) studied the antimicrobial efficacy of AuNP and AgNP, AuNP were synthesised and added to *E. coli*; results showed no zones of inhibition from the AuNP, this may be an indication of no antibacterial properties of AuNP, but more so because AuNP are unable to release diffusive ions like AgNP are able to do when oxidised. The release of Ag^+ ions have the antibacterial efficacy effect.

As expected the silver nanomaterials had the most effective antimicrobial zones, due to presence of silver ions Ag^+ , with clear zones of inhibition around the discs **Figures 5.4Ai-Ci**. **Figure 5.5** showing the average zone sizes in (mm), presents AgNP as the metallic nanoparticle with the highest antibacterial efficacy against both gram-negative and gram-positive strains, at both volumes 5 μL and 10 μL . The average zone size for AgNP against *S. aureus* was measured at 18.84 mm and the smallest zone size was 16.07 mm from the CuNPs. Increasing the volume also increased sizes of zones, however the same result ensued with AgNP displaying an average zone size 23.61 mm, moreover AgP particles displayed a zone size of 23.14 mm, showing similar efficacy. Between the synthesised silver nanomaterials, the nanowire showed the lowest antibacterial efficacy against both *S. aureus* and *E. coli* regardless of volume added, this may be due to the difference in shape, as the nanowire shape may lead to less interactions with bacterial cells, moreover, it could be due to the spherical and polygonal shaped exhibiting higher surface area to volume ratio increasing contact with bacteria. Visually, when observing and comparing **Figures 5.4 Ai, Bi and Ci** for *S. aureus* it is clear to see the zones for **Ai** are the biggest followed by **Ci** then **Bi**. Furthermore, when comparing images for *E. coli* (5 μL),

Figures 5.4 Aii, Bii and Cii, it is observed the zones for **Aii** are the biggest then **Cii** and then **Bii**. These results remained the same with an increased volume of 10 μL .

AgNPs exhibit antibacterial effects, through different mechanisms, most of which are well known and documented, including the generation of silver ions through oxidation; these ions freely bind to the bacterial cell membrane, enhancing the damage to the bacterial cell wall. Second proposed mechanism is the formation of ROS, presence of silver ions enhances the production of ROS through interactions with thiol groups on the respiratory chain enzyme. The final proposed mechanism is direct damage, where AgNPs or silver ions directly bind to bacterial cell walls causing an inhibitory effect leading to bacterial cell death (Jones et al, 2018).

The antibacterial effect of silver has been well documented and known for many centuries. Liao et al, 2019, explained the smaller the size of nanoparticle the better the inhibition, due to smaller size binding to the bacterial cell wall better than larger diameter particles, moreover it was found when AgNPs are in the presence of bacteria, growth of ROS occurs. ROS develop in a time dependant relationship, more so at the beginning of interaction. AgNPs synthesised by (Valenti and Giacomelli, 2017), using the citrate reduction method, showed the capping of AgNPs varies oxidation results. When capping with citrate, oxidation of AgNPs was incomplete, so amount of ROS released can be controlled depending on capping agent used. The main difference between gram-negative and gram-positive bacteria is the thickness of the peptidoglycan layer. Shrivastava et al, 2007, explained the difference in antibacterial efficacy is related to thickness of the layer, as a thicker peptidoglycan layer makes it more difficult for silver nanoparticles to attach onto the cell wall. For gram-positive bacteria *S. aureus* (Li et al, 2010) published data showing the effects varying concentrations of AgNPs has on *S. aureus*, it was found that an MBC of 20 $\mu\text{g/mL}$ was required. Salomoni et al, 2017, synthesised AgNPs to test on *Pseudomonas aeruginosa* (a bacterium resistant to commonly known antibiotics). Results showed a 5 $\mu\text{g/mL}$ concentration had a bactericidal effect on the bacteria, through enzyme inhibition, results showed the use of AgNPs as an alternative to antibiotics, which bacteria have developed resistance to, is promising and shows results of efficacy and inhibition.

AgNWs have also shown antibacterial efficacy, as they essentially possess the properties of silver, so the bactericidal or bacteriostatic effect still comes from the generation of silver ions. The experimental set up was to assess whether the change in shape would show differing antibacterial efficacy. Visnapuu et al, 2013, synthesised silver nanowires (70–150 nm diameter

and 3–8 μm length), to compare with spherical silver nanoparticles (98 nm diameter). Results show the shape did not have an effect on antibacterial efficacy, instead, increased efficacy depended on the increased production of Ag^+ . Moreover, (Hong et al, 2015) produced silver nanocubes, nanospheres and nanowires, antibacterial tests showed bacterial concentration in CFU/mL, the MIC of nanocubes, nanospheres, and nanowires were 37.5, 75, and 100 $\mu\text{g}/\text{mL}$, respectively. The wire exhibited the worse antibacterial activity compared with the nanocubes and nanospheres. AgNPs that exhibit larger effective contact areas exhibit stronger antibacterial activity. The antibacterial activity it seems then, depends on both the production of silver ions as well as the surface area in contact with the bacteria, (Helmlinger et al, 2016) produced spheres (diameter 40–80 and 120–180 nm), platelets (20–60 nm), cubes (140–180 nm), and rods (diameter 80–120 nm, length over 1 μm). Results showed antibacterial activity again was highly dependent on production of Ag^+ , higher surface area did show an increase in activity but the effect was not as enhanced as increased production of Ag^+ shows.

For the AgP particles, the antibacterial efficacy is shown to be higher than that of silver nanowires, from **Figure 5.5** although following a similar method of synthesis, this may be due to the increased surface area interactions of the shaped nanoparticles compared to nanowires as (Hong et al, 2015) showed the increased antibacterial activity of the nanocubes was the increased contact through formation of sides with bacteria that led to an increase in efficacy. Pal et al, 2007, synthesised spherical, nanoparticles of many shapes and nanowires. Results showed the antibacterial efficacy was higher in nanoparticles of many shapes compared to nanowires, this was attributed to the preferred facet growth phase determined from XRD diffractograms, data showed the nanoparticles growing in the (111) plane show the most antibacterial activity. From Figure 3.7 it can be seen all silver particles synthesised had the sharpest peaks in the (111) plane of growth therefore indicating the difference here in antibacterial efficacy, was due to production of Ag^+ and higher surface area contact with bacteria.

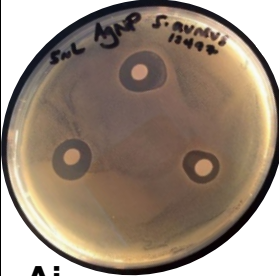



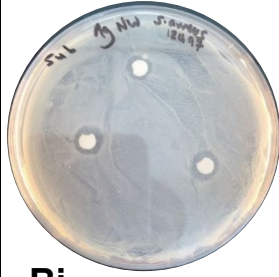
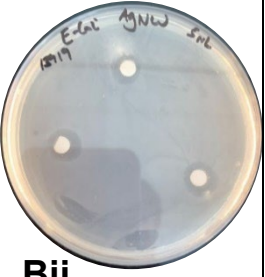
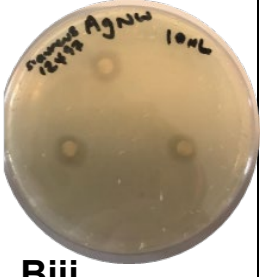

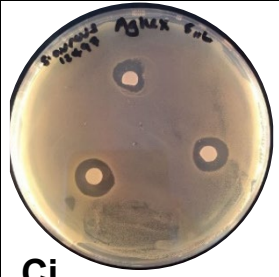
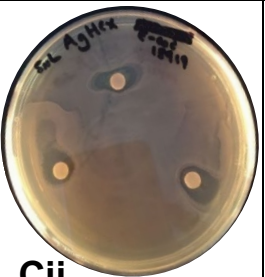

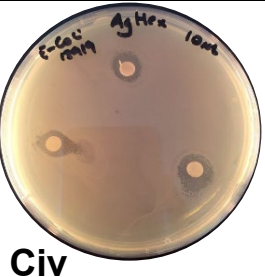

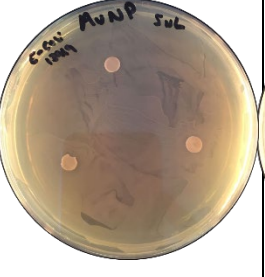





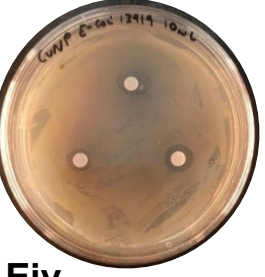
The CuNPs showed a lesser antibacterial effect against both strains of bacteria when compared to the silver nanomaterials, as observed in **Figure 5.4**, when comparing **Ai**, **Bi** or **Ci** to **Ei** the zones for the silver nanomaterials are much larger, the same when results are observed when using *E.coli*, images **Aii**, **Bii** and **Cii** show larger zones of inhibition than **Eii** does, the reasons for this may be due to lower production of copper ions, or due to incomplete oxidation of nanoparticles, (Harikumar et al, 2016) synthesised copper nanoparticles using a similar reduction technique, and found that the average zone size in disc diffusion against *E. coli* was

16 mm, which is similar to the average zone size shown here. Moreover, (Chatterjee et al, 2014) synthesised CuNPs and studied the antibacterial activity using *E. coli*. They found activity was highly dependent on production of ROS, which in turn increases when increasing concentrations of CuNPs are added. When comparing AgNPs and CuNPs in regards to antibacterial activity, (Nabipour and Rostamzad, 2015) produced AgNPs and CuNPs, using them against many strains of bacteria including *S. aureus*. Optical density results showed, when increasing the concentration to 1.5% of silver and copper added, silver induced a higher antibacterial effect. Furthermore, (Zia et al, 2018) synthesised CuNPs and AgNPs through the reduction method and tested efficacy using the disk diffusion method against *S. aureus* and *E. coli*. Results showed, at lower concentrations, AgNPs exhibited higher efficacy through larger zone sizes (mm). When using *S. aureus* AgNPs and CuNPs were added at a molar concentration of 0.3; for AgNPs zone sizes of 24 ± 0.21 mm were recorded, in comparison CuNPs at the same concentration recorded zone sizes of 15 ± 0.28 mm. Against *E. coli* the difference in antibacterial activity again showed silver to be a better antibacterial agent, at a molar concentration of 0.7, AgNPs showed zone sizes of 20 ± 0.21 mm, whereas for CuNPs zone sizes were 18 ± 0.21 mm. This is further evidence that the AgNPs display better antibacterial efficacy than CuNPs and confirms the disc diffusion results observed.

Figure 5.4Fi displays the antibacterial efficacy of AMX alone against *S. aureus*, zones of inhibition are observed confirming the susceptibility of *S. aureus* to AMX, *E. coli* however is resistant to AMX, hence no zones of inhibition. The average size of the zone against *S. aureus* displayed in **Figure 5.5** shows its at 19.4 mm, this size is slightly larger than the AgNPs zone size at 18.8 mm, this is expected as AMX is the antibacterial active agent, at higher volumes 10 μ L zone size for AMX against *S. aureus* was 25.1 mm.

Kim et al, 2017, synthesised silver nanoparticles varying in size and shape to test efficacy through OD against *E. coli*. AgNPs 10, 20 and 70 nm in size, were added at varying concentrations results showed, the 10 nm size showed better efficacy then 20 nm and 70 nm at the same concentrations. For example, at a concentration of 30 ng/mL, the OD value remains below 0.1 for the 10 nm sized particles until the 10 hour point where only a slight increase occurs, however the 20 nm and 70 nm sized nanoparticles, both show an increase in OD values after 8 hours, and the OD value rises to above 0.4. Furthermore, in regards to shape effects cube, sphere and plate shaped nanoparticles were synthesised, all used at 70 nm size. Results here indicated the cube shape had the highest efficacy, at the same concentration of 150 ng/mL the OD value rose after 8 hours slightly and at the 10-hour mark was recorded below 0.2. For

the spherical shaped nanoparticle OD value rose sharply at the 8-hour point, above 0.2, and for the plate shaped nanoparticles the OD value rose slightly not as high as the spherical particles, but just above 0.2. This result suggests shape of nanoparticle may affect efficacy, and the cube shape with increased surface area to volume ratio caused increased antibacterial efficacy.

	5 μ L		10 μ L	
	<i>S. aureus</i>	<i>E. coli</i>	<i>S. aureus</i>	<i>E. coli</i>
AgNP	 Ai	 Aii	 Aiii	 Aiv
AgNW	 Bi	 Bii	 Biii	 Biv
AgP	 Ci	 Cii	 Ciii	 Civ
AuNP	 Di	 Dii	 Diii	 Div
CuNP	 Ei	 Eii	 Eiii	 Eiv

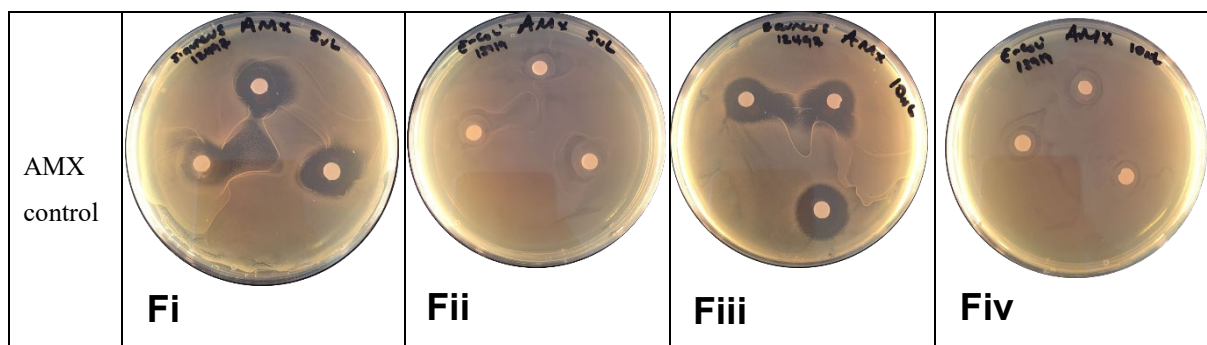


Figure 5. 4: Disk diffusion zones against *E. coli* and *S. aureus* at varying volumes of metallic nanoparticles with the control as AMX. (i) *S. aureus* and 5 μL of metal suspension; (ii) *E. coli* and 5 μL of metal suspension; (iii) *S. aureus* and 10 μL of metal suspension; (iv) *E. coli* and 10 μL of metal suspension. (A) AgNP; (B) AgNW; (C) AgP; (D) AuNP; (E) CuNP; (F) AMX control.

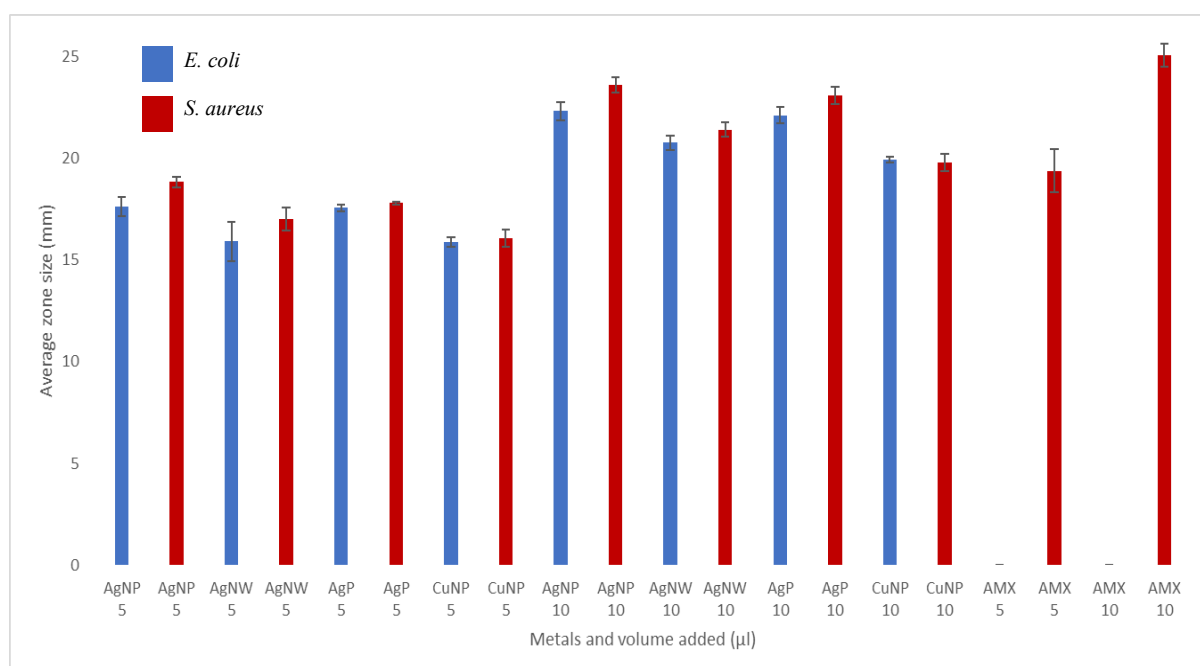


Figure 5. 5: Size of disk diffusion zones against *E. coli* and *S. aureus* at varying volumes of metallic nanoparticles with the control as AMX.

5.4.3.1.2 Full formulation Results

The full formulations synthesised, F2-F7 have shown encapsulation of drug, presence of metallic nanoparticles and varying drug release depending on the formulation when incubated at 37 °C. The next step was to assess the antibacterial properties of the formulations, to determine if the EHDA process is a good alternative for synthesising antibacterial composite formulations, as it is an easy one step process, allows for encapsulation of poorly soluble drugs, and can inculcate many types of antibacterial agents.

The full formulations were used here, against methicillin resistant *S. aureus* and penicillin resistant *E. coli*, to determine whether the addition of metallic nanoparticles can enhance the effect of the drug AMX, and in the case of *E. coli*, help overcome the resistance. **Figure 5.6** shows the results of the disc diffusion tests, the images used for comparison are **Ai-Fi** and **Aii** to **Fii**, where 15 µL had been added. **Figure 5.7** for F2, displays the average disc diffusion zone against *S. aureus* at 28.15mm using, this was used as the base when comparing with the rest of the formulations, to see if metallic nanoparticles can enhance the efficacy through a synergistic effect, hence zone sizes should increase if this was the case.

When comparing **Figure 5.6Ai** for F2 to **5.6Bi** for F3 the zones of inhibition increase, from **Figure 5.7**, it is calculated that the average zone size is now recorded at 30.8 mm an increase of 1.09-fold. When comparing with F4 **Ci** in **Figure 5.7**, the average zone size increases further to 34.16 mm an increase of 1.2-fold. As for F5 from **Figure 5.6Di** it can be observed the zone size is a lot bigger than all other formulations present, **Ai-Fi**. The average zone size is measured at 41.21 mm an increase of 1.46-fold.

The disk diffusion results for F6Ai indicates the inhibition of *S. aureus*, as it is known AuNPs exhibit no disk diffusion efficacy due to its nature, these results then are attributed to the presence of AMX, the zone size measured in **Figure 5.7** gives an average zone size of 29.2 mm, the average zone size is slightly higher than F2, which may be due to the presence of AuNPs dispersed amongst the polymeric matrix, therefore increasing surface area, leading to an increased amount of drug particles released into the medium. For disk diffusion image F7 **Ei** the zone sizes measured were smaller than those observed by formulations F3-F5, the average zone size had reduced to 20.97 mm, an average smaller than that for F2 Ai.

The results here overall, indicate a synergistic effect of silver nanomaterials and AMX does exist, as increase in zone sizes is evident with addition of silver nanomaterials, compared with AMX alone. However, when comparing with the penicillin resistant *E. coli*, results are inconclusive, for F2 in **Figure 5.6Aii** as expected no zones of inhibition were recorded, when analysing F3 **Bii** the image in **Figure 5.7**, shows a zone of inhibition at an average size of 17.48mm, this zone size is smaller than the zone AgNPs displayed against *E. coli*, in **Figure 5.4Aii**, therefore the zone of inhibition observed here in F3 **Bii** may be a result of the silver ions present in the supernatant of the sample as oppose to a synergistic effect of AgNP and AMX.

For F4 **Cii** in **Figure 5.7** the zone of inhibition is measured at 15.22 mm, when comparing this zone size to that of AgNWs against *E. coli* in **Figure 5.5** the zone has reduced, in the presence of AMX, this therefore indicates no synergistic efficacy against *E. coli*. For F5 **Dii** the zones of inhibition are at an average size of 25.1mm, when comparing to AgP against *E. coli*, in **Figure 5.5** the zones of inhibition have increased, this may be due to a synergistic effect, where the bacteria and AMX may have increased efficacy working together, one possible reason for this result is the surface area to volume of the AgP particles being much larger than the other silver nanomaterials, this is evident through better drug loading, and a higher AMX cumulative release curve after 24%, the reasons for this were attributed to the increased hydrolysis of polymer chain, releasing more of the drug particles, along with more silver ions when compared to F3 and F4. Another benefit of the particle possessing sides and a varying morphology, may be increased interactions with polymeric matrix, which destabilises the matrix, making it less rigid and more degradable.

Figure 5.6Eii no zones of inhibition were observed, as expected, AuNP shows no efficacy in disk diffusion testing, and *E. coli* is resistant to AMX. For **Figure 5.6Fii** again there are no zones present, however, when comparing with **Figure 5.4Fii**, zones were present averaging 15.8 mm this indicates no enhancement of efficacy against *E. coli*.

Increasing the efficacy of commonly used antibiotics through addition of metallic nanoparticles is still relatively novel and reasons for activity still not yet understood, (Kaur and Kumar, 2019) tested the enhanced efficacy of polymer stabilised AgNP in conjugation with different antibiotics, the bacteria used were *S. aureus* and *E. coli*, the antibiotics used were vancomycin (Van) and amikacin (Amk), results from disc diffusion method showed zones of inhibition for Amk against *E. coli* and *S. aureus* were approximately around 9 and 5 mm, respectively for three different concentrations whereas the zones of inhibition for Amk with AgNP against *E. coli* and *S. aureus* was increased up to 20 and 10 mm, respectively.

Furthermore, it is known *E. coli* is totally resistant to Van, therefore when Van was added no zones of inhibition were observed, however when adding Van with AgNP at different concentrations, the bacterial growth was inhibited to some extent. The zones of inhibition with Van and AgNP for *E. coli* increases from 0 to 8 mm and made the bacteria also sensitive to this conjugate. In case of *S. aureus*, bacterial growth inhibition also enhances from 7 to 11 mm. These results confirm, increased bacterial efficacy can occur when combining metallic nanoparticles with antibiotics, even if bacteria is known to be resistant to specific antibiotics. This may help in the race against increasing bacterial resistance against many strains of antibiotics.

The increase in zone sizes for formulations F3-F5 Bi-Di in **Figure 5.6**, can be attributed to enhancement in efficacy, when combining the metallic nanoparticle and AMX. Shahverdi et al, 2007, tested the differences in efficacy when using a range of raw antibiotics including AMX against known bacterial strains *S. aureus* and *E. coli*; and when adding AgNPs to the drug. Results showed the zone of inhibition for *S. aureus* in mm when adding AMX was 7.5 mm, when adding AgNPs with the AMX the zone size increased to 14 mm, when adding AMX to *E. coli* no zone size was observed however when adding the AMX plus AgNPs the zone size increased 0.44 in fold area. This result shows resistance can be overcome with combination therapy, combining different antibacterial agents to overcome the resistance of certain bacteria.

For F5 Di and Dii in **Figure 5.6 and 5.7**, it is clear average zone sizes are bigger than F3 Bi and Bii, when comparing AgNPs and AgPs from **Figure 5.5** it is also clear to observe AgNPs showed bigger zones of inhibition. The difference then was related to the production of Ag⁺ ions, as through the citrate reduction method increased amount of silver ions are produced. It is known citrate degrades at 30 °C (Torres et al, 2018), therefore increasing amount of AgNPs, leading to higher formation of silver ions. However, when comparing F3 with F5 it can be

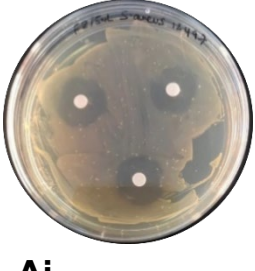
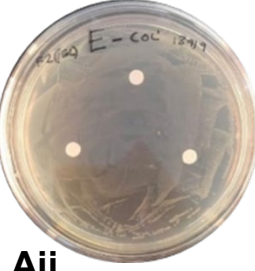
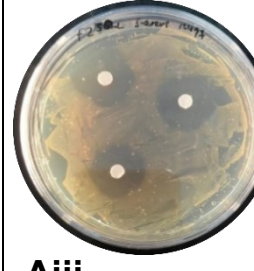
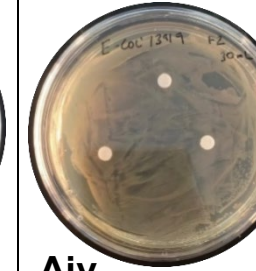
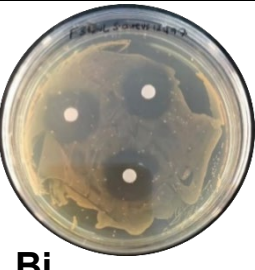
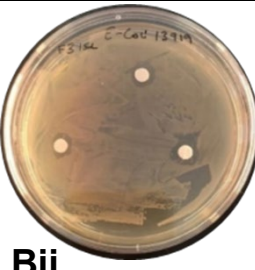
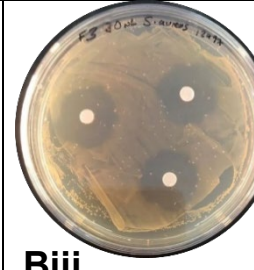
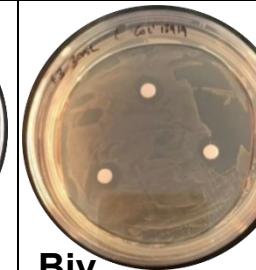
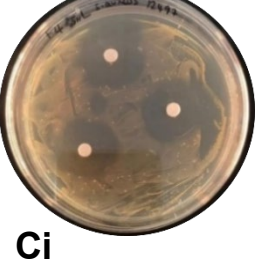

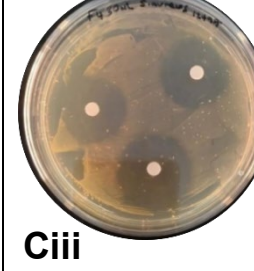
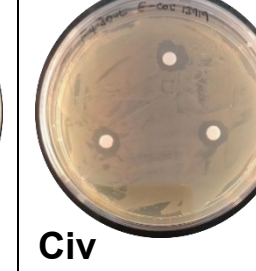
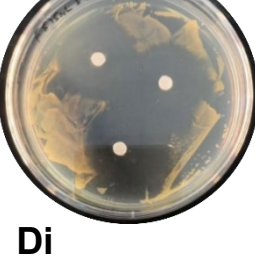

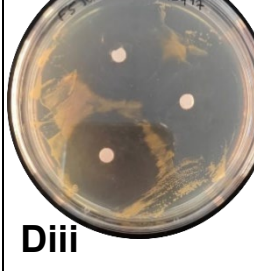
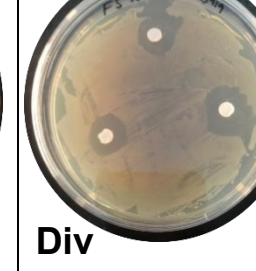

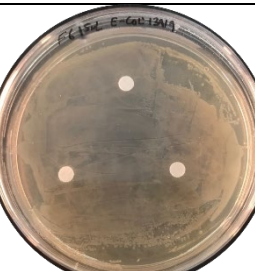
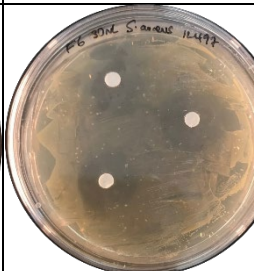
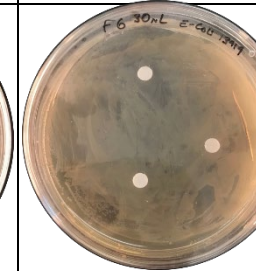
explained the increased surface area to volume ratio of AgP particles present, may have led to increased contact with drug particles, hence at the right conditions for release at 37 °C more drug particles are released. Furthermore, the larger surface area due to presence of edges and sides increases contact with polymeric chains, destabilising the polymeric system and increasing amount of free drug particles. As more drug particles are free increased efficacy can be observed in **Figure 5.6Di** compared to F3 **Bi**.

Zhang et al, 2016, presented a review paper, describing the effects of AgNPs embedded within polymers through the electrospinning process, the electrospinning method allows for one step encapsulation of the AgNPs, and an increase in antibacterial activity. Zhang et al, 2009, used nylon-6 which shows no antibacterial activity, however when adding AgNPs into the polymeric matrix a 99.9% efficacy was shown against *E. coli*, moreover, it is described to increase hydrolysis of the bulk polymer inclusion of AgNPs allows for this. Bu et al, 2013, showed inclusion of AgNPs loaded onto the graphene–ZnO quasi-shell–core composites significantly improved the photocatalytic rhodamine B degradation capability of the graphene–ZnO quasi-shell–core composite. Zhang et al, 2016, explains further that the AgNPs have strong catalytic properties for hydrolysis and electrolysis of organic materials when being added into AgNPs/polymer composites, however the catalytic activity is controlled through size of nanoparticle, a larger surface area to volume ratio increases the catalytic ability. This then explains why F5 showed better drug loading, increased drug release and enhanced efficacy against bacteria. As raw metals the Ag⁺ production dictates the efficacy, however when incorporated within a polymeric system the surface area interactions play a bigger role it seems. The increased hydrolysis of polymeric chains may have led to release of more Ag⁺ compared to F3, hence why the zone sizes were larger.

As for F7 **Figure 5.6Ei** the zone of inhibition was smaller than F2, this may have been due to the presence of encapsulated CuNPs not allowing for release of drug as freely as AMX can in F2, as the encapsulation of CuNPs reduced oxidation of nanoparticles, therefore less ROS were present reducing hydrolysis of polymeric matrix, causing more AMX drug particles to remain embedded within the polymer. The increase in surface area increases the amount of drug particles present, however if the CuNPs are evenly dispersed and embedded then release from PLGA may be over a longer period of time, as these results were taken after 24 hours, increased incubation time may have led to increased zones of inhibition.

Palza et al, 2015, synthesised polymer composites embedded with copper nano/micro particles, results showed release rate of copper ions was better when the copper used was of nano-size, moreover, release of copper ions from the polymeric matrix is affected by the hydrophobic nature of the polymer, as a more hydrophobic polymer slows down release rates of ions. This may be another reason for the reduced antibacterial efficacy, as CuNPs in **Figure 5.4Ei** showed smaller zones of inhibition compared to other metallic nanoparticles, hence why in a polymeric system efficacy may have been reduced. For F7 when adding, a higher amount of the formulation (30 μ L) small zones of inhibition were observed **Figure 5.6Fiv**.

Results here show use of EHDA for antibacterial alternatives may have a future, not enough data is yet available, but with further research the reasons behind the efficacy shown can be explored. Zhang et al, 2017, synthesised AgNWs through the polyol method, with the polymer PVA to form nanofibers, these nanofibers exhibited antibacterial properties, displayed through absorbance values against *S. aureus* and *E. coli*, concentration of AgNWs used was increased and results showed at 100 μ L of AgNWs added the absorbance value was below 0.20 for *S. aureus*, adding the same amount to *E. coli* the absorbance value interestingly was above 0.25, although the gram-positive *S. aureus* has a thicker peptidoglycan layer the inhibition of this bacteria was higher.

	15 μ L		30 μ L	
	<i>S. aureus</i>	<i>E. coli</i>	<i>S. aureus</i>	<i>E. coli</i>
F2	 Ai	 Aii	 Aiii	 Aiv
F3	 Bi	 Bii	 Biii	 Biv
F4	 Ci	 Cii	 Ciii	 Civ
F5	 Di	 Dii	 Diii	 Div
F6	 Ei	 Eii	 Eiii	 Eiv

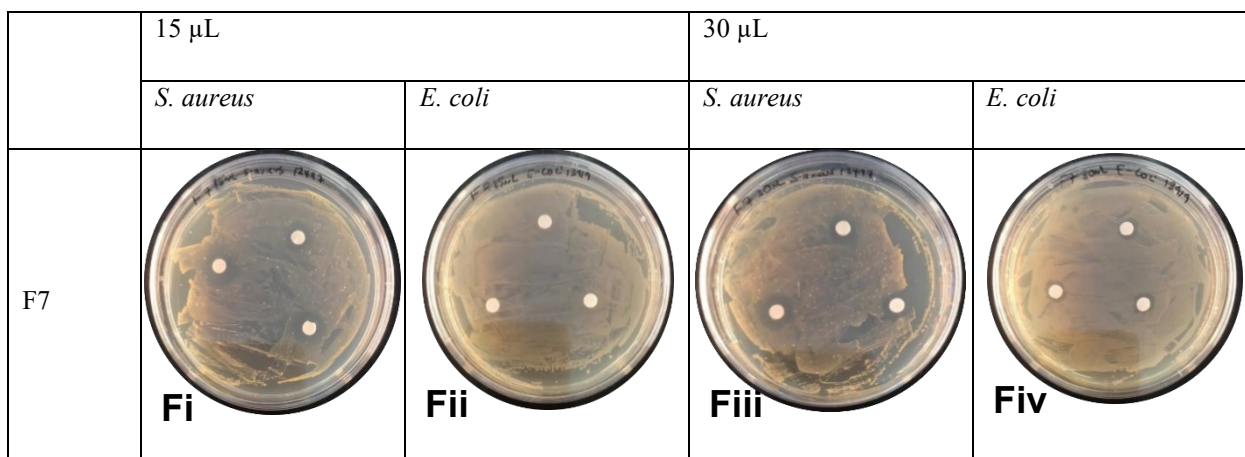


Figure 5. 6: Disk diffusion zones against *E. coli* and *S. aureus* at varying volumes of formulations F2-F7 (i) *S. aureus* and 15 μ L of metal suspension; (ii) *E. coli* and 15 μ L of metal suspension; (iii) *S. aureus* and 30 μ L of metal suspension; (iv) *E. coli* and 30 μ L of metal suspension. (A) F2; (B) F3; (C) F4; (D) F5; (E) F6; (F) F7.

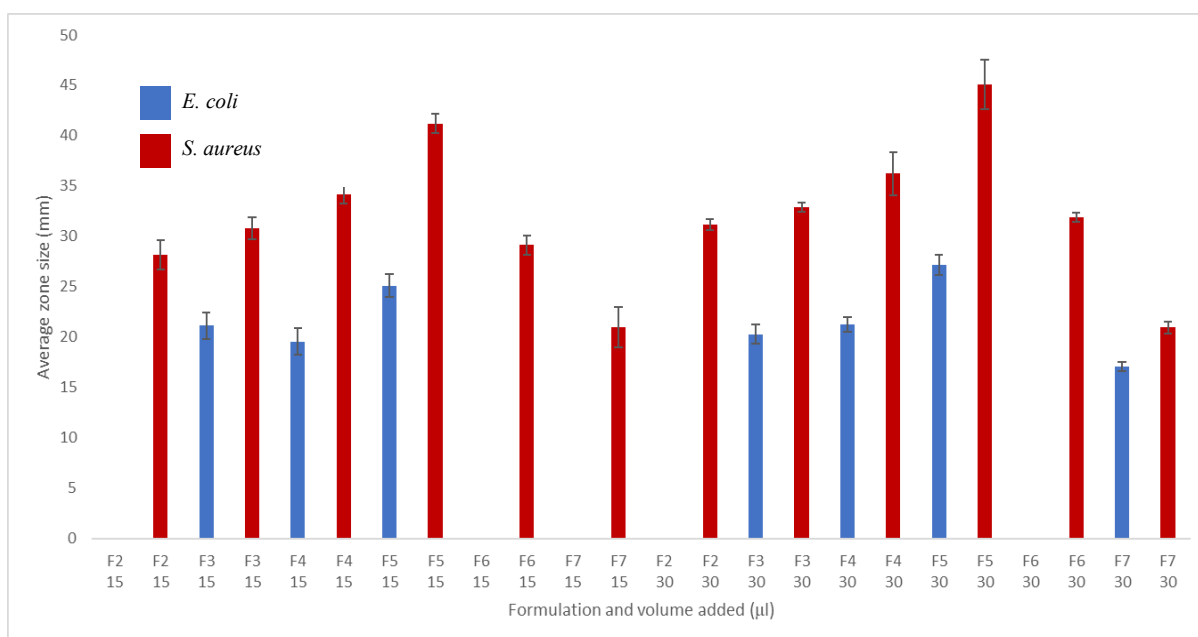
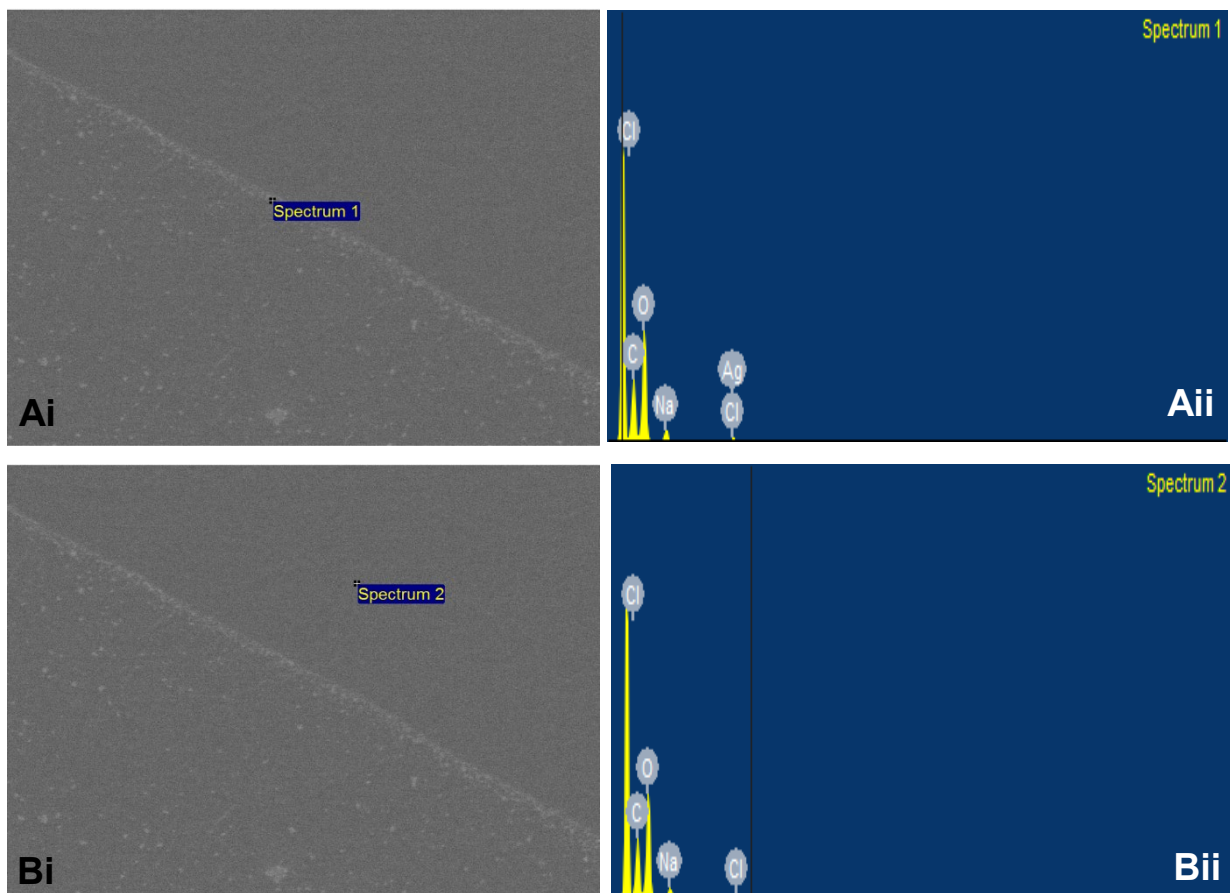


Figure 5. 7: Size of disk diffusion zones against *E. coli* and *S. aureus* at varying volumes for formulations F2-F7.

5.4.3.2.1 SEM analysis of bacterial death

SEM analysis was carried out to visually assess the cell damage caused by the metallic nanoparticles, images were taken from AgNPs and AgP disc diffusion plates. **Figure 5.8Ai** shows the zones of bacterial inhibition, the particles observed are AgNPs particles, at the border of the inhibition zone, beyond this as seen in **Figure 5.8Bii** there is no silver present, this region was where the bacteria were growing. **Figure 5.8Ci** taken from an AgP disc, highlights once again the border zones of the diffusion disk, where the AgP particles have accumulated and inhibited bacterial growth, however beyond this from Figure Di no silver is present, this is where the *S. aureus* bacteria continues growing. **Figure 5.8Ei** is an image at a higher magnification, which shows clear zones, no presence of *S. aureus*, and as **Figure 5.8Eii** confirms, silver is present. **Figures 5.8F** and **G** are back scatter images taken from SEM, the charged particles present here indicate the presence of metallic nanoparticles amongst the bacterial cells, the areas circled on both images show where the metallic nanoparticles have attached to the bacterial cells and cause disruption of the cells, as is presented bacterial cells have lost morphology no longer appear spherical, appearing more stretched out and elongated indicating cell death, confirmed through similar morphology found by (Hartmann et al, 2010, Zajmi et al, 2015).



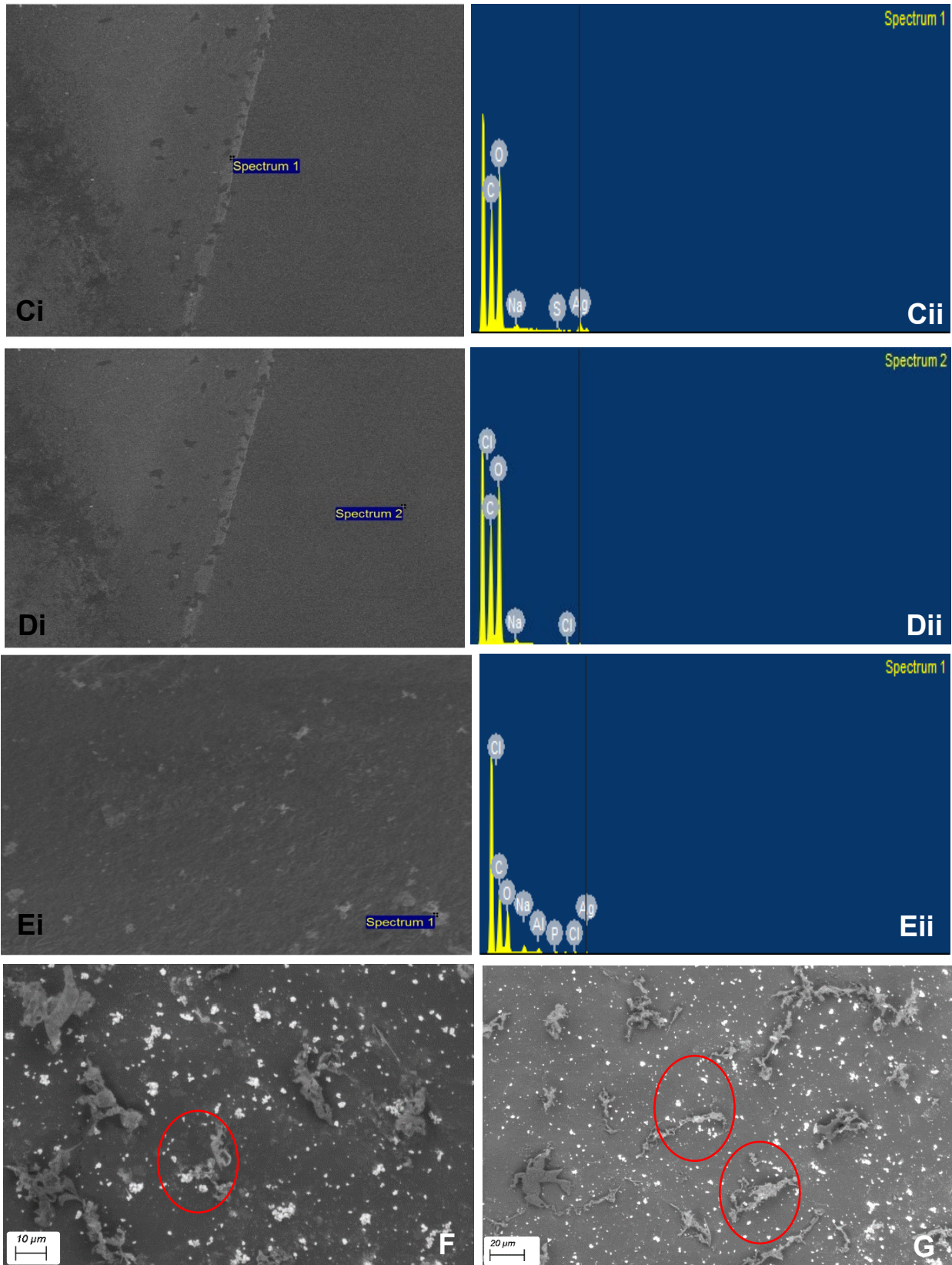


Figure 5. 8: SEM/EDS analysis of *S. aureus* cell death. (i) SEM image; (ii) EDS analysis.

5.4.4 Optical Density (OD 600_{nm})

5.4.4.1 Metal nanoparticle results

Optical density (OD) results presented, show how the growth curves of chosen bacterial strains *E. coli* and *S. aureus*, develop over 24 hours, alone and with the addition of metallic nanoparticles varying in shape and size, the wavelength chosen to analyse differences in OD values was 600 nm. McBirney et al, 2016, described OD measurements as the preferred choice to detect bacterial growth, due to its simplicity and rapid answer. Furthermore, for bacterial analysis 600 nm is frequently used. Biesta-Peters et al, 2010, also conducted comparative studies in detecting bacterial growth and found determining OD measurements as a more useful technique when compared to plate counting. Furthermore, (Vukomanovic et al, 2019) explained, obtaining more accurate measurements (with fewer preparation steps), of samples following the growth curve of bacteria, is best examined by following the gradual change in the turbidity at 600 nm using OD600.

Results obtained from OD curves usually follow the pattern of bacterial growth, with an initial lag phase, exponential growth phase, stationary phase and death phase. As shown below in **Figure 5.9**. When adding antibacterial agents, this growth curve should alter, an increase in lag time before growth indicates inhibition occurring, a shorter growth phase, or the death phase occurring much earlier all may indicate antibacterial properties of your samples.

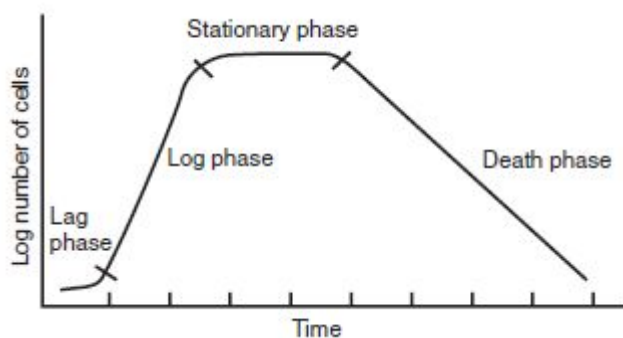


Figure 5.9: General bacterial growth curve.

Figure 5.10 shows the optical density curves for metallic nanoparticles against *S. aureus* at 5 μ L, results displayed correlate with disc diffusion results in **Figure 5.4Ai-Ei**. For the *S. aureus* control, the growth curve follows the general bacterial growth curve as shown in **Figure 5.9**, with an initial but short lag phase, exponential growth from 1 hour onwards to around 6-hour point. The stationary phase where the nutrients are available for growth have now been used up, which leads onto the slow death phase after the 20-hour point. For the metallic nanoparticles

used AgNPs again show the highest inhibitory effect, as the optical density drastically reduced from 0.26 at 0-hour point to 0.14 after 5 hours. This shows a clear bactericidal effect, as the value declined when exposed to the metallic nanoparticles at 37 °C. Moreover, an initial burst release of silver ions may have led to the death of bacterial cells. Similar results observed in **Figure 5.12** with the bacterial strain *E. coli*, the AgNPs exhibit bactericidal effects reducing OD from 0.20 to 0.098, over the 24 hours. Results also indicate the metallic nanoparticles have similar effects against both *S. aureus* and *E. coli*.

For the AgP the growth phase (**Figure 5.10**) the curve follows a similar pattern to the AgNPs curves at both 5 µL and 10 µL, again showing an immediate death phase from 0.28 to 0.16 after 8 hours, followed by a stationary phase for a number of hours, and then further decrease in OD values, as for the AgNW, the growth phase follows similar patterns it displays an initial death phase, which then leads to a stationary phase, but interestingly at the end a growth phase is observed at around the 21 hour mark, AgNW therefore may not have shown a complete bactericidal effect, and some of the bacteria began to grow under optimum conditions using nutrients available. Against *E. coli* the AgP show higher antibacterial efficacy reducing the OD from 0.24 to 0.11, following a similar pattern to AgNPs, this may be due to the thinner peptidoglycan layer in *E. coli* making it more susceptible to AgP. For the AgNW the results against *E. coli* show a steady decline in OD values indicative of inhibitory effects from 0.15 to 0.13 after 6 hours of incubation, followed by a steady rise and decrease in OD values, however at the 20 hour point the OD begins to rise due to bacterial growth, therefore results of AgNWs against both strains of bacteria show reduced efficacy compared to other AgNPs synthesised.

As disk diffusion did not work for AuNPs, due to its nature, assessment here would show if AuNP exhibit any antibacterial activity at all. Results shown in **Figure 5.10** display a longer lag phase, followed by a slight rise in bacterial growth, thereafter a steady decline, indicating AuNP exhibit antibacterial activity, overall the OD value began at 0.22 and after 24 hours was recorded as 0.15, the difference may not be as great as what silver nanomaterials displayed, it does however confirm the antibacterial properties of AuNP, moreover it seems AuNP exhibit bacteriostatic properties, as oppose to bactericidal.

AuNP against *E. coli* in **Figure 5.12** showed similar results, a longer lag phase is observed with OD remaining constant indicating the antibacterial effects of AuNPs with no rise in OD values. Mohamed et al, 2017, published findings displaying the antibacterial properties of AuNP, using *Corynebacterium pseudotuberculosis* results showed at a concentration of 100 µg/mL,

inhibition of bacterial cell growth did occur, using the colony forming unit (CFU) method. Elbehiry et al, 2018, published results of antibacterial activity, comparing efficacy of AgNPs and AuNP both synthesised using the citrate reduction method, against a strain of *S. aureus*, it was found at a concentration of 100 µg/mL, AuNPs with a 10 nm diameter inhibited 100% of *S. aureus* growth. Moreover, (Zhou et al, 2012) produced citrate reduced AuNP and tested against different strains of bacteria including *E. coli*, results showed a lesser concentration of AuNP used induced a higher antibacterial effect, at high concentration particles are more likely to aggregate, therefore decreasing the antibacterial effect, however at lower concentrations, particles appear more monodisperse and have a higher chance of interaction with bacterial cell walls to induce an antibacterial effect.

For CuNPs in **Figure 5.10**, results show a lag time of up to 13 hours, the CuNPs inhibit the growth of bacteria as the OD value remains constant, however after the 13-hour point, a steady rise is observed as growth of bacteria is occurring, this confirms bacteriostatic properties of CuNPs. CuNPs synthesised by (Jamshidi and Jahangiri-Rad, 2014) showed antibacterial activity, results of OD against *E. coli* showed the gradual decrease in OD values over time, at concentration of 150 µg/mL the OD value decreased from 0.2 to below 0.1 indicating the antibacterial properties of CuNPs.

For CuNPs against *E. coli* in **Figure 5.12** results show a bacteriostatic effect, as the growth of bacteria is prevented through a larger lag time, eventually however after the 14 hour point the OD curve begins to rise indicating growth of bacteria. Overall less efficacy is shown of the CuNPs, as described previously the ROS generated from silver has a higher efficacy than those generated from CuNPs, leading to differences in antibacterial activity.

For the AgNPs no lag phase was detected, with the first phase being the death phase this may have been due to the 125 µg/mL concentration used, (Surwade et al, 2018) described the relationship between concentration of AgNPs used (µg/mL) and the cell death (%), the bacteria used was methicillin resistant *S. aureus*, data showed a concentration of 20 µg/mL was enough to cause 100% cell death after just 30 minutes of incubation. (Hwan et al, 2010) synthesised AgNPs to test against bacterial strains *E. coli* and *S. aureus*, results showed at concentrations of 100 µg/mL and 150 µg/mL, no lag phase occurred, immediate death of the bacterial cells for both strains, was observed as OD values decreased from 0.15 to below 0.1, the concentration difference between 100 µg/mL and 150 µg/mL, did not vary the end OD value, only the initial death phase was sharper at a higher concentration. Maiti et al, 2014, synthesised

AgNPs to test the antibacterial efficacy of *E. coli* grown in LB, OD curve with an initial value of 0.2 showed declined immediately within 1 hour to almost 0, this was obtained using a silver nanoparticle concentration of 80 $\mu\text{g/mL}$.

Having already determined the bacterial effect of AgNPs, is more due to the presence of ions than shape, these results correlate with disk diffusion results shown in **Figure 5.4**. Data published by (Pal et al, 2007) shows the effects of different shaped nanoparticles on growth of bacteria, at 100 $\mu\text{g/mL}$, spherical, triangular and wire shaped AgNPs have inhibited the growth of *E. coli*, more so the spherical and triangular shaped nanoparticles as oppose to nanowires. Furthermore, when comparing the effects of varying shapes, it was found, using a colony forming unit method showed, at 100 $\mu\text{g/mL}$ both the spherical and triangular shaped nanoparticles inhibited growth of *E. coli* but the wire shaped nanoparticles, still had growth of colonies. The overall inhibitory nature of the silver nanomaterials has been enhanced through direct contact with the bacteria, as oppose to diffusing through the disk onto the agar plate.

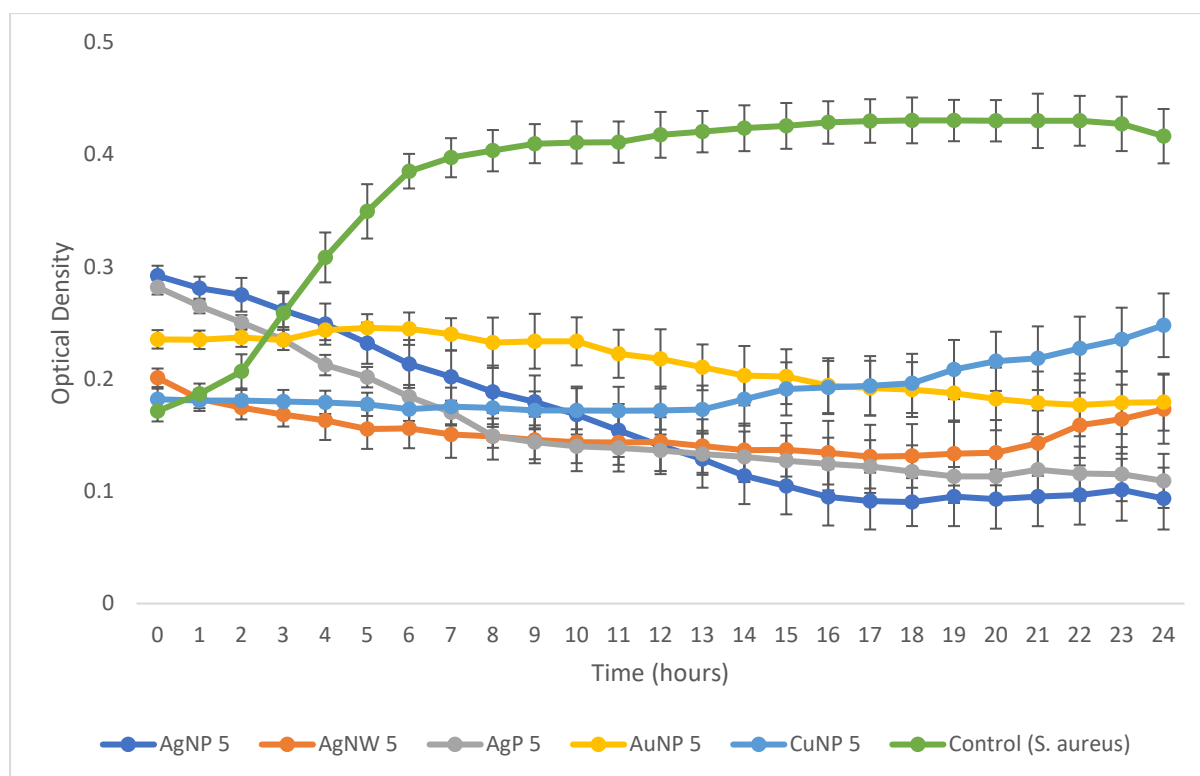


Figure 5. 10: Optical density curves of metallic nanoparticles against *S. aureus* at 5 μL .

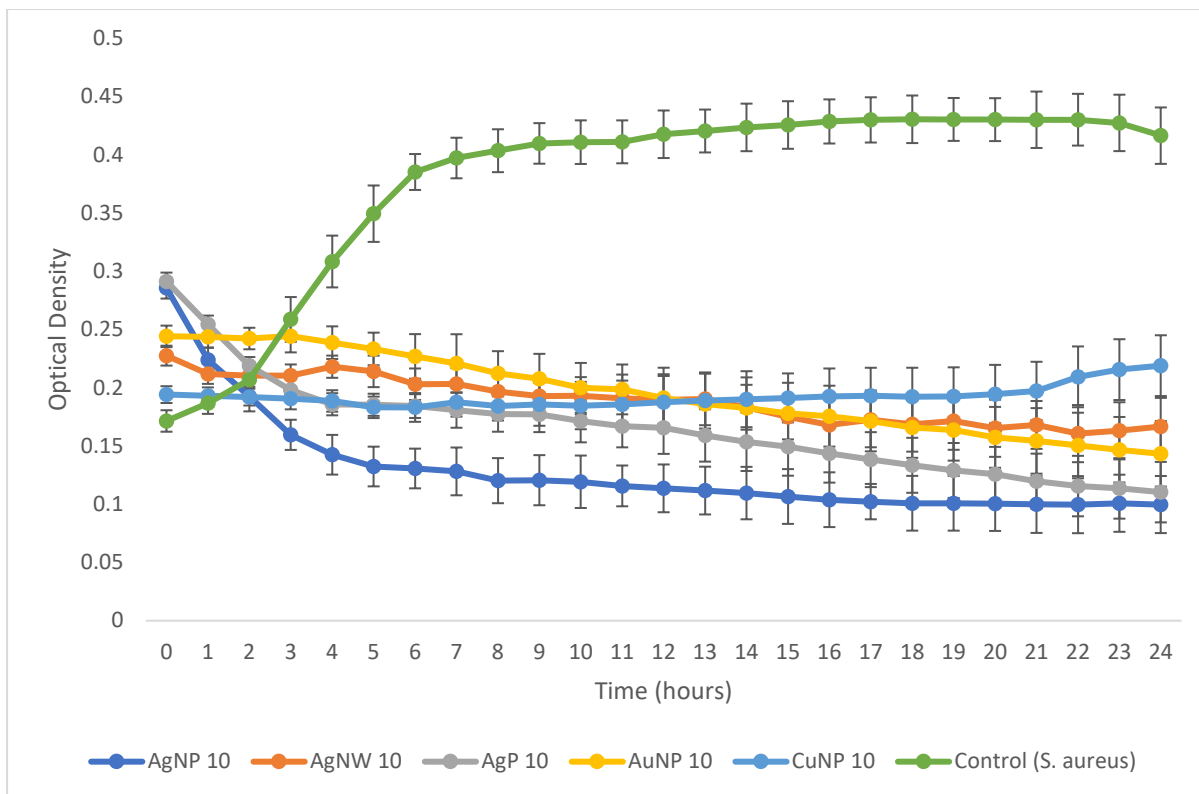


Figure 5. 11: Optical density curves of metallic nanoparticles against *S. aureus* at 10 μL .

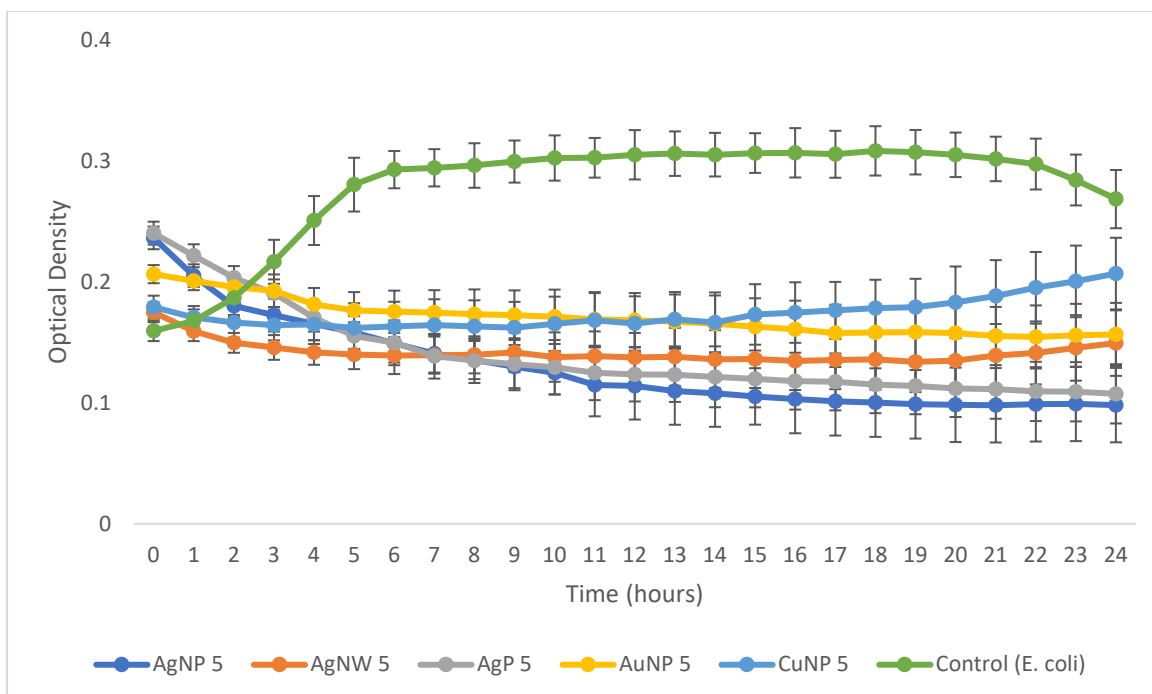


Figure 5. 12: Optical density curves of metallic nanoparticles against *E. coli* at 5 μL .

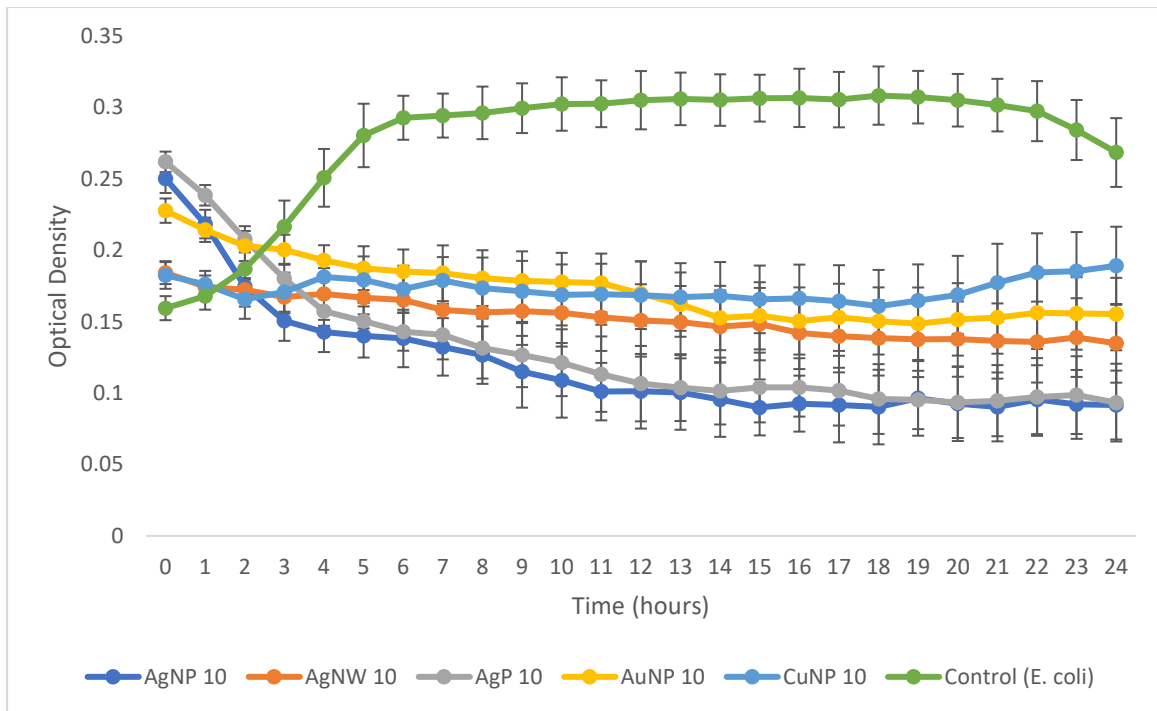


Figure 5. 13: Optical density curves of metallic nanoparticles against *E. coli* at 10 μ L.

5.4.4.2 Full formulation results

From the full formulation results, for both bacterial strains *E. coli* and *S. aureus* all curves observed show growth of bacterial cells, which follows the general bacterial growth curve. **Figure 5.14** shows the growth of *S. aureus* against formulations F2-F7, to indicate antibacterial activity here would be through increased lag times, before the increased exponential growth of bacteria occurs, a shorter growth curve or a quicker death rate. F2 shows a steady lag phase, however OD value has increased from 0.22 to 0.26 before the exponential growth occurs at the 6-hour point. For formulations F3-F5 lag times have increased, the exponential growth phase appears at the 11, 8, and 14 hour point respectively for F3, F4 and F5. An increase in lag time therefore suggests the enhanced efficacy of the AgNPs and AMX inhibited the growth of bacteria.

When comparing the optical density curve results to **Figure 5.6** for the disc diffusion zones, results show similar correlation, as once again F5 shows the highest antibacterial efficacy and F4 the lowest, when comparing F3-F5. As for F6 the exponential growth phase begins at the 7-hour point, an increase compared to F2, which may indicate synergistic efficacy, however, the exponential growth phase rises higher in F6 up to 0.46, whereas for F2 the highest point is 0.37, for F6 it remains inconclusive as to whether AMX and the AuNP worked together to enhance efficacy.

Formulation F7 began at a higher OD compared to the other formulations, at 0.29 the reason for this may have been leaching of colour from the CuNPs formulated as shown in **Figure 4.1G**, into the supernatant this gave it a yellow colour over 24 hours in incubation. The growth curve for F7 did not show much inhibition to bacterial growth, as it continued growing and seemed to follow the growth curve of bacteria.

In comparison **Figure 5.16** shows the growth curves of formulations in *E. coli*, the difference here is apparent, all formulations display much shorter lag phases, and sharper exponential growth phases, which indicates similarly to **Figure 5.7**, the synergy between metallic nanoparticles and AMX against *E. coli* did not show enough indication of combined efficacy.

F2 almost mirrored the growth phase of the bacteria, as expected because of the resistance, F3-F5 displayed lag times, of shorter durations compared to the lag times in **Figure 5.14**. Furthermore, F5 controlled bacterial growth keeping it in the lag phase longer than the other formulations, again when comparing the growth curve of *E. coli* against metallic nanoparticles AgP and AgNP in **Figure 5.12** results showed AgNPs had better antibacterial efficacy,

however here it is evident F5 shows the longest lag time when compared to F3, this may therefore be attributed to increased amount of drug and metallic ion particles in direct contact with the bacteria. For F3 and F4 lag times are present, with direct contact of metallic ions and bacterial cells, inhibition is expected to occur, but unlike **Figure 5.14** AMX here is ineffective hence why the exponential growth curves begin earlier for both formulations.

From literature it is known enhancing efficacy of antibacterial agents is possible through addition of metallic nanoparticles, the increase in lag times for F3-F5 in **Figures 5.14** and **5.16** compared to the bacteria, is evidence of this enhancement, (Deng et al, 2016) tested the antibacterial efficacy when combining silver nanoparticles and common antibiotics, to test against *Salmonella*, six different antibiotics were chosen, the results for β -lactam antibiotics, penicillin or ampicillin, showed an increase in inhibition of *Salmonella*, at higher concentrations of the composites, which may indicate synergistic antibacterial efficacy, however when compared with other antibiotics used in the study inhibition of bacterial growth was greater.

Silvero et al, 2018, synthesised amoxi@AuNP also through a simple one step process reducing the gold by using AMX to form AuNP. When tested against MRSA, efficacy was compared between AMX alone and amoxi@AuNP results showed increased antibacterial activity for amoxi@AuNP as after only 20 minutes complete inhibition of MRSA colonies was shown, however for AMX colonies remained and increased in growth over the time used.

Guoqing Wan et al, 2016, combined antibiotics polymyxin B and rifampicin with AgNPs and found enhanced synergistic therapeutic efficacy, of the AgNPs with both antibacterial agents combined against *Acinetobacter baumannii*. Hair et al, 2018, synthesised AgNPs with vancomycin to assess synergistic effects against *S. aureus*, results showed the two treatments work in concert to eliminate biofilm mass. The dual treatment was more effective than either treatment alone for the group of MRSA isolates.

The optical density values are also determined when antibacterial formulation is in direct contact with bacterial cells, as opposed to being separated and having to diffuse through a paper disk, this was investigated by (Bondarenko et al, 2013) who synthesised AgNPs alone, and coated with PVP and a polymer. Results showed direct contact between AgNPs and bacteria increased the efficacy of all formulations compared to when membranes are present between AgNPs and bacterial cells. Furthermore, as all metallic nanoparticles synthesised in **Tables 3.1-3.5**, displayed negative zeta potential values, when in aqueous medium, they then have the

potency to attract counter-ions like Ag^+ and H^+ cations into their diffuse layer, by chemisorption. After direct contact with bacterial cells that are negatively charged, the increased concentration of both, Ag^+ and H^+ ions on the particle surface would then lead to additional damage upon bacterial cell membranes, because of the higher local concentration of Ag ions. The accumulation of ions on the surface of the bacterial cell walls, can lead to development of ROS within the bacterial cell leading to cell death.

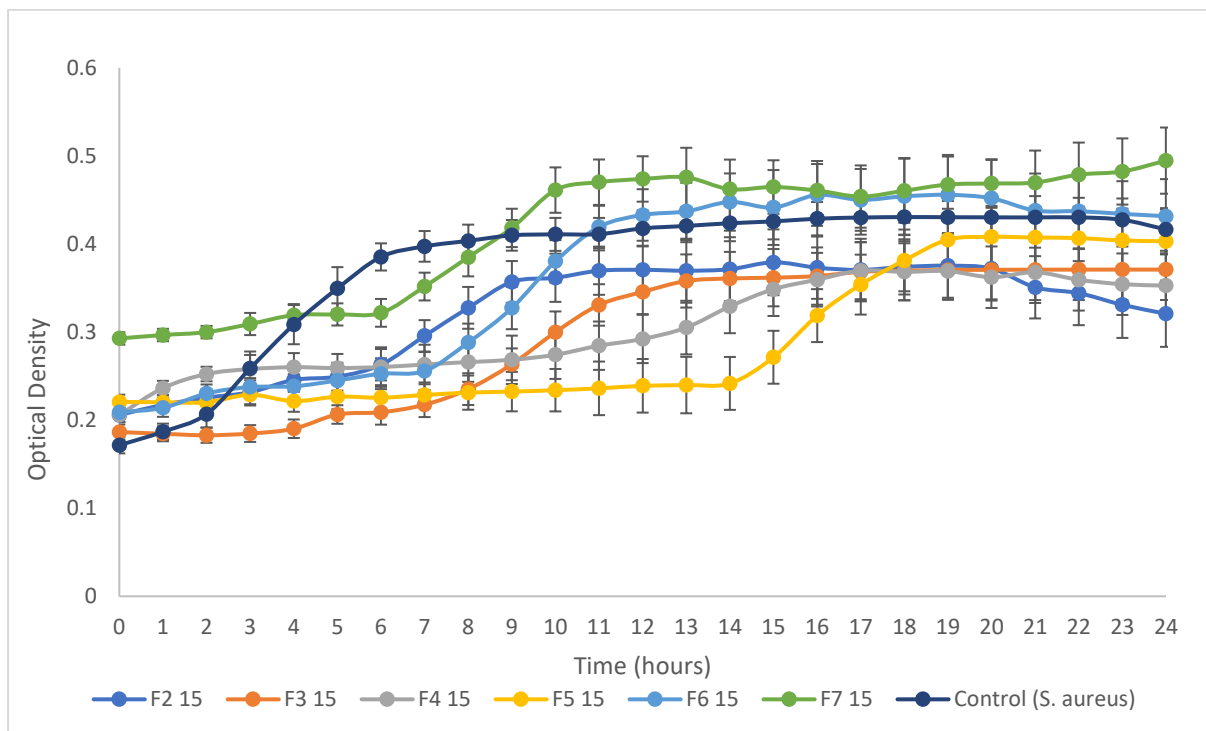


Figure 5. 14: Optical density curves of the formulations F2-F7 at 15 μL against *S. aureus*.

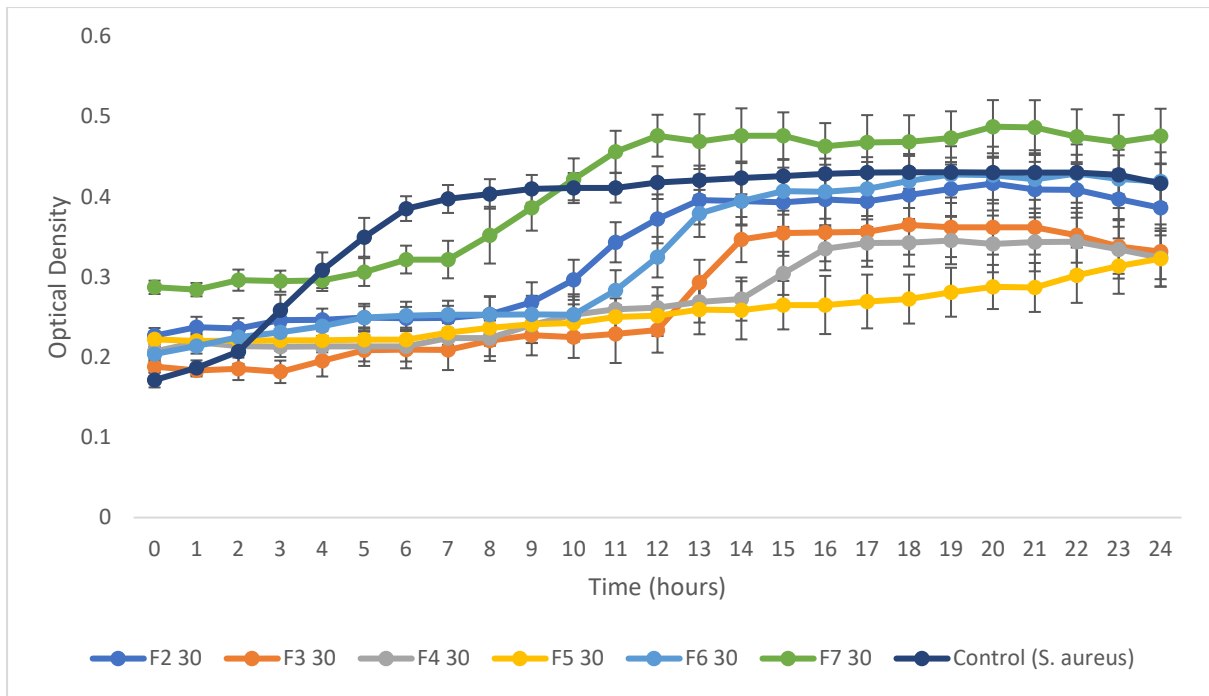


Figure 5.15: Optical density curves of the formulations F2-F7 at 30 µL against *S. aureus*.

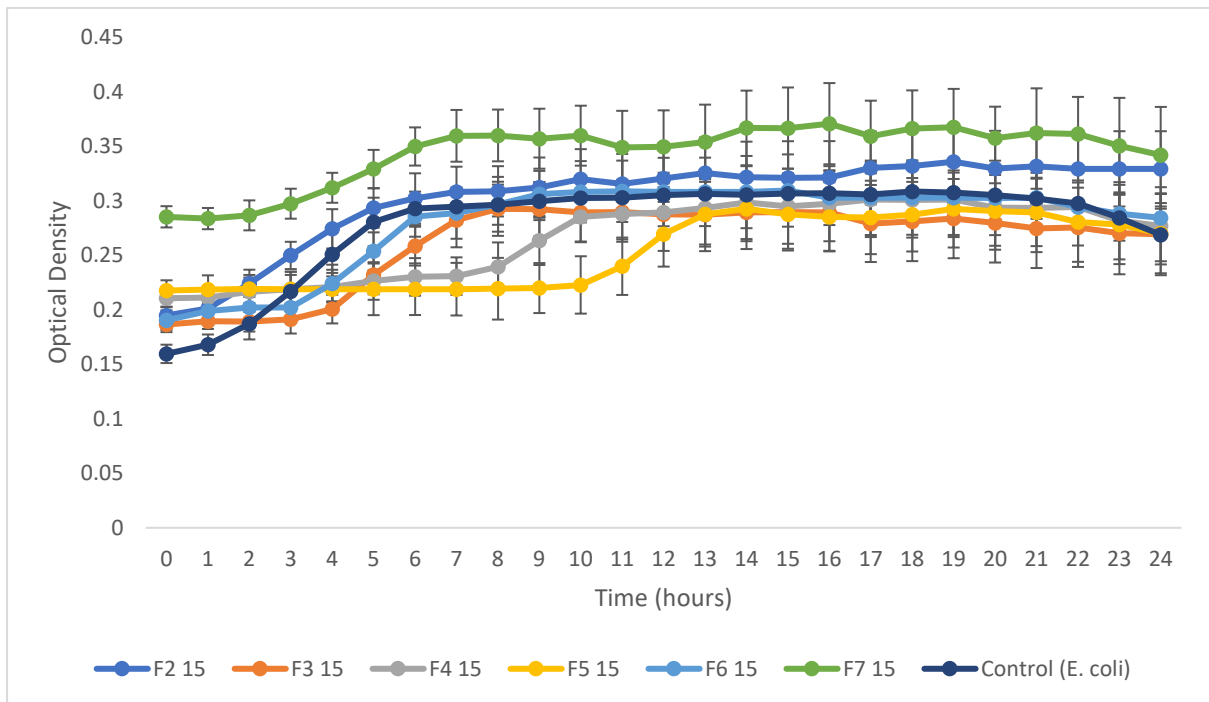


Figure 5.16: Optical density curves of the formulations F2-F7 at 15 µL against *E. coli*.

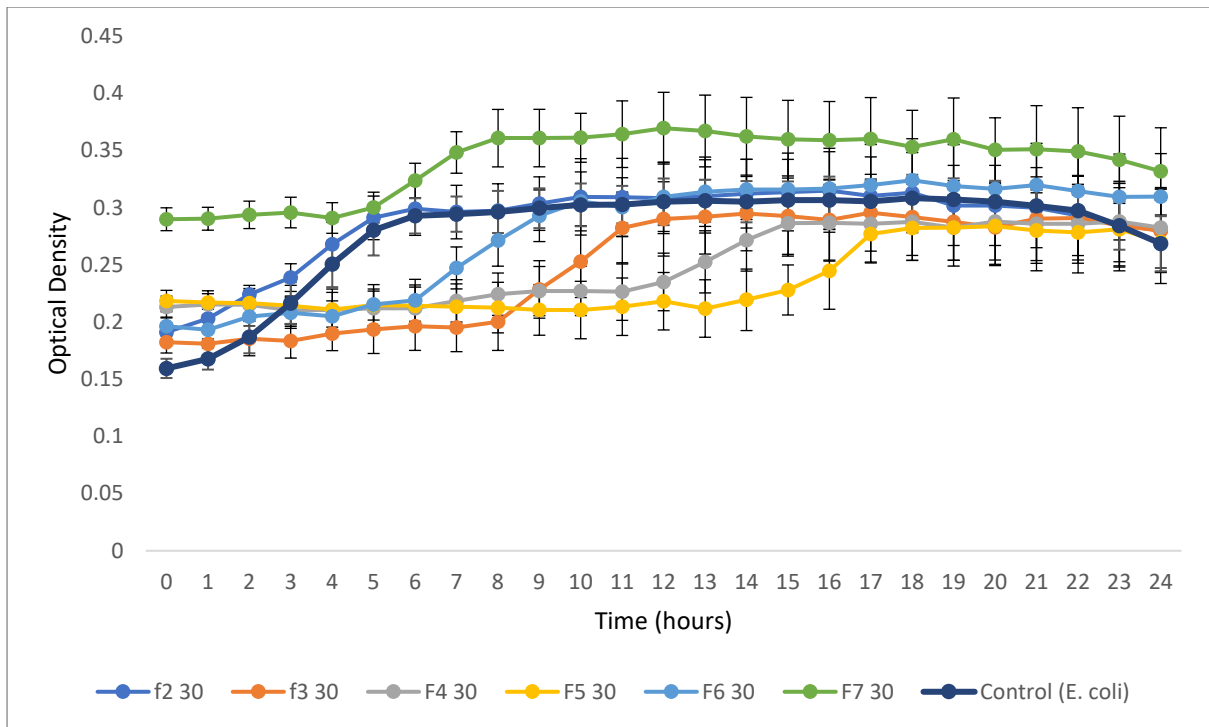


Figure 5. 17: Optical density curves of the formulations F2-F7 at 30 μ L against *E. coli*.

5.4.5 Cell culture studies

Upon synthesis of novel antibacterial therapies, it is vital to understand the cytotoxicity of synthesised samples. To test cytotoxicity the MTT assay is used and is one of the quickest and most reliable ways of testing cell viability. The MTT assay allows for easy differentiation between living cells and dead cells, as living cells contain the enzyme NAD(P)H-dependant cellular oxidoreductase which works by reducing the tetrazolium MTT dye which is red to yellow in colour, to a purple insoluble colour belonging to formazan (Satyavani et al, 2012). Formazan has to be solubilised, for it to have valid absorbance readings and therefore DMSO is used; isopropanol can also be used, but here DMSO works better, especially when there is a significant amount of residue still left in the wells. Upon incubation the absorbance is ready to be recorded by the spectrophotometer (Satyavani et al, 2012).

Data obtained from the MTT assay, was for each individual metallic nanoparticle, PLGA with AMX, and the polymeric drug metallic nanoparticle composites at varying concentrations of 1 $\mu\text{g/mL}$, 10 $\mu\text{g/mL}$ and 125 $\mu\text{g/mL}$. For cell viability results a good result is between 80-100% cell viability, a toxic sample exhibits cell viability at 50% or below.

Tables 5.2-5.6 display the concentrations of each of the formulations added to the 48 well plate, the positive control hydrogen peroxide and the negative control of just cells. From **Figure 5.18** at a concentration of 1 $\mu\text{g/mL}$, the AgNP show a cell viability of 100%, F2 was used for all **Figures 5.18-5.22** to compare the effects, on the addition of metallic nanoparticles have on cell viability. The cell viability in F2 at this concentration reduced to 94%, this may have been an anomaly, as when the concentration increased to 10 $\mu\text{g/mL}$ the viability increased.

Furthermore, for the full formulation F3, as the concentration increased from 10 $\mu\text{g/mL}$ to 125 $\mu\text{g/mL}$ cell viability reduced, this would have been expected when comparing with AgNPs at 125 $\mu\text{g/mL}$, the cell viability reduced to 11%, indicating toxicity of the nanoparticles. Beer et al, 2012, synthesized metallic nanoparticles, and used MTT assay to determine the cytotoxicity effect at varying silver ion concentrations, this was to determine the effect an increase in silver ion concentration has on the cell viability, the cell line used was an A549 human lung carcinoma epithelial-like cell line, results showed when increasing ion concentration cell viability reduces, the concentration used was 1.5 $\mu\text{g/mL}$, but the ion concentration increased from 39% to 69%, and the cell viability was recorded at 94% and 54% respectively. However, this result from **Figure 5.18** does indicate encapsulation of the nanoparticles within a polymer drug matrix can help reduce the toxicity, and when comparing with previous figures showing

the release of drug, and antibacterial efficacy, the positives outweigh the negatives hence why, researching further into improving the cytotoxicity of this composite may be useful.

Results from F2 remained similar in all tests, at high concentrations of 125 $\mu\text{g/mL}$, the cell viability was 100% in **Figure 5.21**, and overall from all Figures the cell viability does not show cell cytotoxicity. Chaubey et al, 2014, synthesized AgNPs loaded PLGA composites, and cytotoxicity data confirmed with an increase in concentration of the composites cell viability reduces, however data for PLGA on its own showed no cell mortality. Furthermore, when testing the efficacy against cancer cells, data obtained showed composites loaded with the protein induced cell death against cancer cells when compared to AgNPs alone.

Figure 5.19 displayed cell viability (%) of synthesised AgNWs alone and the full formulation F4. At 1 $\mu\text{g/mL}$ the AgNWs showed a 100% cell viability, F2 here also showed 100% cell viability, F4 here was slightly lower at 97%. When concentration increased to 125 $\mu\text{g/mL}$, results presented a decrease in AgNW cell viability to 74%, much different to the result in **Figure 5.18** for AgNPs at the same concentration. Furthermore, F4 showed an overall cell viability of 64% at the same concentration, which when compared to F3 was surprisingly lower, when considering the difference between AgNPs and AgNW at the same concentration also.

Yan et al, 2017, synthesised AgNWs through the polyol method and formed AgNW-loaded polydimethylsiloxane and tested the cell viability, when varying concentrations from 0.2-1 mg of the nanowires loaded polydimethylsiloxane, the mortality (%) remained between 0.8-1 %, showing when metallic nanoparticles are loaded onto polymers or similar materials the cytotoxicity can be reduced.

However, (Polívková et al, 2017) synthesised AgNW arrays supported on laser-treated polyethylene naphthalate, cytotoxicity results showed, considerable cytotoxicity of AgNW samples increased with time, indicating cytotoxicity varies depending on the type of material used as the substrate, upon which AgNW are attached to or embedded upon.

Figure 5.20 shows the results for AgP nanoparticles as well as F5 at varying concentrations, again. At low concentrations 1 $\mu\text{g/mL}$ AgP nanoparticles reduced cell viability to 73%, however, at a much higher concentration of 125 $\mu\text{g/mL}$ the cell viability reduced to only 69%, this result and the AgNW show similar toxicity, this may be due to the synthesis method applied. At higher concentrations 125 $\mu\text{g/mL}$ F5 shows cell viability at 71%, when comparing with the other silver nanomaterial formulations, the result is similar, indicating once the particles are dispersed within the polymeric matrix toxicity is not as high as it is alone.

Figure 5.21 for F6, displays the cytotoxicity of the synthesised AuNP at varying concentrations, the cytotoxicity observed is very low compared to the other metallic particles synthesised, this is due to the inert nature of AuNP, at higher concentrations of 125 $\mu\text{g/mL}$ the cell viability remains high at 87%, much higher than all other metallic nanoparticles at this concentration. The full formulation F6 shows a reduced cytotoxicity level of 78%, this however is still the highest cell viability when compared to the other formulations. Vijayakumar et al, 2012, synthesised citrate reduced AuNPs and tested the cell viability through the MTT assay, and assessed the cell viability using mammalian Chinese hamster ovary (CHO22) cell line, results showed citrate reduced AuNPs showed 76% cell viability at a concentration of 140 $\mu\text{g/mL}$. Moreover, when analysing the effects of citrate reduced AuNPs over 72 hours, the cell viability remained close to 80%.

Figure 5.22 shows the cell viability studies of CuNPs, with increasing concentration CuNPs exhibit higher cytotoxicity, at 1 $\mu\text{g/mL}$ cell viability is at 90%, with increase in concentration to 125 $\mu\text{g/mL}$ the cell viability reduces to 7%, indicating very high cytotoxicity towards cells, this reflects for the full formulation F7 as the cell viability reduces to 40%, much lower when compared to the other formulations F2-F6, and when comparing with F2 the difference in cell viability is almost 67%. This difference may be due to rapid oxidation properties of copper nanoparticles, forming copper oxide, upon oxidation higher chance of copper ions leaching and contributing to the production of ROS species which in turn can enhance cytotoxicity.

Ahamed et al, 2010, assessed the cytotoxicity of CuO nanoparticles, results showed at 50 $\mu\text{g/mL}$ the cell viability had reduced to 48%, using A549 cells. Azizi et al, 2017, synthesised CuNPs to assess cell viability against MDA-MB 231 cells and MCF-10A cells, results showed at a concentration of 100 μM , which equates to roughly 6.35 $\mu\text{g/mL}$, the cell viability was recorded at below 40% for both cell lines at this concentration.

Table 5. 2: Table of reagents in each well for AgNP.

	1	2	3	4	5	6	7
A	Media only	Media only	Media only	AgNP 1µg/mL	AgNP 1µg/mL	AgNP 1µg/mL	Hydrogen peroxide
B	Negative control	Negative control	Negative control	AgNP 10 µg/mL	AgNP 10 µg/mL	AgNP 10 µg/mL	Hydrogen peroxide
C	AgNP-P-Ab 1µg/mL	AgNP-P-Ab 1µg/mL	AgNP-P-Ab 1µg/mL	AgNP 125 µg/mL	AgNP 125 µg/mL	AgNP 125 µg/mL	Hydrogen peroxide
D	AgNP-P-Ab 10 µg/mL	AgNP-P-Ab 10 µg/mL	AgNP-P-Ab 10 µg/mL	P-Ab 1µg/mL	P-Ab 1µg/mL	P-Ab 1µg/mL	
E	AgNP-P-Ab 125 µg/mL	AgNP-P-Ab 125 µg/mL	AgNP-P-Ab 125 µg/mL	P-Ab 10 µg/mL	P-Ab 10 µg/mL	P-Ab 10 µg/mL	
F				P-Ab 125 µg/mL	P-Ab 125 µg/mL	P-Ab 125 µg/mL	

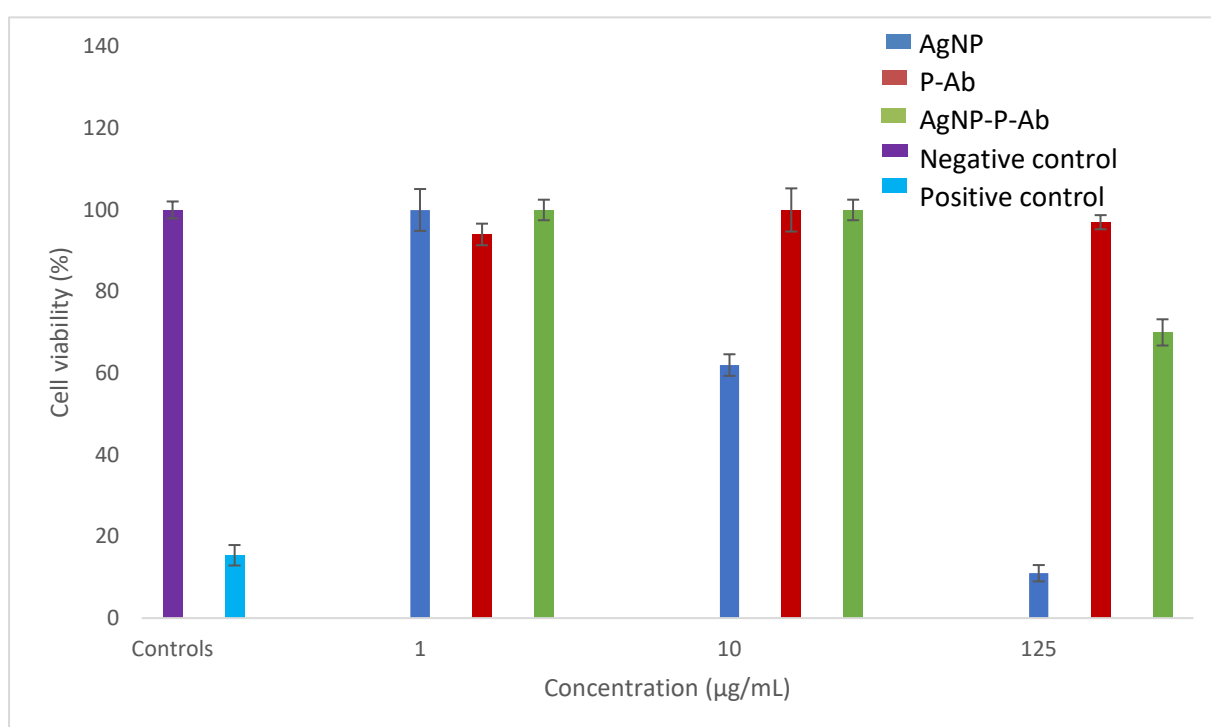


Figure 5. 18: Cell viability graph of AgNP formulations at different concentrations.

Table 5. 3: Table of reagents in each well for AgNW.

	1	2	3	4	5	6	7
A	Media only	Media only	Media only	AgNW 1µg/mL	AgNW 1µg/mL	AgNW 1µg/mL	Hydrogen peroxide
B	Negative control	Negative control	Negative control	AgNW 10 µg/mL	AgNW 10 µg/mL	AgNW 10 µg/mL	Hydrogen peroxide
C	AgNW-P-Ab 1µg/mL	AgNW-P-Ab 1µg/mL	AgNW-P-Ab 1µg/mL	AgNW 125 µg/mL	AgNW 125 µg/mL	AgNW 125 µg/mL	Hydrogen peroxide
D	AgNW-P-Ab 10 µg/mL	AgNW-P-Ab 10 µg/mL	AgNW-P-Ab 10 µg/mL	P-Ab 1µg/mL	P-Ab 1µg/mL	P-Ab 1µg/mL	
E	AgNW-P-Ab 125 µg/mL	AgNW-P-Ab 125 µg/mL	AgNW-P-Ab 125 µg/mL	P-Ab 10 µg/mL	P-Ab 10 µg/mL	P-Ab 10 µg/mL	
F				P-Ab 125 µg/mL	P-Ab 125 µg/mL	P-Ab 125 µg/mL	

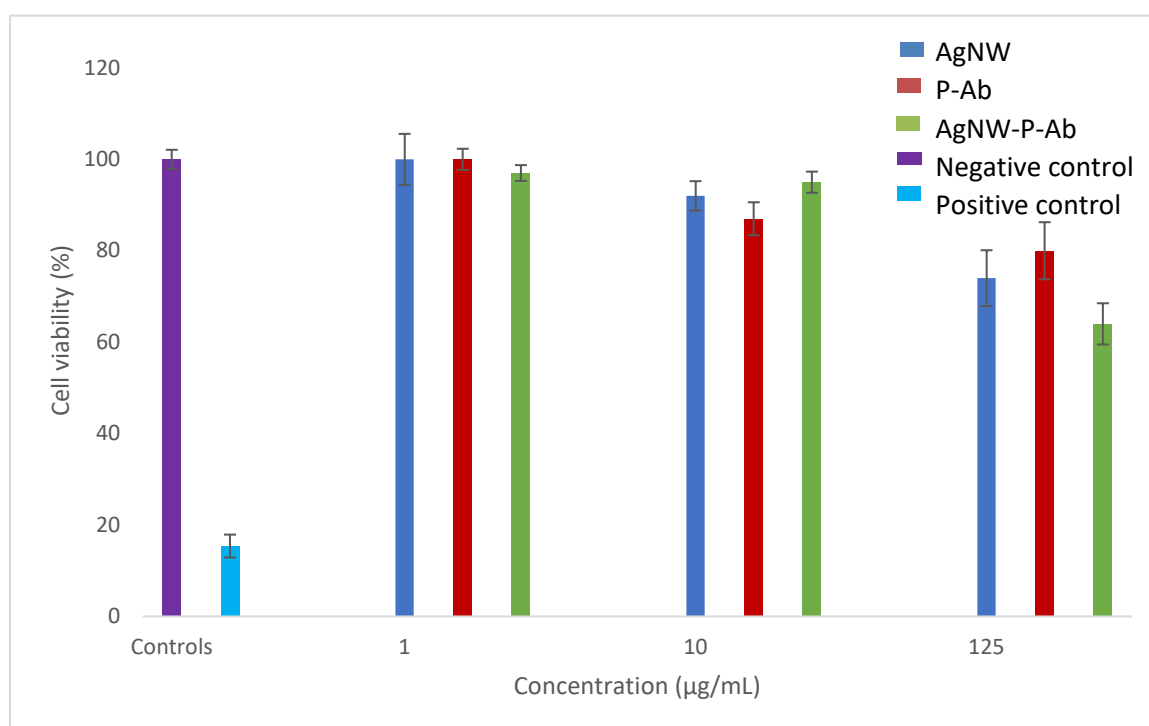


Figure 5. 19: Cell viability graph of AgNW formulations at different concentrations.

Table 5. 4: Table of reagents in each well for AgP.

	1	2	3	4	5	6	7
A	Media only	Media only	Media only	AgP 1µg/mL	AgP 1µg/mL	AgP 1µg/mL	Hydrogen peroxide
B	Negative control	Negative control	Negative control	AgP 10 µg/mL	AgP 10 µg/mL	AgP 10 µg/mL	Hydrogen peroxide
C	AgP-P-Ab 1µg/mL	AgP-P-Ab 1µg/mL	AgP-P-Ab 1µg/mL	AgP 125 µg/mL	AgP 125 µg/mL	AgP 125 µg/mL	Hydrogen peroxide
D	AgP-P-Ab 10 µg/mL	AgP-P-Ab 10 µg/mL	AgP-P-Ab 10 µg/mL	P-Ab 1µg/mL	P-Ab 1µg/mL	P-Ab 1µg/mL	
E	AgP-P-Ab 125 µg/mL	AgP-P-Ab 125 µg/mL	AgP-P-Ab 125 µg/mL	P-Ab 10 µg/mL	P-Ab 10 µg/mL	P-Ab 10 µg/mL	
F				P-Ab 125 µg/mL	P-Ab 125 µg/mL	P-Ab 125 µg/mL	

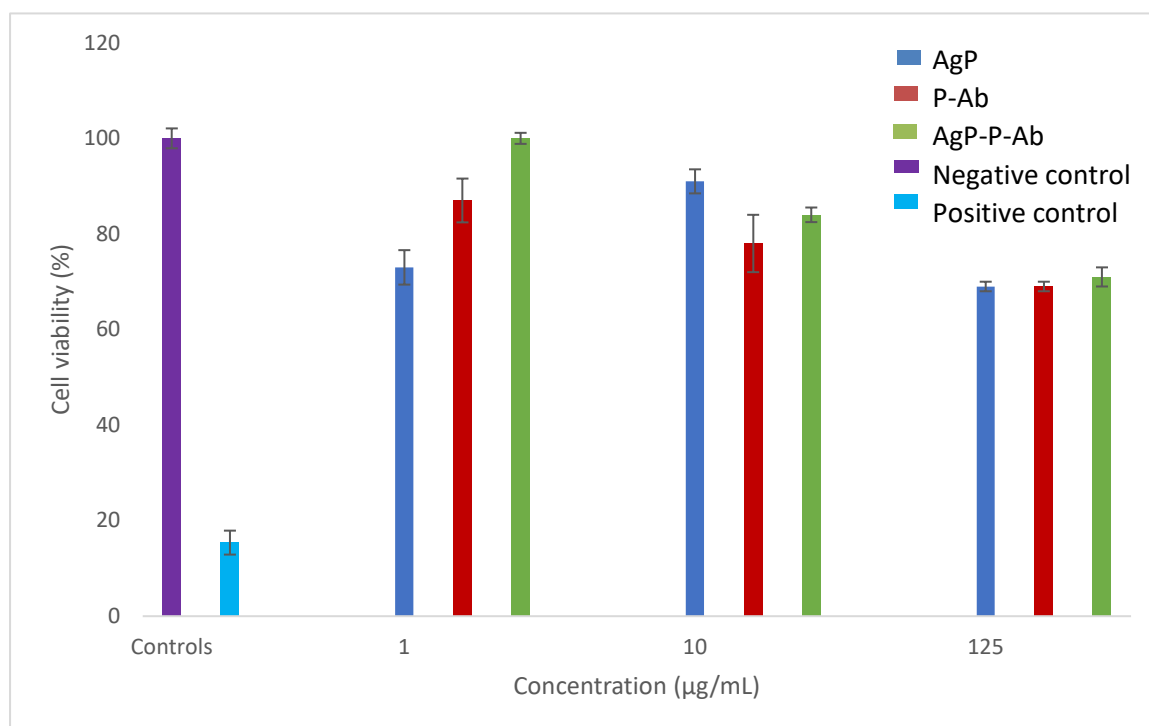


Figure 5. 20: Cell viability graph of AgP formulations at different concentrations.

Table 5. 5: Table of reagents in each well for AuNP.

	1	2	3	4	5	6	7
A	Media only	Media only	Media only	AuNP 1µg/mL	AuNP 1µg/mL	AuNP 1µg/mL	Hydrogen peroxide
B	Negative control	Negative control	Negative control	AuNP 10 µg/mL	AuNP 10 µg/mL	AuNP 10 µg/mL	Hydrogen peroxide
C	AuNP-P-Ab 1µg/mL	AuNP-P-Ab 1µg/mL	AuNP-P-Ab 1µg/mL	AuNP 125 µg/mL	AuNP 125 µg/mL	AuNP 125 µg/mL	Hydrogen peroxide
D	AuNP-P-Ab 10µg/mL	AuNP-P-Ab 10µg/mL	AuNP-P-Ab 10µg/mL	P-Ab 1µg/mL	P-Ab 1µg/mL	P-Ab 1µg/mL	
E	AuNP-P-Ab 125µg/mL	AuNP-P-Ab 125µg/mL	AuNP-P-Ab 125µg/mL	P-Ab 10 µg/mL	P-Ab 10 µg/mL	P-Ab 10 µg/mL	
F				P-Ab 125 µg/mL	P-Ab 125 µg/mL	P-Ab 125 µg/mL	

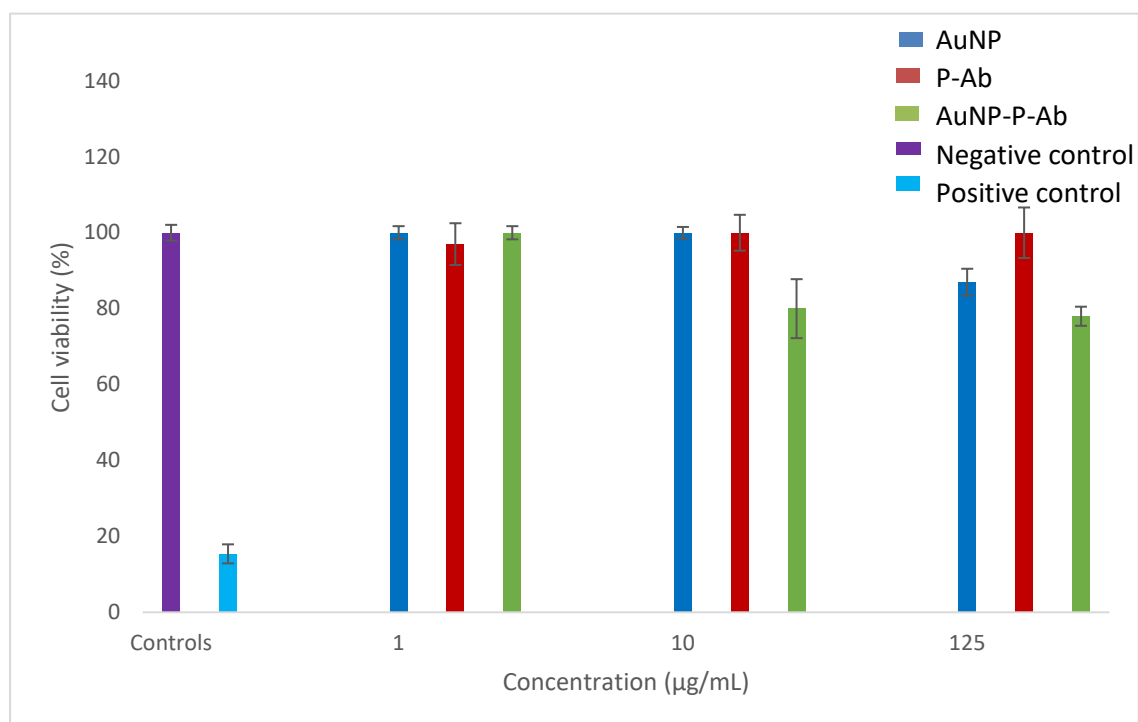


Figure 5. 21: Cell viability graph of AuNP formulations at different concentrations.

Table 5. 6: Table of reagents in each well for CuNP.

	1	2	3	4	5	6	7
A	Media only	Media only	Media only	CuNP 1µg/mL	CuNP 1µg/mL	CuNP 1µg/mL	Hydrogen peroxide
B	Negative control	Negative control	Negative control	CuNP 10 µg/mL	CuNP 10 µg/mL	CuNP 10 µg/mL	Hydrogen peroxide
C	CuNP-P-Ab 1µg/mL	CuNP-P-Ab 1µg/mL	CuNP-P-Ab 1µg/mL	CuNP 125 µg/mL	CuNP 125 µg/mL	CuNP 125 µg/mL	Hydrogen peroxide
D	CuNP-P-Ab 10µg/mL	CuNP-P-Ab 10µg/mL	CuNP-P-Ab 10µg/mL	P-Ab 1µg/mL	P-Ab 1µg/mL	P-Ab 1µg/mL	
E	CuNP-P-Ab 125µg/mL	CuNP-P-Ab 125µg/mL	CuNP-P-Ab 125µg/mL	P-Ab 10 µg/mL	P-Ab 10 µg/mL	P-Ab 10 µg/mL	
F				P-Ab 125 µg/mL	P-Ab 125 µg/mL	P-Ab 125 µg/mL	

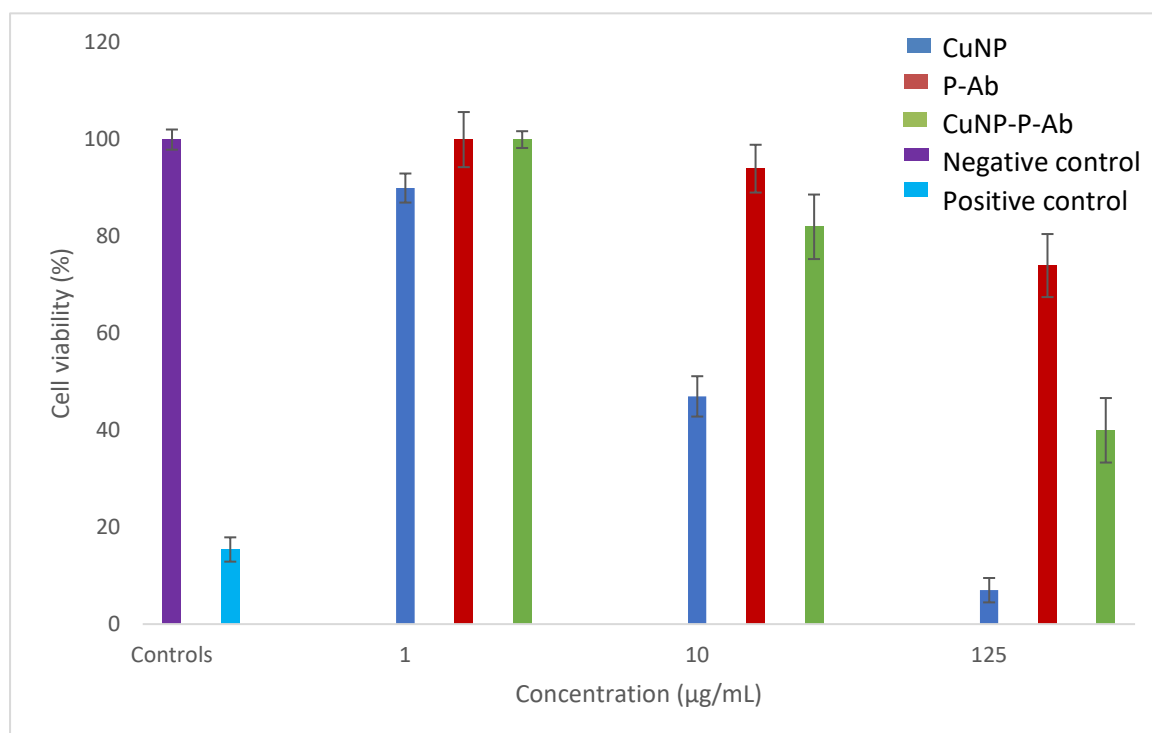


Figure 5. 22: Cell viability graph of CuNP formulations at different concentrations.

5.5 Conclusion

In this thesis, the hypothesis was to determine if polymeric composites, made up of an insoluble drug and metallic nanoparticles can be prepared using the EHDA technique. If these composites can demonstrate good drug release data, enhanced antibacterial efficacy through synergy and non-toxicity towards mammalian cells, then the use of the EHDA system has been successful. Results presented in each chapter show this hypothesis was achieved. Metallic nanoparticles were synthesised varying in morphology and size. These particles were incorporated into a polymer drug suspension and then successfully electrosprayed as SEM/EDS analysis confirmed. Further analysis including ATR-FTIR, DSC, TGA and XRD confirmed AMX had been embedded within the PLGA matrix and now taken a more amorphous state. These synthesised composites were then analysed to confirm how much drug was present, through release studies of the drug over 24 hours and the antibacterial efficacy.

Polymeric composites synthesised, showed successful drug loading, with varying encapsulation efficiencies, F2 had an encapsulation efficiency of 24.89%, as expected as the drug was insoluble therefore drug loading and encapsulation efficiencies would be low. For formulations F3-F7 the drug loading and encapsulation efficiencies increased, this was attributed to the increase in surface area and increased hydrolysis of polymeric chains; here once again formulation F5 as expected showed the highest drug loading due to its morphology increasing the surface area. The key point here was to show electrospraying was a suitable method to encapsulate an insoluble drug within a polymer to form microparticles.

Drug release data showed, similar trends to drug loading (%), F2 as expected released the lowest amount of drug over 24 hours at 18% and F5 released the most drug over the same time frame at 56%. The antibacterial tests showed all metallic nanoparticles synthesised possess antibacterial efficacy, apart from AuNPs as shown in disk diffusion images in Figure 5.4. The full formulations prepared were also tested and their antibacterial efficacy; the key here was to understand if the use of AMX and metallic nanoparticles can enhance antibacterial efficacy. Results using the bacteria *S. aureus*, showed this is possible, as zone sizes increased especially for formulations F3-F5, however when using penicillin resistant *E. coli* results proved inconclusive, as no zone sizes increased apart from zone size for formulation F5.

The optical density (OD) curves for metallic nanoparticles show inhibition of bacterial growth over the 24 hours, similar to the disk diffusion results, silver nanomaterials showed the greatest efficacy. To determine antibacterial properties of samples, the growth phases upon the curve

were analysed. A longer lag phase, shorter exponential growth phase and a quicker start to the death phase, all may indicate antibacterial efficacy. Results presented in Figure 5.10 and 5.12 were compared for *S. aureus* and *E. coli* respectively. Data obtained showed bacterial growth inhibition, as curves remained at similar OD values with no curve following the bacterial growth curve. The AgNPs once again showed to have the most antibacterial efficacy, as OD values were reduced greatly in the presence of AgNPs, this result was consistent against both bacteria used. For the full formulations F2-F7, the curves all grew following the bacterial growth curve, here antibacterial efficacy was assessed by comparing the length of the lag phase, F5 proved to have the most antibacterial efficacy as it extended lag times against both bacteria for the longest as seen in Figures 5.14 and 5.16. From the combination of bacterial disk diffusion and optical density data, the synergy effect, or enhancement of antibacterial activity when combining two antibacterial agents was shown. Formulations F3-F5 showed the most promise as possible future novel antibacterial composites. Thereafter, cell culture studies namely the MTT assay was carried out to confirm the cytotoxicity of the formulations, as drug release and antibacterial results proved promising. MTT assay results showed full formulations F2-F7 varied in viability. All formulations were assessed at concentrations of 1, 10 and 125 $\mu\text{g}/\text{mL}$. F2 was viable as on average the viability remained between 80-90% at the highest concentration, the formulations F3-F6 were also viable, as they remained close to the range of 80-90%, however F7 was toxic, at 125 $\mu\text{g}/\text{mL}$ viability reduced to 40%.

Overall the thesis followed a story, to synthesise polymeric drug composite particles with the inclusion of metallic nanoparticles; at each step of the way synthesis was successful, and the composites were formulated. Antibacterial tests proved the efficacy and also showed enhanced efficacy when combining antibacterial agents, as opposed to when used alone.

5.6 Future work

In the future, the concentrations of excipients will also be varied to develop a bigger range of composites with varying amounts of polymer, drug and metallic nanoparticles, in order to assess the differences in particle morphologies, drug release data and antibacterial efficacy.

Another aspect would be to understand the antibacterial effect of polymer and metallic composites together - to see their antibacterial effects without the drug and to assess how the leeching of ions occurs from metallic particles embedded within a polymer. Formulation F5 would be tested upon further as it showed promising sustained drug release data and antibacterial efficacy. Further testing would include drug release over a prolonged number of days, antibacterial efficacy against a bigger range of bacteria and strains and increasing the number of days in incubation.

Furthermore, assessing the effects of different antibiotics aside from amoxicillin to form a larger range of drug composites of F5. Upon further research and testing, a scale up method would be applied in order to develop an alternative novel antibacterial drug delivery system.

Results from cell culture studies showed that when incorporating metallic particles like silver and copper, known to leach ions within a polymeric system the resulting toxicity towards cells can significantly be reduced. This also shows potential as a future study, as toxicity of metallic materials remains the main issue preventing use within the body, if such results and further research show reduction in toxicity through incorporation then alternative therapies could be plentiful.

Chapter 6 – References

Abdelmalek, Ilham, Kaddour, Guemra, Boukhouya, Imene, Bakouri, Hichem, Amrane, Meriem, 2018. Controlled release of amoxicillin from PMMA and Poly (Butylsuccinate) microspheres. *Chemistry International*, 4.

Abdelrazek Khalil, K. 2013. Preparation and Characterization of Electrospun PLGA/silver Composite Nanofibers for Biomedical Applications. *International Journal of Electrochemical Science*, 8, 3483 - 3493.

Abed, N., Couvreur, P., 2014. Nanocarriers for antibiotics: A promising solution to treat intracellular bacterial infections. *International Journal of Antimicrobial Agents*, 43, 485-496.

Agarwal, A., Agrawal, R., Khandelwal, N., Invernizzi, A., Aggarwal, K., Sharma, A., Singh, R., Bansal, R., Sharma, K., Singh, N., Gupta, V., 2017. Choroidal Structural Changes in Tubercular Multifocal Serpiginoid Choroiditis. *Ocular Immunology and Inflammation*, 26, 838-844.

Agel, M., Baghdan, E., Pinnapireddy, S., Lehmann, J., Schäfer, J., Bakowsky, U., 2019. Curcumin loaded nanoparticles as efficient photoactive formulations against gram-positive and gram-negative bacteria. *Colloids and Surfaces B: Biointerfaces*, 178, 460-468.

Ahamed, M., Siddiqui, M., Akhtar, M., Ahmad, I., Pant, A., Alhadlaq, H., 2010. Genotoxic potential of copper oxide nanoparticles in human lung epithelial cells. *Biochemical and Biophysical Research Communications*, 396.578-583.

Ahmad, B., Hafeez, N., Bashir, S., Rauf, A., Mujeeb-ur-Rehman, 2017. Phytofabricated gold nanoparticles and their biomedical applications. *Biomedicine & Pharmacotherapy*, 89, 414-425.

Ahmad, Z., Zhang, H., Farook, U., Edirisinghe, M., Stride, E., Colombo, P., 2008. Generation of multilayered structures for biomedical applications using a novel tri-needle coaxial device and electrohydrodynamic flow. *Journal of The Royal Society Interface*, 5, 1255-1261.

Ahmadian-Fard-Fini, S., Salavati-Niasari, M., Ghanbari, D., 2018. Hydrothermal green synthesis of magnetic Fe₃O₄-carbon dots by lemon and grape fruit extracts and as a photoluminescence sensor for detecting of E. coli bacteria. *Spectrochimica Acta Part A: Molecular and Biomolecular Spectroscopy*, 203, 481-493.

Ahn, Y., Park, S., Kim, G., Hwang, Y., Lee, C., Shin, H., Lee, J., 2006. Development of high efficiency nanofilters made of nanofibers. *Current Applied Physics*, 6, 1030-1035.

Akova, M., 2016. Epidemiology of antimicrobial resistance in bloodstream infections. *Virulence*, 7, 252-266.

Alharbi, A., Alarifi, I., Khan, W. and Asmatulu, R. (2016). Synthesis and Analysis of Electrospun SrTiO₃Nanofibers with NiO Nanoparticles Shells as Photocatalysts for Water Splitting. *Macromolecular Symposia*, 365(1), pp.246-257.

Ali, H., 2014. Evaluation of a Nanodispersion Formulation Prepared through Microfluidic Reactors for Pulmonary Delivery of Budesonide Using Nebulizers. *Iranian Journal of Pharmaceutical Research*, 3, 785-795.

Alimohammadi, S., Salehi, R., Amini, N., Davaran, S., 2012. Synthesis and Physicochemical Characterization of Biodegradable PLGA-based Magnetic Nanoparticles Containing Amoxicilin. *Bulletin of the Korean Chemical Society*, 33, 3225-3232.

Alkilany, A., Abulateefeh, S., Murphy, C., 2018. Facile Functionalization of Gold Nanoparticles with PLGA Polymer Brushes and Efficient Encapsulation into PLGA Nanoparticles: Toward Spatially Precise Bioimaging of Polymeric Nanoparticles. *Particle & Particle Systems Characterization*, 1800414.

Allahverdiyev, A., Kon, K., Abamor, E., Bagirova, M., Rafailovich, M., 2011. Coping with antibiotic resistance: combining nanoparticles with antibiotics and other antimicrobial agents. *Expert Review of Anti-infective Therapy*, 9, 1035-1052.

Almajhdi, F., Fouad, H., Khalil, K., Awad, H., Mohamed, S., Elsarnagawy, T., Albarrag, A., Al-Jassir, F., Abdo, H., 2013. In-vitro anticancer and antimicrobial activities of PLGA/silver nanofiber composites prepared by electrospinning. *Journal of Materials Science: Materials in Medicine*, 25, 1045-1053.

Almany, L., Seliktar, D., 2005. Biosynthetic hydrogel scaffolds made from fibrinogen and polyethylene glycol for 3D cell cultures. *Biomaterials*, 26, 2467-2477.

Al-thabaiti, S., Malik, A., Maqsood, Al-youbi, Abdulrahman, Khan, Hussain, Z., Ijaz, J., 2013. Effects of Surfactant and Polymer on the Morphology of Advanced Nanomaterials in Aqueous Solution. *International journal of electrochemical science*, 8, 204-218.

Anu Bhushani, J., Anandharamakrishnan, C., 2014. Electrospinning and electrospraying techniques: Potential food based applications. *Trends in Food Science & Technology*, 38, 21-33.

Ardila, N., Aji, Z., Heuzey, M., Aji, A., 2018. Chitosan electrospraying: Mapping of process stability and micro and nanoparticle formation. *Journal of Aerosol Science*, 126, 85-98.

Argudín, M., Mendoza, M., González-Hevia, M., Bances, M., Guerra, B., Rodicio, M., 2012. Genotypes, Exotoxin Gene Content, and Antimicrobial Resistance of *Staphylococcus aureus* Strains Recovered from Foods and Food Handlers. *Applied and Environmental Microbiology*, 78, 2930-2935.

Arya, N., Chakraborty, S., Dube, N., Katti, D., 2009. Electro spraying: A facile technique for synthesis of chitosan-based micro/nanospheres for drug delivery applications. *Journal of Biomedical Materials Research Part B: Applied Biomaterials*, 88B, 17-31.

Asoro, M., Damiano, J., Ferreira, P., 2009. Size Effects on the Melting Temperature of Silver Nanoparticles: In-Situ TEM Observations. *Microscopy and Microanalysis*, 15, 706-707.

Avendaño, C., Menéndez, J., 2008. Cancer Chemoprevention. *Medicinal Chemistry of Anticancer Drugs*, 417-429.

Awasthi, R., Kulkarni, G., Pawar, V., Garg, G., 2011. Optimization Studies on Gastroretentive Floating System Using Response Surface Methodology. *AAPS PharmSciTech*, 13, 85-93.

Azizi, M., Ghourchian, H., Yazdian, F., Dashtestani, F., AlizadehZeinabad, H., 2017. Cytotoxic effect of albumin coated copper nanoparticle on human breast cancer cells of MDA-MB 231. *PLOS ONE*, 12, 0188639.

Bai, M., Hu, Y., 2014. Development of alpha-lipoic acid encapsulated chitosan monodispersed particles using an electro spray system: synthesis, characterisations and anti-inflammatory evaluations. *Journal of Microencapsulation*, 31, 373-381.

Barrientos, L., Bignon, A., Gueguen, C., de Chaisemartin, L., Gorges, R., Sandré, C., Mascarell, L., Balabanian, K., Kerdine-Römer, S., Pallardy, M., Marin-Esteban, V., Chollet-Martin, S., 2014. Neutrophil Extracellular Traps Downregulate Lipopolysaccharide-Induced Activation of Monocyte-Derived Dendritic Cells. *The Journal of Immunology*, 193, 5689-5698.

Bartemes, K., Kita, H., 2018. Innate and adaptive immune responses to fungi in the airway. *Journal of Allergy and Clinical Immunology*, 142, 353-363.

Baumgarten, P., 1971. Electrostatic spinning of acrylic microfibers. *Journal of Colloid and Interface Science*, 36, 71-79.

Beck, D. E., Wexner, S. D., 1990. AIDS and the colorectal surgeon. Part II; anorectal diseases. *Postgrad Adv Colorectal Surg*, 2, 1-13.

Beer, C., Foldbjerg, R., Hayashi, Y., Sutherland, D., Autrup, H., 2012. Toxicity of silver nanoparticles—Nanoparticle or silver ion?. *Toxicology Letters*, 208, 286-292.

Behera, S., Patra, J., Pramanik, K., Panda, N., Thatoi, H., 2012. Characterization and Evaluation of Antibacterial Activities of Chemically Synthesized Iron Oxide Nanoparticles. *World Journal of Nano Science and Engineering*, 2, 196-200.

Besinis, A., Peralta, T., Handy, R., 2014. The antibacterial effects of silver, titanium dioxide and silica dioxide nanoparticles compared to the dental disinfectant chlorhexidine on *Streptococcus mutans* using a suite of bioassays. *Nanotoxicology*, 8, 1–16.

Bessey, P., 2007. Wound care. *Total Burn Care*, 127-135.

Betts, J., Hornsey, M. and La Ragione, R., 2018. Novel Antibacterials: Alternatives to Traditional Antibiotics. *Advances in Microbial Physiology*, 123-169.

Beyth, N., Houry-Haddad, Y., Domb, A., Khan, W., Hazan, R., 2015. Alternative Antimicrobial Approach: Nano-Antimicrobial Materials. *Evidence-Based Complementary and Alternative Medicine*, 1-16.

Bhalla, A., Bansal, N., Kumar, S., Bischoff, K., Sani, R., 2013. Improved lignocellulose conversion to biofuels with thermophilic bacteria and thermostable enzymes. *Bioresource Technology*, 128, 751-759.

Bhardwaj, N., Kundu, S., 2010. Electrospinning: A fascinating fiber fabrication technique. *Biotechnology Advances*, 28, 325-347.

Biesta-Peters, E., Reij, M., Joosten, H., Gorris, L., Zwietering, M., 2010. Comparison of Two Optical-Density-Based Methods and a Plate Count Method for Estimation of Growth Parameters of *Bacillus cereus*. *Applied and Environmental Microbiology*, 76, 1399-1405.

Biglari, H., Mojtahedi, A., Taheri Kalani, M., Ashraf, A., Shakiba, M., 2019. Investigation of vancomycin susceptibility and toxic shock syndrome toxin 1 gene among *Staphylococcus aureus* strains isolated from patients and ICU staff in the north of Iran. *Gene Reports*, 14, 138-141.

Bloomfield, G., Alenezi, F., Barasa, F., Lumsden, R., Mayosi, B., Velazquez, E., 2015. Human Immunodeficiency Virus and Heart Failure in Low- and Middle-Income Countries. *JACC: Heart Failure*, 3, 579-590.

Bock, N., Dargaville, T., Woodruff, M., 2012. Electrospaying of polymers with therapeutic molecules: State of the art. *Progress in Polymer Science*, 37, 1510-1551.

Bock, N., Woodruff, M., Hutmacher, D., Dargaville, T., 2011. Electro spraying, a Reproducible Method for Production of Polymeric Microspheres for Biomedical Applications. *Polymers*, 3, 131-149.

Boda, S., Li, X., Xie, J., 2018. Electro spraying an enabling technology for pharmaceutical and biomedical applications: A review. *Journal of Aerosol Science*, 125, 164-181.

Bogdanović, U., Lazić, V., Vodnik, V., Budimir, M., Marković, Z., Dimitrijević, S., 2014. Copper nanoparticles with high antimicrobial activity. *Materials Letters*, 128, 75-78.

Boland, E., Wnek, G., Simpson, D., Pawlowski, K., Bowlin, G., 2001. Tailoring tissue engineering scaffolds using electrostatic processing techniques: a study of poly(glycolic acid) electrospinning. *Journal of macromolecular science Part A*, 38, 231-1243.

Bondarenko, O., Ivask, A., Käkinen, A., Kurvet, I., Kahru, A., 2013. Particle-Cell Contact Enhances Antibacterial Activity of Silver Nanoparticles. *PLoS ONE*, 8, 64060.

Bornat, A., 1987. Production of electrostatically spun products. *Us Patent* 4689186.

Bradberry, S., 2007. Acetone. *Medicine*, 35, 581.

Brandelli, A., Lopes, N. and Boelter, J., 2017. Food applications of nanostructured antimicrobials. *Food Preservation*, 35-74.

Browne, E., Charifou, R., Worku, Z., Babu, R., Healy, A. 2019. Amorphous solid dispersions of ketoprofen and poly-vinyl polymers prepared via electro spraying and spray drying: A comparison of particle characteristics and performance. *International Journal of Pharmaceutics*, 566, 173-184.

Bu, Y., Chen, Z., Li, W., 2013. Dramatically enhanced photocatalytic properties of Ag-modified graphene–ZnO quasi-shell–core heterojunction composite material. *RSC Advances*, 3, 24118.

Buchko, C., Chen, L., Shen, Y., Martin, D., 1999. Processing and microstructural characterization of porous biocompatible protein polymer thin films. *Polymer*, 40, 7397-7407.

Byarugaba, D., 2010. Mechanisms of antimicrobial resistance. In *Antimicrobial Resistance in Developing Countries*, Springer. 2010. 15-26.

Byrd, A., Belkaid, Y., Segre, J., 2018. The human skin microbiome. *Nature Reviews Microbiology*, 16, 143-155.

Carbone, M., Donia, D., Sabbatella, G., Antiochia, R., 2016. Silver nanoparticles in polymeric matrices for fresh food packaging. *Journal of King Saud University - Science*, 28, 273-279.

Carney, E. 2011. Ethylene glycol. *Reproductive and Developmental Toxicology*, 607-615.

Casadevall, A., 2012. Fungi and the Rise of Mammals. *PLoS Pathogens*, 8, 1002808.

Chae, D., Kim, B., 2005. Effects of zinc oxide nanoparticles on the physical properties of polyacrylonitrile. *Journal of Applied Polymer Science*, 99, 1854-1858.

Chaibenjawong, P., Foster, S., 2010. Desiccation tolerance in *Staphylococcus aureus*. *Archives of Microbiology*, 193, 125-135.

Chakraborty, S., Liao, I., Adler, A., Leong, K., 2009. Electrohydrodynamics: A facile technique to fabricate drug delivery systems. *Advanced Drug Delivery Reviews*, 61, 1043-1054.

Chambers, H., DeLeo, F., 2009. Waves of resistance: *Staphylococcus aureus* in the antibiotic era. *Nature Reviews Microbiology*, 7, 629-641.

Chatterjee, A., Chakraborty, R., Basu, T., 2014. Mechanism of antibacterial activity of copper nanoparticles. *Nanotechnology*, 25, 135101.

Chatterjee, A., Sarkar, R., Chattopadhyay, A., Aich, P., Chakraborty, R., Basu, T., 2012. A simple robust method for synthesis of metallic copper nanoparticles of high antibacterial potency against *E. coli*. *Nanotechnology*, 23, 085103.

Chaturvedi, Kaushalendra, Chitlange, Sohan., 2011. Simultaneous Determination of Amoxicillin Trihydrate and Ambroxol Hydrochloride in Solid Dosage Form By Spectrophotometric and Stability Indicating RP-HPLC Method. *Asian Journal of Research in Chemistry*, 4, 1025-1030.

Chaubey, N., Sahoo, A., Chattopadhyay, A., Ghosh, S., 2014. Silver nanoparticle loaded PLGA composite nanoparticles for improving therapeutic efficacy of recombinant IFN γ by targeting the cell surface. *Biomaterials Science*, 2, 1080.

Chen, C., Wang, L., Yu, H., Jiang, G., Yang, Q., Zhou, J., Xiang, W., Zhang, J., 2008. Study on the growth mechanism of silver nanorods in the nanowire-seeding polyol process. *Materials Chemistry and Physics*, 107, 13-17.

Chong, E., Phan, T., Lim, I., Zhang, Y., Bay, B., Ramakrishna, S., Lim, C., 2007. Evaluation of electrospun PCL/gelatin nanofibrous scaffold for wound healing and layered dermal reconstitution. *Acta Biomaterialia*, 3, 321-330.

Chopade, B., Salunke, G., Ghosh, S., Santosh, R., Khade, S., Vashisth, P., Kale, T., Chopade, S., Pruthi, V., Kundu, G., Bellare, J., 2014. Rapid efficient synthesis and characterization of silver, gold, and bimetallic nanoparticles from the medicinal plant *Plumbago zeylanica* and their application in biofilm control. *International Journal of Nanomedicine*, 2635.

Christensen, G., Brüggemann, H., 2014. Bacterial skin commensals and their role as host guardians. *Beneficial Microbes*, 5, 201-215.

Christenson and Korgenski, 2012. 286 - Laboratory Diagnosis of Infection Due to Bacteria, Fungi, Parasites, and Rickettsiae. *Principles and Practice of Pediatric Infectious Diseases (Fourth Edition)*, 4, 1373-1384.

Chuang, Y., Huang, Y., Lin, T., 2005. Toxic Shock Syndrome in Children. *Pediatric Drugs*, 7, 11-25.

Chung, Y., Copeland, L., Doerfler, D., Ward, M., 2010. The relative allergenicity of *Stachybotrys chartarum* compared to house dust mite extracts in a mouse model. *Inhalation Toxicology*, 22, 460-468.

Cioffi, N., Torsi, L., Ditaranto, N., Tantillo, G., Ghibelli, L., Sabbatini, L., Bleve-Zacheo, T., D'Alessio, M., Zambonin, P., Traversa, E., 2005. Copper Nanoparticle/Polymer Composites with Antifungal and Bacteriostatic Properties. *Chemistry of Materials*, 17, 5255-5262.

Cole, L., Kramer, P., 2016. Bacteria, Virus, Fungi, and Infectious Diseases. *Human Physiology, Biochemistry and Basic Medicine*, 193-196.

Conly, J., Johnston, B., 2005 Where are all the new antibiotics? The new antibiotic paradox. *Canadian Journal of Infectious Diseases and Medical Microbiology*, 16, 159–160.

Copetti, M., 2019. Fungi as industrial producers of food ingredients. *Current Opinion in Food Science*, 25, 52-56.

Corbierre, M., Cameron, N., Sutton, M., Mochrie, S., Lurio, L., Ruhm, A., Lennox, R., 2001. Polymer-stabilised gold nanoparticles and their incorporation into polymer matrices. *Journal of the American Chemical Society*, 123, 10411-10412.

Coskun, S., Aksoy, B., Unalan, H., 2011. Polyol Synthesis of Silver Nanowires: An Extensive Parametric Study. *Crystal Growth & Design*, 11, 4963-4969.

Crago, B., Ferrato, C., Drews, S., Svenson, L., Tyrrell, G., Louie, M., 2012. Prevalence of *Staphylococcus aureus* and methicillin-resistant *S. aureus* (MRSA) in food samples associated with foodborne illness in Alberta, Canada from 2007 to 2010. *Food Microbiology*, 32, 202-205.

Cuya Huaman, J., Urushizaki, I., Jeyadevan, B., 2018. Large-Scale Cu Nanowire Synthesis by PVP-Ethylene Glycol Route. *Journal of Nanomaterials*, 1-10.

D'Avila Carvalho Erbeta, C., 2012. Synthesis and Characterization of Poly(D,L-Lactide-co-Glycolide) Copolymer. *Journal of Biomaterials and Nanobiotechnology*, 03, 208-225.

Dang, T., Le, T., Fribourg-Blanc, E. and Dang, M., 2011. Synthesis and optical properties of copper nanoparticles prepared by a chemical reduction method. *Advances in Natural Sciences: Nanoscience and Nanotechnology*, 2, 015009.

Dasgupta, A. and Wahed, A., 2014. Testing for Ethyl Alcohol (Alcohol) and Other Volatiles. *Clinical Chemistry, Immunology and Laboratory Quality Control*, 317-335.

Dasgupta, A., Klein, K., 2014. Oxidative Stress Induced by Household Chemicals. *Antioxidants in Food, Vitamins and Supplements*, 77-95.

David, M., Dryden, M., Gottlieb, T., Tattevin, P., Gould, I., 2017. Recently approved antibacterials for methicillin-resistant *Staphylococcus aureus* (MRSA) and other Gram-positive pathogens: the shock of the new. *International Journal of Antimicrobial Agents*, 50, 303-307.

de Faria, A., Martinez, D., Meira, S., de Moraes, A., Brandelli, A., Filho, A. and Alves, O. (2014). Anti-adhesion and antibacterial activity of silver nanoparticles supported on graphene oxide sheets. *Colloids and Surfaces B: Biointerfaces*, 113, pp.115-124.

de Melo, A., Levesque, S., Moineau, S., 2018. Phages as friends and enemies in food processing. *Current Opinion in Biotechnology*, 49, 185-190.

Deepashree, C., Kumar, J., Komal, Prasad, Devi, A., Zarei, Mahsa, Gopal, Shubha, 2013. FTIR Spectroscopic Studies on *Cleome gynandra* – Comparative Analysis of Functional Group Before and After Extraction. *Romanian Journal of Biophysics*, 22, 137-143.

DeLeo, F., Otto, M., Kreiswirth, B., Chambers, H., 2010. Community-associated methicillin-resistant *Staphylococcus aureus*. *The Lancet*, 375, 1557-1568.

Deng, H., McShan, D., Zhang, Y., Sinha, S., Arslan, Z., Ray, P., Yu, H., 2016. Mechanistic Study of the Synergistic Antibacterial Activity of Combined Silver Nanoparticles and Common Antibiotics. *Environmental Science & Technology*, 50, 8840-8848.

Denning, D., 2006. The link between fungi and severe asthma: a summary of the evidence. *European Respiratory Journal*, 27, 615-626.

Des Jarlais, D., 2013. Systematic review research on needle/syringe programs and opiate substitution programs in low- and middle-income countries. *Journal of Food and Drug Analysis*, 21, 59-61.

Desai, R., Mankad, V., Gupta, S., Jha, P., 2012. Size Distribution of Silver Nanoparticles: UV-Visible Spectroscopic Assessment. *Nanoscience and Nanotechnology Letters*, 4, 30-34.

Dever, L., Dermody, T., 1991. Mechanisms of bacterial resistance to antibiotics. *Archives of Internal Medicine*, 151, 886-95.

Ding, L., Lee, T., Wang, C., 2005. Fabrication of monodispersed Taxol-loaded particles using electrohydrodynamic atomization. *Journal of Controlled Release*, 102, 395-413.

Dizaja, S., Lotfipoura, F., Barzegar-Jalalia, M., Zarrintana, M., Adibkia, K., 2014. Antimicrobial activity of the metals and metal oxide nanoparticles. *Materials Science and Engineering: C*, 44, 278-284.

Dong, X., Ji, X., Wu, H., Zhao, L., Li, J., Yang, W., 2009. Shape Control of Silver Nanoparticles by Stepwise Citrate Reduction. *The Journal of Physical Chemistry C*, 113, 6573-6576.

Doshi, J., Reneker, D., 1995. Electrospinning process and applications of electrospun fibers. *Journal of Electrostatics*, 35, 151-160.

Downs, S., Mitakakis, T., Marks, G., Car, N., Belousova, E., Leüppi, J., Xuan, W., Downie, S., Tobias, A., Peat, J., 2001. Clinical Importance of *Alternaria* Exposure in Children. *American Journal of Respiratory and Critical Care Medicine*, 164, 455-459.

Duncan, S., Chang, H., 2012. Implications of Light Energy on Food Quality and Packaging Selection. *Advances in Food and Nutrition Research Volume 67*, 25-73.

Dykman, L., Khlebtsov, N., 2012. Gold nanoparticles in biomedical applications: recent advances and perspectives. *Chemical Society Reviews*, 41, 2256-2282.

Elbehiry, A., Al-Dubaib, M., Marzouk, E., Moussa, I., 2018. Antibacterial effects and resistance induction of silver and gold nanoparticles against *Staphylococcus aureus* -induced mastitis and the potential toxicity in rats. *MicrobiologyOpen*, 8, 00698.

El-Houssiny, A., Ward, A., Mostafa, D., Abd-El-Messieh, S., Abdel-Nour, K., Darwish, M., Khalil, W., 2016. Drug-polymer interaction between glucosamine sulfate and alginate nanoparticles: FTIR, DSC and dielectric spectroscopy studies.

El-Shahawy, A., Abo El-Ela, F., Mohamed, N., Eldine, Z., El Roubay, W., 2018. Synthesis and evaluation of layered double hydroxide/doxycycline and cobalt ferrite/chitosan nanohybrid efficacy on gram positive and gram negative bacteria. *Materials Science and Engineering: C*, 91, 361-371.

Esteban-Cubillo, A., Pecharromán, C., Aguilar, E., Santarén, J., Moya, J., 2006. Antibacterial activity of copper monodispersed nanoparticles into sepiolite. *Journal of Materials Science*, 41, 5208-5212.

Fang, H., Liu, A., Sun, J., Kitz, A., Dirsch, O., Dahmen, U., 2013. Granulocyte Colony Stimulating Factor Induces Lipopolysaccharide (LPS) Sensitization via Upregulation of LPS Binding Protein in Rat. *PLoS ONE*, 8, 56654.

Faraji, A., Wipf, P., 2009. Nanoparticles in cellular drug delivery. *Bioorganic & Medicinal Chemistry*, 17, 2950-2962.

Faraji, S., Sadri, B., Vajdi Hokmabad, B., Jadidoleslam, N., Esmailzadeh, E., 2017. Experimental study on the role of electrical conductivity in pulsating modes of electrospraying. *Experimental Thermal and Fluid Science*, 81, 327-335.

Farokhzad, O., Langer, R., 2006. Nanomedicine: Developing smarter therapeutic and diagnostic modalities. *Advanced Drug Delivery Reviews*, 58, 1456-1459.

Felder, C., Blanco-Prieto, M., Heizmann, J., Merkle, H., Gander, B., 2003. Ultrasonic atomization and subsequent polymer desolvation for peptide and protein microencapsulation into biodegradable polyesters. *Journal of Microencapsulation*, 20, 553-567.

Feng, P., Weagant, F., Grant, M., Burkhardt, W., 2002. BAM: enumeration of *Escherichia coli* and the Coliform bacteria. *Bacteriological Analytical Manual*, 6, 1-13.

Fertala, A., Han, W., Ko, F., 2001. Mapping critical sites in collagen II for rational design of gene-engineered proteins for cell-supporting materials. *Journal of Biomedical Materials Research*, 57, 48-58.

Findley, K., Oh, J., Yang, J., Conlan, S., Deming, C., Meyer, J., Schoenfeld, D., Nomicos, E., Park, M., Kong, H., Segre, J., 2013. Topographic diversity of fungal and bacterial communities in human skin. *Nature*, 498, 367-370.

Fischbach, M., Walsh, C., 2009. Antibiotics for Emerging Pathogens. *Science*, 325, 1089-1093.

Fleurot, I., Aigle, M., Fleurot, R., Darrigo, C., Hennekinne, J., Gruss, A., Borezée-Durant, E., Delacroix-Buchet, A., 2014. Following Pathogen Development and Gene Expression in a Food Ecosystem: the Case of a *Staphylococcus aureus* Isolate in Cheese. *Applied and Environmental Microbiology*, 80, 5106-5115.

Fluit, A., 2012. Livestock-associated *Staphylococcus aureus*. *Clinical Microbiology and Infection*, 18, 735-744.

Fortunati, E., Latterini, L., Rinaldi, S., Kenny, J., Armentano, I., 2011. PLGA/Ag nanocomposites: in vitro degradation study and silver ion release. *Journal of Materials Science: Materials in Medicine*, 22, 2735-2744.

Foxman, B., 2013. Urinary Tract Infection. *Women and Health*, 553-564.

Franci, G., Falanga, A., Galdiero, S., Palomba, L., Rai, M., Morelli, G., Galdiero, M., 2015. Silver Nanoparticles as Potential Antibacterial Agents. *Molecules*, 20, 8856-8874.

Frenot, A., Chronakis, I., 2003. Polymer nanofibers assembled by electrospinning. *Current Opinion in Colloid & Interface Science*, 8, 64-75.

Friess, W., 1998. Collagen – biomaterial for drug delivery¹Dedicated to Professor Dr. Eberhard Nürnberg, Friedrich-Alexander-Universität Erlangen-Nürnberg, on the occasion of his 70th birthday.1. *European Journal of Pharmaceutics and Biopharmaceutics*, 45, 113-136.

Frost, M., Dempsey, M., Whitehead, D., 2017. The response of citrate functionalised gold and silver nanoparticles to the addition of heavy metal ions. *Colloids and Surfaces A: Physicochemical and Engineering Aspects*, 518, 15-24.

Gaitanis, G., Magiatis, P., Hantschke, M., Bassukas, I., Velegraki, A., 2012. The *Malassezia* Genus in Skin and Systemic Diseases. *Clinical Microbiology Reviews*, 25, 106-141.

Gakiya-Teruya, M., Palomino-Marcelo, L., Rodriguez-Reyes, J., 2018. Synthesis of Highly Concentrated Suspensions of Silver Nanoparticles by Two Versions of the Chemical Reduction Method. *Methods and Protocols*, 2, 3.

Gao, Y., Jiang, P., Song, L., Liu, L., Yan, X., Zhou, Z., Liu, D., Wang, J., Yuan, H., Zhang, Z., Zhao, X., Dou, X., Zhou, W., Wang, G., Xie, S., 2005. Growth mechanism of silver nanowires synthesized by polyvinylpyrrolidone-assisted polyol reduction. *Journal of Physics D: Applied Physics*, 38, 1061-1067.

Gasaymeh, S., 2010. Synthesis and Characterization of Silver/Polyvinylpyrrolidone (Ag/PVP) Nanoparticles Using Gamma Irradiation Techniques. *American Journal of Applied Sciences*. 7. 892-901.

Gawande, M., Goswami, A., Felpin, F., Asefa, T., Huang, X., Silva, R., Zou, X., Zboril, R., Varma, R., 2016. Cu and Cu-Based Nanoparticles: Synthesis and Applications in Catalysis. *Chemical Reviews*, 116, 3722-3811.

Gebeyehu, M., Chala, T., Chang, S., Wu, C., Lee, J., 2017. Synthesis and highly effective purification of silver nanowires to enhance transmittance at low sheet resistance with simple polyol and scalable selective precipitation method. *RSC Advances*, 7, 16139-16148.

Ghayempour, S., Mortazavi, S., 2014. Antibacterial activity of peppermint fragrance micro-nanocapsules prepared with a new electro spraying method. *Journal of Essential Oil Research*, 26, 492-498.

Ghozatloo, A., 2015. Investigation of Nanoparticles Morphology on Viscosity of Nanofluids and New Correlation for Prediction. *Journal of Nanostructures*, 5, 161-168.

Gibson, P., Schreuder-Gibson, H., Rivin, D., 1999. Electrospun fiber mats: Transport properties. *AIChE Journal*, 45, 190-195.

Goh, P., Ismail, A., Ng, B., 2017. Raman Spectroscopy. *Membrane Characterization*, 31-46.
Gomathi, T., Govindarajan, C., Rose H., M., Sudha, P., Imran, P., Venkatesan, J., Kim, S., 2014. Studies on drug-polymer interaction, in vitro release and cytotoxicity from chitosan particles excipient.

Gomes, J., Batra, J., Chopda, V., Kathiresan, P., Rathore, A., 2018. Monitoring and Control of Bioethanol Production from Lignocellulosic Biomass. *Waste Biorefinery*, 727-749.

Gorty, A., Barringer, S., 2011. Electrohydrodynamic spraying of chocolate. *Journal of Food Processing and Preservation*, 35, 542-549.

Gottlieb, M., Long, B., Koyfman, A., 2018. The Evaluation and Management of Toxic Shock Syndrome in the Emergency Department: A Review of the Literature. *The Journal of Emergency Medicine*, 54, 807-814.

Grayson, A., Cima, M., Langer, R., 2005. Size and temperature effects on poly(lactic-co-glycolic acid) degradation and microreservoir device performance.

Grice, E., Segre, J., 2011. The skin microbiome. *Nature Reviews Microbiology*, 9, 244-253.

Gubler, D., 1998. Dengue and Dengue Hemorrhagic Fever. *Clinical Microbiology Reviews*, 11, 480-496.

Guo, H., Xing, G., Yang, Z., 2015. The Controllable Synthesis of Silver Nanowires by Using the Polyol Method with Trace Agent. *Proceedings of the 2015 International Symposium on Material, Energy and Environment Engineering*.

Gupta, A., Bhardwaj, S., Sharma, A., Kim, K., Deep, A., 2019. Development of an advanced electrochemical biosensing platform for *E. coli* using hybrid metal-organic framework/polyaniline composite. *Environmental Research*, 171, 395-402.

Hahn, T., Botzenhart, K., Schweinsberg, F., 2019. Toxic Effects of Solvent Exposure. *Handbook of Solvents*, 1347-1454.

Haider, M., Mehdi, M., 2014. Study of morphology and Zeta Potential analyser for the Silver Nanoparticles: *International Journal of Scientific & Engineering Research*, 5.

Hair, B., Conley, M., Wienclaw, T., Conley, M., Berges, B., 2018. Synergistic Activity of Silver Nanoparticles and Vancomycin Against a Spectrum of *Staphylococcus aureus* Biofilm Types.

Haj Ahmad, R., Elkordy, A., Chaw, C., Moore, A., 2013. Compare and contrast the effects of surfactants (Pluronic®F-127 and Cremophor®EL) and sugars (β -cyclodextrin and inulin) on properties of spray dried and crystallised lysozyme. *European Journal of Pharmaceutical Sciences*, 49, 519-534.

Haj-Ahmad, R., Rasekh, M., Nazari, K., Li, Y., Fu, Y., Li, B., Zhang, Q., Xia, Z., Liu, H., Gu, T., Wang, G., Kucuk, I., Khan, H., Arshad, M., Li, X., Ahmad, Z., 2015. EHDA Spraying: A Multi-Material Nano-Engineering Route, 21, 3239–3247.

Hajipour, M., Fromm, K., Ashkarran, A., Jimenez de Aberasturi, D., Ruiz de Larramendi, I., Rojo, T., Serpooshan, V., Parak, W., Mahmoudi, M., 2012. Antibacterial properties of nanoparticles. Trends in Biotechnology, 12, 499–511.

Hajjeh, R., Reingold, A., Weil, A., Shutt, K., Schuchat, A., Perkins, B., 1999. Toxic Shock Syndrome in the United States: Surveillance Update, 1979–1996. Emerging Infectious Diseases, 5, 807-810.

Hameed, B., Bhatt, C., Nagaraj, B., Suresh, A., 2018. Chromatography as an Efficient Technique for the Separation of Diversified Nanoparticles. Nanomaterials in Chromatography, 503-518.

Harikumar, P., 2016. Antibacterial Activity of Copper Nanoparticles and Copper Nanocomposites against Escherichia Coli Bacteria. International Journal of Sciences, 2, 83-90.

Harmata, A., Guelcher, S., 2016. Effects of surface modification on polymeric biocomposites for orthopedic applications. Nanocomposites for Musculoskeletal Tissue Regeneration, 67-91.

Hartmann, M., Berditsch, M., Hawecker, J., Ardakani, M., Gerthsen, D., Ulrich, A. 2010. Damage of the Bacterial Cell Envelope by Antimicrobial Peptides Gramicidin S and PGLa as Revealed by Transmission and Scanning Electron Microscopy. Antimicrobial Agents and Chemotherapy, 54, 3132-3142.

Hasunuma, T., Kondo, A., 2012. Consolidated bioprocessing and simultaneous saccharification and fermentation of lignocellulose to ethanol with thermotolerant yeast strains. Process Biochemistry, 47, 1287-1294.

Hazeri, N., Tavanai, H., Moradi, A., 2012. Production and properties of electrosprayed sericin nanopowder. *Science and Technology of Advanced Materials*, 13, 035010.

Helmlinger, J., Sengstock, C., Groß-Heitfeld, C., Mayer, C., Schildhauer, T., Köller, M., Epple, M., 2016. Silver nanoparticles with different size and shape: equal cytotoxicity, but different antibacterial effects. *RSC Advances*, 6, 18490-18501.

Hennekinne, J., De Buyser, M., Dragacci, S., 2012. Staphylococcus aureus and its food poisoning toxins: characterization and outbreak investigation. *FEMS Microbiology Reviews*, 36, 815-836.

Hladik, F., McElrath, M., 2008. Setting the stage: host invasion by HIV. *Nature Reviews Immunology*, 8, 447-457.

Holmes-Hampton, G., Tong, W., Rouault, T., 2014. Biochemical and Biophysical Methods for Studying Mitochondrial Iron Metabolism. *Methods in Enzymology*, 275-307.

Homan, K., Chen, J., Schiano, A., Mohamed, M., Willets, K., Murugesan, S., Stevenson, K., Emelianov, S., 2011. Silver-Polymer Composite Stars: Synthesis and Applications. *Advanced Functional Materials*, 21, 1673-1680.

Hong, X., Wen, J., Xiong, X., Hu, Y., 2015. Shape effect on the antibacterial activity of silver nanoparticles synthesized via a microwave-assisted method. *Environmental Science and Pollution Research*, 23, 4489-4497.

Hong, Y., Li, Y., Yin, Y., Li, D., Zou, G., 2008. Electrohydrodynamic atomization of quasi-monodisperse drug-loaded spherical/wrinkled microparticles. *Journal of Aerosol Science*, 39, 525-536.

Hossain, K., Patel, U., Ahmed, I., 2014. Development of microspheres for biomedical applications: a review. *Progress in Biomaterials*, 4, 1-19.

Houser, K., Subbarao, K., 2015. Influenza Vaccines: Challenges and Solutions. *Cell Host & Microbe*, 17, 295-300.

Hu, R., Zhou, F., Zhou, T., Shen, J., Wang, Z., Zhao, Z., Qin, A., Tang, B., 2018. Specific discrimination of gram-positive bacteria and direct visualization of its infection towards mammalian cells by a DPAN-based AIEgen. *Biomaterials*, 187, 47-54.

Huang, H., Toit, H., Besenhard, M., Ben-Jaber, S., Dobson, P., Parkin, I., Gavriilidis, A., 2018. Continuous flow synthesis of ultrasmall gold nanoparticles in a microreactor using trisodium citrate and their SERS performance. *Chemical Engineering Science*, 189, 422-430.

Huang, Z., He, C., Yang, A., Zhang, Y., Han, X., Yin, J., Wu, Q., 2006. Encapsulating drugs in biodegradable ultrafine fibers through co-axial electrospinning. *Journal of Biomedical Materials Research Part A*, 77A, 169-179.

Huang, Z., Zhang, Y., Kotaki, M., Ramakrishna, S., 2003. A review on polymer nanofibers by electrospinning and their applications in nanocomposites. *Composites Science and Technology*, 63, 2223-2253.

Huh, A., Kwon, Y., 2011. "Nanoantibiotics": A new paradigm for treating infectious diseases using nanomaterials in the antibiotics resistant era. *Journal of Controlled Release*, 156, 128-145.

Hurst, H., Martin, M., 2017. Toxicology. *Pharmacology and Therapeutics for Dentistry*, 603-620.

Hwan, Soo, Lee, Hyeong-Seon, Ryu, Deok-Seon, Choi, Soo-Jae, Lee, Dong-Seok, 2010. Antibacterial Activity of Silver-Nanoparticles Against Staphylococcus Aureus and Escherichia Coli. Korean Journal of Microbiology and Biotechnology, 39.

Ibelings, M., Bruining, H., 2003. Methicillin-resistant Staphylococcus aureus: acquisition and risk of death in patients in the intensive care unit. European Journal of Surgery, 164, 411-418.

Ikeuchi, M., Tane, R., Ikuta, K., 2011. Electrospray deposition and direct patterning of polylactic acid nanofibrous microcapsules for tissue engineering. Biomedical Microdevices, 14, 35-43.

Iliev, I., Funari, V., Taylor, K., Nguyen, Q., Reyes, C., Strom, S., Brown, J., Becker, C., Fleshner, P., Dubinsky, M., Rotter, J., Wang, H., McGovern, D., Brown, G., Underhill, D., 2012. Interactions Between Commensal Fungi and the C-Type Lectin Receptor Dectin-1 Influence Colitis. Science, 336, 1314-1317.

Ingle, A., Duran, N., Rai, M., 2013. Bioactivity, mechanism of action, and cytotoxicity of copper-based nanoparticles: A review. Applied Microbiology and Biotechnology, 98, 1001-1009.

Iravani, S., 2014. Bacteria in Nanoparticle Synthesis: Current Status and Future Prospects. International Scholarly Research Notices, 1-18.

Jahangir, M., Rumi, T., Wahab, M., Khan, M., Rahman, M., Sayed, Z., 2017. Poly Lactic Acid (PLA) Fibres: Different Solvent Systems and Their Effect on Fibre Morphology and Diameter. American Journal of Chemistry, 7, 177-186.

Jahangiri, M., Jamshidi, A., 2014. Synthesis of Copper Nanoparticles and its Antibacterial Activity against Escherichia coli. *Asian Journal of Biological Sciences*, 7, 183-186.

Jamshidi, A., Jahangiri-rad, M., 2014. Synthesis of Copper Nanoparticles and its Antibacterial Activity against Escherichia coli. *Asian Journal of Biological Sciences*, 7, 183-186.

Jang, H., Hwang, B., Lee, K., Kim, Y., Kim, J., 2018. Controlling the size of silver nanowires produced by a tetrabutylammonium dichlorobromide salt-based polyol process: Kinetics of silver crystal growth. *AIP Advances*, 8, 025303.

Jazayeri, M., Amani, H., Pourfatollah, A., Pazoki-Toroudi, H., Sedighimoghaddam, B., 2016. Various methods of gold nanoparticles (GNPs) conjugation to antibodies. *Sensing and Bio-Sensing Research*, 9, 17-22.

Jeevanandam, J., Chan, Y., Danquah, M., 2016. Biosynthesis of Metal and Metal Oxide Nanoparticles. *ChemBioEng Reviews*, 3, 55-67.

Jeong, E., Yang, J., Youk, J., 2007. Preparation of polyurethane cationomer nanofiber mats for use in antimicrobial nanofilter applications. *Materials Letters*, 61, 991-994.

Jha, A., Prasad, K., Kulkarni, A., 2009. Synthesis of TiO₂ nanoparticles using microorganisms. *Colloids and Surfaces B: Biointerfaces*, 71, 226-229.

Ji, X., Song, X., Li, J., Bai, Y., Yang, W., Peng, X., 2007. Size Control of Gold Nanocrystals in Citrate Reduction: The Third Role of Citrate. *Journal of the American Chemical Society*, 129, 13939-13948.

Jia, J., Duan, Y., Wang, S., Zhang, S., Wang, Z., 2003. Preparation and characterization of antibacterial silver-containing nanofibers for wound dressing applications. *Journal of US-China Medical Science*, 4, 52-54.

Jiang, H., Fang, D., Hsiao, B., Chu, B., Chen, W., 2004. Preparation and characterization of ibuprofen-loaded poly(lactide-co-glycolide)/poly(ethylene glycol)-g-chitosan electrospun membranes. *Journal of Biomaterials Science, Polymer Edition*, 15, 279-296.

Jin, H., Fridrikh, S., Rutledge, G., Kaplan, D., 2002. Electrospinning Bombyxmori Silk with Poly(ethylene oxide). *Biomacromolecules*, 3, 1233-1239.

Jo, J., Deming, C., Kennedy, E., Conlan, S., Polley, E., Ng, W., Segre, J., Kong, H., 2016. Diverse Human Skin Fungal Communities in Children Converge in Adulthood. *Journal of Investigative Dermatology*, 136, 2356-2363.

Johnson, L., Mossong, J., Dorrington, R., Schomaker, M., Hoffmann, C., Keiser, O., Fox, M., Wood, R., Prozesky, H., Giddy, J., Garone, D., Cornell, M., Egger, M., Boulle, A., 2013. Life Expectancies of South African Adults Starting Antiretroviral Treatment: Collaborative Analysis of Cohort Studies. *PLoS Medicine*, 10, 1001418.

Jones, R., Draheim, R., Roldo, M., 2018. Silver Nanowires: Synthesis, Antibacterial Activity and Biomedical Applications. *Applied Sciences*, 8, 673.

Kabalka, G., Varma, R., 1991. Reduction of Nitro and Nitroso Compounds. *Comprehensive Organic Synthesis*, 363-379.

Kadariya, J., Smith, T., Thapaliya, D., 2014. Staphylococcus aureus and Staphylococcal Food-Borne Disease: An Ongoing Challenge in Public Health. *BioMed Research International*, 2014, 1-9.

Kamrupi, I., Dolui, S., 2010. Synthesis of copper-polystyrene nanocomposite particles using water in supercritical carbon dioxide medium and its antimicrobial activity. *Journal of Applied Polymer Science*, 120, 1027-1033.

Kandi, V., Kandi, S., 2015. Antimicrobial properties of nanomolecules: potential candidates as antibiotics in the era of multi-drug resistance. *Epidemiol Health*, 37, 2015020.

Kanwal, Z., Raza, M., Riaz, S., Manzoor, S., Tayyeb, A., Sajid, I., Naseem, S., 2019. Synthesis and characterization of silver nanoparticle-decorated cobalt nanocomposites (Co@AgNPs) and their density-dependent antibacterial activity. *Royal Society Open Science*, 6, 182135.

Karaman, R., 2015. Chapter 5 – From Conventional Prodrugs to Prodrugs Designed by Molecular Orbital Methods. *Frontiers in Computational Chemistry*, 2, 187–249.

Kariduraganavar, M., Kittur, A., Kamble, R., 2014. *Polymer Synthesis and Processing. Natural and Synthetic Biomedical Polymers*, 1-31.

Kattamuri, N., Shin, J., Kang, B., Lee, C., Lee, J., Sung, C., 2005. Development and surface characterization of positively charged filters. *Journal of Materials Science*, 40, 4531-4539.

Katti, D., Robinson, K., Ko, F., Laurencin, C., 2004. Bioresorbable nanofiber-based systems for wound healing and drug delivery: Optimization of fabrication parameters. *Journal of Biomedical Materials Research*, 70, 286-296.

Kaur, A., Kumar, R., 2019. Enhanced bactericidal efficacy of polymer stabilized silver nanoparticles in conjugation with different classes of antibiotics. *RSC Advances*, 9, 1095-1105.

Kaye, K., Pogue, J., 2015. Infections Caused by Resistant Gram-Negative Bacteria: Epidemiology and Management. *Pharmacotherapy: The Journal of Human Pharmacology and Drug Therapy*, 35, 949-962.

Keerthana, K., 2016. Comparative study on durability properties of bacteria concrete. *International Research Journal of Engineering and Technology*, 3, 129-132.

Kenawy, E., Bowlin, G., Mansfield, K., Layman, J., Simpson, D., Sanders, E., Wnek, G., 2002. Release of tetracycline hydrochloride from electrospun poly(ethylene-co-vinylacetate), poly(lactic acid), and a blend. *Journal of Controlled Release*, 81, 57-64.

Khan, A., Rashid, A., Younas, R., Chong, R., 2015. A chemical reduction approach to the synthesis of copper nanoparticles. *International Nano Letters*, 6, 21-26.

Khatoun, U., Rao, G., Mohan, M., Ramanaviciene, A., Ramanavicius, A., 2018. Comparative study of antifungal activity of silver and gold nanoparticles synthesized by facile chemical approach. *Journal of Environmental Chemical Engineering*, 6, 5837-5844.

Kibret, Abera, 2011. Antimicrobial susceptibility patterns of *E. coli* from clinical sources in northeast Ethiopia. *African Health Sciences*, 11, S40-S45.

Kim, D., Park, J., Jeon, G., Kim, C., Seo, J., 2017. Effect of the size and shape of silver nanoparticles on bacterial growth and metabolism by monitoring optical density and fluorescence intensity. *Biotechnology and Bioprocess Engineering*, 22, 210-217.

Kim, J., Kuk, E., Yu, K., Kim, J., Park, S., Lee, H., Kim, S., Park, Y., Park, Y., Hwang, C., Kim, Y., Lee, Y., Jeong, D., Cho, M., 2007. Antimicrobial effects of silver nanoparticles. *Nanomedicine*, 3, 95-101.

Kim, K., Luu, Y., Chang, C., Fang, D., Hsiao, B., Chu, B., Hadjiargyrou, M., 2004. Incorporation and controlled release of a hydrophilic antibiotic using poly(lactide-co-glycolide)-based electrospun nanofibrous scaffolds. *Journal of Controlled Release*, 98, 47-56.

Kim, W., Kim, S., 2011. Synthesis of biodegradable triple-layered capsules using a triaxial electro spray method. *Polymer*, 52, 3325-3336.

Knutsen, A., Bush, R., Demain, J., Denning, D., Dixit, A., Fairs, A., Greenberger, P., Kariuki, B., Kita, H., Kurup, V., Moss, R., Niven, R., Pashley, C., Slavin, R., Vijay, H. Wardlaw, A., 2012. Fungi and allergic lower respiratory tract diseases. *Journal of Allergy and Clinical Immunology*, 129, 280-291.

Koombhongse, S., Liu, W., Reneker, D., 2001. Flat polymer ribbons and other shapes by electrospinning. *Journal of Polymer Science Part B: Polymer Physics*, 39, 2598-2606.

Kost, J., Langer, R., 2001. Responsive polymeric delivery systems. *Advanced Drug Delivery Reviews*, 46, 125-148.

Kourmouli, A., Valenti, M., van Rijn, E., Beaumont, H., Kalantzi, O., Schmidt-Ott, A., Biskos, G., 2018. Can disc diffusion susceptibility tests assess the antimicrobial activity of engineered nanoparticles?. *Journal of Nanoparticle Research*, 20.

Krammer, F., Palese, P., 2013. Influenza virus hemagglutinin stalk-based antibodies and vaccines. *Current Opinion in Virology*, 3, 521-530.

Krammer, F., Palese, P., 2015. Advances in the development of influenza virus vaccines. *Nature Reviews Drug Discovery*, 14, 167-182.

Krishnamurthy, S., Esterle, A., Sharma, N., Sahi, S., 2014. Yucca-derived synthesis of gold nanomaterial and their catalytic potential. *Nanoscale Research Letters*, 9, 627.

Krstić, M., Medarević, Đ., Đuriš, J., Ibrić, S., 2018. Self-nanoemulsifying drug delivery systems (SNEDDS) and self-microemulsifying drug delivery systems (SMEDDS) as lipid nanocarriers for improving dissolution rate and bioavailability of poorly soluble drugs. *Lipid Nanocarriers for Drug Targeting*, 473-508.

Kum, W., Cameron, S., Hung, R., Kalyan, S., Chow, A., 2001. Temporal Sequence and Kinetics of Proinflammatory and Anti-Inflammatory Cytokine Secretion Induced by Toxic Shock Syndrome Toxin 1 in Human Peripheral Blood Mononuclear Cells. *Infection and Immunity*, 69, 7544-7549.

Kumar, S., Gandhi, K., Kumar, R., 2007. Modeling of Formation of Gold Nanoparticles by Citrate Method. *Industrial & Engineering Chemistry Research*, 46, 3128-3136.

Kumari, A., Yadav, S., Yadav, S., 2010. Biodegradable polymeric nanoparticles-based drug delivery systems.

Kunio, N., Schreiber, M., 2013. Topical Hemostatic Agents. *Consultative Hemostasis and Thrombosis*, 538-545.

Kwieceński, J., Jacobsson, G., Karlsson, M., Zhu, X., Wang, W., Bremell, T., Josefsson, E. Jin, T., 2013. Staphylokinase Promotes the Establishment of Staphylococcus aureus Skin Infections While Decreasing Disease Severity. *The Journal of Infectious Diseases*, 208, 990-999.

Lappin, E., Ferguson, A., 2009. Gram-positive toxic shock syndromes. *The Lancet Infectious Diseases*, 9, 281-290.

Lemire, J., Harrison, J., Turner, R., 2013. Antimicrobial activity of metals: mechanisms, molecular targets and applications. *Nature Reviews Microbiology*, 11, 371-384.

Leonard, F., Markey, B., 2008. Meticillin-resistant *Staphylococcus aureus* in animals: A review. *The Veterinary Journal*, 175, 27-36.

Leonardi, I., Li, X., Semon, A., Li, D., Doron, I., Putzel, G., Bar, A., Prieto, D., Rescigno, M., McGovern, D., Pla, J., Iliev, I., 2018. CX3CR1+ mononuclear phagocytes control immunity to intestinal fungi. *Science*, 359, 232-236.

León-Silva, S., Fernández-Luqueño, F., López-Valdez, F., 2016. Silver Nanoparticles (AgNP) in the Environment: a Review of Potential Risks on Human and Environmental Health. *Water, Air, & Soil Pollution*, 227.

Li, C., Vepari, C., Jin, H., Kim, H., Kaplan, D., 2006. Electrospun silk-BMP-2 scaffolds for bone tissue engineering. *Biomaterials*, 27, 3115-3124.

Li, J., He, A., Zheng, J., Han, C., 2006. Gelatin and Gelatin-Hyaluronic Acid Nanofibrous Membranes Produced by Electrospinning of Their Aqueous Solutions. *Biomacromolecules*, 7, 2243-2247.

Li, M., Mondrinos, M., Gandhi, M., Ko, F., Weiss, A., Lelkes, P., 2005. Electrospun protein fibers as matrices for tissue engineering. *Biomaterials*, 26, 5999-6008.

Li, W., Laurencin, C., Caterson, E., Tuan, R., Ko, F., 2002. Electrospun nanofibrous structure: A novel scaffold for tissue engineering. *Journal of Biomedical Materials Research*, 60, 613-621.

Li, W., Li, X., Wang, Q., Pan, Y., Wang, T., Wang, H., Song, R., Deng, H., 2014. Antibacterial activity of nanofibrous mats coated with lysozyme-layered silicate composites via electrospaying. *Carbohydrate Polymers*, 99, 218-225.

Li, W., Xie, X., Shi, Q., Duan, S., Ouyang, Y., Chen, Y., 2010. Antibacterial effect of silver nanoparticles on *Staphylococcus aureus*. *BioMetals*, 24, 135-141.

Li, X., Robinson, S., Gupta, A., Saha, K., Jiang, Z., Moyano, D., Sahar, A., Riley, M., Rotello, V., 2014. Functional Gold Nanoparticles as Potent Antimicrobial Agents against Multi-Drug-Resistant Bacteria. *ACS Nano*, 8, 10682–10686.

Li, Y., Kröger, M., Liu, W., 2012. Nanoparticle Geometrical Effect on Structure, Dynamics and Anisotropic Viscosity of Polyethylene Nanocomposites. *Macromolecules*, 45, 2099-2112.

Liao, S., Zhang, Y., Pan, X., Zhu, F., Jiang, C., Liu, Q., Cheng, Z., Dai, G., Wu, G., Wang, L., Chen, L., 2019. Antibacterial activity and mechanism of silver nanoparticles against multidrug-resistant *Pseudomonas aeruginosa*. *International Journal of Nanomedicine*, 14, 1469-1487.

Lima, E., Guerra, R., Lara, V., Guzmán, A., 2013. Gold nanoparticles as efficient antimicrobial agents for *Escherichia coli* and *Salmonella typhi*. *Chemistry Central Journal*, 7, 11.

Lima, M., Andrade, A., Oliveira, G., Nicoli, J., Martins, F., Kroon, E., Abrahão, J., 2019. Virus and microbiota relationships in humans and other mammals: An evolutionary view. *Human Microbiome Journal*, 11, 100050.

Limon, J., Skalski, J., Underhill, D., 2017. Commensal Fungi in Health and Disease. *Cell Host & Microbe*, 22, 156-165.

Lin, J., Hsueh, Y., Huang, J., Wu, J., 2015. Effect of silver nitrate concentration of silver nanowires synthesized using a polyol method and their application as transparent conductive films. *Thin Solid Films*, 584, 243-247.

Lin, M., Pei, H., Yang, F., Fan, C., Zuo, X., 2013. Applications of Gold Nanoparticles in the Detection and Identification of Infectious Diseases and Biothreats. *Advanced Materials*, 25, 3490-3496.

Liu, J., Hurt, R., 2010. Ion Release Kinetics and Particle Persistence in Aqueous Nano-Silver Colloids. *Environmental Science & Technology*, 44, 2169-2175.

Long, Y., Hu, L., Yan, X., Zhao, X., Zhou, Q., Cai, Y., Jiang, G., 2017. Surface ligand controls silver ion release of nanosilver and its antibacterial activity against *Escherichia coli*. *International Journal of Nanomedicine*, 12, 3193-3206.

Loverde, S., Klein, M., Discher, D., 2011. Nanoparticle Shape Improves Delivery: Rational Coarse Grain Molecular Dynamics (rCG-MD) of Taxol in Worm-Like PEG-PCL Micelles. *Advanced Materials*, 24, 3823-3830.

Lu, G., Gao, P., 2010. Emulsions and Microemulsions for Topical and Transdermal Drug Delivery. *Handbook of Non-Invasive Drug Delivery Systems*, 59-94.

Luo, W., Hu, W., Xiao, S., 2008. Size Effect on the Thermodynamic Properties of Silver Nanoparticles. *The Journal of Physical Chemistry C*, 112, 2359-2369.

Luty-Błoch, M., Paclawski, K., Wojnicki, M., Fitzner, K., 2013. The kinetics of redox reaction of gold (III) chloride complex ions with l-ascorbic acid. *Inorganica Chimica Acta*, 395, 189-196.

Luu, Y., Kim, K., Hsiao, B., Chu, B., Hadjiargyrou, M., 2003. Development of a nanostructured DNA delivery scaffold via electrospinning of PLGA and PLA-PEG block copolymers. *Journal of Controlled Release*, 89, 341-353.

Lynn, D., 2009. Cell Culture. *Encyclopedia of Insects*, pp.144-145.

MacGowan, A., Macnaughton, E., 2013. Antibiotic resistance. *Medicine*, 41, 642-648.

Mai, Z., Chen, J., He, T., Hu, Y., Dong, X., Zhang, H., Huang, W., Ko, F., Zhou, W., 2017. Electro spray biodegradable microcapsules loaded with curcumin for drug delivery systems with high bioactivity. *RSC Advances*, 3.

Maisch, T., Szeimies, R-M., Jori, G., Abels, C., 2004. Antibacterial photodynamic therapy in dermatology. *Photochemical and Photobiological Sciences*, 3, 907.

Maiti, S., Krishnan, D., Barman, G., Ghosh, S., Laha, J., 2014. Antimicrobial activities of silver nanoparticles synthesized from *Lycopersicon esculentum* extract. *Journal of Analytical Science and Technology*, 5.

Malik, Z., Ladan, H., Nitzan, Y., 1992. Photodynamic inactivation of Gram-negative bacteria: Problems and possible solutions. *Journal of Photochemistry and Photobiology B: Biology*, 14, 262-266.

Mäntele, W., Deniz, E., 2017. UV-VIS absorption spectroscopy: Lambert-Beer reloaded. *Spectrochimica Acta Part A: Molecular and Biomolecular Spectroscopy*, 173, 965-968.

Mari, A., Schneider, P., Wally, V., Breitenbach, M., Simon-Nobbe, B., 2003. Sensitization to fungi: epidemiology, comparative skin tests, and IgE reactivity of fungal extracts. *Clinical Experimental Allergy*, 33, 1429-1438.

Marin, Alvaro, Loscertales, Ignacio, Barrero, Antonio, 2012. Surface tension effects on immersed electrosprays.

Marshall, B., Levy, S., 2011. Food Animals and Antimicrobials: Impacts on Human Health. *Clinical Microbiology Reviews*, 24, 718-733.

Marthina, K., Barringer, S., 2011. Confectionery Coating with an Electrohydrodynamic (EHD) System. *Journal of Food Science*, 77, E26-E31.

Mathelié-Guinlet, M., Béven, L., Moroté, F., Moynet, D., Grauby-Heywang, C., Gammoudi, I., Delville, M., Cohen-Bouhacina, T., 2017. Probing the threshold of membrane damage and cytotoxicity effects induced by silica nanoparticles in *Escherichia coli* bacteria. *Advances in Colloid and Interface Science*, 245, 81-91.

Mathison, J.C., Tobias, P.S., Wolfson, E., Ulevitch, R.J., 1992. Plasma lipopolysaccharide (LPS)-binding protein: A key component in macrophage recognition of Gram-negative LPS. *Journal of Immunology*, 149, 200-206.

McBirney, S., Trinh, K., Wong-Beringer, A., Armani, A., 2016. Wavelength-normalized spectroscopic analysis of *Staphylococcus aureus* and *Pseudomonas aeruginosa* growth rates. *Biomedical Optics Express*, 7, 4034.

McKeon-Fischer, K., Freeman, J. 2010. Characterization of electrospun poly(L-lactide) and gold nanoparticle composite scaffolds for skeletal muscle tissue engineering.

Mead, P., Griffin, P., 1998. *Escherichia coli* O157:H7. *The Lancet*, 352, 1207-1212.

Meghana, S., Kabra, P., Chakraborty, S., Padmavathy, N., 2015. Understanding the pathway of antibacterial activity of copper oxide nanoparticles. *RSC Adv*, 5, 12293-12299.

Memoli, M., Athota, R., Reed, S., Czajkowski, L., Bristol, T., Proudfoot, K., Hagey, R., Voell, J., Fiorentino, C., Ademposi, A., Shoham, S., Taubenberger, J., 2013. The Natural History of Influenza Infection in the Severely Immunocompromised vs Nonimmunocompromised Hosts. *Clinical Infectious Diseases*, 58, 214-224.

Mendis, E., Rajapakse, N., Byun, H., Kim, S., 2005. Investigation of jumbo squid (*Dosidicus gigas*) skin gelatin peptides for their in vitro antioxidant effects. *Life Sci*, 77, 2166-2178.

Meng, F., Jiang, Y., Sun, Z., Yin, Y., Li, Y., 2009. Electrohydrodynamic liquid atomization of biodegradable polymer microparticles: Effect of electrohydrodynamic liquid atomization variables on microparticles. *Journal of Applied Polymer Science*, 113, 526-534.

Meyer, H., Schmidhalter, D., 2012. Microbial expression systems and manufacturing from a market and economic perspective. *Innovations in Biotechnology*, 211-250.

Miao, J., Chen, L., Wang, J., Wang, W., Chen, D., Li, L., Li, B., Deng, Y., Xu, Z., 2017. Current methodologies on genotyping for nosocomial pathogen methicillin-resistant *Staphylococcus aureus* (MRSA). *Microbial Pathogenesis*, 107,17-28.

Min, B., Lee, G., Kim, S., Nam, Y., Lee, T., Park, W., 2004. Electrospinning of silk fibroin nanofibers and its effect on the adhesion and spreading of normal human keratinocytes and fibroblasts in vitro. *Biomaterials*, 25, 1289-1297.

Mir, M., Ahmed, N., Rehman, A., 2017. Recent applications of PLGA based nanostructures in drug delivery. *Colloids and Surfaces B: Biointerfaces*, 159, 217-231.

Mit-uppatham, C., Nithitanakul, M., Supaphol, P., 2004. Ultrafine Electrospun Polyamide-6 Fibers: Effect of Solution Conditions on Morphology and Average Fiber Diameter. *Macromolecular Chemistry and Physics*, 205, 2327-2338.

Moghadam, H., Samimi, M., Samimi, A., Khorram, M., 2009. Study of Parameters Affecting Size Distribution of Beads Produced from Electro-Spray of High Viscous Liquids. *Iranian Journal of Chemical Engineering*, 6, 88-98.

Mohamed, M., Fouad, S., Elshoky, H., Mohammed, G., Salaheldin, T., 2017. Antibacterial effect of gold nanoparticles against *Corynebacterium pseudotuberculosis*. *International Journal of Veterinary Science and Medicine*, 5, 23-29.

Mohammadi, M., Hamzehloo, M., 2019. Densities, viscosities, and refractive indices of binary and ternary mixtures of methanol, acetone, and chloroform at temperatures from (298.15–318.15) K and ambient pressure. *Fluid Phase Equilibria*, 483, 14-30.

Monette, D., 2009. Coating removal techniques in the aerospace industry. *Corrosion Control in the Aerospace Industry*, 225-247.

Muñoz-Bonilla, A., Fernández-García, M., 2012. Polymeric materials with antimicrobial activity. *Progress in Polymer Science*, 37, 281-339.

Nabipour, Y., Rostamzad, A., 2015. Comparing the antimicrobial effects of silver and copper nanoparticles against pathogenic and resistant bacteria of *Klebsiella pneumoniae*, *Pseudomonas aeruginosa* and *Staphylococcus aureus*. *Cumhuriyet University Faculty of Science Journal*, 36.

Naides, S., 2012. Arboviruses Causing Fever and Rash Syndromes. *Goldman's Cecil Medicine*, 2156-2161.

Narang, A., Mantri, R., Raghavan, K., 2017. Excipient Compatibility and Functionality. *Developing Solid Oral Dosage Forms*, 151-179.

Nath, S., Son, S., Sadiasa, A., Min, Y., Lee, B., 2013. Preparation and characterization of PLGA microspheres by the electrospraying method for delivering simvastatin for bone regeneration. *International Journal of Pharmaceutics*, 443, 87-94.

Nghia, V., Truong, N., Thong, N., Hung, N., 2012. Synthesis of Nanowire-Shaped Silver by Polyol Process of Sodium Chloride. *International Journal of Materials and Chemistry*, 2, 75-78.

Nguyen, D., Clasen, C., Van den Mooter, G., 2016. Pharmaceutical Applications of Electrospraying. *Journal of Pharmaceutical Sciences*, 105, 2601-2620.

Nichols, J., LeDuc, J., 2009. Influenza. Vaccines for Biodefense and Emerging and Neglected Diseases, 497-525.

Nichols, W., Guthrie, K., Corey, L., Boeckh, M., 2004. Influenza Infections after Hematopoietic Stem Cell Transplantation: Risk Factors, Mortality, and the Effect of Antiviral Therapy. *Clinical Infectious Diseases*, 39, 1300-1306.

Nordmann, P., Naas, T., Fortineau, N., Poirel, L., 2007. Superbugs in the coming new decade; multidrug resistance and prospects for treatment of *Staphylococcus aureus*, *Enterococcus* spp. and *Pseudomonas aeruginosa* in 2010. *Current Opinion in Microbiology*, 10, 436-440.

Norman, R., Stone, J., Gole, A., Murphy, C., Sabo-Attwood, T., 2008. Targeted Photothermal Lysis of the Pathogenic Bacteria, *Pseudomonas aeruginosa*, with Gold Nanorods. *Nano Letters*, 8, 302-306.

Norrby, S., 2010. Urinary tract infections. *Antibiotic and Chemotherapy*, 694-701.

O'Connell, K., Hodgkinson, J., Sore, H., Welch, M., Salmond, G., Spring, D., 2013. Combating Multidrug-Resistant Bacteria: Current Strategies for the Discovery of Novel Antibacterials. *Angewandte Chemie International Edition*, 52, 10706-10733.

Otto, M., 2010. Basis of Virulence in Community-Associated Methicillin-Resistant *Staphylococcus aureus*. *Annual Review of Microbiology*, 64, 143-162.

Otto, M., 2014. *Staphylococcus aureus* toxins. *Current Opinion in Microbiology*, 17, 32-37.

Ouellette, R., Rawn, J., 2014. Aldehydes and Ketones. *Organic Chemistry*, 595-628.

Packer, L., Witt, E., Tritschler, H., 1995. Alpha-lipoic acid as a biological antioxidant. *Free Radical Biology and Medicine*, 19, 227-250.

Paez-Espino, D., Eloie-Fadrosh, E., Pavlopoulos, G., Thomas, A., Huntemann, M., Mikhailova, N., Rubin, E., Ivanova, N., Kyrpides, N., 2016. Uncovering Earth's virome. *Nature*, 536, 425-430.

Pal, S., Tak, Y., Song, J., 2007. Does the Antibacterial Activity of Silver Nanoparticles Depend on the Shape of the Nanoparticle? A Study of the Gram-Negative Bacterium *Escherichia coli*. *Applied and Environmental Microbiology*, 73, 1712-1720.

Palza, H., Quijada, R., Delgado, K., 2015. Antimicrobial polymer composites with copper micro- and nanoparticles: Effect of particle size and polymer matrix. *Journal of Bioactive and Compatible Polymers*, 30, 366-380.

Pantidos, N., 2014. Biological Synthesis of Metallic Nanoparticles by Bacteria, Fungi and Plants. *Journal of Nanomedicine & Nanotechnology*, 05.

Pantosti, A., Sanchini, A., Monaco, M., 2007. Mechanisms of antibiotic resistance in *Staphylococcus aureus*. *Future Microbiology*, 2, 323-334.

Parhizkar, M., Reardon, P., Knowles, J., Browning, R., Stride, E., Pedley, R., Grego, T., Edirisinghe, M., 2017. Performance of novel high throughput multi electro spray systems for forming of polymeric micro/nanoparticles. *Materials & Design*, 126, 73-84.

Park, J., Park, S., Kim Y., 2012. Electrospraying fabrication and characterization of low molecular weight poly(vinyl alcohol)/silver composite nanospheres for antibacterial applications. *Polymers & Polymer Composites*, 20, 253-259.

Park, K., Jung, S., Lee, S., Min, B., Park, W., 2006. Biomimetic nanofibrous scaffolds: Preparation and characterization of chitin/silk fibroin blend nanofibers. *International Journal of Biological Macromolecules*, 38, 165-173.

Parlet, C., Brown, M., Horswill, A., 2019. Commensal *Staphylococci* Influence *Staphylococcus aureus* Skin Colonization and Disease. *Trends in Microbiology*.

Paulino, L., Tseng, C., Strober, B., Blaser, M., 2006. Molecular Analysis of Fungal Microbiota in Samples from Healthy Human Skin and Psoriatic Lesions. *Journal of Clinical Microbiology*, 44, 2933-2941.

Pawar, A., Thakkar, S., Misra, M., 2018. A bird's eye view of nanoparticles prepared by electrospraying: advancements in drug delivery field. *Journal of Controlled Release*, 286, 179-200.

Payne, J., Waghvani, H., Connor, M., Hamilton, W., Tockstein, S., Moolani, H., Chavda, F., Badwaik, V., Lawrenz, M., Dakshinamurthy, R., 2016. Novel Synthesis of Kanamycin Conjugated Gold Nanoparticles with Potent Antibacterial Activity. *Frontiers in Microbiology*, 7.

Peay, K., Kennedy, P., Talbot, J., 2016. Dimensions of biodiversity in the Earth mycobiome. *Nature Reviews Microbiology*, 14, 434-447.

Pennington, H., 2010. *Escherichia coli* O157. *The Lancet*, 376. 1428-1435.

Pham-Huy, L.A., He, H., Pham-Huy, C., 2008. Free radicals, antioxidants in disease and health. *International Journal of Biomedical Science*, 4, 89-96.

Pillai, Z., Kamat, P., 2004. What Factors Control the Size and Shape of Silver Nanoparticles in the Citrate Ion Reduction Method?. *The Journal of Physical Chemistry B*, 108, 945-951.

Pohanish, R., 2017. *E. Sittig's Handbook of Toxic and Hazardous Chemicals and Carcinogens*, 1405-1582.

Polívková, M., Hubáček, T., Staszek, M., Švorčík, V., Siegel, J., 2017. Antimicrobial Treatment of Polymeric Medical Devices by Silver Nanomaterials and Related Technology. *International Journal of Molecular Sciences*, 18, 419.

Pontrelli, S., Chiu, T., Lan, E., Chen, F., Chang, P., Liao, J., 2018. *Escherichia coli* as a host for metabolic engineering. *Metabolic Engineering*, 50, 16-46.

Pozdnyakov, A., Emel'yanov, A., Kuznetsova, N., Ermakova, T., Fadeeva, T., Sosedova, L. and Prozorova, G. (2016). Nontoxic hydrophilic polymeric nanocomposites containing silver nanoparticles with strong antimicrobial activity.

Prabhakaran, M., Zamani, M., Felice, B., Ramakrishna, S., 2015. Electrospraying technique for the fabrication of metronidazole contained PLGA particles and their release profile. *Materials Science and Engineering: C*, 56, 66-73.

Prabhu, S., Poulose, E., 2012. Silver nanoparticles: mechanism of antimicrobial action, synthesis, medical applications, and toxicity effects. *International Nano Letters*, 2.

Prabukumar, C., Bhat, K., 2018. Purification of Silver Nanowires Synthesised by Polyol Method. *Materials Today: Proceedings*, 5, 22487-22493.

Prasanna, A., Venkatasubbu, G., 2018. Sustained release of amoxicillin from hydroxyapatite nanocomposite for bone infections. *Progress in Biomaterials*, 7, 289-296.

Qiao, M., Ying, G., Singer, A., Zhu, Y., 2018. Review of antibiotic resistance in China and its environment. *Environment International*, 110, 160-172.

Qureshi, A., 2016. Ebola Virus Disease Epidemic in Light of Other Epidemics. *Ebola Virus Disease*, 39-65.

Raafat, D., Otto, M., Reppschläger, K., Iqbal, J., Holtfreter, S., 2019. Fighting *Staphylococcus aureus* Biofilms with Monoclonal Antibodies. *Trends in Microbiology*, 27, 303-322.

Rai, M., Deshmukh, S., Ingle, A., Gade, A., 2012. Silver nanoparticles: the powerful nanoweapon against multidrug-resistant bacteria. *Journal of Applied Microbiology*, 112, 841-852.

Rajawat, S., Qureshi, M., 2012. Comparative Study on Bactericidal Effect of Silver Nanoparticles, Synthesized Using Green Technology, in Combination with Antibiotics on Salmonella Typhi. *Journal of Biomaterials and Nanobiotechnology*, 03, 480-485.

Ramachandran, G., 2013. Gram-positive and gram-negative bacterial toxins in sepsis. *Virulence*, 5, 213-218.

Ramakrishna, S., Fujihara, K., Teo, W., Yong, T., Ma, Z., Ramaseshan, R., 2006. Electrospun nanofibers: solving global issues. *Materials Today*, 9, 40-50.

Ramos, A., Tapia, A., Piñol, C., Lantican, N., del Mundo, M., Manalo, R., Herrera, M., 2019. Effects of reaction temperatures and reactant concentrations on the antimicrobial characteristics of copper precipitates synthesized using L-ascorbic acid as reducing agent. *Journal of Science: Advanced Materials and Devices*, 4, 66-71.

Rampersaud, S., Fang, J., Wei, Z., Fabijanic, K., Silver, S., Jaikaran, T., Ruiz, Y., Houssou, M., Yin, Z., Zheng, S., Hashimoto, A., Hoshino, A., Lyden, D., Mahajan, S., Matsui, H., 2016. The Effect of Cage Shape on Nanoparticle-Based Drug Carriers: Anticancer Drug Release and Efficacy via Receptor Blockade Using Dextran-Coated Iron Oxide Nanocages. *Nano Letters*, 16, 7357-7363.

Rampino, A., Borgogna, M., Blasi, P., Bellich, B., Cesàro, A., 2013. Chitosan nanoparticles: preparation, size evolution and stability. *Int J Pharm.* 455, 219-228.

Ranoszek-Soliwoda, K., Tomaszewska, E., Socha, E., Krzyczmonik, P., Ignaczak, A., Orłowski, P., Krzyzowska, M., Celichowski, G., Grobelny, J., 2017. The role of tannic acid and sodium citrate in the synthesis of silver nanoparticles. *Journal of Nanoparticle Research*, 19.

Ravishankar Rai, V., Jamuna Bai, A., 2011. Nanoparticles and Their Potential Application as Antimicrobials, *Science against Microbial Pathogens: Communicating Current Research and Technological Advances*. In: Méndez-Vilas, A., Ed., Formatex, Microbiology Series, 3, 197-209.

Raza, M., Kanwal, Z., Rauf, A., Sabri, A., Riaz, S., Naseem, S., 2016. Size- and Shape-Dependent Antibacterial Studies of Silver Nanoparticles Synthesized by Wet Chemical Routes. *Nanomaterials*, 6, 74.

Reddy, K., Feris, K., Bell, J., Wingett, D., Hanley, C., Punnoose, A., 2007. Selective toxicity of zinc oxide nanoparticles to prokaryotic and eukaryotic systems. *Applied Physics Letters*, 90, 213902.

Reingold, A., Broome, C., Gaventa, S., Hightower, A., 1989. Risk Factors for Menstrual Toxic Shock Syndrome: Results of a Multistate Case-Control Study. *Clinical Infectious Diseases*, 11, 35-42.

Reneker, D., Chun, I., 1996. Nanometre diameter fibres of polymer, produced by electrospinning. *Nanotechnology*, 7, 216-223.

Resnik, R., Cillo, J., 2018. Intraoperative Complications. *Misch's Avoiding Complications in Oral Implantology*, 294-328.

Richter, M., Drown, B., Riley, A., Garcia, A., Shirai, T., Svec, R., Hergenrother, P., 2017. Predictive compound accumulation rules yield a broad-spectrum antibiotic. *Nature*, 545, 299-304.

Rick, E., Woolnough, K., Pashley, C., Wardlaw, A., 2016. Allergic Fungal Airway Disease. *Journal of Investigational Allergology and Clinical Immunology*, 26, 344-354.

Riley, M., Lizotte-Waniewski, M., 2009. Population Genomics and the Bacterial Species Concept. *Horizontal Gene Transfer*, 367-377.

Rinke-Kneapler, C., Sigman, M., 2014. Applications of laser spectroscopy in forensic science. *Laser Spectroscopy for Sensing*, 461-495.

Rodrigues, J., Caruthers, C., Azmeh, R., Dykewicz, M., Slavin, R., Knutsen, A., 2016. The spectrum of allergic fungal diseases of the upper and lower airways. *Expert Review of Clinical Immunology*, 12, 531-550.

Roy Biswas, Gopa, Majee, Sutapa, Das, Ushasi, 2014. Gum karaya: A release modifier employed in the formulation of matrix granules containing Amoxicillin trihydrate as a model drug. *International Journal of Research in Pharmaceutical Sciences*, 5, 124-131.

Roy, W., 2016. The Environmental Fate of Representative Antistatic Agents and Components. *Handbook of Antistatics*, 421-431.

Rubab, M., Shahbaz, H., Olaimat, A., Oh, D., 2018. Biosensors for rapid and sensitive detection of *Staphylococcus aureus* in food. *Biosensors and Bioelectronics*, 105, 49-57.

Rucker, R., Morris, J., Fascetti, A., 2008. Vitamins. *Clinical Biochemistry of Domestic Animals*, 695-730.

Russo, V., Tammaro, L., Di Marcantonio, L., Sorrentino, A., Ancora, M., Valbonetti, L., Turriani, M., Martelli, A., Cammà, C., Barboni, B., 2016. Amniotic epithelial stem cell biocompatibility for electrospun poly(lactide- co -glycolide), poly(ϵ -caprolactone), poly(lactic acid) scaffolds. *Materials Science and Engineering: C*, 69, 321-329.

Ryan, C., Smith, K., Stark, J., 2012. The influence of geometry on the flow rate sensitivity to applied voltage within cone-jet mode electrospray. *Journal of Applied Physics*, 112, 1-7.

Sabin, C., 2013. Do people with HIV infection have a normal life expectancy in the era of combination antiretroviral therapy?. *BMC Medicine*, 11.

Sada, R., Fukuda, S., Ishimaru, H., 2017. Toxic shock syndrome due to community-acquired methicillin-resistant *Staphylococcus aureus* infection: Two case reports and a literature review in Japan. *IDCases*, 8, 77-80.

Saeb, A., Alshammari, A., Al-Brahim, H., Al-Rubeaan, K., 2014. Production of Silver Nanoparticles with Strong and Stable Antimicrobial Activity against Highly Pathogenic and Multidrug Resistant Bacteria.

Salomoni, R., Léo, P., Montemor, A., Rinaldi, B., Rodrigues, M., 2017. Antibacterial effect of silver nanoparticles in *Pseudomonas aeruginosa*, *Nanotechnology, Science and Applications*, 10, 115-121.

Samson, J., Moineau, S., 2013. Bacteriophages in Food Fermentations: New Frontiers in a Continuous Arms Race. *Annual Review of Food Science and Technology*, 4, 347-368.

Sandle, T., 2016. Antibiotics and preservatives. *Pharmaceutical Microbiology*, 171-183.

Santhoshkumara, T., Rahumana, A., Jayaseelana, C., Rajakumara, G., Marimuthua, S., Kirthia, A., Velayuthama, K., Thomasb, J., Venkatesanc, J., Kim, S., 2017. Green synthesis of titanium dioxide nanoparticles using *Psidium guajava* extract and its antibacterial and antioxidant properties. *Asian Pacific Journal of Tropical Medicine*, 7, 968-976.

Santos, C., Albuquerque, A., Sampaio, F., Keyson, D., 2013. Nanomaterials with Antimicrobial Properties: Applications in Health Sciences. In: *Microbial pathogens and strategies for combating them: science, technology and education* (A. Méndez-Vilas, Ed.). FORMATEX, 143-154.

Satyavani, K., Gurudeeban, S., Ramanathan, T., Balasubramanian, T., 2012. Toxicity Study of Silver Nanoparticles Synthesized from *Suaeda monoica* on Hep-2 Cell Line. *Avicenna Journal of Medical Biotechnology*, 4, 35-39.

Schindler, B., Kaatz, G., 2016. Multidrug efflux pumps of Gram-positive bacteria. *Drug Resistance Updates*, 27, 1-13.

Schreuder-Gibson, H., Gibson, P., Senecal, K., Sennett, M., Walker, J., Yeomans, W., Ziegler, D., Tsai, P., 2002. Protective textile materials based on electrospun nanofibers. *Journal of Advanced Materials*, 34, 44-55.

Schwarz, S., Kehrenberg, C., Doublet, B., Cloeckaert, A., 2004. Molecular basis of bacterial resistance to chloramphenicol and florfenicol. *FEMS Microbiology Reviews*, 28, 519-542.

Seyyed Mousavi, M., Mehramuz, B., Sadeghi, J., Alizadeh, N., Oskouee, M., Kafil, H., 2017. The pathogenesis of *Staphylococcus aureus* in autoimmune diseases. *Microbial Pathogenesis*, 111, 503-507.

Shahbaz, H., Yoo, S., Seo, B., Ghafoor, K., Kim, J., Lee, D., Park, J., 2015. Combination of TiO₂-UV Photocatalysis and High Hydrostatic Pressure to Inactivate Bacterial Pathogens and Yeast in Commercial Apple Juice. *Food and Bioprocess Technology*, 9, 182-190.

Shahverdi, A., Fakhimi, A., Shahverdi, H., Minaian, S., 2007. Synthesis and effect of silver nanoparticles on the antibacterial activity of different antibiotics against *Staphylococcus aureus* and *Escherichia coli*. *Nanomedicine: Nanotechnology, Biology and Medicine*, 3, 168-171.

Shams, T., Illangakoon, U., Parhizkar, M., Harker, A., Edirisinghe, S., Orlu, M., Edirisinghe, M., 2018. Electrospayed microparticles for intestinal delivery of prednisolone. *Journal of The Royal Society Interface*, 15, 20180491.

Shao, H., Fang, J., Wang, H., Lin, T., 2015. Effect of electrospinning parameters and polymer concentrations on mechanical-to-electrical energy conversion of randomly-oriented electrospun poly(vinylidene fluoride) nanofiber mats. *RSC Advances*, 5, 14345-14350.

Sharma, V., Yngard, R., Lin, Y., 2009. Silver nanoparticles: Green synthesis and their antimicrobial activities. *Advances in Colloid and Interface Science*, 145, 83-96.

Sheerin, N., 2011. Urinary tract infection. *Medicine*, 39, 384-389.

Shenoy, S., Bates, W., Frisch, H., Wnek, G., 2005. Role of chain entanglements on fiber formation during electrospinning of polymer solutions: good solvent, non-specific polymer–polymer interaction limit. *Polymer*, 46, 3372-3384.

Shrestha, A., Dorevitch, S., 2019. Evaluation of rapid qPCR method for quantification of *E. coli* at non-point source impacted Lake Michigan beaches. *Water Research*, 156, 395-403.

Shrivastava, S., Bera, T., Roy, A., Singh, G., Ramachandrarao, P., Dash, D. 2007. Characterization of enhanced antibacterial effects of novel silver nanoparticles. *Nanotechnology*, 18, 225103.

Sill, T., von Recum, H., 2008. Electrospinning: Applications in drug delivery and tissue engineering. *Biomaterials*, 29, 1989-2006.

Silva, A., Cardoso, B., Silva, M., Freitas, R., Sousa, R., 2015. Synthesis, Characterization, and Study of PLGA Copolymer & Degradation. *Journal of Biomaterials and Nanobiotechnology*, 06, 8-19.

Silvero C., M., Rocca, D., de la Villarmois, E., Fournier, K., Lanterna, A., Pérez, M., Becerra, M., Scaiano, J., 2018. Selective Photoinduced Antibacterial Activity of Amoxicillin-Coated Gold Nanoparticles: From One-Step Synthesis to in Vivo Cytocompatibility. *ACS Omega*, 3, 1220-1230.

Singhvi and Singh, 2011. Review: In-vitro drug release characterisation models. *International journal of pharmaceutical studies and research*, 2, 77-84.

Smith, D., Reneker, D., McManus, A., Schreuder-Gibson, H., Mello, C., Sennett, M., Gibson, P., 2001. Electrospun Fibers and an Apparatus Therefore. PCT International Application No: PCT/US00/27776.

Sofokleous, P., Stride, E., Edirisinghe, M., 2013. Preparation, Characterization, and Release of Amoxicillin from Electrospun Fibrous Wound Dressing Patches. *Pharmaceutical Research*, 30, 1926-1938.

Sood, S., Nagpal, M., 2013. Role of curcumin in systemic and oral health: An overview. *Journal of Natural Science, Biology and Medicine*, 4, 3.

Sousa, F., Luzardo-Álvarez, A., Pérez-Estévez, A., Seoane-Prado, R., Blanco-Méndez, J., 2010. Development of a novel AMX-loaded PLGA/zein microsphere for root canal disinfection. *Biomedical Materials*, 5, 055008.

Steckiewicz, K., Barcinska, E., Malankowska, A., Zauszkiewicz-Pawlak, A., Nowaczyk, G., Zaleska-Medynska, A., Inkielewicz-Stepniak, I., 2019. Impact of gold nanoparticles shape on their cytotoxicity against human osteoblast and osteosarcoma in in vitro model. Evaluation of the safety of use and anti-cancer potential. *Journal of Materials Science: Materials in Medicine*, 30.

Stevens, D., 2003. Community-acquired *Staphylococcus aureus* infections: increasing virulence and emerging methicillin resistance in the new millennium. *Current Opinion in Infectious Diseases*, 16, 189-191.

Sun S., Liu, P., Shao, F., Miao, Q., 2015. Formulation and evaluation of PLGA nanoparticles loaded capecitabine for prostate cancer. *International journal of clinical and experimental medicine*, 8, 19670-19681.

Sun, Y., Yin, Y., Mayers, B., Herricks, T., Xia, Y., 2002. Uniform Silver Nanowires Synthesis by Reducing AgNO₃ with Ethylene Glycol in the Presence of Seeds and Poly(Vinyl Pyrrolidone). *Chemistry of Materials*, 14, 4736-4745.

Surwade, P., Ghildyal, C., Weikel, C., Luxton, T., Peloquin, D., Fan, X., Shah, V., 2018. Augmented antibacterial activity of ampicillin with silver nanoparticles against methicillin-resistant *Staphylococcus aureus* (MRSA). *The Journal of Antibiotics*, 72, 50-53.

Sussman, M., 2015. Urinary Tract Infections. *Molecular Medical Microbiology*, 1365-1371.

Szekely, G., Didaskalou, C., 2016. Biomimics of Metalloenzymes via Imprinting. *Molecularly Imprinted Catalysts*, 121-158.

Takahashi, C., Ogawa, N., Kawashima, Y., Yamamoto, H., 2015. Observation of antibacterial effect of biodegradable polymeric nanoparticles on *Staphylococcus epidermidis* biofilm using FE-SEM with an ionic liquid. *Microscopy*, 64, 169-180.

Tao, F., Miao, J., Shi, G., Zhang, K., 2005. Ethanol fermentation by an acid-tolerant *Zymomonas mobilis* under non-sterilized condition. *Process Biochemistry*, 40, 183-187.

Tapia-Hernández, J.A., Rodríguez-Félix, D.E., Plascencia-Jatomea, M., Rascón-Chu, A., López-Ahumada, G.A., Ruiz-Cruz, S., Barreras-Urbina, C.G., Rodríguez-Félix, F., 2003. Porous wheat gluten microparticles obtained by electrospray: preparation and characterization. *Adv. Polym. Technol.*, 1-11.

Templeton, S., Buskirk, A., Green, B., Beezhold, D., Schmechel, D., 2010. Murine models of airway fungal exposure and allergic sensitization. *Medical Mycology*, 48, 217-228.

Tenaillon, O., Skurnik, D., Picard, B., Denamur, E., 2010. The population genetics of commensal *Escherichia coli*. *Nature Review Microbiology*, 8, 207-217.

Theron, A., Zussman, E., Yarin, A., 2001. Electrostatic field-assisted alignment of electrospun nanofibres. *Nanotechnology*, 12, 384-390.

Torres, R., Segura-Bailón, B., Lapidus, G., 2018. Effect of temperature on copper, iron and lead leaching from e-waste using citrate solutions. *Waste Management*, 71, 420-425.

Townsend-Nicholson, A., Jayasinghe, S., 2006. Cell Electrospinning: a Unique Biotechnology for Encapsulating Living Organisms for Generating Active Biological Microthreads/Scaffolds. *Biomacromolecules*, 7, 3364-3369.

Tsai, P., Schreuder-Gibson, H., 2001. Effect of electrospinning material and conditions upon residual electrostatic charge of polymer nanofibers. *Journal of Textile Apparel, Technology Management*, 1.

Tuhkanen, T., Ignatev, A., 2018. Humic and Fulvic Compounds. Reference Module in Chemistry, Molecular Sciences and Chemical Engineering.

Tulchinsky, T., Varavikova, E., 2014. Communicable Diseases. *The New Public Health*, 149-236.

Tulkens, P., 1991. Intracellular distribution and activity of antibiotics. *European Journal of Clinical Microbiology and Infectious Diseases*, 10, 100–106.

Twaroch, T., Curin, M., Valenta, R., Swoboda, I., 2015. Mold Allergens in Respiratory Allergy: From Structure to Therapy. *Allergy, Asthma & Immunology Research*, 7, 205.

Tyagi, H., Kushwaha, A., Kumar, A., Aslam, M., 2016. A Facile pH Controlled Citrate-Based Reduction Method for Gold Nanoparticle Synthesis at Room Temperature. *Nanoscale Research Letters*, 11.

Ulevitch, R., Tobias, P., 1999. Recognition of Gram-negative bacteria and endotoxin by the innate immune system. *Current Opinion in Immunology*, 11, 19-22.

Undurraga, E., Halasa, Y., Shepard, D., 2016. Economic Analysis of Genetically Modified Mosquito Strategies. *Genetic Control of Malaria and Dengue*, 375-408.

Uysal, O., Sevimli, T., Sevimli, M., Gunes, S., Eker Sariboyaci, A., 2018. Cell and Tissue Culture. *Omics Technologies and Bio-Engineering*, 391-429.

Valenti, L., Giacomelli, C., 2017. Stability of silver nanoparticles: agglomeration and oxidation in biological relevant conditions. *Journal of Nanoparticle Research*, 19.

van Hal, S., Jensen, S., Vaska, V., Espedido, B., Paterson, D., Gosbell, I., 2012. Predictors of Mortality in *Staphylococcus aureus* Bacteremia. *Clinical Microbiology Reviews*, 25, 362-386.

van Loo, I., Huijsdens, X., Tiemersma, E., de Neeling, A., van de Sande-Bruinsma, N., Beaujean, D., Voss, A., Kluytmans, J., 2007. Emergence of Methicillin-Resistant *Staphylococcus aureus* of Animal Origin in Humans. *Emerging Infectious Diseases*, 13, 1834-1839.

Vedha Hari, B., Narayanan, N., Dhevedaran, K., 2015. Efavirenz–eudragit E-100 nanoparticle-loaded aerosol foam for sustained release: in-vitro and ex-vivo evaluation. *Chemical Papers*, 69.

Velegraki, A., Cafarchia, C., Gaitanis, G., Iatta, R., Boekhout, T., 2015. *Malassezia* Infections in Humans and Animals: Pathophysiology, Detection, and Treatment. *PLoS Pathogens*, 11, 1004523.

Verreck, G., Chun, I., Peeters, J., Rosenblatt, J., Brewster, M., 2003. Preparation and characterization of nanofibers containing amorphous drug dispersions generated by electrostatic spinning. *Pharmaceutical Research*, 20, 810-817.

Vigil, K., Adachi, J., Chemaly, R., 2010. Analytic Review: Viral Pneumonias in Immunocompromised Adult Hosts. *Journal of Intensive Care Medicine*, 25, 307-326.

Vijayakumar, S., Ganesan, S., 2012. In Vitro Cytotoxicity Assay on Gold Nanoparticles with Different Stabilizing Agents. *Journal of Nanomaterials*, 2012.

Visnapuu, M., Joost, U., Juganson, K., Künis-Beres, K., Kahru, A., Kisand, V., Ivask, A., 2013. Dissolution of Silver Nanowires and Nanospheres Dictates Their Toxicity to *Escherichia coli*. *BioMed Research International*, 2013, 1-9.

Vukomanovic, M., Torrents, E., 2019. High time resolution and high signal-to-noise monitoring of the bacterial growth kinetics in the presence of plasmonic nanoparticles. *Journal of Nanobiotechnology*, 17.

Wahyudiono, Ozawa, H., Machmudah, S., Kanda, H., Goto, M., 2019. Electro spraying technique under pressurized carbon dioxide for hollow particle production. *Reactive and Functional Polymers*, 142, 44-52.

Walker, A., Fodor, E., 2019. Interplay between Influenza Virus and the Host RNA Polymerase II Transcriptional Machinery. *Trends in Microbiology*, 27, 398-407.

Wan, G., Ruan, L., Yin, Y., Yang, T., Ge, M., Cheng, X., 2016. Effects of silver nanoparticles in combination with antibiotics on the resistant bacteria *Acinetobacter baumannii*. *International Journal of Nanomedicine*, 11, 3789-3800.

Wang, C., Huang, X., Deng, W., Chang, C., Hang, R., Tang, B., 2014. A nano-silver composite based on the ion-exchange response for the intelligent antibacterial applications. *Materials Science and Engineering: C*, 41, 134-141.

Wang, H., Jiang, Y., Zhang, Y., Zhang, Z., Yang, X., Ali, M., Fox, E., Gobius, K., Man, C., 2018. Silver nanoparticles: A novel antibacterial agent for control of *Cronobacter sakazakii*. *Journal of Dairy Science*, 101, 10775-10791.

Wang, L., Hu, C., Shao, L., 2017. The antimicrobial activity of nanoparticles: present situation and prospects for the future. *International Journal of Nanomedicine*, 12, 1227-1249.

Wang, Y., Strohm, E., Sun, Y., Wang, Z., Zheng, Y., Wang, Z., Kolios, M., 2016. Biodegradable polymeric nanoparticles containing gold nanoparticles and Paclitaxel for cancer imaging and drug delivery using photoacoustic methods. *Biomedical Optics Express*, 7, 4125.

Wayne, J., McDowell, C., Shields, K., Tuan, R., 2005. In Vivo Response of Polylactic Acid–Alginate Scaffolds and Bone Marrow-Derived Cells for Cartilage Tissue Engineering. *Tissue Engineering*, 11, 953-963.

Wegman, M., Janssen, M., van Rantwijk, F., Sheldon, R., 2001. Towards Biocatalytic Synthesis of β -Lactam Antibiotics. *Advanced Synthesis & Catalysis*, 343, 559-576.

Weledji, E., 2013. Human immunodeficiency virus and the anorectum. *Alexandria Journal of Medicine*, 49, 163-167.

Wernick, D., Pontrelli, S., Pollock, A., Liao, J., 2016. Sustainable biorefining in wastewater by engineered extreme alkaliphile *Bacillus marmarensis*. *Scientific Reports*, 6, 20224.

Wheeler, M., Limon, J., Bar, A., Leal, C., Gargus, M., Tang, J., Brown, J., Funari, V., Wang, H., Crother, T., Arditi, M., Underhill, D., Iliev, I., 2016. Immunological Consequences of Intestinal Fungal Dysbiosis. *Cell Host & Microbe*, 19, 865-873.

Wiley, B., Xiong, Y., Li, Z., Yin, Y., Xia, Y., 2006. Right Bipyramids of Silver: A New Shape Derived from Single Twinned Seeds. *Nano Letters*, 6, 765-768.

Wilks, J., Beilinson, H., Golovkina, T., 2013. Dual role of commensal bacteria in viral infections. *Immunological Reviews*, 255, 222-229.

Wilson, G., Seo, K., Cartwright, R., Connelley, T., Chuang-Smith, O., Merriman, J., Guinane, C., Park, J., Bohach, G., Schlievert, P., Morrison, W., Fitzgerald, J., 2011. A Novel Core Genome-Encoded Superantigen Contributes to Lethality of Community-Associated MRSA Necrotizing Pneumonia. *PLoS Pathogens*, 7.

Worsfold, P., Zagatto, E., 2017. Spectrophotometry: Overview. Reference Module in Chemistry, Molecular Sciences and Chemical Engineering.

Wu, Y., Duong, A., James Lee, L., Wyslouzil, B., 2012. Electrospray Production of Nanoparticles for Drug/Nucleic Acid Delivery. *The Delivery of Nanoparticles*, 10, 223-243.

Xia, J., Wang, W., Hai, X., E, S., Shu, Y., Wang, J., 2019. Improvement of antibacterial activity of copper nanoclusters for selective inhibition on the growth of gram-positive bacteria. *Chinese Chemical Letters*, 30, 421-424.

Xie, J., Jiang, J., Davoodi, P., Srinivasan, M., Wang, C., 2015. Electrohydrodynamic atomization: A two-decade effort to produce and process micro-/nanoparticulate materials. *Chemical Engineering Science*, 125, 32-57.

Xie, J., Marijnissen, J., Wang, C., 2006. Microparticles developed by electrohydrodynamic atomization for the local delivery of anticancer drug to treat C6 glioma in vitro. *Biomaterials*, 27, 3321-3332.

Xie, Y., He, Y., Irwin, P., Jin, T., Shi, X., 2011. Antibacterial Activity and Mechanism of Action of Zinc Oxide Nanoparticles against *Campylobacter jejuni*. *Appl. Environ. Microbiol.* 77, 2325-2331.

Xu, Q., Czernuszka, J., 2008. Controlled release of amoxicillin from hydroxyapatite-coated poly(lactic-co-glycolic acid) microspheres. *Journal of Controlled Release*, 127, 146-153.

Xu, X., Yang, Q., Wang, Y., Yu, H., Chen, X. and Jing, X. (2006). Biodegradable electrospun poly(l-lactide) fibers containing antibacterial silver nanoparticles. *European Polymer Journal*, 42(9), pp.2081-2087.

Xue, K., Moncla, L., Bedford, T., Bloom, J., 2018. Within-Host Evolution of Human Influenza Virus. *Trends in Microbiology*, 26, 781-793.

Yacoub, S., Farrar, J., 2014. Dengue. *Manson's Tropical Infectious Diseases*, 162-170.

Yadav, Jyoti, 2018. Synthesis and Characterization of Gold Nanoparticles. *International Journal on Future Revolution in Computer Science & Communication Engineering*, 4.

Yadav, R., Kumar, A., Singh, V., Jayshree, Yadav, S., 2018. Prevalence and antibiotyping of *Staphylococcus aureus* and methicillin-resistant *S. aureus* (MRSA) in domestic animals in India. *Journal of Global Antimicrobial Resistance*, 15, 222-225.

Yan, S., Jiang, C., Guo, J., Fan, Y., Zhang, Y., 2019. Synthesis of Silver Nanoparticles Loaded onto Polymer-Inorganic Composite Materials and Their Regulated Catalytic Activity. *Polymers*, 11, 401.

Yandrapu, S., Kompella, U., 2013. Development of Sustained-Release Microspheres for the Delivery of SAR 1118, an LFA-1 Antagonist Intended for the Treatment of Vascular Complications of the Eye. *Journal of Ocular Pharmacology and Therapeutics*, 29, 236-248.

Yang, F., Chang, T., Liu, T., Wu, D., Du, H., Liang, J., Tian, F., 2019. Label-free detection of *Staphylococcus aureus* bacteria using long-period fiber gratings with functional polyelectrolyte coatings. *Biosensors and Bioelectronics*, 133, 147-153.

Yang, Z., Qian, H., Chen, H., Anker, J., 2010. One-pot hydrothermal synthesis of silver nanowires via citrate reduction. *Journal of Colloid and Interface Science*, 352, 285-291.

Yoo, H., Lee, E., Yoon, J., Park, T., 2005. Hyaluronic acid modified biodegradable scaffolds for cartilage tissue engineering. *Biomaterials*, 26, 1925-1933.

Yuliza, E., Murniati, R., Rajak, A., Khairurrijal, K., Abdullah, M., 2014. Effect of Particle Size on the Electrical Conductivity of Metallic Particles. *Proceedings of the 2014 International Conference on Advances in Education Technology*.

Zafar, Nosheen, Shamaila, Shahzadi, Khalid, Hina, 2015. Synthesis of Copper Nanoparticles by Chemical Reduction Method.

Zajmi, A., Mohd Hashim, N., Noordin, M., Khalifa, S., Ramli, F., Mohd Ali, H., El-Seedi, H., 2015. Ultrastructural Study on the Antibacterial Activity of Artonin E versus Streptomycin against *Staphylococcus aureus* Strains. *PLOS ONE*, 10, 0128157.

Zeng, J., Xu, X., Chen, X., Liang, Q., Bian, X., Yang, L., Jing, X., 2003. Biodegradable electrospun fibers for drug delivery. *Journal of Controlled Release*, 92, 227-231.

Zetola, N., Francis, J., Nuermberger, E., Bishai, W., 2005. Community-acquired meticillin-resistant *Staphylococcus aureus*: an emerging threat. *The Lancet Infectious Diseases*, 5, 275-286.

Zeugolis, D., Khew, S., Yew, E., Ekaputra, A., Tong, Y., Yung, L., Hutmacher, D., Sheppard, C., Raghunath, M., 2008. Electro-spinning of pure collagen nano-fibres – Just an expensive way to make gelatin?. *Biomaterials*, 29, 2293-2305.

Zhang, C., Yuan, X., Wu, L., Han, Y., Sheng, J. 2005. Study on morphology of electrospun poly(vinyl alcohol) mats. *European Polymer Journal*, 41, 423-432.

Zhang, J., Chen, Y., Miller, K., Ganewatta, M., Bam, M., Yan, Y., Nagarkatti, M., Decho, A., Tang, C., 2014. Antimicrobial Metallopolymers and Their Bioconjugates with Conventional Antibiotics against Multidrug-Resistant Bacteria. *Journal of the American Chemical Society*, 136, 4873-4876.

Zhang, J., Hoshino, K., 2019. Optical transducers: Optical molecular sensing and spectroscopy. *Molecular Sensors and Nanodevices*, 231-309.

Zhang, J., Oueslati, R., Cheng, C., Zhao, L., Chen, J., Almeida, R., Wu, J., 2018. Rapid, highly sensitive detection of Gram-negative bacteria with lipopolysaccharide based disposable aptasensor. *Biosensors and Bioelectronics*, 112, 48-53.

Zhang, L., Wang, Z., Xiao, Y., Liu, P., Wang, S., Zhao, Y., Shen, M. and Shi, X., 2018. Electrospun PEGylated PLGA nanofibers for drug encapsulation and release.

Zhang, S., Shim, W., Kim, J., 2009. Design of ultra-fine nonwovens via electrospinning of Nylon 6: Spinning parameters and filtration efficiency. *Materials & Design*, 30, 3659-3666.

Zhang, S., Tang, Y., Vlahovic, B., 2016. A Review on Preparation and Applications of Silver-Containing Nanofibers. *Nanoscale Research Letters*, 11.

Zhang, X., 2015. Gold Nanoparticles: Recent Advances in the Biomedical Applications. *Cell Biochemistry and Biophysics*, 72, 771-775.

Zhang, X., Xue, X., Zhou, H., Zhao, N., Shan, F., Su, D., Liu, Y., Zhang, T., 2018. Seeds screening aqueous synthesis, multiphase interfacial separation and in situ optical characterization of invisible ultrathin silver nanowires. *Nanoscale*, 10, 15468-15484.

Zhang, Z., Wu, Y., Wang, Z., Zhang, X., Zhao, Y., Sun, L., 2017. Electrospinning of Ag Nanowires/polyvinyl alcohol hybrid nanofibers for their antibacterial properties. *Materials Science and Engineering: C*, 78, 706-714.

Zheng, F., Wang, S., Wen, S., Shen, M., Zhu, M., Shi, X., 2013. Characterization and antibacterial activity of amoxicillin-loaded electrospun nano-hydroxyapatite/poly(lactic-co-glycolic acid) composite nanofibers. *Biomaterials*, 34, 1402-1412.

Zheng, L., Lin, Y., Lu, S., Zhang, J., Bogdanov, M., 2017. Biogenesis, transport and remodeling of lysophospholipids in Gram-negative bacteria. *Biochimica et Biophysica Acta (BBA) - Molecular and Cell Biology of Lipids*, 1862, 1404-1413.

Zhong, S., Teo, W., Zhu, X., Beuerman, R., Ramakrishna, S., Yung, L., 2006. An aligned nanofibrous collagen scaffold by electrospinning and its effects on in vitro fibroblast culture. *Journal of Biomedical Materials Research Part A*, 79, 456-463.

Zhou, Y., Kong, Y., Kundu, S., Cirillo, J., Liang, H., 2012. Antibacterial activities of gold and silver nanoparticles against *Escherichia coli* and *Bacillus Calmette-Guérin*. *Journal of Nanobiotechnology*, 10, 19.

Zia, R., Riaz, M., Farooq, N., Qamar, A., Anjum, S., 2018. Antibacterial activity of Ag and Cu nanoparticles synthesized by chemical reduction method: a comparative analysis. *Materials Research Express*, 5, 075012.

Zikalala, N., Matshetshe, K., Parani, S., Oluwafemi, O., 2018. Biosynthesis protocols for colloidal metal oxide nanoparticles. *Nano-Structures & Nano-Objects*, 16, 288-299.

Zimmel, D., 2014. Urinary Tract Infections. *Equine Infectious Diseases*, 106-109.

Zong, H., Xia, X., Liang, Y., Dai, S., Alsaedi, A., Hayat, T., Kong, F., Pan, J., 2018. Designing function-oriented artificial nanomaterials and membranes via electrospinning and electrospaying techniques. *Materials Science and Engineering: C*, 92, 1075-1091.

Zong, X., Fang, D., Kim, K., Ran, S., Hsiao, B.S., Chu, B., Brathwaite, C., Li, S., Chen, E., 2002. Nonwoven nanofiber membranes of poly(lactide) and poly(glycolide-co-lactide) via electrospinning and applications for anti-adhesions. *American Chemical Society*, 43, 659-660.

Zubair, S., Fischer, A., Liljander, A., Meens, J., Hegerman, J., Gourelé, H., Bishop, R., Roebbelen, I., Younan, M., Mustafa, M., Mushtaq, M., Bongcam-Rudloff, E., Jores, J., 2015. Complete genome sequence of *Staphylococcus aureus*, strain ILRI_Eymole1/1, isolated from a Kenyan dromedary camel. *Standards in Genomic Sciences*, 10.

Zussman, E., Yarin, A., Weihs, D., 2002. A micro-aerodynamic decelerator based on permeable surfaces of nanofiber mats. *Experiments in Fluids*, 33, 315-320.

Zyoud, A., Alkowni, R., Yousef, O., Salman, M., Hamdan, S., Helal, M., Jaber, S., Hilal, H., 2019. Solar light-driven complete mineralization of aqueous gram-positive and gram-negative bacteria with ZnO photocatalyst. *Solar Energy*, 180, 351-359.